



Universidade do Estado do Rio de Janeiro

Faculdade de Engenharia Mecânica

Leon Matos Ribeiro de Lima

**Dynamic Behavior of Single-Phase Natural Convection
Loops Integrated to a Pool**

Rio de Janeiro
2016

Leon Matos Ribeiro de Lima

Dynamic Behavior of Single-Phase Natural Convection Loops Integrated to a Pool

Tese apresentada como requisito parcial para obtenção do título de Doutor em Ciências, ao Programa de Pós-Graduação em Engenharia Mecânica, da Universidade do Estado do Rio de Janeiro. Área de concentração: Fenômenos de Transporte.



Prof. Norberto Mangiavacchi, PhD
Prof. José da Rocha Miranda Pontes, PhD

Rio de Janeiro
2016

RESUMO

LIMA, Leon. *Dynamic Behavior of Single-Phase Natural Convection Loops Integrated to a Pool*. Brasil. 2016. 146f. Dissertação (Doutorado em Engenharia Mecânica) – Faculdade de Engenharia Mecânica, Universidade do Estado do Rio de Janeiro, Rio de Janeiro, 2016.

Sistemas passivos de resfriamento têm aplicações em diversas áreas da engenharia. A indústria nuclear de potência tem buscado a incorporação desses sistemas em novos projetos, na busca de elevar ainda mais os níveis de segurança. Circuitos de convecção natural são sistemas passivos de resfriamento compostos por dois trocadores de calor – um aquecedor e um arrefecedor – e um circuito de interconexão, onde o calor é absorvido no aquecedor e rejeitado no arrefecedor. Na maioria dos projetos, esse arranjo é conectado a uma piscina, que troca calor com o circuito. Circuitos de convecção natural são objeto de pesquisa em muitos trabalhos científicos, porém não integrados à piscina. Este trabalho apresenta um estudo computacional do comportamento dinâmico de circuitos de convecção natural monofásicos integrados a uma piscina, com foco na estabilidade termo-hidráulica do sistema. Métodos de análise linear e não-linear de estabilidade são empregados para caracterizar a dinâmica do sistema. Os resultados indicam relevante influência da piscina, que aumenta as regiões de estabilidade de forma significativa.

Palavras-chave: *Sistemas Passivos de Resfriamento, Circuitos de Convecção Natural, Modelagem Numérica, Análise de estabilidade.*

ABSTRACT

Passive cooling systems find application on many areas of engineering. Nuclear power industry is incorporating such system in new power plant designs, with objective to achieve higher safety levels of operation. Natural convection loops are passive cooling systems consisting of two heat exchangers – a heater and a cooler – a connecting circuit, where heat is absorbed in the heater and rejected in the cooler. In most of designs, the circuit is connected to a pool which transfers heat from/to it. Natural convection loops are the research topic of many scientific works. The connection to the pool, however, is not taken into account. The present work presents a computational study of the dynamic behavior of single-phase natural convection loops integrated to a pool, with focus on the thermo-hydraulic stability. Linear and non-linear analyses are performed in order to characterize the system dynamics. Results indicate a relevant contribution of the pool, significantly enlarging stability regions.

Keywords: *Passive Cooling Systems, Natural Convection Loops, Numerical modeling, Stability analysis.*

LIST OF FIGURES

1	Sketch of Passive Cooling System consisting of a Natural Convection Loop coupled to a pool.	12
2	DKW-Vemag Belcar. This car was manufactured in Brazil from 1958 to 1967 by Vemag, under license of German company DKW (which stands for Dampf Kraft Wagen, i.e., Steam Power Car).	13
3	Passive cooling systems in current commercial nuclear reactors. On the left side: AP1000, from Westinghouse. Passive system guarantees the reactor cooling for 72 hours without any human intervention. Image extracted from Westinghouse website , accessed on 2016-Jun-03. On the right side: ESBWR (Economic Simplified Boiling Water Reactor), from GE-Hitachi. Operational reactor cooling is performed by natural convection. Image extracted from GE-Hitachi website , accessed on 2016-Jun-03.	14
1.1	Instability types according to Prasad et al. [31].	21
2.1	Flexible loop with possibility to operate with horizontal or vertical heater and cooler.	27
3.1	Comparison of friction correlations, taking into account $D = 26.9$ mm and $e = 10^{-7}$ (wall roughness).	39
3.2	Comparison of friction correlation in the transitional region $1500 \leq \text{Re} \leq 4000$	39
3.3	Extraction from Naveen et al. [27] showing a sketch of the experimental NCL.	41
3.4	Steady state for a range operating points.	41
3.5	Steady state for a range operating points.	42
3.6	Sketch representing the experimental loop built at Bhabha Research Atomic Centre, India.	43
3.7	Steady state data from numerical and experimental tests for HHHC loop configuration.	44

3.8	Steady state data from numerical and experimental tests for HHVC loop configuration.	44
3.9	Steady state data from numerical and experimental tests for VHHC loop configuration.	45
3.10	Steady state data from numerical and experimental tests for VHVC loop configuration.	45
3.11	Comparison of the six friction factor correlations and the theoretical friction factor according to eq. 3.22.	47
4.1	Example of fitting of level curve for VHVC configuration and $\psi = 100$. for this case was $R^2 = 0.8928$	55
4.2	Stability map for HHHC 800 mm diameter loop with and without pool. .	55
4.3	Stability map for HHVC 800 mm diameter loop with and without pool. .	56
4.4	Stability map for VHHC 800 mm diameter loop with and without pool. .	56
4.5	Stability map for VHVC 800 mm diameter loop with and without pool. .	57
4.6	Surface $\max[\text{real}(\lambda)] = F(\text{St}, \psi)$	58
4.7	Stability map on $\text{St} - \psi$ plane for HHHC 800 mm diameter loop.	59
4.8	Stability map on $\text{St} - \psi$ plane for HHVC 800 mm diameter loop.	59
4.9	Stability map on $\text{St} - \psi$ plane for VHHC 800 mm diameter loop.	60
4.10	Stability map on $\text{St} - \psi$ plane for VHVC 800 mm diameter loop.	60
4.11	Points selected in stability maps for simulation of effect of ψ on system stability.	62
4.12	Effect of amount of water on the stability of NCL for the four orientations of heater/cooler.	62
4.13	Effect of amount of water on the stability of NCL for the four orientations of heater/cooler.	62
4.14	Effect of amount of water on the stability of NCL for the four orientations of heater/cooler.	63
5.1	Effect of magnitude of perturbation on transient mass flow rate for a stable system.	67
5.2	Effect of magnitude of perturbation on transient mass flow rate for a stable system: frequency domain for -16% perturbation.	67
5.3	Effect of magnitude of perturbation on transient mass flow rate for a stable system: frequency domain for -40% perturbation.	68

5.4	Effect of magnitude of perturbation on transient mass flow rate for a stable system: frequency domain for -100% perturbation.	68
5.5	Effect of magnitude of perturbation on transient mass flow rate for an unstable system.	69
5.6	Effect of magnitude of perturbation on transient mass flow rate for an unstable system: frequency domain for -16% perturbation.	69
5.7	Effect of magnitude of perturbation on transient mass flow rate for an unstable system: frequency domain for -40% perturbation.	70
5.8	Effect of magnitude of perturbation on transient mass flow rate for an unstable system: frequency domain for -100% perturbation.	70
5.9	Points selected in stability maps for simulation loop transients.	72
5.10	Comparison of mass flow time series for the four orientations for system without pool, showing a reduction in oscillating amplitude as vertical components are added to the circuit. Operating point ($St = 25, Gr D/L = 10^{12}$).	74
5.11	Comparison of mass flow time series for the four orientations for NCLs with the pool. Operating point ($St = 25, Gr D/L = 10^{12}$).	75
5.12	Comparison of mass flow time series for the four orientations for NCLs with the pool. Operating point ($St = 10, Gr D/L = 10^{11}$)	76
5.13	Mass flow over time (left) and projection of phase space on the plane mass flow <i>vs</i> temperature difference across heater (right). Operating point ($St = 10, Gr D/L = 10^{11}$).	78
5.14	Detail of mass flow cycle (left) and the frequency spectrum of mass flow (right). Operating point ($St = 10, Gr D/L = 10^{11}$)	78
5.15	Extended time interval for simulation VHHC configuration ar $St = 10.1$, $Gr D/L = 10^{11}$ without pool.	79
5.16	Frequency spectra for the full time range (left) and for the time range after 200 thousand seconds (right). Operating point ($St = 10.1, Gr D/L = 10^{11}$).	80
5.17	Mass flow over time (left) and projection of phase space on the plane mass flow <i>vs</i> temperature difference across heater (right). Operating point ($St = 10.1, Gr D/L = 10^{11}$).	81
5.18	Detail of mass flow cycle (left) and the frequency spectrum of mass flow (right). Operating point ($St = 10.1, Gr D/L = 10^{11}$)	81
5.19	Typical curve of mean deviation between trajectories for unstable Lyapunov unstable point. Extracted from [29].	85

5.20 Deviation of mass flow rate for an unstable case (left) and a stable one (right).	86
A.1 Points selected in stability maps for simulation loop transients.	99
A.2 Transient mass flow rate for HHHC loop, St = 25, Gr $D/L = 10^{12}$, $\psi = 0$	100
A.3 Transient mass flow rate for HHHC loop, St = 25, Gr $D/L = 10^{12}$, $\psi = 1$	101
A.4 Space-time chart for temperature in HHHC loop, St = 25, Gr $D/L = 10^{12}$, $\psi = 0$	101
A.5 Space-time chart for temperature in HHHC loop, St = 25, Gr $D/L = 10^{12}$, $\psi = 1$	102
A.6 Comparison of time series for mass flow rate using $\psi = 0$ and $\psi = 1$, in HHHC loop, St = 25, Gr $D/L = 10^{12}$	102
A.7 Comparison of time series for temperature difference across heater using $\psi = 0$ and $\psi = 1$, in HHHC loop, St = 25, Gr $D/L = 10^{12}$	103
A.8 Transient mass flow rate for HHVC loop, St = 25, Gr $D/L = 10^{12}$, $\psi = 0$	103
A.9 Transient mass flow rate for HHVC loop, St = 25, Gr $D/L = 10^{12}$, $\psi = 1$	104
A.10 Space-time chart for temperature in HHVC loop, St = 25, Gr $D/L = 10^{12}$, $\psi = 0$	104
A.11 Space-time chart for temperature in HHVC loop, St = 25, Gr $D/L = 10^{12}$, $\psi = 1$	105
A.12 Comparison of time series for mass flow rate using $\psi = 0$ and $\psi = 1$, in HHVC loop, St = 25, Gr $D/L = 10^{12}$	105
A.13 Comparison of time series for temperature difference across heater using $\psi = 0$ and $\psi = 1$, in HHVC loop, St = 25, Gr $D/L = 10^{12}$	106
A.14 Transient mass flow rate for VHHC loop, St = 25, Gr $D/L = 10^{12}$, $\psi = 0$	106
A.15 Transient mass flow rate for VHHC loop, St = 25, Gr $D/L = 10^{12}$, $\psi = 1$	107
A.16 Space-time chart for temperature in VHHC loop, St = 25, Gr $D/L = 10^{12}$, $\psi = 0$	107
A.17 Space-time chart for temperature in VHHC loop, St = 25, Gr $D/L = 10^{12}$, $\psi = 1$	108
A.18 Comparison of time series for mass flow rate using $\psi = 0$ and $\psi = 1$, in VHHC loop, St = 25, Gr $D/L = 10^{12}$	108
A.19 Comparison of time series for temperature difference across heater using $\psi = 0$ and $\psi = 1$, in VHHC loop, St = 25, Gr $D/L = 10^{12}$	109
A.20 Transient mass flow rate for VHVC loop, St = 25, Gr $D/L = 10^{12}$, $\psi = 0$	109
A.21 Transient mass flow rate for VHVC loop, St = 25, Gr $D/L = 10^{12}$, $\psi = 1$	110

A.22 Space-time chart for temperature in VHVC loop, St = 25, Gr $D/L = 10^{12}$, $\psi = 0$.	110
A.23 Space-time chart for temperature in VHVC loop, St = 25, Gr $D/L = 10^{12}$, $\psi = 1$.	111
A.24 Comparison of time series for mass flow rate using $\psi = 0$ and $\psi = 1$, in VHVC loop, St = 25, Gr $D/L = 10^{12}$	111
A.25 Comparison of time series for temperature difference across heater using $\psi = 0$ and $\psi = 1$, in VHVC loop, St = 25, Gr $D/L = 10^{12}$.	112
A.26 Points selected in stability maps for simulation loop transients.	113
A.27 Transient mass flow rate for HHHC loop, St = 10, Gr $D/L = 10^{11}$, $\psi = 0$.	114
A.28 Transient mass flow rate for HHHC loop, St = 10, Gr $D/L = 10^{11}$, $\psi = 1$.	114
A.29 Frequency domain of mass flow for HHHC loop, St = 10, Gr $D/L = 10^{11}$, $\psi = 0$.	115
A.30 Frequency domain of mass flow for HHHC loop, St = 10, Gr $D/L = 10^{11}$, $\psi = 1$.	115
A.31 Space-time chart for temperature in HHHC loop, St = 10, Gr $D/L = 10^{11}$, $\psi = 0$.	116
A.32 Space-time chart for temperature in HHHC loop, St = 10, Gr $D/L = 10^{11}$, $\psi = 1$.	116
A.33 Comparison of time series for mass flow rate using $\psi = 0$ and $\psi = 1$, in HHHC loop, St = 10, Gr $D/L = 10^{11}$	117
A.34 Comparison of time series for temperature difference across heater using $\psi = 0$ and $\psi = 1$, in HHHC loop, St = 10, Gr $D/L = 10^{11}$.	117
A.35 Transient mass flow rate for HHVC loop, St = 10, Gr $D/L = 10^{11}$, $\psi = 0$.	118
A.36 Transient mass flow rate for HHVC loop, St = 10, Gr $D/L = 10^{11}$, $\psi = 1$.	118
A.37 Frequency domain of mass flow for HHVC loop, St = 10, Gr $D/L = 10^{11}$, $\psi = 0$.	119
A.38 Frequency domain of mass flow for HHVC loop, St = 10, Gr $D/L = 10^{11}$, $\psi = 1$.	119
A.39 Space-time chart for temperature in HHVC loop, St = 10, Gr $D/L = 10^{11}$, $\psi = 0$.	120
A.40 Space-time chart for temperature in HHVC loop, St = 10, Gr $D/L = 10^{11}$, $\psi = 1$.	120
A.41 Comparison of time series for mass flow rate using $\psi = 0$ and $\psi = 1$, in HHVC loop, St = 10, Gr $D/L = 10^{11}$	121

A.42 Comparison of time series for temperature difference across heater using $\psi = 0$ and $\psi = 1$, in HHVC loop, St = 10, Gr $D/L = 10^{11}$.	121
A.43 Transient mass flow rate for VHHC loop, St = 10, Gr $D/L = 10^{11}$, $\psi = 0$.	122
A.44 Transient mass flow rate for VHHC loop, St = 10, Gr $D/L = 10^{11}$, $\psi = 1$.	122
A.45 Frequency domain of mass flow for VHHC loop, St = 10, Gr $D/L = 10^{11}$, $\psi = 0$.	123
A.46 Frequency domain of mass flow for VHHC loop, St = 10, Gr $D/L = 10^{11}$, $\psi = 1$.	123
A.47 Space-time chart for temperature in VHHC loop, St = 10, Gr $D/L = 10^{11}$, $\psi = 0$.	124
A.48 Space-time chart for temperature in VHHC loop, St = 10, Gr $D/L = 10^{11}$, $\psi = 1$.	124
A.49 Comparison of time series for mass flow rate using $\psi = 0$ and $\psi = 1$, in VHHC loop, St = 10, Gr $D/L = 10^{11}$.	125
A.50 Comparison of time series for temperature difference across heater using $\psi = 0$ and $\psi = 1$, in VHHC loop, St = 10, Gr $D/L = 10^{11}$.	125
A.51 Transient mass flow rate for VHVC loop, St = 10, Gr $D/L = 10^{11}$, $\psi = 0$.	126
A.52 Transient mass flow rate for VHVC loop, St = 10, Gr $D/L = 10^{11}$, $\psi = 1$.	126
A.53 Frequency domain of mass flow for VHVC loop, St = 10, Gr $D/L = 10^{11}$, $\psi = 0$.	127
A.54 Frequency domain of mass flow for VHVC loop, St = 10, Gr $D/L = 10^{11}$, $\psi = 1$.	127
A.55 Space-time chart for temperature in VHVC loop, St = 10, Gr $D/L = 10^{11}$, $\psi = 0$.	128
A.56 Space-time chart for temperature in VHVC loop, St = 10, Gr $D/L = 10^{11}$, $\psi = 1$.	128
A.57 Comparison of time series for mass flow rate using $\psi = 0$ and $\psi = 1$, in VHVC loop, St = 10, Gr $D/L = 10^{11}$.	129
A.58 Comparison of time series for temperature difference across heater using $\psi = 0$ and $\psi = 1$, in VHVC loop, St = 10, Gr $D/L = 10^{11}$.	129
A.59 Points selected in stability maps for simulation loop transients.	130
A.60 Transient mass flow rate for HHHC loop, St = 2, Gr $D/L = 10^{11}$, $\psi = 0$.	131
A.61 Transient mass flow rate for HHHC loop, St = 2, Gr $D/L = 10^{11}$, $\psi = 1$.	131
A.62 Frequency domain of mass flow for HHHC loop, St = 2, Gr $D/L = 10^{11}$, $\psi = 0$.	132

A.63 Frequency domain of mass flow for HHHC loop, St = 2, Gr D/L = 10 ¹¹ , $\psi = 1$	132
A.64 Space-time chart for temperature in HHHC loop, St = 2, Gr D/L = 10 ¹¹ , $\psi = 0$	133
A.65 Space-time chart for temperature in HHHC loop, St = 2, Gr D/L = 10 ¹¹ , $\psi = 1$	133
A.66 Comparison of time series for mass flow rate using $\psi = 0$ and $\psi = 1$, in HHHC loop, St = 2, Gr D/L = 10 ¹¹	134
A.67 Comparison of time series for temperature difference across heater using $\psi = 0$ and $\psi = 1$, in HHHC loop, St = 2, Gr D/L = 10 ¹¹	134
A.68 Transient mass flow rate for HHVC loop, St = 2, Gr D/L = 10 ¹¹ , $\psi = 0$	135
A.69 Transient mass flow rate for HHVC loop, St = 2, Gr D/L = 10 ¹¹ , $\psi = 1$	135
A.70 Frequency domain of mass flow for HHVC loop, St = 2, Gr D/L = 10 ¹¹ , $\psi = 0$	136
A.71 Frequency domain of mass flow for HHVC loop, St = 2, Gr D/L = 10 ¹¹ , $\psi = 1$	136
A.72 Space-time chart for temperature in HHVC loop, St = 2, Gr D/L = 10 ¹¹ , $\psi = 0$	137
A.73 Space-time chart for temperature in HHVC loop, St = 2, Gr D/L = 10 ¹¹ , $\psi = 1$	137
A.74 Comparison of time series for mass flow rate using $\psi = 0$ and $\psi = 1$, in HHVC loop, St = 2, Gr D/L = 10 ¹¹	138
A.75 Comparison of time series for temperature difference across heater using $\psi = 0$ and $\psi = 1$, in HHVC loop, St = 2, Gr D/L = 10 ¹¹	138
A.76 Transient mass flow rate for VHHC loop, St = 2, Gr D/L = 10 ¹¹ , $\psi = 0$	139
A.77 Transient mass flow rate for VHHC loop, St = 2, Gr D/L = 10 ¹¹ , $\psi = 1$	139
A.78 Frequency domain of mass flow for VHHC loop, St = 2, Gr D/L = 10 ¹¹ , $\psi = 0$	140
A.79 Frequency domain of mass flow for VHHC loop, St = 2, Gr D/L = 10 ¹¹ , $\psi = 1$	140
A.80 Space-time chart for temperature in VHHC loop, St = 2, Gr D/L = 10 ¹¹ , $\psi = 0$	141
A.81 Space-time chart for temperature in VHHC loop, St = 2, Gr D/L = 10 ¹¹ , $\psi = 1$	141
A.82 Comparison of time series for mass flow rate using $\psi = 0$ and $\psi = 1$, in VHHC loop, St = 2, Gr D/L = 10 ¹¹	142

A.83 Comparison of time series for temperature difference across heater using $\psi = 0$ and $\psi = 1$, in VHHC loop, St = 2, Gr $D/L = 10^{11}$.	142
A.84 Transient mass flow rate for VHVC loop, St = 2, Gr $D/L = 10^{11}$, $\psi = 0$.	143
A.85 Transient mass flow rate for VHVC loop, St = 2, Gr $D/L = 10^{11}$, $\psi = 1$.	143
A.86 Frequency domain of mass flow for VHVC loop, St = 2, Gr $D/L = 10^{11}$, $\psi = 0$.	144
A.87 Frequency domain of mass flow for VHVC loop, St = 2, Gr $D/L = 10^{11}$, $\psi = 1$.	144
A.88 Space-time chart for temperature in VHVC loop, St = 2, Gr $D/L = 10^{11}$, $\psi = 0$.	145
A.89 Space-time chart for temperature in VHVC loop, St = 2, Gr $D/L = 10^{11}$, $\psi = 1$.	145
A.90 Comparison of time series for mass flow rate using $\psi = 0$ and $\psi = 1$, in VHVC loop, St = 2, Gr $D/L = 10^{11}$.	146
A.91 Comparison of time series for temperature difference across heater using $\psi = 0$ and $\psi = 1$, in VHVC loop, St = 2, Gr $D/L = 10^{11}$.	146

SUMMARY

NATURAL CONVECTION LOOPS AND PASSIVE COOLING SYSTEMS	11
Introduction	11
Stability of NCLs	15
Objectives and thesis outline	16
1 LITERATURE REVIEW	18
1.1 Types of instability	18
1.2 Precursors	20
1.3 State of the art	22
2 MATHEMATICAL MODEL	26
2.1 Considerations on geometry	27
2.2 Balance equations	28
2.3 Scaling	30
2.4 Numerical model	32
3 STEADY STATE	34
3.1 Friction factor correlations	36
3.2 Steady state results	40
3.2.1 Effect of heater/cooler orientation	43
3.2.2 Theoretical friction factor	45
4 LINEAR STABILITY ANALYSIS	48
4.1 Linear model	48
4.2 Stability maps	52
4.3 Effect of amount of water on stability	61
4.4 Summary of observations	64

5	NON-LINEAR STABILITY ANALYSIS	65
5.1	Effect of perturbation	66
5.2	Transient results	71
5.2.1	Stable steady states	72
5.2.2	Periodic regimes	76
5.2.3	Chaotic regimes	81
6	SUMMARY AND CONCLUSION	87
6.1	Steady state	88
6.2	Linear stability analysis	88
6.3	Non-linear stability analysis	89
6.4	Conclusion	89
6.5	Comment on electricity matrix	90
BIBLIOGRAPHY		92
A	TRANSIENT RESULTS	98
A.1	Stable regimes	99
A.1.1	HHHC	100
A.1.2	HHVC	103
A.1.3	VHHC	106
A.1.4	VHVC	109
A.2	Unstable regimes without pool, stable with pool	113
A.2.1	HHHC	114
A.2.2	HHVC	118
A.2.3	VHHC	122
A.2.4	VHVC	126
A.3	Unstable regimes	130
A.3.1	HHHC	131
A.3.2	HHVC	135
A.3.3	VHHC	139
A.3.4	VHVC	143

NATURAL CONVECTION LOOPS AND PASSIVE COOLING SYSTEMS

Introduction

Gravity is a potential source of energy available everywhere on earth. It is gravity that acts differently on fluid portions of higher density generating thermal convective flows. Engineers always seek for efficient, low energy consuming systems, and gravity is a reliable and free source of energy available for any application. Natural Convection Loops (referred to throughout this text as NCLs, as commonly used in related literature) are gravity driven systems which perform the function of heat transfer without the use of active components, where the transferred heat itself provides the necessary energy to maintain a circulation throughout the circuit. NCLs are the core element of the most common type of Passive Cooling Systems, which are those consisting of a heater, a cooler and the connecting pipelines. So NCLs are a particular type of Passive Cooling Systems (referred to as PCSs in this text). The working fluid absorbs heat through the heater and then flows, by natural convection, to the cooler, where the heat is rejected (cf. fig. 1). In the process depicted in fig. 1, heat can be transferred to a pool and then absorbed by the circuit. This is the most common design. But the coupling to the pool is neglected in current models, which consider heat directly imposed on the heater, usually a constant flux. The effect of this coupling on the dynamics of the system will be especially addressed in this thesis.

Another characteristic of PCSs is that, for not depending on active components, they are cheaper, require less maintenance and are more reliable in comparison to active systems. And, most important, they are inherently safe systems. Nevertheless, one drawback is that PCSs are less compact than an equivalent active system: larger flow rates require larger geodetic heights of the circuit, whereas for active systems high flow rates can be achieved by selecting a proper pump.

A second – and important – disadvantage of PCSs, which is the focus of the present work, is that NCLs are highly subject to thermo-hydraulic instabilities. Vijayan [47] cites three types of instability that can be associated to single-phase NCLs: stability of the rest state, metastable equilibrium and periodic oscillations with growing amplitudes. The third type, which is a dynamic type of instability (following the classification of Boure

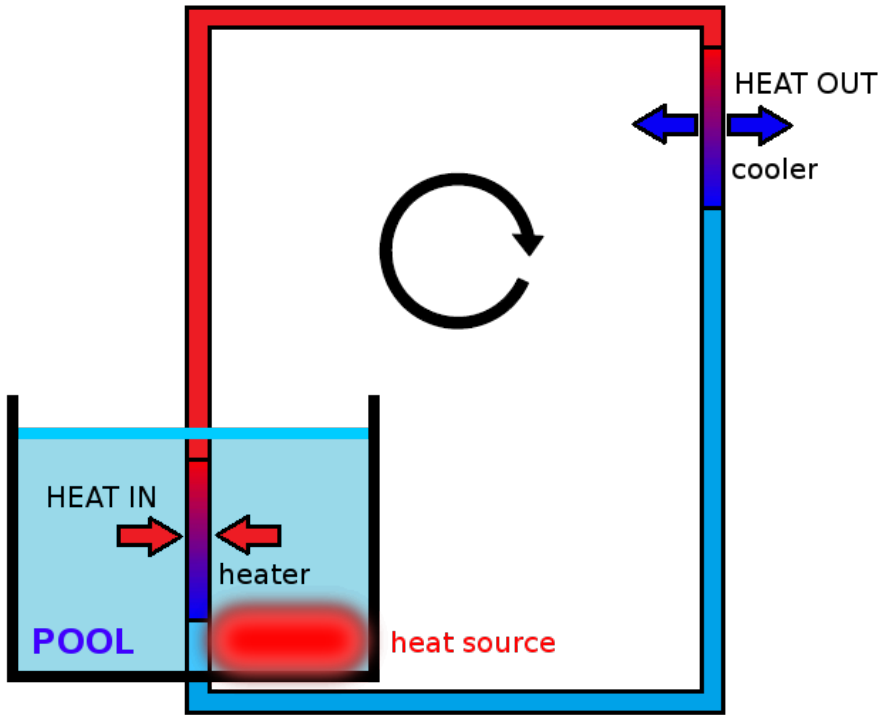


Figure 1: Sketch of Passive Cooling System consisting of a Natural Convection Loop coupled to a pool.

et al. [9]), is the most relevant among the three. In this case, since NCLs have no active control elements, the response time of the system after a perturbation is a function of the interaction between buoyancy and frictional forces only. Without control mechanisms over the response time, depending on the configuration of the system, a perturbation can result in oscillations with increasing amplitudes, reaching unstable regimes.

Although not part of the present work, two-phase NCLs can also develop instabilities. Indeed, because of the phase change, more types of instabilities may occur in two-phase NCLs, making such systems much more susceptible to unstable regimes. Boure et al. [9] provided a first classification of the thermo-dynamic instabilities in two-phase systems, in an attempt to harmonize the understandings about the different forms of unstable regimes at that time. Chapter 1 brings further information on the types of instabilities.

There is a third class of NCLs which operates at very high temperatures and pressures: the supercritical systems. These are single-phase loops with characteristics of two-phase systems. Many fossil fuel fired power plants use supercritical water because of the high efficiency of the thermal cycle. While conventional cycles may have efficiencies up to 36%, supercritical cycles may provide up to 50% efficiency [39]. Additionally, the design of passive systems with supercritical fluids is favored by the high density gradients

close to pseudo-critical points¹. One of the designs of Generation IV nuclear reactors² consists of a reactor cooled by supercritical water, possibly in a passive system.

According to Vijayan and Nayak [48], the first large-scale application of NCLs took place in the automobile industry, in the cooling of engine blocks, by the first half of the 20th century. After 1940, with the introduction of internal combustion engines with high compression ratios, the use of NCLs in the automobile industry decreased. Nevertheless, the DKW-Vemag (fig. 2), a car manufactured in Brazil from 1958 to 1967, employed a natural convection based cooling system, which happened to be one of the causes for the long lifetime of this model.



Figure 2: DKW-Vemag Belcar. This car was manufactured in Brazil from 1958 to 1967 by Vemag, under license of German company DKW (which stands for Dampf Kraft Wagen, i.e., Steam Power Car).

Today, Natural Convection Loops find many industrial applications in chemical processes, cooling of electronic devices and power generation. Some solar and geothermal power plants operate through a natural convection circuit. But the main commercial use of NCLs nowadays occurs in the nuclear power industry. Current generation of commercial nuclear reactors – Generation III+ – are characterized by the incorporation of passive systems for core cooling. Vijayan and Nayak [48] mentioned some innovative designs where natural convection is the operational mode for core cooling, like in CAREM (27 MW small PWR³ under construction by CNEA, Argentina), VK-300 (300 MW BWR⁴ under design by RDIPE, Russia), AHWR (300 MW heavy water reactor under design by BARC, India) and ESBWR (a 1600 MW commercial BWR designed by GE Hitachi). And as just mentioned, there is a version of the Generation IV Supercritical Water Cooled

¹For each isobaric curve above the thermodynamic critical pressure, there is a supercritical temperature which defines a pseudo-critical point in this isobaric at which the specific heat at constant pressure exhibits a maximum value.

²www.gen-4.org

³Pressurized Water Reactor.

⁴Boiling Water Reactor.

Reactor in which the operational core cooling is performed by natural convection [38], [15], [44].

Many other nuclear power plant designs employ passive systems for reactor cooling also under abnormal and/or accident conditions, like the AP1000⁵ (Westinghouse PWR design) and the ESBWR. But the use of natural convection systems in nuclear power plants is not recent. In Generation II of nuclear power plants (NPPs), like Brazilian NPPs, after a loss of external power supply, the reactor coolant pumps are unavailable, and the decay heat generated by the reactor is removed by natural convection.

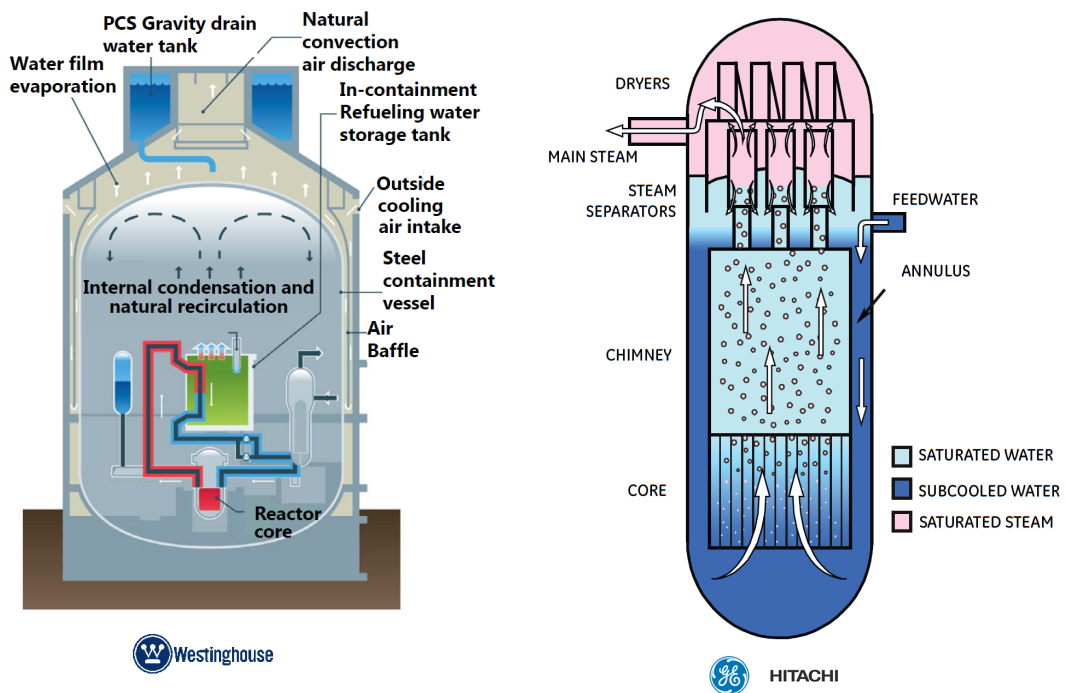


Figure 3: Passive cooling systems in current commercial nuclear reactors. On the left side: AP1000, from Westinghouse. Passive system guarantees the reactor cooling for 72 hours without any human intervention. Image extracted from [Westinghouse website](#), accessed on 2016-Jun-03. On the right side: ESBWR (Economic Simplified Boiling Water Reactor), from GE-Hitachi. Operational reactor cooling is performed by natural convection. Image extracted from [GE-Hitachi website](#), accessed on 2016-Jun-03.

This movement towards passive systems was intensified after the events of March 11, 2011, in Fukushima, Japan. On that occasion, three of the six units of Fukushima Daiichi nuclear station suffered a core meltdown caused by a loss-of-coolant-accident. The unavailability of external energy supply and emergency diesel generators, flooded by the tsunami that hit the nuclear station, were the cause for the loss of cooling capacity.

In the wake of this trend, Brazil has designed a nuclear installation for storage of Spent Fuel Elements provided with a fully passive heat removal system, consisting of a

⁵ Although the PCS in the AP1000 does not follow the configuration of heater and cooler connected by pipelines, the cooling cycle consists on the condensation of the wet atmosphere after a loss-of-coolant-accident on the containment walls.

set of NCLs in parallel.

In Brazil, electricity production counts with the contribution of two NPPs: Angra 1 and Angra 2⁶, which generate together 2,000 MW. Angra 3, the third plant of the nuclear station, is under construction and will supply 1,405 MW to the electrical grid. The nuclear fuel assemblies, after a work cycle, are removed from the reactor and stored in the respective storage pool. Each one of the NPPs is provided with a spent fuel pool, which has a limited storage capacity, and do not suffice for the whole lifetime of the plants. Thus, a complementary storage facility must be provided for the nuclear station for the NPPs to keep operation.

[Eletronuclear](#), the company responsible for construction and operation of NPPs in Brazil, has designed a wet SFA storage facility⁷ in order to fulfill the demand for space. According to the design, the storage facility will be provided with a fully passive cooling system for removal of the residual heat. Worldwide, there is only one installation with a similar solution, which is operating in Gösgen, Switzerland. The PCS for the SFA storage facility designed by Eletronuclear is composed by modules consisting of a single-phase hydraulic circuit which connects two heat exchangers: one immersed in the spent fuel pool (water-water heat exchanger) and another rejecting the heat in a dry cooling tower (water-air heat exchanger). So this is again the basic structure employed in most of current safety PCSs for new designs of nuclear power plants, i.e., a Natural Cooling Loop (NCL) connected to a heat source and a heat sink.

Stability of NCLs

Instabilities are undesired because they cause vibrations, alter local heat transfer characteristics and, in the case of nuclear reactors, influence thermal power because of the coupling to neutron flux.

The dynamical behavior of an NCL depends on the geometrical and operating parameters of the system. There are configurations and operating conditions for which, after a perturbation, density wave oscillations (DWO) of increasing amplitude are generated, characterizing an unstable regime. In non-linear systems, like the NCL, amplitudes grow until non-linear effects are large enough to damp the inertia effects. At this point the system reaches the limit-cycle oscillations, which can be periodic, quasi-periodic or aperiodic (chaotic regime). Density wave oscillations is the type of instability that occurs

⁶Angra 1 is a 657 MW Westinghouse design and is operating since 1982; Angra 2 is a 1350 MW KWU/Siemens design and is operating since 2000; Angra 3 is a 1405 MW KWU/Siemens/Areva design and is under construction.

⁷Facilities for storage of Spent Fuel Assemblies (SFAs) which are not directly connected to the reactor building are referred to as “away from reactor” storage facilities. There are two main types of SFA storage in away from reactor facilities: dry storage and wet storage. In both cases, the installation must be provided with a solution to remove residual heat generated by the spent fuel.

in single-phase NCLs. In the classification proposed by Boure et al. [9], thermal oscillations can also be assigned to single-phase systems, although it occurs during film boiling situations. If temperature in the pipe walls is too high, nucleate boiling occurs, which can evolve to form a film, decreasing the heat transfer. This, in turn, generates a cold water pocket that, after going through the cooler, can lead the vapor film to condensation, restoring the original heat transfer capacity through the pipe walls. It is, however, on the frontier of two-phase systems. The other types of instability, including static instabilities, occurs only in two-phase and supercritical systems.

Heat removal systems are designed to keep a component or another system below a temperature limit, so for an optimized PCS instabilities are highly undesirable. The mass flow rate during an unstable regime can oscillate up to flow reversal, i.e., a loop that is flowing clock-wise starts to flow counter-clock-wise, passing through zero mass flow. It is therefore clearly important to have information about the stability region, in terms of the system design parameters, as a function of the operating conditions.

In the present work, stability of single-phase NCLs are studied, motivated by the large applications just described. The interest in single-phase systems rely on the fact that many PCSs currently employed in the nuclear power industry are single-phase. In addition, the study of DWO, which occurs both in single and two-phase systems, is more effective without the influence of other instability types in the same problem.

Objectives and thesis outline

The present work consists of a numerical study of the dynamics of single-phase NCLs, taking the coupling to a pool into account. The selection of friction factor correlation and aspects of the numerical model are also addressed. The objective is to provide information about the effect of the thermal inertia introduced by the pool on the systems stability, which is seen as of great relevance for the design of PCSs. The object of the present study is the system represented in fig. 1.

NCL stability is studied by means of linear and non-linear analyses. The 1D model described by Vijayan and Austregesilo [46] was adapted to account for the coupling of the pool, including the linear stability analysis model. A scaling for the system of NCL-pool will be proposed as well, and stability maps were generated as a function of non-dimensional groups. From the linear analysis and the scaling proposed, an expression for a critical non-dimensional parameter for stability is provided.

Before going through the modeling details, a literature review is presented, showing a brief background on single-phase NCLs, followed by the types of instability and the state of the art.

In chapter 2, the mathematical model is described, followed by aspects of numerical

formulation and the non-dimensional form of equations.

Next, chapter 3 presents steady state results generated by the stationary version of the balance equations and compares it to experimental data from literature. In chapter 4 results from linear stability are presented. Stability maps for different loop configurations are shown. The effect of the amount of water in the pool on the system stability is also evaluated by means of the linear model.

From the stability maps generated by the linear model, key operational points were selected for non-linear stability analysis, with the objective of stressing the applicability of linear analysis and observing the role played by the non-linear effects neglected. The results of non-linear analysis are presented in chapter 5.

Chapter 6 closes the text summarizing the main results and presenting the conclusions.

1 LITERATURE REVIEW

This literature review intends to describe the main path of scientific works on single-phase NCLs, starting from the precursor works and then going through the process of building up the state of the art on the topic. The efforts to overcome the main challenges on the modeling of such systems are reviewed, identifying the points which are still open.

Although this thesis is devoted to single-phase loops, there are some fundamental concepts related to two-phase NCLs – and also supercritical NCLs – which have to be part of the knowledge structure. Hence, this chapter starts from a review of the types of instabilities which are encountered in both single and two-phase systems, through a study of the main works on this topic.

1.1 Types of instability

Natural Convection Loops may present different unstable regimes. In particular, two-phase NCLs may develop several types of thermo-hydraulic instabilities, much more than single-phase systems, and the work of Boure et al. [9] was the first to provide a widely accepted classification of the types of instability in this kind of system. The paper became a classic on the topic and their classification was adopted by other authors [24, 31].

Boure et al. [9] identified a confusion regarding the types of instabilities at their time. Their first contribution was grouping the types of instability into static or dynamic. In relation to the static types, the authors first address what they called fundamental static instability. Within this group there is Ledinegg instability, which occurs when an increase in mass flow generates a decrease in pressure drop (in other words, the system curve has negative (descending) slope). Within the scope of fundamental instabilities, authors address the occurrence of flow excursion in systems with parallel channels. The next type is called fundamental relaxation instability. This type is related to the transition of flow pattern from bubbly flow to annular flow. For the compound relaxation instability, authors cite bumping, geysering and chugging processes.

As to the group of dynamic instabilities, Boure et al. [9] say that the characteristic

that differentiate static from dynamic instabilities is the presence of disturbance propagation in the latter. These disturbances can be transported by two kinds of waves: acoustic waves or density waves. The main characteristic of these waves is that the former presents relatively high frequencies – 10 Hz to 100 Hz – and the latter presents low frequencies – with oscillating periods one to two times the time required by a fluid particle to travel along the whole circuit. Authors comment about very high frequency of acoustic waves within audible range (1000-10000 Hz) observed in a supercritical loop, where the sound produced (a whistle like sound) increased with decreasing inlet temperature and increasing mass flow. Concerning density wave oscillations, this is classified as the most common type of instability encountered in NCLs.

Boure et al. [9] also present comments about the influence of (i) inlet and outlet restrictions (where inlet restrictions tend to stabilize the flow and outlet tend to destabilize it), (ii) parallel channels, where high bypass ratios destabilizes the flow (in this case, cross connections can make the system more stable, and rod bundles are said to be more stable than simple parallel sections), (iii) pressure, which is more related to two-phase systems, (iv) inlet subcooling, whose effect is minimum, (v) mass velocity and power, (vi) cosine heat flux and (vii) condensing instability.

Twenty years later, March-Leuba and Rey [24] published a paper reviewing the instabilities associated to the coupling of thermo-hydraulics to neutronics in BWRs¹ (which are compound instabilities). They were motivated by a series of instability events in operating BWRs, like the case in Caorso, Italy, 1984, and in LaSalle, US, 1988 (references can be found in [24]). Authors list three types of instabilities viz. (i) control system instability, (ii) channel thermo-hydraulic instability and (iii) coupled neutronic-thermo-hydraulic instability, also called reactivity instability, which are considered by the authors the most relevant type for BWR operation. Reactivity instabilities are subdivided into core-wide and out-of-phase types. The authors also address the mechanisms behind instabilities in BWRs and the computer codes employed in the industry.

More recently, Prasad et al. [31], another important reference in the field of instabilities in single and two-phase systems, extended the classification set by Boure et al. [9], adding two other groups: the instabilities associated to control systems and the ones associated to neutron kinetics (see fig. 1.1).

Analyzing Ledinegg instability, the authors cited the work of Rao et al. [32], which concludes that this type of instability is only related to thermo-hydraulics (independent of the neutronics). They also classified Density wave oscillations (DWOs) into type I and type II: type I DWO is dominated by gravity effects, and type II DWO is dominated by two-phase frictional pressure drop (therefore related to two-phase systems). The authors

¹Currently there are 78 BWR NPPs out of 447 NPPs operating worldwide. PWRs are the most common type, with 288 plants operating. Information extracted from [PRIS/IAEA website](#).

address coupled neutronic instabilities, and classify their feedbacks into thermo-hydraulic feedback due to void regions, Doppler reactivity caused feedback and power feedback due to thermo-hydraulics. These instabilities can be classified into two types: core wide and out-of-phase (following the concept of March-Leuba and Rey [24]).

Prasad et al. [31] dedicate a section to start up transients, and include the Geysering, natural circulation instability and flashing into this category. The mathematical models for stability analysis are then addressed. Coupling to neutronics can be simulated basically by two approaches: point neutron kinetics and 3D neutron kinetics. The most used 1D models for boiling loops are separated flow models (two-fluid), drift model and Homogeneous Equilibrium Mixture (HEM). The authors say that the drift flux model has the simplicity of HEM models and the accuracy of two-fluid models. The choice of model depends on the type of instability to be analyzed. As for the numerical codes, the authors say they can be classified into two groups: frequency domain codes and time domain codes. The numerical codes can also be classified in Thermo-hydraulics, Neutron kinetics and Severe Accident Analysis. Another difference between the models is whether they consider or not thermal equilibrium between the phases. The assumption of thermal equilibrium between the phases is in fact a simplification. Linear stability theory applies to the onset of instabilities and system behavior after small perturbations around a steady state. Linear stability analysis can be done both in time or frequency domain. But, if perturbations are above a certain lower bound, non-linear phenomena increase in relevance, and linear analysis no longer applies. “Therefore, in order to predict the effect of large perturbations [...] non-linear dynamics analysis is required”, the authors say. Figure 1.1 reproduces the instability classification diagram provided by the authors.

The classification proposed by Boure et al. [9] and expanded by other authors is the current basis for determination of the instability types in NCLs, including single and two-phase regimes. The classifications were actually elaborated for systems with phase change, but they naturally encompass single-phase systems, mainly within the Density Wave Oscillations type of instability. Still, single-phase NCLs were thought not to present unstable regimes until theoretical demonstrations pointed to that possibility. That is the subject of the next section, which addresses the early findings on instability of single-phase systems, starting from the very first scientific advances in natural convection.

1.2 Precursors

As a phenomenon which is present almost everywhere in nature, natural convection is one of the main research topics in thermal sciences and engineering. One of the first relevant marks on the field was set by the German engineer Franz Grashof. The non-dimensional group which carries his name (eq.1.1) is a known relation between buoyancy

and viscous forces, therefore an important scale in the characterization of natural convection flows. After Grashof, Lord Rayleigh, British physicist, can be cited as a great precursor in the field. The Rayleigh-Bénard convection cells were named after him and the also widely known Rayleigh number is a product of Grashof and Prandtl numbers.

$$\text{Gr} = \frac{D^3 \rho_0^2 \beta g Q_{NCL} H}{\mu^3 A c_p} \quad (1.1)$$

In fact, until the middle of the 20th century, most of scientists attention had been paid to the Rayleigh-Bénard convection, while the unstable and turbulent regimes of natural convection flows inside pipelines was still poorly known, as affirmed by Welander [53].

The knowledge on single-phase natural convection loops and its non-linear dynamics started to be built after the work of Keller [17]. Almost all scientific literature on single-phase NCLs relies on his work. Before it, only two-phase systems were known to develop unstable regimes. While two-phase NCLs are much more susceptible to instabilities, there are conditions in which single-phase systems may become unstable, and this is the information that Keller [17] introduced.

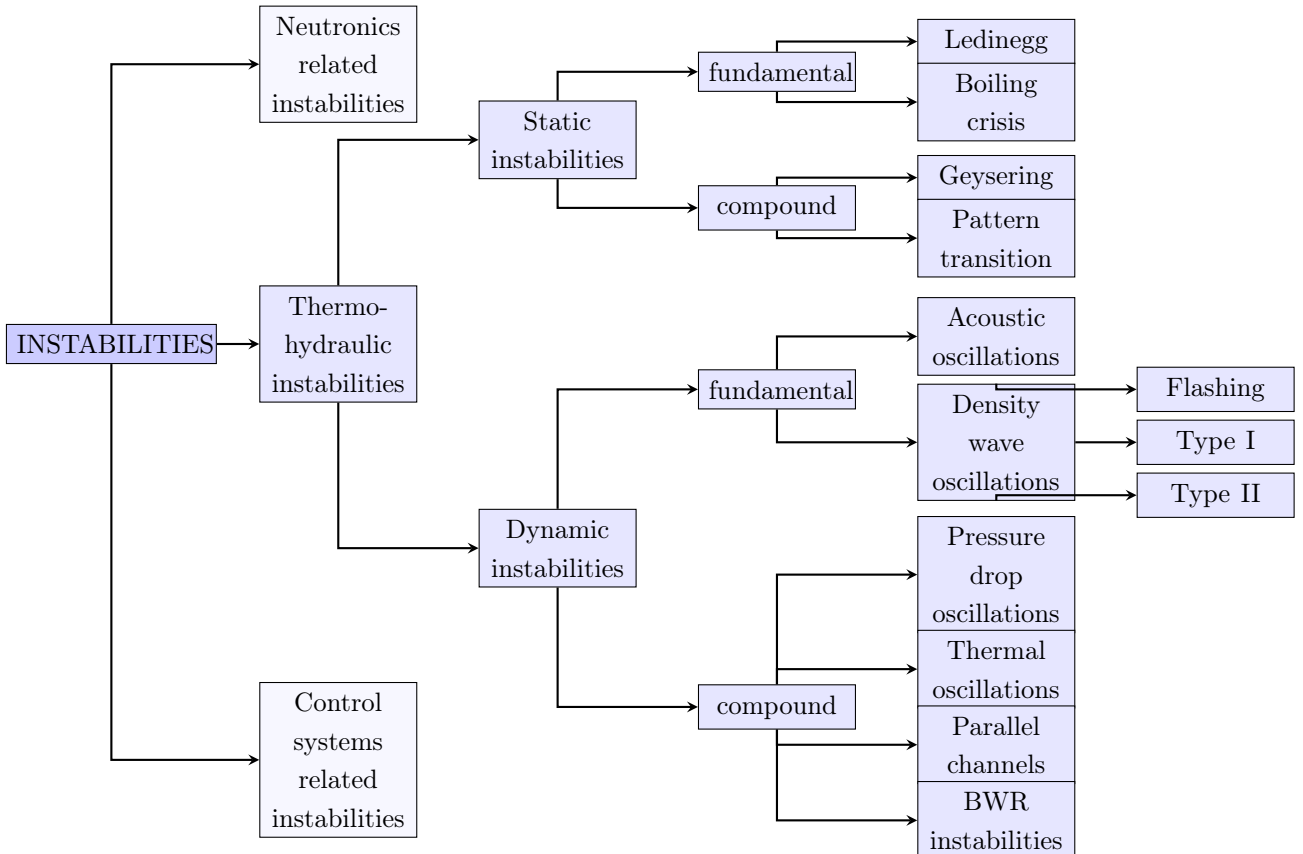


Figure 1.1: Instability types according to Prasad et al. [31].

Welander [53] extended his results and offered a very comprehensive explanation of the oscillatory mechanism, illustrating the system dynamics by means of the motion of hot and cold fluid pockets. He analyzed the oscillatory behavior in an idealized NCL with point heat source and sink, by means of analytical and numerical studies. The author sets stability maps as a function of non-dimensional gravity and friction factor, which clearly relates to the Grashof number adopted in current works to characterize NCL systems. In the end of the manuscript, the author explicitly thanks Dr. Joseph Keller [17], making their collaboration explicit in these first steps of the research on single-phase NCLs.

Almost a decade later, the first experimental evidence came through the work of Creveling et al. [12], for a toroidal loop. The authors commented that, before them, instabilities in single-phase NCLs were only experimentally reproduced in systems operating at conditions close to the pseudo critical point.

After these works, stability of single-phase NCLs started to receive more attention from many researchers. Wacholder et al. [52] developed a numerical model for stability analysis in a toroidal loop. The intention was to simulate the experiment of Creveling et al. [12]. Their increment in comparison to other computational works on toroidal loops already published until 1982 was the incorporation of the expansion tank in the model. Ishii and Kataoka [16] suggested a scaling criterion for single-phase and two-phase NCLs, based on Richardson and Biot numbers, geometrical groups and a time constant ratio. The authors say that the Stanton number is redundant after these scaling parameters. The effect of loop inclination was numerically observed by Sen et al. [40]. The authors also proposed an exact expression for the steady state of single-phase NCL, which provided from zero up to three steady state velocities, characterizing static instability, i.e., different steady state solutions for the same system. Lavine et al. [21] performed 3D simulations, again in a toroidal loop, to look for the effects not captured by the widely employed 1D models. Another important author in the 1980 decade was Yoram Zvirin [56, 54, 57]. Among his numerous works on dynamic behavior of single-phase NCL, it is worth to cite his mention to the existence of a critical value of the modified Rayleigh number Ra , above which the rest state of the flow is unconditionally unstable and the existence of a monotonously growing perturbation, whose rate increases with Ra and decreases with the modified Prandtl number. When Ra is below the threshold for instability, then the rest state is unconditionally stable.

1.3 State of the art

In the beginning of 1990 decade, researchers from the Bhabha Atomic Research Centre (BARC), in India, started working on NCLs. Today they concentrate a great part of the scientific advances on the topic, having wide experimental data and mature numerical

models for single-phase, two-phase and supercritical NCLs.

In Vijayan and Austregesilo [46], a simplified scaling law for single-phase NCLs was proposed in which the system is characterized by a version of the Stanton and Grashof numbers. The authors showed experimental results and a 1D numerical model, which was presented in more detail by Nayak et al. [28]. The numerical model generated much more conservative results than the experiments. Employing their new scaling law, authors arrived at a friction factor correlation for natural convection (eq.1.2) which is still recognized as applicable to similar systems at low Grashof numbers [25, 27].

$$f = \frac{22.26}{Re^{0.6744}} \quad (1.2)$$

These attempts to simulate NCLs started to reveal the challenge of a proper selection of the friction factor correlation. Swapnalee and Vijayan [45] suggested a multiple wall constitutive law to overcome the non-applicability of known correlations to the whole loop. Friction factor was also the topic addressed by Ambrosini et al. [2] for transitional flow regimes. The authors pointed out the need for further investigation on the applicability of forced flow friction correlations to natural convection. As an alternative to simulate NCLs without concerns on wall constitutive laws, the authors suggested the use of 3D simulations. Their suggestion was followed by Naveen et al. [25], who developed a model to simulate start up from rest and analyzed the applicability of classical forced flow friction factors on natural convection systems by comparing the 1D model with 3D simulations. The authors concluded that, for low Reynolds numbers, forced flow correlations do not apply to natural convection. For such operating condition, they suggested the correlation proposed by Vijayan and Austregesilo [46]. For $Gr > 10^{11}$, the authors concluded that forced flow correlations predict the loop behavior reasonably well.

Frictional losses with secondary flow under diabatic conditions have been studied by Naveen et al. [27], making comparisons to experimental data. They confirmed the conclusions drawn by Naveen et al. [25] about the general inadequacy of classical forced flow correlations to natural convection systems. Authors proposed a new wall friction correlation for horizontal pipe sections with heat fluxes through the wall. The proposed correlation performed well for steady state predictions in horizontal pipes, but failed in the simulation of natural convection flow dynamics, especially in vertical pipes. They say that new similar correlations need to be proposed for such task. Friction factor for NCLs was also addressed by Ruiz et al. [36], who employed a new correlation based on experimental data for steady state flow in a straight infinite pipe. Recently, Lima and Mangiavacchi [22] performed a comparison between forced flow correlations and a friction model proposed by Vijayan et al. [51], and found that the latter predicts steady state considerably well, but fails with transient predictions. Details on classical and state of the art friction correlations

will be described in section 3.1.

The use of 3D models, as suggested by Ambrosini et al. [2], was also employed by Pilkhwal et al. [30], who compared results provided by 1D and 3D models. A few years later, a 2D model was employed by Ridouane et al. [33] and a 3D was implemented by Ridouane et al. [34], both to simulate a toroidal loop. In both investigations the authors detected secondary flow motions in the loop, linking it to the onset of dynamic instabilities.

Along the first decade of the 21st century, much research was devoted to the analysis of the effect of different system parameters, such as heater and cooler orientations, loop diameter and input power, on stability of single-phase NCLs. Loop diameter was the parameter analyzed by Vijayan et al. [51], considering also two-phase systems, basically concluding that the larger the diameter, the more the system tends to instability. The same group performed a study on the effect of loop orientation in Vijayan et al. [50], through experimental and numerical simulations. Essentially, a combination of vertical and horizontal heater and cooler was considered, with an experimental loop that allowed the use of both orientations. They introduced the four letter nomenclature to identify the orientation in rectangular loops, where

- HHHC - horizontal heater and horizontal cooler;
- HVHC - horizontal heater and vertical cooler;
- VHHC - vertical heater and horizontal cooler;
- VHVC - vertical heater and vertical cooler.

Authors observed that the HHHC configuration is the most unstable one, whilst VHVC is the most stable.

The influence of geometrical parameters was also the object of research of Basu et al. [7], who also analyzed the influence of operating loop parameters and proposed an expression to calculate the threshold of stability based on the Richardson number, applicable to rectangular single-phase NCLs within some geometrical constraints. Among their conclusions, geodetic height difference is pointed out as the most effective stabilizing parameter, because increasing loop height increases friction losses, which is a stabilizing process, but is also enhances mass flow because of larger buoyancy. The same group studied the effects of different heat input transients in Basu et al. [6], considering step four types of input signals: step, ramp, exponential signals and a modified exponential signal. Most of these works employed a 1D numerical model for the single-phase NCL, based on cross-section average properties, integrating the incompressible momentum equation along the loop volume, using Boussinesq's hypothesis about the force term. Investigations

performed in these works were concerned about instabilities associated to Density Wave Oscillations (cf. sec. 1.1).

In Brazil, single-phase NCLs were object of research of Sabundjian et al. [37] and Angelo et al. [3], which provided experimental and numerical data from single and two-phase VHVC (vertical heater vertical cooler) NCL test facilities, performed by the Institute of Energetic and Nuclear Research (IPEN), in São Paulo. Sabundjian et al. [37] compared results from experiment and predictions obtained with RELAP5 system code. Good agreement was reached by the authors. In Angelo et al. [3], 3D simulations were presented and compared to experiments. Authors said that a hybrid 1D/3D model could be a way to avoid high computational costs in regions where the flow is not complex, such as pipelines.

Single-phase NCLs with different operating fluids are under research, as can be illustrated by the works of Kudariyawar et al. [19] and Srivastava et al. [43], where numerical and experimental models were developed for molten salt NCLs, Kumar and Gopal [20], who performed numerical and analytical studies on a CO₂ single-phase NCL. Supercritical loops can also be mentioned as a subject of interest, where thermo-hydraulic stability, friction factor and, most importantly, heat transfer correlations, because of the heat transfer deterioration, concentrate the research efforts [11, 10, 4, 42, 35]. A great part of the motivation for these projects are the new designs of nuclear reactors, specially Generation IV designs. Supercritical Water Cooled Reactor faces a problem with the cladding material: there is not yet a proper material available that (i) does not absorb much neutron and (ii) is resistant at the thermodynamic supercritical conditions for water. For the long term, Molten Salt Reactors with Thorium as nuclear fuel are a promising design from Gen. IV: operation at ambient pressure, online reprocessing, low percentage of long half-life fission products.

Today, there are still open points with respect to the modeling of single-phase NCL dynamics. There is not a consensus concerning friction factor correlations for natural convection at high Grashof numbers, as concluded by Naveen et al. [25] and Naveen et al. [27]. 3D simulations still can provide enlightening information about the role of secondary motion on the system dynamics and contribute to the development of a suitable friction correlation. Another point for improvement may arise from the work of [18], which made a study on the applicability of the Boussinesq approximation, employed in the vast majority of 1D and 3D models of single-phase NCLs. Authors concluded that it is not an adequate choice for non-linear stability analysis of NCLs, mainly at higher input powers.

2 MATHEMATICAL MODEL

The modeling of single-phase NCLs can be simple, allowing fair predictions of steady state regimes and qualitative good agreements in transient simulations. Most researchers employ 1D models, considering no variation of thermo-hydraulic properties over the cross-section, with Boussinesq approximation. But the selection of the friction factor is critical and there is not a consensual correlation. Many researchers addressed this topic, discussing the use of classical forced flow correlations in natural convection or suggesting new correlations for NCLs [46, 2, 27, 25]. Generally, forced flow correlations tend to produce conservative results concerning stability and better system performance in terms of steady state. Another modeling challenge is the startup from rest. The temperature transport in the stagnant fluid is not reproduced by the standard model for single-phase NCLs, as addressed by Naveen et al. [25] and Naveen et al. [26].

In addition, the numerical model requires special attention to some aspects, like order of discretization and time advance scheme (implicit, explicit). It is known that implicit schemes are numerically stable, but generate additional diffusion, while explicit schemes are considerably less diffusive, but much more restrictive in terms of numerical stability. The choice of the numerical formulation is therefore of crucial importance for stability analysis. In this sense, the work of Ambrosini and Ferreri [1] presents a low diffusion scheme and Naveen et al. [25] describe an optimized mesh structure, both for 1D models.

To include the pool, the simplest option is a global energy balance. The drawback is that information about the flow dynamics in the pool are lost. A 3D simulation would reveal the convection cells possibly formed, and perhaps stratified configurations, but the computational cost would be much higher. A 2D approach may be a solution to partly evaluate the dynamics in the pool with computational cost one degree of magnitude smaller.

This chapter describes the mathematical model developed in this work to simulate NCLs with coupling to a cooling pool and the numerical formulation of the model. The linear version of the perturbed equations, employed on the linear stability analyses, is

described in chapter 4.

2.1 Considerations on geometry

The geometry of the problem is a rectangular hydraulic closed circuit with diabatic parts – the heater and the cooler – and adiabatic parts – the piping. Heater and cooler can be horizontally or vertically oriented, as shown in fig. 2.1, allowing for four possible configurations:

- HHHC - horizontal heater and horizontal cooler;
- HHVC - horizontal heater and vertical cooler;
- VHHC - vertical heater and horizontal cooler;
- VHVC - vertical heater and vertical cooler.

The coupling to a pool is characterized by the way heat is supplied to the loop. Without coupling, a constant uniformly distributed heat input is imposed on the heater (cf. eq. 2.8). If the loop is coupled to a pool, as sketched in fig. 1, heat is supplied the water in the pool and transferred to the loop with a heat transfer coefficient (eq. 2.7). Thus geometry is not affected by the variants coupling/uncoupling to a pool; only source term in energy balance equation is changed, as will be seen in the following section.

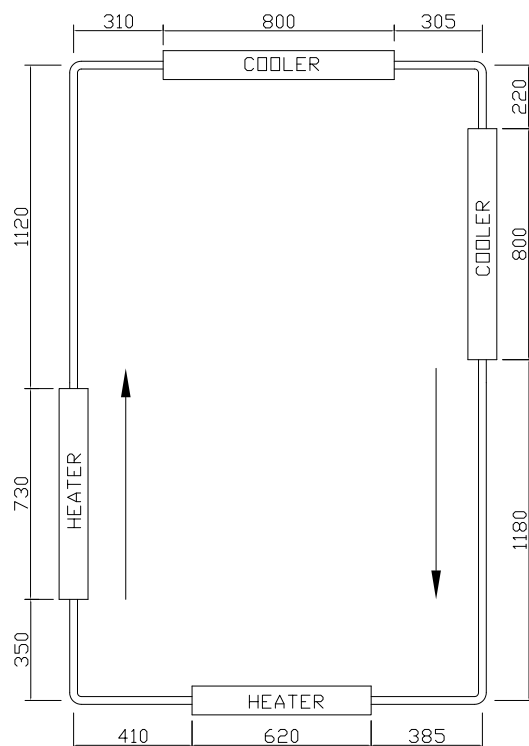


Figure 2.1: Flexible loop with possibility to operate with horizontal or vertical heater and cooler.

The parameters that define the geometry of the problem are

- loop internal diameter
- loop horizontal length
- loop vertical length (height)
- heater and cooler lengths
- heater and cooler orientations
- position of heater and cooler
- coefficient of local pressure losses
- tilting angle

2.2 Balance equations

The model developed to simulate NCLs in this work considers a heater and a cooler connected by pipes, forming a rectangular circuit. Circuits with higher complexity can be simulated by establishing a proper coefficient of local losses. Heater and cooler are modeled as tube sections with conducting walls and can be vertical or horizontal. Again, adequate coefficients of local losses can simulate heaters and/or coolers with higher geometrical complexity. The following assumptions are also taken into account.

- all physical properties are assumed to be constant in the cross section area;
- the circuit walls are adiabatic along the entire loop except for heater and cooler.
- axial heat conduction is neglected, as well as viscous heating;
- no boundary layer development length is considered in heated and cooled sections.

Introducing the space coordinate s in the axial direction and the axial velocity component u , the continuity equation, for incompressible flow, reduces to

$$\frac{\partial u}{\partial s} = 0 \quad (2.1)$$

This restriction allows the axial component of momentum equation to be written in cylindrical coordinates as

$$\rho \frac{\partial u}{\partial t} = -\frac{\partial p}{\partial s} + \mu \left[\frac{1}{r} \frac{\partial}{\partial r} \left(r \frac{\partial u}{\partial r} \right) \right] + \rho g_s \quad (2.2)$$

where t is time, r is the radial space coordinate, ρ is the fluid density, p is the pressure field, μ is viscosity, g_s is the s component of the gravity acceleration vector \mathbf{g} . Boussinesq hypothesis is adopted to write density as a linear function of temperature in the gravity term of momentum equation to solve the inconsistency between incompressibility assumption and the presence of buoyancy. Thus, density is written as $\rho = \rho_0 [1 - \beta(T - T_0)]$, where the subscript 0 represents a value based on mean temperature and β is the thermal expansion coefficient (also evaluated at T_0). Now, let L , D and A be the length, diameter and cross section area (constant) of the loop, and let $w = \frac{1}{\rho A} \int_A u dA$ be the mass flow rate of the system. Integration along the whole loop volume then produces

$$\frac{L}{A} \frac{dw}{dt} = - \left(f \frac{L}{D} + K \right) \frac{w^2}{2\rho_0 A^2} + \rho_0 g \beta \oint T dz \quad (2.3)$$

Here, g is the module of gravity field. The friction factor f and the local losses coefficient K were introduced. The buoyancy term is a function of the temperature field T . Note that the pressure gradient vanishes and the viscous term gives rise to the term associated to friction losses.

Regarding the temperature distribution, after applying the simplifying assumptions, energy conservation is expressed by

$$\frac{\partial h}{\partial t} + u \frac{\partial h}{\partial s} = \bar{q} \quad (2.4)$$

where h is the specific enthalpy and \bar{q} is a heat power source per unit mass. Introducing the specific heat at constant pressure c_p defined as $c_p = \frac{\partial h}{\partial T}$ the energy equation can be written in terms of T , i.e.,

$$\rho_0 c_p \left(\frac{\partial T}{\partial t} + u \frac{\partial T}{\partial s} \right) = \dot{q} \quad (2.5)$$

Note that $\dot{q} = \rho_0 \bar{q}$. After integration over the circuit cross section, equation 2.5 can be expressed as

$$\frac{\partial T}{\partial t} + \frac{w}{\rho_0 A} \frac{\partial T}{\partial s} = \frac{\dot{q}}{\rho_0 c_p} \quad (2.6)$$

It is now convenient to split the energy equation into heater, cooler and adiabatic tube

sections, which implies in different forms of the heat source \dot{q} and results in

$$\text{heater: } \frac{\partial T}{\partial t} + \frac{w}{\rho_0 A} \frac{\partial T}{\partial s} = -\frac{4U_h(T - T_{\text{pool}})}{D\rho_0 c_p} \quad (2.7\text{a})$$

$$\text{cooler: } \frac{\partial T}{\partial t} + \frac{w}{\rho_0 A} \frac{\partial T}{\partial s} = -\frac{4U_c(T - T_s)}{D\rho_0 c_p} \quad (2.7\text{b})$$

$$\text{pipes: } \frac{\partial T}{\partial t} + \frac{w}{\rho_0 A} \frac{\partial T}{\partial s} = 0 \quad (2.7\text{c})$$

where U_h and U_c are respectively the heat transfer coefficient for heater and cooler ($\text{kW/m}^2/\text{K}$ in the International System of Units). Without coupling to pool, i.e., heat is constantly injected in the loop via heater, the energy equation becomes

$$\text{heater: } \frac{\partial T}{\partial t} + \frac{w}{\rho_0 A} \frac{\partial T}{\partial s} = \frac{Q}{L_h A \rho_0 c_p} \quad (2.8\text{a})$$

$$\text{cooler: } \frac{\partial T}{\partial t} + \frac{w}{\rho_0 A} \frac{\partial T}{\partial s} = -\frac{4U_c(T - T_s)}{D\rho_0 c_p} \quad (2.8\text{b})$$

$$\text{pipes: } \frac{\partial T}{\partial t} + \frac{w}{\rho_0 A} \frac{\partial T}{\partial s} = 0 \quad (2.8\text{c})$$

with Q as the total power input and L_h as the length of the heater.

To complete the system, the energy balance in the pool is considered, which is expressed as

$$M c_p \frac{dT_{\text{pool}}}{dt} = Q - U_h \pi D \left(T_{\text{pool}} L_h - \int_h T ds \right) \quad (2.9)$$

where M is the water mass and T_{pool} is the temperature of the pool. Q here represents the primary (constant) heat load injected in the pool.

Flow dynamics in the pool are not taken into account, although natural convection may reach important oscillating regimes in the pool, with high Rayleigh numbers.

To summarize, the system of equations that define the mathematical model is given by equations 2.3, 2.7 and 2.9. Solution of the system provides w , T and T_{pool} .

2.3 Scaling

This section presents a non-dimensional form of the mathematical model so that results can be compared to every similar problem.

To do so, a scaling criterion must be adopted. The scaling laws proposed by Vrijayan and Austregesilo [46] based on Stanton-Grashof-Reynolds, defined according to

eqs. 2.10, 2.11 and 2.12, are the most widely accepted for single-phase NCLs. Basu et al. [5] endorses this information, but they argued that the scaling based on Stanton-Grashof-Reynolds is not justifiable because inertia would have a small influence in comparison to the interplay between friction and buoyancy forces. They proposed the Richardson number (eq. 2.13) as a more suitable scale than Grashof number. However, since unstable behaviors are essentially triggered by thermal and momentum inertia, the scaling laws proposed by Vijayan and Austregesilo [46] are employed in the present work.

$$St = 4 \frac{ULA}{D\bar{w}c_p} \quad (2.10)$$

$$Gr = \frac{D^3 \rho_0^2 \beta g Q_{NCL} H}{\mu^3 A c_p} \quad (2.11)$$

$$Re = \frac{D\bar{w}}{A\mu} \quad (2.12)$$

$$Ri = \frac{g\beta Q_{NCL} H \rho^2 A^2}{\bar{w}^3 c_p} \quad (2.13)$$

where \bar{w} denotes the steady state mass flow and H is the height of the loop.

The non-dimensional variables are defined as

$$\omega = \frac{w}{\bar{w}} \quad (2.14a)$$

$$\tau = \frac{t\bar{w}}{V\rho_0} \quad (2.14b)$$

$$\theta = \frac{T - T_s}{\Delta\bar{T}_h} \quad (2.14c)$$

$$\theta_{pool} = \frac{T_{pool} - \bar{T}_h}{\Delta\bar{T}_h} \quad (2.14d)$$

$$S = \frac{s}{H} \quad (2.14e)$$

$$Z = \frac{z}{H} \quad (2.14f)$$

The subscript h stands for heater, and \bar{T} is the steady state temperature field. Note that a scaling is proposed for the non-dimensional temperature in the pool θ_{pool} . Another differing point in the present study is that two Stanton numbers need to be defined: one associated to the cooler, St_c , and another associated to the heater, St_h , which will differ by the respective heat transfer coefficients, U_c and U_h . After proper substitutions, the non-dimensional form eqs. 2.3, 2.7 and 2.9 is given by

$$\frac{d\omega}{d\tau} = - \left(f \frac{L}{D} + K \right) \frac{\omega^2}{2} + \frac{\text{Gr}}{\text{Re}^3} \oint \theta dZ \quad (2.15)$$

$$\frac{\partial \theta}{\partial \tau} + \phi \omega \frac{\partial \theta}{\partial S} = \text{St}_h \left[\theta_{\text{pool}} - \theta + \frac{\bar{T}_h + T_s}{\Delta \bar{T}_h} \right] \quad (2.16a)$$

$$\frac{\partial \theta}{\partial \tau} + \phi \omega \frac{\partial \theta}{\partial S} = \text{St}_c \theta \quad (2.16b)$$

$$\frac{\partial \theta}{\partial \tau} + \phi \omega \frac{\partial \theta}{\partial S} = 0 \quad (2.16c)$$

$$\psi \frac{d\theta_{\text{pool}}}{d\tau} = 1 - \text{St}_h \left[\theta_{\text{pool}} - \frac{H}{L_h} \int_h \theta dS - \frac{T_s}{\Delta \bar{T}_h} \right] \quad (2.17)$$

where we define

$$\phi = V/(AH) \quad (2.18)$$

and

$$\psi = M/(V\rho_0) \quad (2.19)$$

2.4 Numerical model

The system of equations 2.3, 2.7 and 2.9 is numerically solved by a Finite Difference Scheme. First order upwind and forward Euler methods are employed to solve the system of equations 2.3, 2.7 and 2.9. The equilibrium values of mass flow and temperature field is obtained from the steady state form of equations 2.3 and 2.7, found by means of an iterative procedure. From the mathematical point of view, the instability of a dynamical system can be associated to the competition between multiple solutions to the set of equations [49], and the calculation of the steady state is subject to such multiplicity of solutions. Consequently, the procedure to solve the steady state of a NCL may not converge. To solve this, a controlled time step was introduced, determined by a relaxation parameter based on the residuals of the previous iteration. So the “artificial” transient character prevents the solution from diverging, holding it towards the stationary solution. Additionally, the energy conservation equation follows an implicit formulation in order to guarantee a numerical stability in the calculation procedure.

With respect to the energy equation, Vijayan and Austregesilo [46] proposed explicit Euler for time advance with first order upwind discretization for the temperature

convection term. If $CFL = 1$, then this formulation is capable to transport temperature without losses in each time step, following a Lagrangian behavior, which suits well for the hyperbolic character of equation 2.7. However, to set $CFL = 1$ is not a straightforward task because the flow velocity is constantly changing. Moreover, when the system is close to reversal, time increment Δt can be too large, and the time step can grow larger than the oscillating period. A solution is to set an upper limit for Δt , but this implies in the introduction of numerical diffusion (due to the first order approximation) and requires a criterion for definition of maximum Δt . So the chosen upper bound value was the time increment used by Ambrosini et al. [2], i.e., $\Delta t_{\max} = 0.1$. The explicit forward Euler form for the discretized energy equation for time step n and mesh node i is given by

$$\begin{aligned} T_i^{n+1} &= T_i^n + \\ &+ \Delta t \left[-\frac{w_n}{\rho_0 A} \frac{T_i^n - T_{i-1}^n}{\Delta s} + \frac{Q_{NCL}}{L_h A \rho_0 c_p} \right] \end{aligned} \quad (2.20a)$$

$$\begin{aligned} T_i^{n+1} &= T_i^n + \\ &+ \Delta t \left[-\frac{w_n}{\rho_0 A} \frac{T_i^n - T_{i-1}^n}{\Delta s} - \frac{4U(T_i^n - T_s)}{D \rho_0 c_p} \right] \end{aligned} \quad (2.20b)$$

$$T_i^{n+1} = \Delta t \left(-\frac{w_n}{\rho_0 A} \frac{T_i^n - T_{i-1}^n}{\Delta s} \right) + T_i^n \quad (2.20c)$$

Some details concerning the solution of the momentum equation (an ODE) are worth to mention as well. After time discretization, the momentum equation, in implicit form, is written as

$$\frac{w_{n+1} - w_n}{\Delta t} = - \left(f \frac{L}{D} + K \right) \frac{w_{n+1}^2}{2\rho_0 A^2} + \rho_0 g \beta \oint T^{n+1} dz \quad (2.21)$$

so that the solution w_{n+1} are the roots of a parabola, which means that two solutions will be available. Hence, a criterion to select one of the roots must be established. In most cases, a positive and a negative root will satisfy 2.21, and the positive one would be selected. But this is not a general case, because of the possibility of flow reversal. The criterion adopted in the present model was to select the root corresponding to the closest time derivative to that of the previous value (at time step n). Since the momentum equation has a quadratic form of the mass flow, friction losses are always acting in the same direction, which is not true if flow reverses. To overcome this limitation, the flow is always considered to be in the same direction, i.e., w_n is always positive during the solution procedure.

3 STEADY STATE

The engineering of a system requires the knowledge of steady regime at maximum operation conditions. For a cooling system, it has to be designed so that a constant maximum thermal load is steadily removed within the temperature limits. This thesis is concerned about stability of the steady state of cooling systems that operate by natural convection. The reason is because it is not enough to know the steady operating condition of the cooling system. Engineers also have to assure that the system has a stable steady operating condition, in the sense that the steady state is recovered after a perturbation.

The steady state of single-phase NCLs is mathematically characterized by the steady form equations 2.3, 2.7 and 2.9, and is given by

$$\left(f \frac{L}{D} + K \right) \frac{w^2}{2\rho_0 A^2} = \rho_0 g \beta \oint T dz \quad (3.1)$$

$$\text{heater: } \frac{dT}{ds} = -\frac{U_h \pi D (T - T_{\text{pool}})}{w c_p} \quad (3.2a)$$

$$\text{cooler: } \frac{dT}{ds} = -\frac{U_c \pi D (T - T_s)}{w c_p} \quad (3.2b)$$

$$\text{pipes: } \frac{dT}{ds} = 0 \quad (3.2c)$$

$$Q = U_h \pi D \left(T_{\text{pool}} L_h - \int_h T ds \right) \quad (3.3)$$

From the momentum balance it can be seen that the equilibrium in the loop will be achieved when buoyancy is equal to friction losses. Integration of the temperature field along the heat gives

$$\int_h T ds = (T_{h,\text{in}} - T_{\text{pool}}) \frac{w c_p}{U_h \pi D} \left(e^{\frac{U_h \pi D L_h}{w c_p}} - 1 \right) + T_{\text{pool}} L_h \quad (3.4)$$

Plugging this expression back into eq. 3.3 provides

$$Q = (T_{h,\text{in}} - T_{\text{pool}}) w c_p \left(e^{\frac{U_h \pi D L_h}{w c_p}} - 1 \right) \quad (3.5)$$

It is reasonable to assume that the influence of the pool is small for the steady state in the NCL, which means that it can be calculated with uniformly distributed heat input. Mathematically, the consequence is that energy balance in the heater becomes

$$\frac{dT}{ds} = \frac{Q}{L_h A \rho c_p} \quad (3.6)$$

This is the model employed in related literature and reflects the experimental models reported in studies of NCLs, i.e., constant heat flux uniformly distributed in the heater. There are works, like that of Basu et al. [6], in which a varying heat input was supplied to the circuit, but it was still a uniformly supplied power. Hence, the steady state results that will be presented in this chapter corresponds to the solution of eq. 3.1 coupled to

$$\text{heater: } \frac{dT}{ds} = \frac{Q}{L_h A \rho c_p} \quad (3.7a)$$

$$\text{cooler: } \frac{dT}{ds} = -\frac{U_c \pi D (T - T_s)}{w c_p} \quad (3.7b)$$

$$\text{pipes: } \frac{dT}{ds} = 0 \quad (3.7c)$$

An approximate temperature in the pool can be calculated from the solution of this system of equations using eq. 3.5, by the expression

$$T_{\text{pool}} = T_{h,\text{in}} - \frac{Q}{w c_p \left[\exp \left(\frac{U_h \pi D L_h}{w c_p} \right) - 1 \right]} \quad (3.8)$$

where subscript in $T_{h,\text{in}}$ refers to heater inlet. It can be noticed that the steady temperature in the pool does not depend on the water mass M , as expected. In the design of a cooling system, the parameters will have be suitably adjusted to keep T_{pool} below specific constraints dependent on the application.

Among other parameters, the solution of eqs. 3.1, 3.7 depends on the friction factor f , which is still a challenge in the modeling of NCLs, as addressed in the following section.

3.1 Friction factor correlations

Equilibrium in NCLs may occur at laminar, transitional or turbulent regimes, with many cases falling in the transitional region, which is precisely where most of friction correlations fails. Some authors go for classical correlations, like Colebrook's or Churchill's, which cover all flow regimes. Other authors question classical correlations because they were developed for forced flows, and proposed new correlations [46, 51, 45, 25, 27, 36]. There are still no consensus on this topic.

The stability analyses that are performed in the following chapters depend on the friction factor. Therefore this section makes a brief evaluation of the most used correlations. Three classical ones and three recently proposed were selected. From the classical models, the first one is a combination of the Poiseuille's expression for laminar flows and the Blasius solution for turbulent regime. The friction factor is expressed by

$$f_{PB} = \left[(64/\text{Re})^2 + (0.316/\text{Re}^{0.25})^2 \right]^{0.5} \quad (3.9)$$

The reason to consider this model is that recent correlations like the one proposed by Ruiz et al. [36] are still based on it. The two other classical models, developed in the context of forced flow, are Churchill's, given by

$$\begin{aligned} f_C &= 8 \left[\left(\frac{8}{\text{Re}} \right)^{12} + (A + B^{-1,5}) \right]^{1/12} \\ A &= \left\{ -2,457 \ln \left[\left(\frac{7}{\text{Re}} \right)^{0,9} + \frac{0,27e}{D} \right] \right\}^{16} \\ B &= \left(\frac{37530}{\text{Re}} \right)^{16} \end{aligned} \quad (3.10)$$

and the maximum between Poiseuille's and Colebrook's correlations, i.e.,

$$\begin{aligned} f_{PC} &= \max(f_P, f_C) \\ f_P &= 64/\text{Re} \\ \frac{1}{\sqrt{f_C}} &= -2 \log \left(\frac{e}{3.7D} + \frac{2.51}{\text{Re} \sqrt{f_C}} \right) \end{aligned} \quad (3.11)$$

Colebrook's correlation is widely accepted for forced flow modeling, as confirmed by the survey performed by Fang et al. [13], but its domain of validity is $4000 \leq \text{Re} \leq 10^8$. Therefore it has to be taken combined with Poiseuille's expression for laminar

regime. Churchill's correlation is equal to Poiseuille-Colebrook except for the transitional region, where Churchill has a non-monotonic curve [2, 22] (cf. fig. 3.1).

From the various correlations developed specifically for NCLs, the following three were selected for evaluation: the models proposed by Vijayan et al. [51], Naveen et al. [27] and Ruiz et al. [36].

Vijayan and Austregesilo [46] performed an experimental campaign and arrived at $f = 22.26 \text{ Re}^{-0.6744}$ as friction factor for their range of tests. This correlation, however, was not valid for fully laminar or turbulent flow regimes. Vijayan et al. [51] defined the limits of validity for this correlation in terms of the scaling parameter $\text{Gr } D/L$, which lies in the transitional range from laminar to turbulent flows. Outside transitional flow, Poiseuille and Blasius correlations are used. The friction factor employed by Vijayan et al. [51] is given by

$$\begin{aligned} f_V &= \max(f_P, f_{Vt}, f_B) \\ f_P &= 64/\text{Re} \\ f_{Vt} &= 22.26/\text{Re}^{0.6744} \\ f_B &= 0.316/\text{Re}^{0.25} \end{aligned} \quad (3.12)$$

Naveen et al. [27] discussed the various correlations developed for NCLs mainly after 1980 and arrived at an expression valid for horizontal pipes under diabatic conditions, based on an experimental campaign. The proposed friction factor f_{Nhp} , where the subscript is a reference to "Naveen, horizontal pipes", is defined as

$$\begin{aligned} f_{Nhp} &= f_L \left[1 + (f_{Tt}/f_L)^{6.4} \right]^{1/6.4} \\ f_{Tt} &= f_T \left[1 + (f_t/f_T)^{-2} \right]^{-1/2} \\ f_L &= (64/\text{Re}) \left[1 + (1.56 \text{ Ra}^{0.15})^{15} \right]^{1/15} \\ f_T &= 0.0791 \text{ Re}^{-0.25} (\mu/\mu_w)^{-0.2} \\ f_t &= 0.03862 (\text{Re}/2000)^6 \end{aligned} \quad (3.13)$$

where the subscript w refers to wall, in a way that μ/μ_w is the ratio between bulk and wall dynamic viscosities. The parameter Ra that is input to the friction model is a film Rayleigh number defined as

$$\text{Ra} = \frac{D^3 \beta g \Delta T_{\text{film}}}{\nu \alpha} \quad (3.14)$$

with α defined as the thermal diffusivity $\alpha = \frac{\kappa}{\rho c_p}$. For the vertical pipe sections, the authors used the Poiseuille-Blasius correlation (eq. 3.9). In the present work, momentum balance is integrated along the loop, and a single averaged friction factor is attributed. Hence this correlation need to be adapted to account for all the loop regions. The strategy adopted was to define the friction factor as an average calculated by

$$f_N = \frac{1}{L_h} \int_h f_{Nhp} ds + \frac{1}{L_c} \int_c f_{Nhp} ds + \frac{1}{L - L_h - L_c} \int_{\text{pipes}} f_{PB} ds \quad (3.15)$$

It should be mentioned that this correlation is valid only for HHHC configurations. If heater and/or cooler is vertically orientated, the friction factor applied is also the Poiseuille-Blasius correlation denoted by f_{PB} .

Ruiz et al. [36] also employed a combination of Poiseuille and Blasius' expression, using a Fermi-Dirac distribution to build a derivative continuous transition between the two correlations. The transition parameter, γ , was determined from the fitting of an experimental campaign in a straight infinite tube. The expression for the correlation is

$$\begin{aligned} f_R &= \frac{a}{\text{Re}^b} \\ a &= 64^\gamma 0.316^{1-\gamma} \\ b &= \gamma + \frac{1}{4}(1 + \gamma) \\ \gamma &= \frac{1}{1 + \exp\left(\frac{\text{Re} - 2530}{120}\right)} \end{aligned} \quad (3.16)$$

Figure 3.1 plots the six friction correlations described – eqs. 3.9, 3.11, 3.12, 3.12, 3.15, 3.16. They are all plotted against Re . It is clear that for full laminar or turbulent flow regimes all correlations are equal except for those of Vijayan et al. [51] and Naveen et al. [27], which are larger than the others. Notice that the contribution from the work of Vijayan et al. [51] is for the range $26 \leq \text{Re} \leq 2 \times 10^4$, assuming a long transitional region, indicating a considerable difference in flow regime for NCLs. It can also be observed that the correlation proposed by Ruiz et al. [36] is almost equal to classical Churchill's correlation, which is "hidden" behind the curve for eq. 3.16. In fig. 3.2 the region between $\text{Re} = 1500$ and $\text{Re} = 4000$ is shown in detail. It lies between laminar and turbulent flow regimes and is where the friction models deviate most.

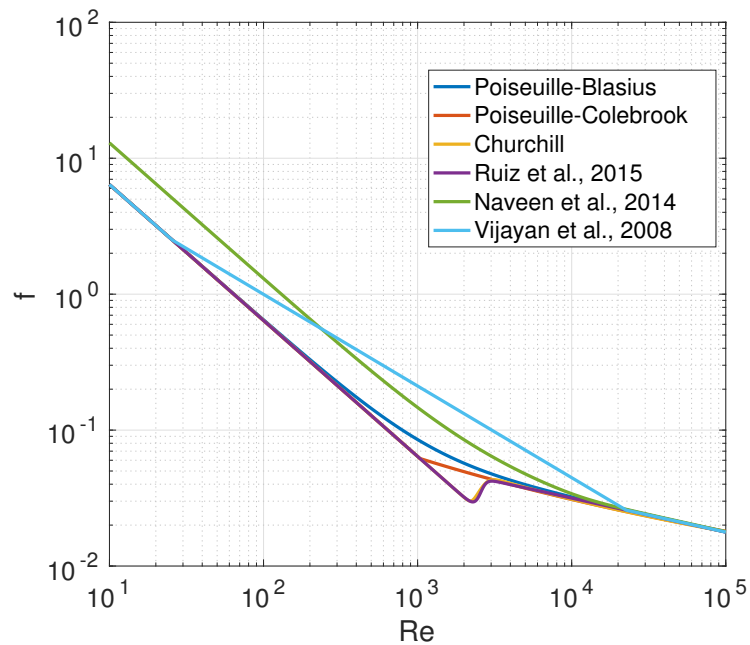


Figure 3.1: Comparison of friction correlations, taking into account $D = 26.9$ mm and $e = 10^{-7}$ (wall roughness).

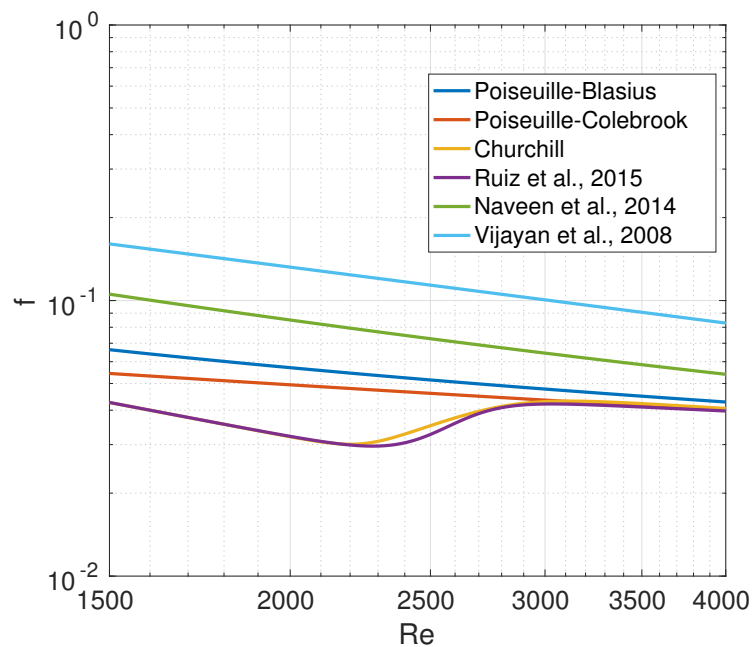


Figure 3.2: Comparison of friction correlation in the transitional region $1500 \leq Re \leq 4000$.

In the next section the friction correlations described here will be evaluated in the steady state calculation against experimental results.

3.2 Steady state results

The six friction correlations were employed in steady state calculations and compared to experimental data from literature. Different orientations of heater and cooler were considered.

Steady state results are presented in terms of the Re number as function of the parameter $\text{Gr} \frac{D}{L}$, which is a non-dimensional form to quantify how much mass flow is obtained from a ratio of buoyancy per viscous losses in the system. As stressed in sec. 2.3, the main non-dimensional groups which characterize the NCL are St and Gr, where St – Stanton number – has the contribution of heat transfer coefficient in the cooler and Gr – Grashof number – brings the effect of power input. These two parameters also combine the contributions of geometric parameters. In the following results, St is fixed at a certain value and a range of Gr is simulated for a loop.

The first case is the HHHC NCL of Naveen et al. [27], which has experimental data for $10^7 \leq \text{Gr} \frac{D}{L} \leq 10^{10}$. Table 3.1 summarizes the geometric and operating parameters simulated. In addition to those data, a very high pressure in the loop (220 bar) was considered in order to keep the system at single-phase, which has negligible influence on the steady state. Figure 3.3 is an extraction from Naveen et al. [27] and shows a sketch of the simulated case.

Table 3.1: Geometric, numerical and operating data for the HHHC 26.9 mm diameter loop from Naveen et al. [27].

L [m]	7.23
D [mm]	26.9
A [mm^2]	568.3
V [m^3]	4.1×10^{-3}
L_h [m]	0.665
L_c [m]	1.000
local losses	4.2
mesh nodes	1000
Gr	$10^5 - 10^{13}$
St	20
T_s [$^\circ\text{C}$]	30
friction correlations:	eqs. 3.9;3.11;3.12;3.12;3.15;3.16

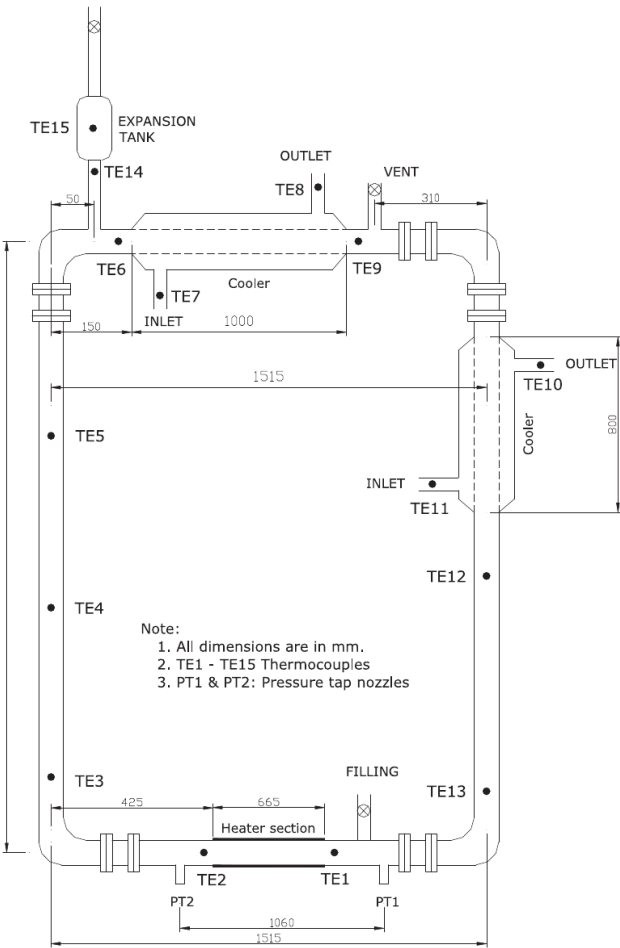


Figure 3.3: Extraction from Naveen et al. [27] showing a sketch of the experimental NCL.

Figure 3.4 shows a plot of the results and 3.5 is a zoom in the region for which experimental data is available.

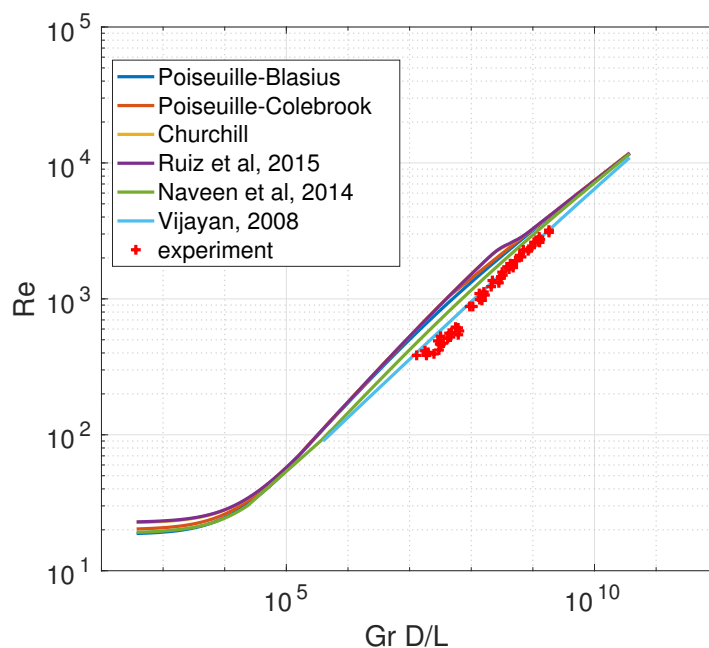
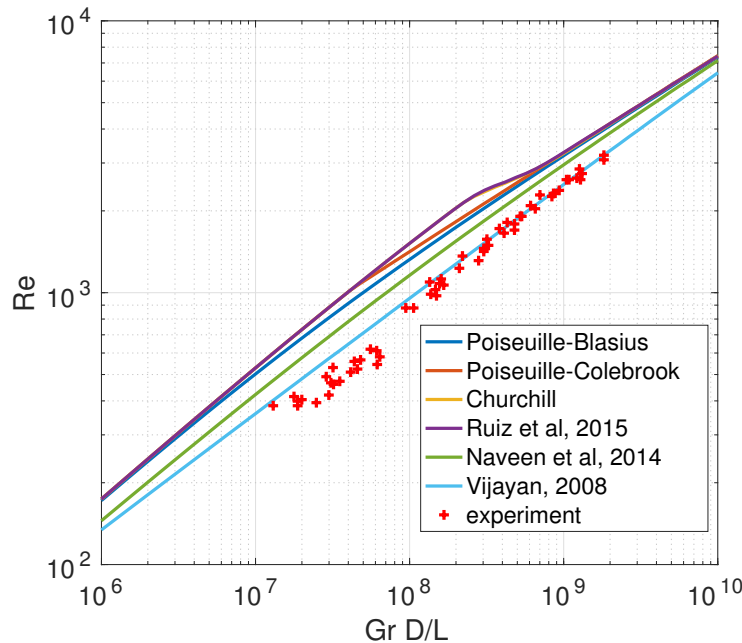


Figure 3.4: Steady state for a range operating points.**Figure 3.5:** Steady state for a range operating points.

As the graphics show, there is a threshold for linear dependence between $\log_{10} \text{Re}$ and $\log_{10}(\text{Gr } \frac{D}{L})$: below approximately $\text{Gr } \frac{D}{L} = 3 \times 10^4$ Re starts to converge to a constant value, as $\text{Gr } \frac{D}{L} \rightarrow 0$. From the six friction correlations, the one which performed best was that of Vijayan et al. [51] (eq. 3.12), as can be observed in the zoomed figure (3.5). Table 3.2 lists the mean deviations from experimental results with all friction models, showing that after Vijayan's model, the one proposed by Naveen et al. [27] performed best. Worst performance was from the model proposed by Ruiz et al. [36]. The response with Churchill's correlation and the one proposed by Ruiz et al. [36] were almost the same; they cannot be distinguished in the plots. Results show clearly that the steady states for this range of $\text{Gr } \frac{D}{L}$ lie in the transition range between laminar and turbulent regimes, and is where friction correlations have the largest deviations between themselves. If flow regime gets more turbulent, the different correlations converge to the same result.

Table 3.2: Mean deviation from numerical results with all friction correlations and experimental data from Naveen et al. [27].

Poiseuille-Blasius	5.8779%
Poiseuille-Colebrook	6.6831%
Churchill	7.1924%
Ruiz et al, 2015	7.2353%
Naveen et al, 2014	4.1123%
Vijayan et al, 2008	1.5417%

3.2.1 Effect of heater/cooler orientation

Vijayan et al. [50] provided a valuable study on the effect of heater and cooler orientations (horizontal or vertical) on the linear and non-linear stabilities of a rectangular NCL. Authors showed experimental and numerical results. In this section their experimental data will be repeated and confronted to numerical results using the six friction factor models of sec. 3.1. Objective is to complement the evaluation of the previous section using the different orientations for heater and cooler.

Figure 3.6 shows a schematic drawing of the experimental loop used by Vijayan et al. [50]. It is basically the same loop described in Naveen et al. [27], with minor differences in heater and cooler lengths.

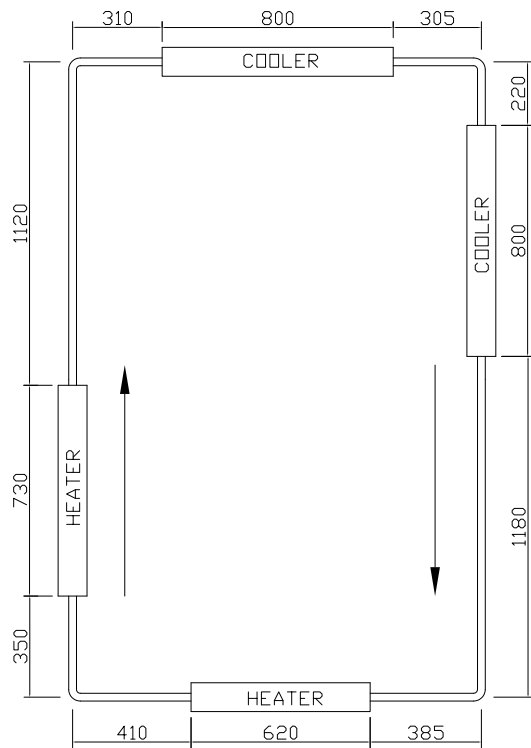


Figure 3.6: Sketch representing the experimental loop built at Bhabha Research Atomic Centre, India.

Table 3.3: Geometric, numerical and operating data for the 26.9 mm diameter loop from Vijayan et al. [50].

L [m]	7.23
D [mm]	26.9
A [mm^2]	568.3
V [m^3]	4.1×10^{-3}
L_h [m]	0.620
L_c [m]	0.800
local losses	4.2
mesh nodes	1000
Gr	$10^9 - 10^{12}$
St	20
T_s [$^\circ\text{C}$]	30
friction correlations:	eqs. 3.9;3.11;3.12;3.12;3.15;3.16

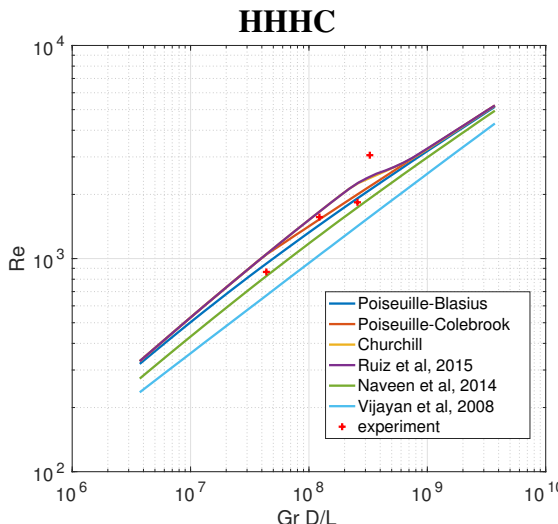


Figure 3.7: Steady state data from numerical and experimental tests for HHHC loop configuration.

Table 3.4: Mean deviation from experimental data from Vijayan et al. [50] with all friction correlations for HHHC configuration.

Poiseuille-Blasius	1.7433%
Poiseuille-Colebrook	1.7083%
Churchill	1.3378%
Ruiz et al, 2015	1.2824%
Naveen et al, 2014	2.5227%
Vijayan et al, 2008	5.3044%

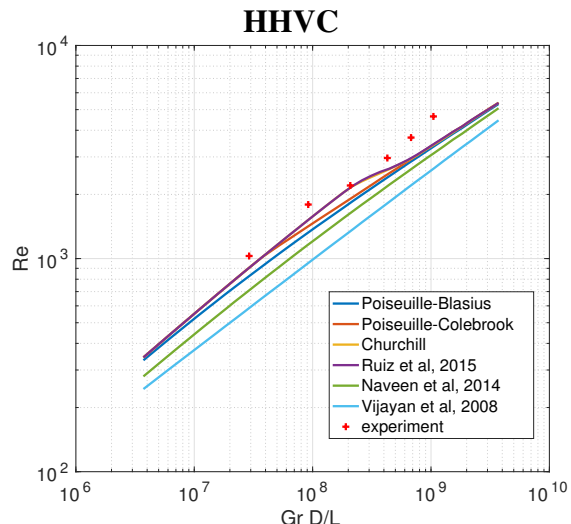


Figure 3.8: Steady state data from numerical and experimental tests for HHVC loop configuration.

Table 3.5: Mean deviation from experimental data from Vijayan et al. [50] with all friction correlations for HHVC configuration.

Poiseuille-Blasius	3.2245%
Poiseuille-Colebrook	2.6034%
Churchill	2.0872%
Ruiz et al, 2015	2.0406%
Naveen et al, 2014	4.6331%
Vijayan et al, 2008	7.0264%

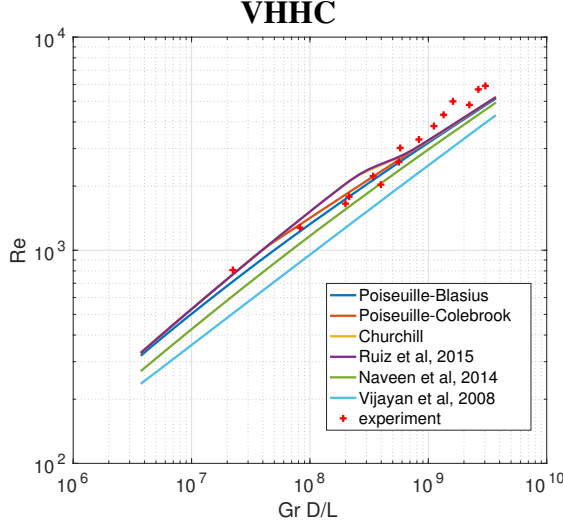


Figure 3.9: Steady state data from numerical and experimental tests for VHHC loop configuration.

Table 3.6: Mean deviation from experimental data from Vijayan et al. [50] with all friction correlations for VHHC configuration.

Poiseuille-Blasius	1.1896%
Poiseuille-Colebrook	1.0172%
Churchill	1.2691%
Ruiz et al, 2015	1.2535%
Naveen et al, 2014	2.3208%
Vijayan et al, 2008	4.5676%

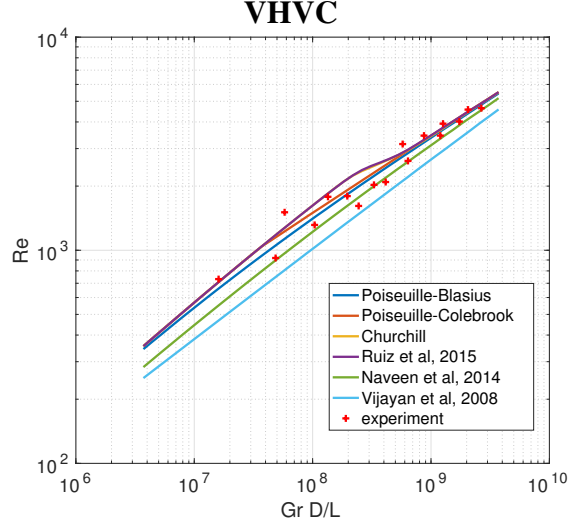


Figure 3.10: Steady state data from numerical and experimental tests for VHVC loop configuration.

Table 3.7: Mean deviation from experimental data from Vijayan et al. [50] with all friction correlations for VHVC configuration.

Poiseuille-Blasius	0.2358%
Poiseuille-Colebrook	0.5739%
Churchill	1.0401%
Ruiz et al, 2015	1.0864%
Naveen et al, 2014	1.4254%
Vijayan et al, 2008	3.5856%

Results now show that the worst performance came from the correlation of Vijayan et al. [51], and after that, the one from Naveen et al. [27], both under predicting steady state Reynolds number. The forced flow models, including the proposed by Ruiz et al. [36], alternate in proximity to the experimental points. In particular, Poiseuille-Blasius correlation has very good agreement in the VHVC case.

3.2.2 Theoretical friction factor

The non-dimensional form of steady state momentum equation is given by

$$\left(f \frac{L}{D} + K \right) \frac{\omega^2}{2} = \frac{\text{Gr}}{\text{Re}^3} \oint \theta dZ \quad (3.17)$$

From the scaling laws (sec. 2.3), at steady state $\omega = 1$. The line integration in eq. 3.17 can be decomposed in parcels for the horizontal pipes and vertical pipes. In the horizontal parts, there is no variation in elevation, so $dZ = 0$, with null contribution to

the integration. For a HHHC configuration, the vertical parts are contained in the hot leg (subscript hl) and in the cold leg (subscript cl), with constant steady state temperature. Thus

$$\oint \theta dZ = \theta_{hl} \int_{hl} dZ + \theta_{cl} \int_{cl} dZ \quad (3.18)$$

Integrations in the right hand side are simply the positive and negative non-dimensional loop height, i.e., $\int_{hl} dZ = 1$ and $\int_{cl} dZ = -1$. Recalling the scaling parameters for temperature, the following expression can be written

$$\oint \theta dZ = \frac{T_{hl} - T_s}{\Delta \bar{T}_h} - \frac{T_{cl} - T_s}{\Delta \bar{T}_h} \quad (3.19)$$

At steady state, the mean temperature difference in the heater is equal to the difference between outlet and inlet, so that

$$\oint \theta dZ = \frac{T_{hl} - T_s}{T_{hl} - T_{cl}} - \frac{T_{cl} - T_s}{T_{hl} - T_{cl}} = 1 \quad (3.20)$$

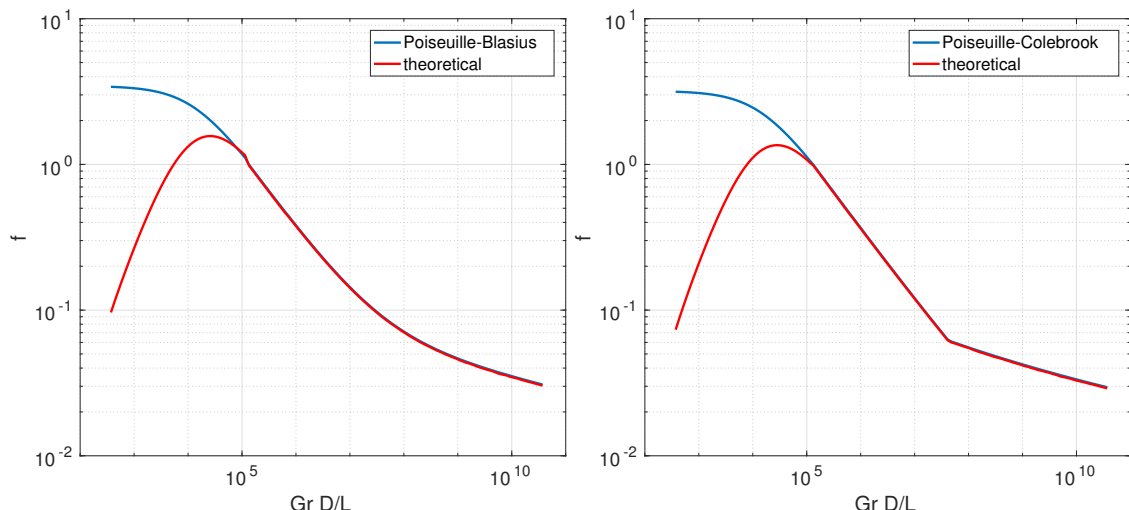
Then eq. 3.17 can be rewritten as

$$\frac{1}{2} \left(f \frac{L}{D} + K \right) = \frac{\text{Gr}}{\text{Re}^3} \quad (3.21)$$

From this result, the friction factor can be expressed as the steady state non-dimensional groups and geometrical parameters as

$$f = \frac{2}{\text{Re}^3} \left(\text{Gr} \frac{D}{L} \right) - K \frac{D}{L} \quad (3.22)$$

The next plots will present a comparison between the theoretical friction factor just derived, expressed by eq. 3.22, and those from the correlations.



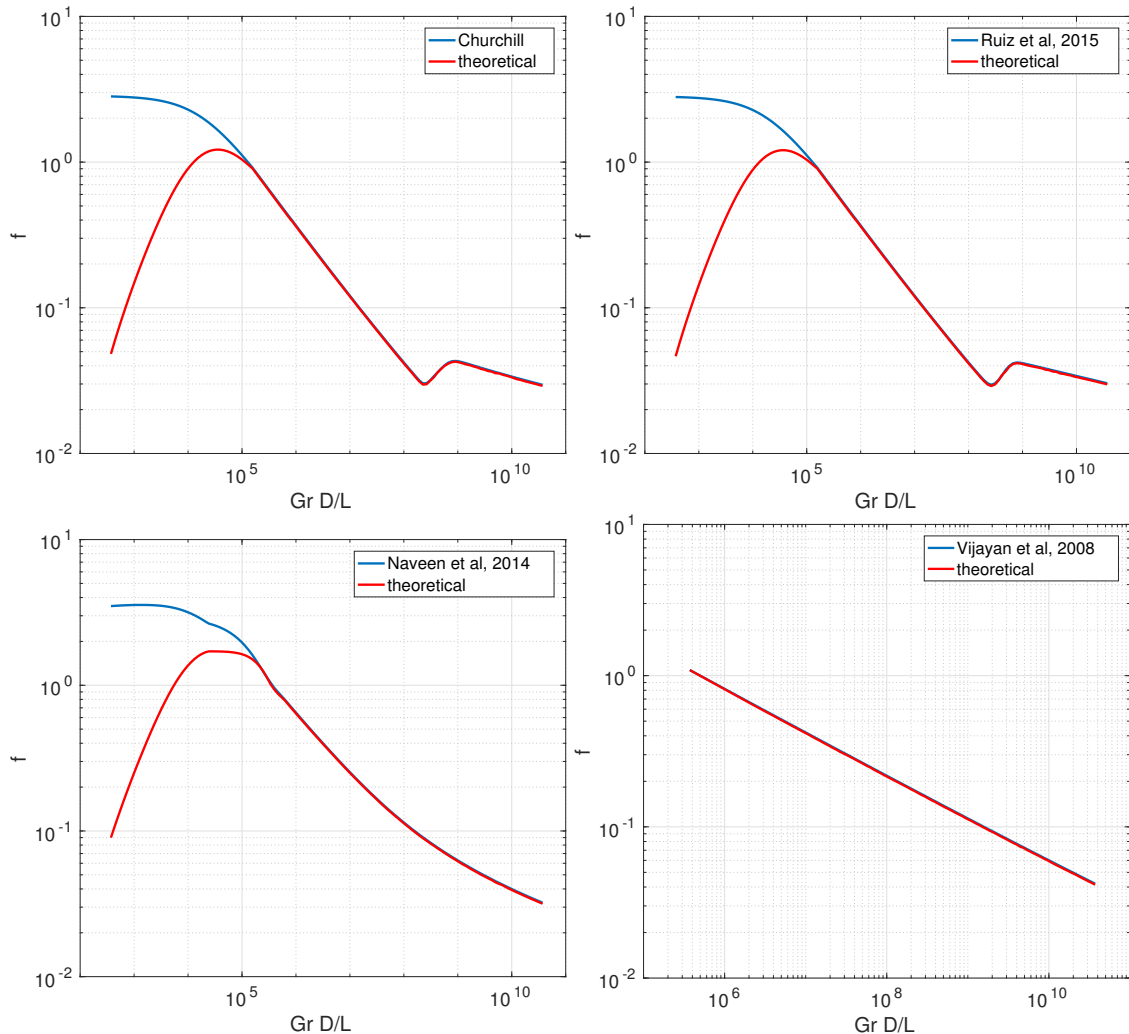


Figure 3.11: Comparison of the six friction factor correlations and the theoretical friction factor according to eq. 3.22.

The conclusion from these plots is that the scaling described in sec 2.3 perform well in the region of linearity between $\log_{10} f$ and $\log_{10}(\text{Gr } \frac{D}{L})$. As already mentioned, for $\text{Gr } \frac{D}{L} < 3 \times 10^4$ theoretical friction factor deviates from the correlation used in the simulation. The operating range $\text{Gr } \frac{D}{L} < 3 \times 10^4$ is actually not practical; it implies in excessively low power loads, which are unreal when it comes to application.

4 LINEAR STABILITY ANALYSIS

As explained in chapter 3, heat removal systems are designed to operate at stationary condition for the most stringent scenarios. They must also be resistant to small perturbations. For example, if a small variation in power input occurs, the system must be designed in a way that it recovers the previous thermo-hydraulic condition after the perturbation. It must be stable to perturbations up to a design limit.

Under this concept of stability, if the system is stable, after a perturbation, it will oscillate with decaying amplitude and converge back to its original condition. The behavior of a system with respect to the development of constant period oscillations with exponential growth or decay is referred to as linear stability. Geometrical and operating parameters will determine if a system is stable or not. For instance, the larger the loop diameter, the more the circuit tends to become unstable. The opposite occurs with the heat transfer coefficient for cooler: the larger it is, the more stable the circuit becomes. It can be noticed from this consideration that energy dissipation is a stabilizing feature; smaller diameters increase the pressure loss by friction, which contributes to stabilize the loop.

Linear stability is changed if the circuit is absorbing heat indirectly from a pool, which is the most common configuration of emergency safety systems in nuclear power installations. The effect of the pool in the stability of single-phase NCLs will be quantitatively evaluated in this chapter. Stability maps for a wide range of operating points will be presented for the four possible configurations in terms of heater/cooler orientation for the case with and without the pool.

Before the results, the linearized model is derived from the balance equations in the following section.

4.1 Linear model

Linear methods to assess stability of a dynamical system is a powerful tool because they provide information about stability without the price of a long transient calculation. The counterpart is that non-linear effects are suppressed. Stability analysis is performed

by the solution of an eigenvalue problem, obtained by the perturbed version of equations 2.3, 2.7 and 2.9. Consider the decompositions

$$w = \bar{w} + \tilde{w} \quad (4.1a)$$

$$T = \bar{T} + \tilde{T} \quad (4.1b)$$

$$T_{\text{pool}} = \bar{T}_{\text{pool}} + \tilde{T}_{\text{pool}} \quad (4.1c)$$

where \bar{w} , \bar{T} and \bar{T}_{pool} define the steady state condition and \tilde{w} , \tilde{T} and \tilde{T}_{pool} are small perturbations imposed on the steady state. Inserting 4.1 into equations 2.3, 2.7 and 2.9, the following set of equations is obtained.

$$\begin{aligned} \frac{L}{A} \left(\frac{d\bar{w}}{dt} + \frac{d\tilde{w}}{dt} \right) &= \rho_0 g \beta \oint (\bar{T} + \tilde{T}) dz - \\ &- \left[f(\bar{w} + \tilde{w}) \frac{L}{D} + K \right] \frac{\bar{w}^2 + 2\bar{w}\tilde{w} + \tilde{w}^2}{2\rho_0 A^2} \end{aligned} \quad (4.2)$$

$$\begin{aligned} \frac{\partial \bar{T}}{\partial t} + \frac{\partial \tilde{T}}{\partial t} + \frac{\bar{w} + \tilde{w}}{\rho_0 A} \left(\frac{\partial \bar{T}}{\partial s} + \frac{\partial \tilde{T}}{\partial s} \right) &= -\frac{4U_h(\bar{T} + \tilde{T})}{D\rho_0 c_p} + \\ &+ \frac{4U_h(\bar{T}_{\text{pool}} + \tilde{T}_{\text{pool}})}{D\rho_0 c_p} \end{aligned} \quad (4.3)$$

$$\begin{aligned} \frac{\partial \bar{T}}{\partial t} + \frac{\partial \tilde{T}}{\partial t} + \frac{\bar{w} + \tilde{w}}{\rho_0 A} \left(\frac{\partial \bar{T}}{\partial s} + \frac{\partial \tilde{T}}{\partial s} \right) &= \frac{4U_c T_s}{D\rho_0 c_p} - \\ &- \frac{4U_c(\bar{T} + \tilde{T})}{D\rho_0 c_p} \end{aligned} \quad (4.4)$$

$$\frac{\partial \bar{T}}{\partial t} + \frac{\partial \tilde{T}}{\partial t} + \frac{\bar{w} + \tilde{w}}{\rho_0 A} \left(\frac{\partial \bar{T}}{\partial s} + \frac{\partial \tilde{T}}{\partial s} \right) = 0 \quad (4.5)$$

$$\begin{aligned} M c_p \left[\frac{d\bar{T}_{\text{pool}}}{dt} + \frac{d\tilde{T}_{\text{pool}}}{dt} \right] &= Q + \\ &+ U_h \pi D \left[\int_h (\bar{T} + \tilde{T}) ds - \bar{T}_{\text{pool}} L_h - \tilde{T}_{\text{pool}} L_h \right] \end{aligned} \quad (4.6)$$

The friction factor $f(\bar{w} + \tilde{w})$ can be written as an expansion in Taylor series, i.e.,

$$f(\bar{w} + \tilde{w}) = f(\bar{w}) + \tilde{w} f'(\bar{w}) + \mathcal{O}(\tilde{w}^2) \quad (4.7)$$

Now, taking into account that \bar{w} , \bar{T} and \bar{T}_{pool} are solutions of the system, and neglecting non-linear terms, making use of the hypothesis of small perturbations, we arrive at

$$\frac{L}{A} \frac{d\tilde{w}}{dt} = - \left(f \frac{L}{D} + K \right) \frac{\bar{w}\tilde{w}}{\rho_0 A^2} - \tilde{w} f' \frac{L}{D} \frac{\bar{w}^2}{2\rho_0 A^2} + \rho_0 g \beta \oint \tilde{T} dz \quad (4.8)$$

$$\frac{\partial \tilde{T}}{\partial t} + \frac{\bar{w}}{\rho_0 A} \frac{\partial \tilde{T}}{\partial s} + \frac{\tilde{w}}{\rho_0 A} \frac{\partial \bar{T}}{\partial s} = \frac{4U_h(\tilde{T}_{\text{pool}} - \tilde{T})}{D\rho_0 c_p} \quad (4.9a)$$

$$\frac{\partial \tilde{T}}{\partial t} + \frac{\bar{w}}{\rho_0 A} \frac{\partial \tilde{T}}{\partial s} + \frac{\tilde{w}}{\rho_0 A} \frac{\partial \bar{T}}{\partial s} = - \frac{4U_c \tilde{T}}{D\rho_0 c_p} \quad (4.9b)$$

$$\frac{\partial \tilde{T}}{\partial t} + \frac{\bar{w}}{\rho_0 A} \frac{\partial \tilde{T}}{\partial s} + \frac{\tilde{w}}{\rho_0 A} \frac{\partial \bar{T}}{\partial s} = 0 \quad (4.9c)$$

$$M c_{pp} \frac{d\tilde{T}_{\text{pool}}}{dt} = U_h \pi D \left(\int_h \tilde{T} ds - \tilde{T}_{\text{pool}} L_h \right) \quad (4.10)$$

The amplitude of the perturbations can be denoted by \hat{w} , \hat{T} and \hat{T}_{pool} , where \hat{w} and \hat{T}_{pool} are constants and $\hat{T} = \hat{T}(s)$ is a function of s . Solution of the system of equations 4.8, 4.9 and 4.10 can then be written as

$$\tilde{w} = \hat{w} e^{\lambda t} \quad (4.11a)$$

$$\tilde{T} = \hat{T}(s) e^{\lambda t} \quad (4.11b)$$

$$\tilde{T}_{\text{pool}} = \hat{T}_{\text{pool}} e^{\lambda t} \quad (4.11c)$$

which express time evolution of small perturbations \tilde{w} , \tilde{T} and \tilde{T}_{pool} , where λ are complex numbers. After 4.11, equations 4.8, 4.9 and 4.10 become

$$\begin{aligned} \frac{L}{A} \lambda \hat{w} e^{\lambda t} &= - \left(f \frac{L}{D} + K \right) \frac{\bar{w} \hat{w} e^{\lambda t}}{\rho_0 A^2} - \hat{w} e^{\lambda t} f' \frac{L}{D} \frac{\bar{w}^2}{2\rho_0 A^2} \\ &\quad + \rho_0 g \beta \oint \hat{T}(s) e^{\lambda t} dz \end{aligned} \quad (4.12)$$

$$\lambda \hat{T} e^{\lambda t} + \frac{\bar{w}}{\rho_0 A} e^{\lambda t} \hat{T}' + \frac{\hat{w} e^{\lambda t}}{\rho_0 A} \bar{T}' = -\frac{4U_c \hat{T} e^{\lambda t}}{D \rho_0 c_p} \quad (4.13a)$$

$$\lambda \hat{T} e^{\lambda t} + \frac{\bar{w}}{\rho_0 A} e^{\lambda t} \hat{T}' + \frac{\hat{w} e^{\lambda t}}{\rho_0 A} \bar{T}' = 0 \quad (4.13b)$$

$$M c_{pp} \lambda \hat{T}_{\text{pool}} e^{\lambda t} = U_h \pi D \left(\int_h \hat{T} e^{\lambda t} ds - \hat{T}_{\text{pool}} e^{\lambda t} L_h \right) \quad (4.14)$$

where \bar{T}' , \hat{T}' correspond to $d\bar{T}/ds$ and $d\hat{T}/ds$, respectively.

Since $e^{\lambda t}$ is a common multiplier to all terms, the system of equations 4.12, 4.13 and 4.14 is equivalent to

$$\begin{aligned} \lambda \hat{w} &= - \left(f \frac{L}{D} + K \right) \frac{\bar{w} \hat{w}}{\rho_0 L A} - \hat{w} f' \frac{\bar{w}^2}{2 D \rho_0 A} \\ &\quad + \frac{A}{L} \rho_0 g \beta \oint \hat{T} dz \end{aligned} \quad (4.15)$$

$$\lambda \hat{T} + \frac{\bar{w}}{\rho_0 A} \hat{T}' + \frac{\hat{w}}{\rho_0 A} \bar{T}' = -\frac{4U_c \hat{T}}{D \rho_0 c_p} \quad (4.16a)$$

$$\lambda \hat{T} + \frac{\bar{w}}{\rho_0 A} \hat{T}' + \frac{\hat{w}}{\rho_0 A} \bar{T}' = 0 \quad (4.16b)$$

$$\lambda \hat{T}_{\text{pool}} = \frac{U_h \pi D}{M c_{pp}} \left(\int_h \hat{T} ds - \hat{T}_{\text{pool}} L_h \right) \quad (4.17)$$

The steady state fields are expressed in a finite dimension space, so that the spatial derivatives \bar{T}' , \hat{T}' can be characterized by a linear operator over the fields \bar{T} and \hat{T} , by using upwind finite differences.

Defining a vector field \mathbf{Y} with components \hat{w} , \hat{T} and \hat{T}_{pool} , the linear system can be expressed in matrix notation by

$$\mathbf{A} \mathbf{Y} = \lambda \mathbf{Y} \quad (4.18)$$

where the eigenfunctions \mathbf{Y} are composed by the amplitudes of the perturbations, and the associated eigenvalues define the frequency of oscillations and the time evolution of the amplitudes, i.e., growth/decay rate, which is given by the real part of λ . The matrix \mathbf{A}

is composed by the coefficients and operators (derivatives and integrations) of \hat{w} , \hat{T} and \hat{T}_{pool} . So the linear analysis is performed by searching the eigenvalues λ (also be referred to as *characteristic exponent* [29]) of the matrix \mathbf{A} .

By the classical criterion of linear analysis, stability of a fixed point is evaluated from the real part of the eigenvalue with largest real part. For the NCL, the fixed point is the steady state, which is a time-independent phase state, from the point of view of system dynamics, and linear stability analysis evaluates the system capacity of recovering the steady state after a small perturbation. If matrix \mathbf{A} has at least one eigenvalue with real part larger than one, i.e. $\text{real}(\lambda) > 1$, then the dynamical system has at least one oscillating mode with exponentially growing amplitude which will dominate over other oscillating modes with smaller values of λ . In other words, if \mathbf{A} has at least one eigenvalue λ such that $\text{real}(\lambda) > 1$, the system is considered unstable. If $\text{real}(\lambda) < 1$ for all λ , then the system is asymptotically stable, in the sense it recovers its original state as $t \rightarrow \infty$.

4.2 Stability maps

Stability maps serve as indicators of the critical values of system parameters for stability. It defines the borders between stable and unstable regimes, which consist of a set of critical parameters. Following the scaling described in section 2.3, stability maps for a NCL can be drawn in terms of its Stanton, associated to the heater transfer in the cooler, and Grashof numbers, combined with a geometrical number – St and $\text{Gr } D/L$ – as also done by Vijayan and Austregesilo [46], Vijayan et al. [50] and other works, understanding that the system can be characterized by these two non-dimensional groups. Since the problem under consideration in this work includes an additional element to the NCL, another non-dimensional parameter is demanded. Following the equation for global energy balance in the pool in non-dimensional form (eq. 4.20, also presented in sec. 2.3), it can be seen that the coupling to the pool is characterized by the parameter ψ , defined as

$$\psi = \frac{M}{V\rho_0} \quad (4.19)$$

$$\psi \frac{d\theta_{\text{pool}}}{d\tau} = 1 - \text{St}_h \left[\theta_{\text{pool}} - \frac{H}{L_h} \int_h \theta dS - \frac{T_s}{\Delta \bar{T}_h} \right] \quad (4.20)$$

If no pool is considered, $\psi = 0$, otherwise, $\psi > 0$. So ψ is the third characterizing parameter of the system.

Coupling to a pool differentiates direct heat input to the NCL, through the heater, from heat input transferred to the water mass contained in the pool which transfers it to the NCL in a rate dependent on heat transfer coefficient and temperature difference. In the latter case, thermal inertia of the pool accommodates perturbations that may occur in

Table 4.1: Four cases considered for stability maps in terms of dimensionless parameter ψ .

no pool coupled to the NCL	$\psi = 0$
pool coupled	$\psi = 10^0$
pool coupled	$\psi = 10^2$
pool coupled	$\psi = 10^4$

the convection loop. For instance, a small reduction in mass flow would result in increase of heater outlet temperature in the case of constant heat input to the circuit (no pool connected), producing an elevation of buoyancy force. Mass flow then increase, lowering heater outlet temperature. Depending on the time taken by this hot and cold fluid pockets to travel through the whole loop, this interplay between mass flow and temperature distribution may oscillate with increasing amplitude. This mechanism was already explained by Welander [53]. When heat is indirectly transferred to the loop by the pool, a small decrease in mass flow result in a transient reduction in the heat transfer rate to the circuit, which is compensated by a temperature elevation of the water mass in the pool. It is naturally expected, consequently, that the larger the amount of water in the pool, the more it can dampen thermal-hydraulic oscillations in the circuit. Results presented in sec. 4.3 however show that this is not what linear analysis predicts.

Another aspect is that the pool has its own oscillating mechanisms, as a natural consequence of thermal transport. Convection cells are created when heat is injected in the water and rejected to the NCL via heater. The dynamics of such currents certainly have an influence on those of the loop. However, the model employed in this work does not take pool dynamics into account. Instead, as expressed by eq. 2.9, it makes a global energy balance for the pool, in a way that instantaneous heat dissipation in the water happens according to the model.

In the stability maps of figs. 4.2 to 4.5, the four cases listed in table 4.1 are adopted for analysis.

A hypothetical NCL was considered for linear stability analysis, whose dimensions are compiled in table 4.2. Pressure in the circuit was set at 220 bar to prevent the system from phase change, and the diameter is very large (800 mm) to allow for calculations with a wide range of Grashof numbers without phase-change. The maps are presented in terms of non-dimensional groups.

The correlation proposed in Ruiz et al. [36] was selected for friction factor. It provided good agreement to steady state experimental data, as shown in chapter 3, and is in the conservative side because for presenting small friction factors in comparison to other correlations, which favors safety.

Figures 4.2, 4.3, 4.4 and 4.5 present the stability maps as function of St and the

Table 4.2: Geometric, numerical and operating data for the HHHC 26.9 mm diameter loop.

L [m]	28.00
D [mm]	800.00
A [m^2]	0.5027
V [m^3]	14.0743
local losses	1.8
mesh nodes	750
$\text{Gr } D/L$	$10^7 - 10^{14}$
St	1 – 30
T_s [$^\circ\text{C}$]	30
friction correlation	Ruiz et al., 2015

group $\text{Gr } D/L$ for the four possible configurations in terms of heater/cooler orientation. Each figure brings the region of stability, colored in gray scale, with and without coupling to a pool. They are presented as projections of the surface $\psi_c = F(\text{St}, \text{Gr } D/L)$, ψ_c standing for the critical ψ , that divides stable and unstable regime areas on the $(\text{St}, \text{Gr } D/L)$ plane for the four values of ψ listed in table 4.1.

For each of the four combinations of heater/cooler orientations (HHHC, HHVC, VHHC and VHVC, cf. 2.1), the regions of stability associated the four variants of ψ are superposed in the same plot, following the order that larger regions are located behind smaller ones. They are differentiated by colors in gray scale, and identified by labels indicating the corresponding value of ψ . In each figure, the darkest area is the stability region respective to the NCL without pool, and the other areas in gray are stability regions with different values of ψ for NCL coupled to a pool. The stability regions shown in the maps were constructed from the level curves corresponding to zero eigenvalues, from the solution of the eigenvalue problem of eq. 4.18. From the points of the level curve, a smooth curve is generated by fitting polynomial functions. Quality of the fittings are measured by the coefficient of determination R^2 (where $R^2 = 1$ corresponds to a perfect fitting), shown in table 4.3 for the sixteen cases considered. It provides information on the accuracy of the stability curves of the maps. The lowest reliability occurred in the VHVC configuration for $\psi = 10^4$.

Table 4.3: Coefficient of determination from the fittings of the stability maps shown by figs. 4.2 to 4.5.

ψ	R^2			
	HHHC	HHVC	VHHC	VHVC
0	0.9860	0.9887	0.9900	0.9940
10^0	0.9604	0.9559	0.9567	0.9680
10^2	0.9528	0.9508	0.9476	0.8928
10^4	0.9492	0.9398	0.9406	0.8891

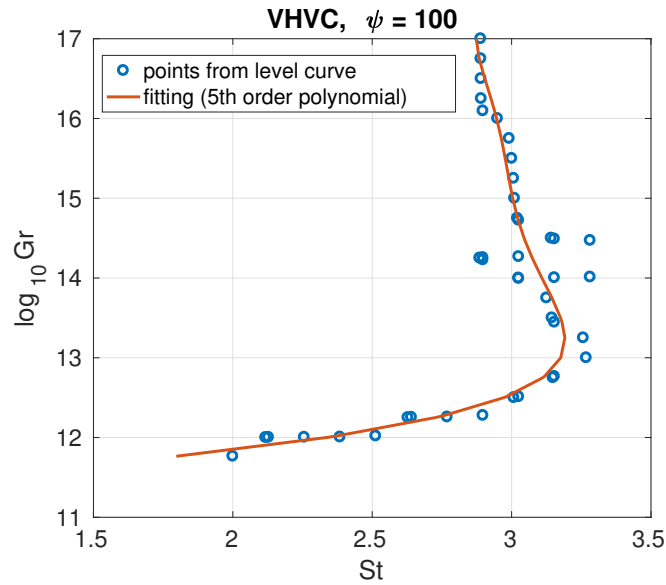


Figure 4.1: Example of fitting of level curve for VHVC configuration and $\psi = 100$. for this case was $R^2 = 0.8928$.

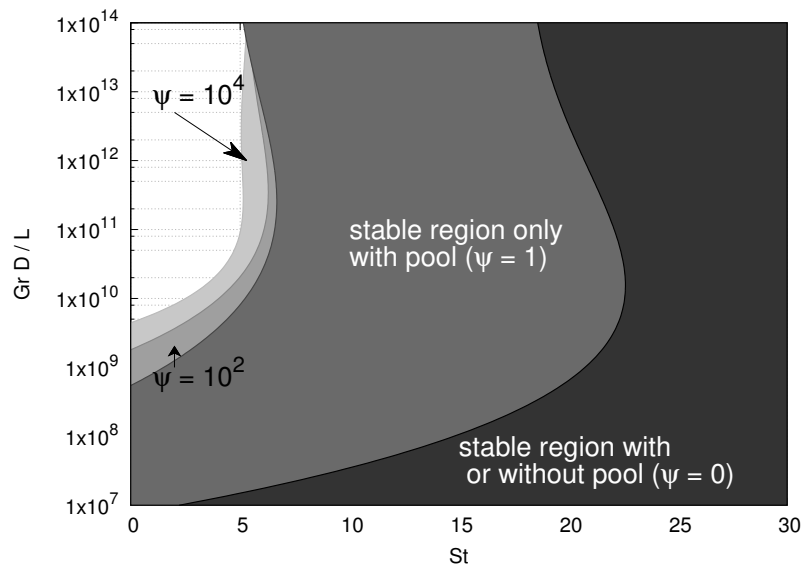


Figure 4.2: Stability map for HHHC 800 mm diameter loop with and without pool.

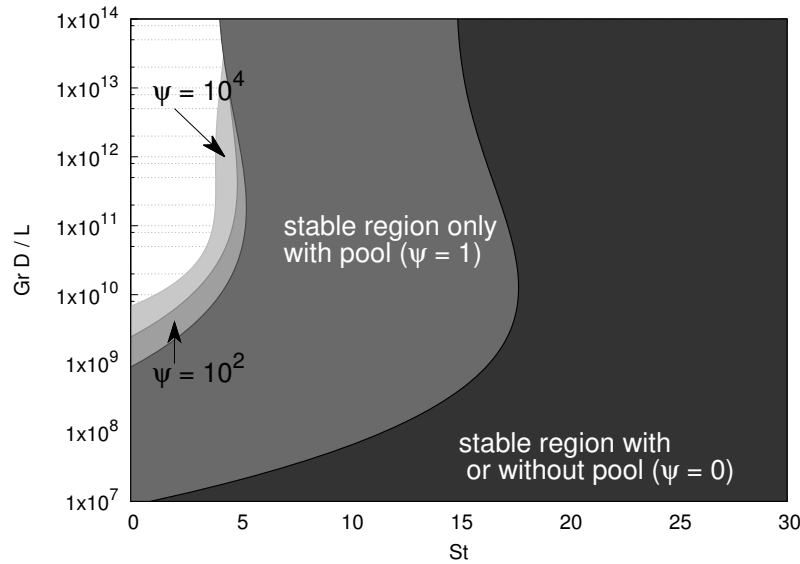


Figure 4.3: Stability map for HHVC 800 mm diameter loop with and without pool.

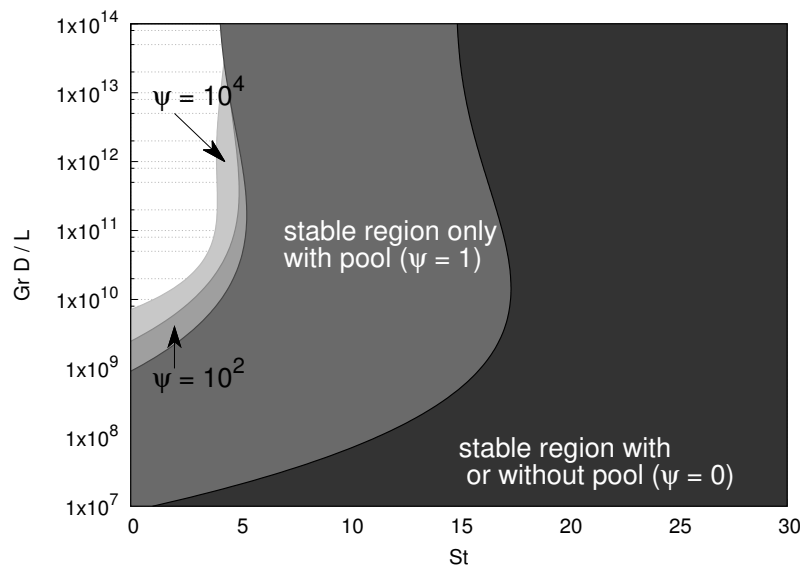


Figure 4.4: Stability map for VHHC 800 mm diameter loop with and without pool.

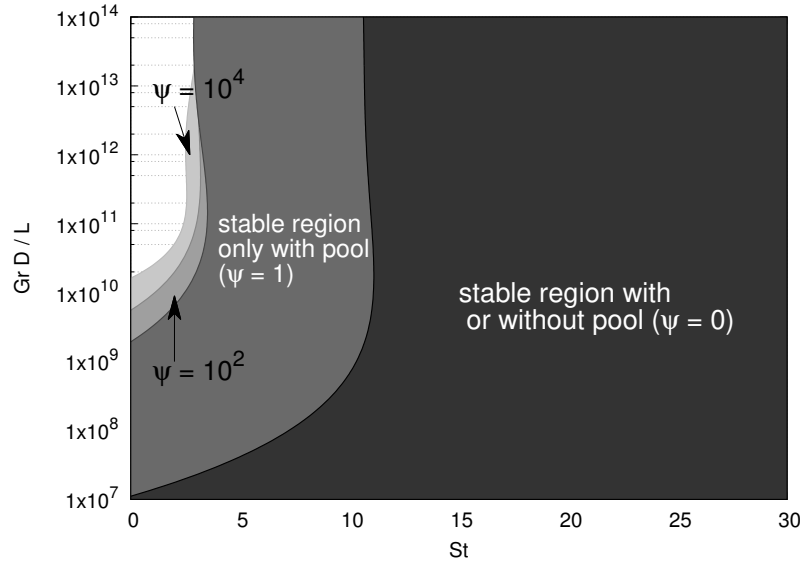


Figure 4.5: Stability map for VHVC 800 mm diameter loop with and without pool.

First clear impression is that taking the coupling of the pool to the NCL into account produces significantly different limits of linear stability, strongly enlarging the stable region. The amount of water, however, represented by the non-dimensional parameter ψ , seems to have small influence on the map of stability. It can also be noticed that orientation of heater and cooler changes the dynamical behavior of the system, which was the main result from the work of Vijayan et al. [50], with vertically oriented heater and/or cooler resulting in more stable / less unstable conditions.

Observe that a critical Stanton number St_c can be associated to each stability region, defining a bounding value above which the system is unconditionally stable. The effect of the pool on the circuit significantly reduces St_c , providing much larger areas of stability. Quantitative figures are summarized in table 4.4.

For $\psi = 1$, critical Stanton number St_c is reduced by 67.12%, 67.63%, 66.45% and 66.76% respectively for HHHC, HHVC, VHHC and VHVC in comparison to St_c for $\psi = 0$. Therefore, linear stability analysis shows that to neglect the pool, an element that is present in the majority of emergency safety systems of nuclear power plants, produces

Table 4.4: Critical Stanton numbers St_c for the four configuration of the loop described by table 4.2.

ψ	St_c			
	HHHC	HHVC	VHHC	VHVC
0	22.17	17.33	16.81	10.92
10^0	7.29	5.61	5.64	3.63
10^2	6.40	4.94	5.03	3.28
10^4	5.59	4.56	4.56	3.23

highly conservative results with respect to stability.

Results show that increasing ψ from 10^0 to 10^4 does not change the stability threshold significantly, as corroborated by the values of St_c in table 4.4. But these results show stability areas for only four values of ψ . In figs. 4.7 to 4.10, stability maps are shown for two planes (St, ψ), corresponding to $Gr D/L = 10^{12}$ and $Gr D/L = 10^{14}$. Again, there are four figures, each for a loop configuration. Stable regions are highlighted in gray scale, limited by the level curve at $\max[\text{real}(\lambda)] = 0$. For illustration, fig. 4.6 shows the surface $\max[\text{real}(\lambda)] = F(St, \psi)$ and the level curve on it.

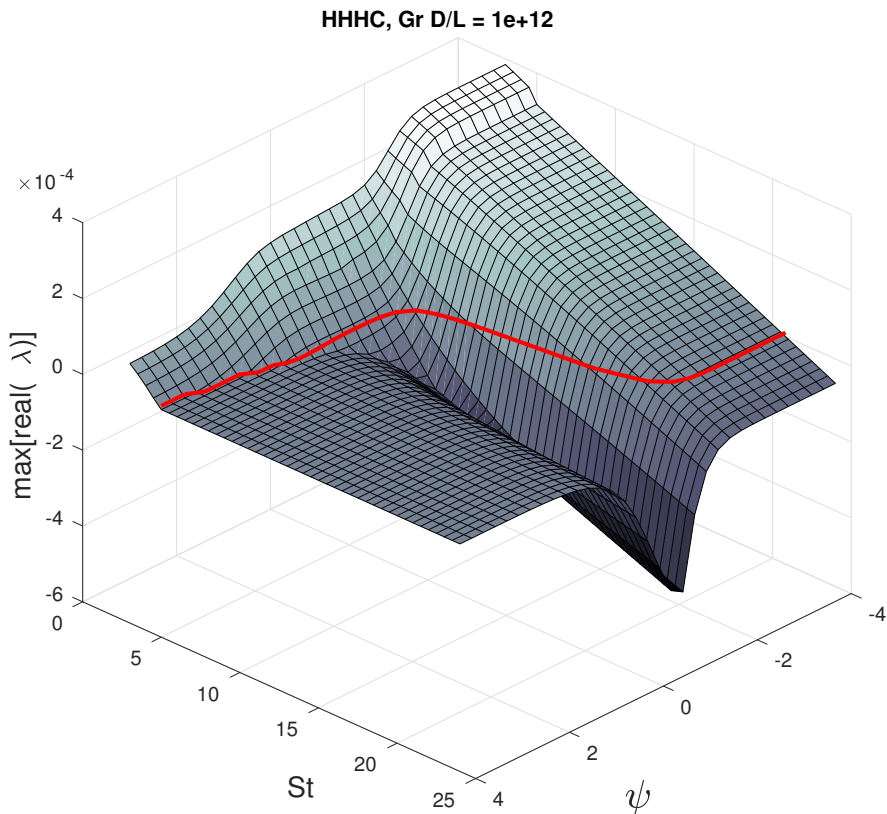


Figure 4.6: Surface $\max[\text{real}(\lambda)] = F(St, \psi)$.

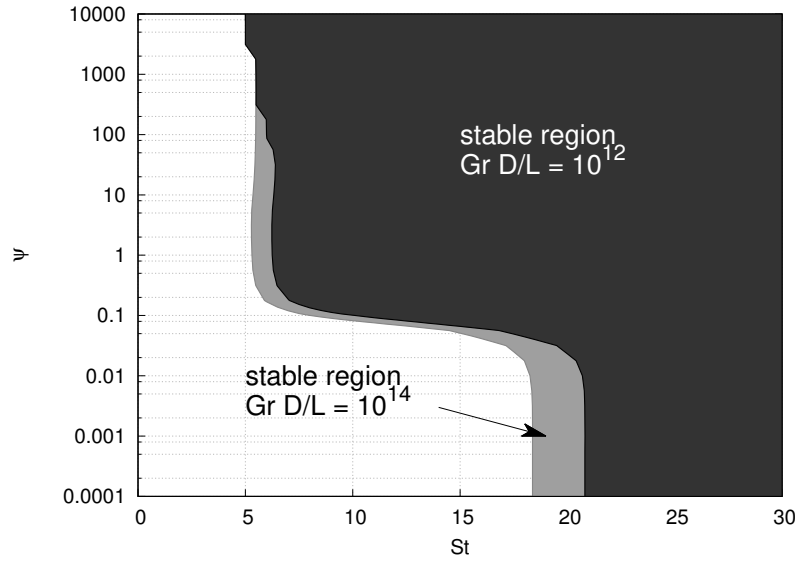


Figure 4.7: Stability map on $St - \psi$ plane for HHHC 800 mm diameter loop.

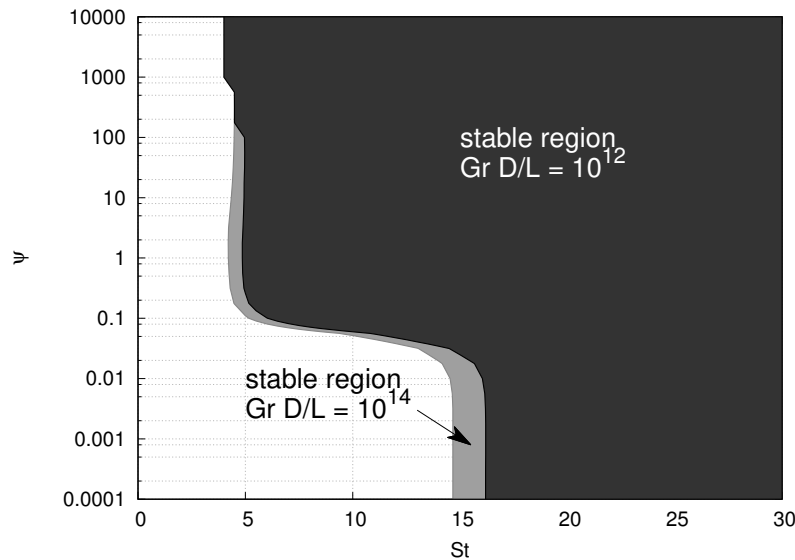


Figure 4.8: Stability map on $St - \psi$ plane for HHVC 800 mm diameter loop.

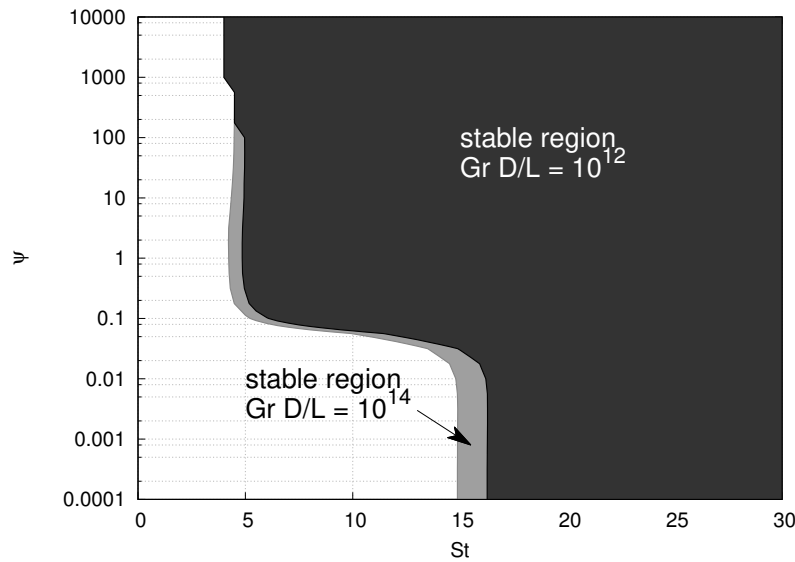


Figure 4.9: Stability map on $St - \psi$ plane for VHHC 800 mm diameter loop.

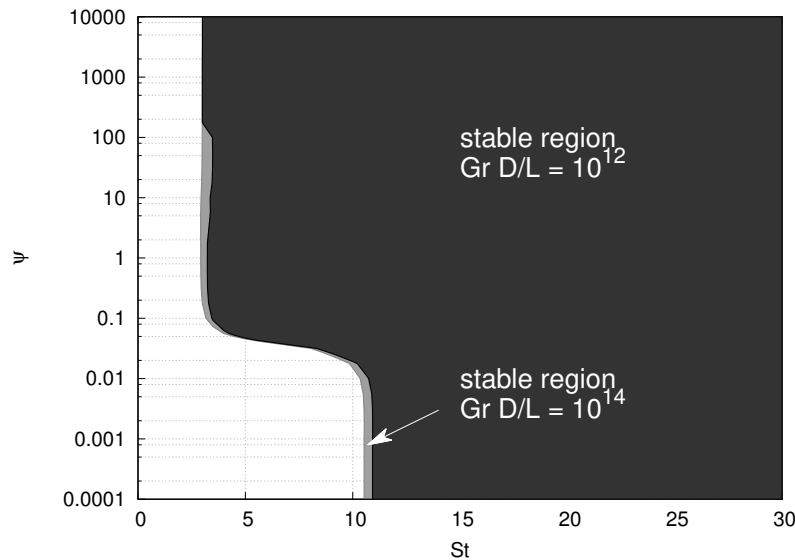


Figure 4.10: Stability map on $St - \psi$ plane for VHVC 800 mm diameter loop.

Irrespective of the configuration, the stability maps have the same shape: critical value of St is constant up to a limiting ψ , beyond which the stable area grows rapidly until reaching another approximately constant critical St . In the four cases, this increase in the stable area within the interval $-2 \leq \log_{10} \psi \leq -1$. It can therefore be concluded that:

- for $\psi \leq 10^{-2}$, the stability of the system is that of an isolated NCL, without pool
- for $\psi \geq 10^{-1}$, the stability is significantly changed with strong increase in stable regime region

- after that increase, the amount of water does not influence on the stable area

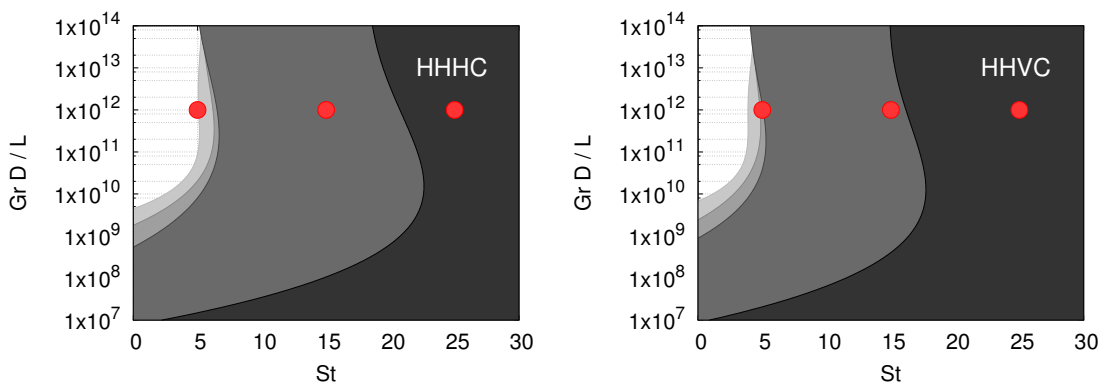
The effect of heater/cooler orientation can be observed from the shift of the threshold for stability to the left, increasing the region of stable regimes with inclusion of vertical components.

These results provide interesting information on the effect of a water mass between the primary heat source and the heater in the NCL. Nevertheless, the surface of fig. 4.6 indicate an unexpected behavior of the system stability with the variation of ψ . The following section addresses the influence of variation in amount of water on stability, this time considering a wide spectrum for ψ for certain points of the stability maps of figs. 4.2 to 4.5, trying to add information on this topic.

4.3 Effect of amount of water on stability

If dynamical behavior is altered by the coupling of the NCL to a pool, it is expected that the amount of water in the pool defines how much dynamics are modified. As shown in the previous section (figs. 4.2 to 4.5), the regions of stable regime does not change significantly with the amount of water (represented by the non-dimensional parameter $\psi = M/(V\rho_0)$, eq. 2.19), but this information is insufficient for a conclusion on how NCL dynamics are altered by the amount of water in the pool.

In this section, a spectrum of non-dimensional water mass ψ in the interval $10^{-4} \leq \psi \leq 10^4$ is simulated for the loop of table 4.2. Figures are showing selected cuts on the surfaces like that of fig. 4.6. Three operating points $(St, Gr D/L)$ are considered for each of the four orientations of heater/cooler. The selected operating points are indicated by the red dots in fig. 4.3. They are the same for the four orientations and are intended to cover three main stability regions: (i) stable with or without pool, (ii) stable only with pool and (iii) unstable with or without pool. Figures 4.12, 4.13 and 4.14 plot the maximum of the real parts of eigenvalues of matrix A (eq. 4.18), i.e., $\max[\text{real}(\lambda)]$.



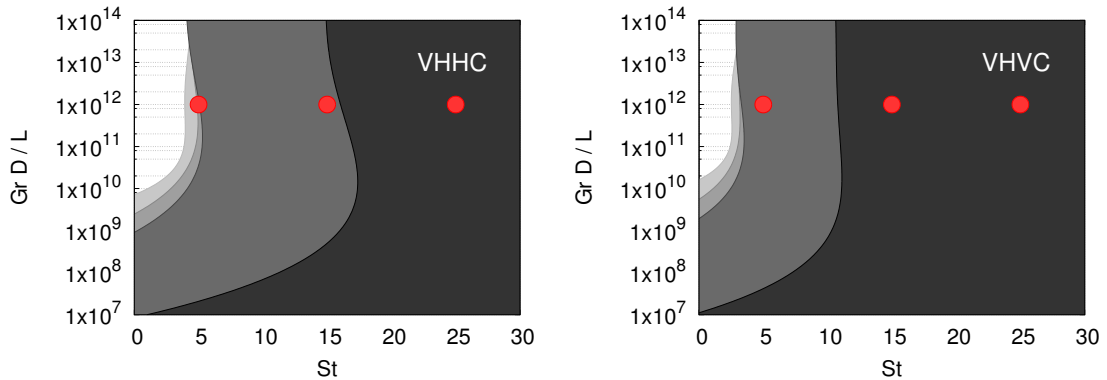


Figure 4.11: Points selected in stability maps for simulation of effect of ψ on system stability.

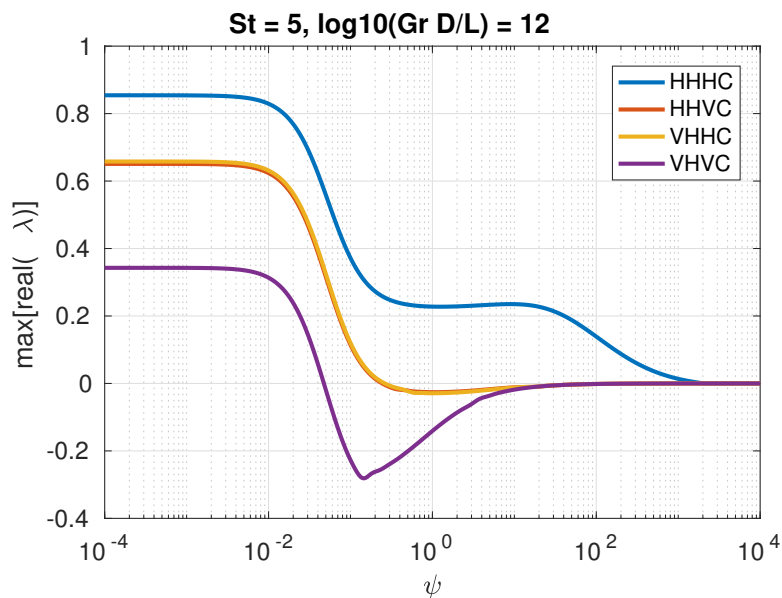


Figure 4.12: Effect of amount of water on the stability of NCL for the four orientations of heater/cooler.

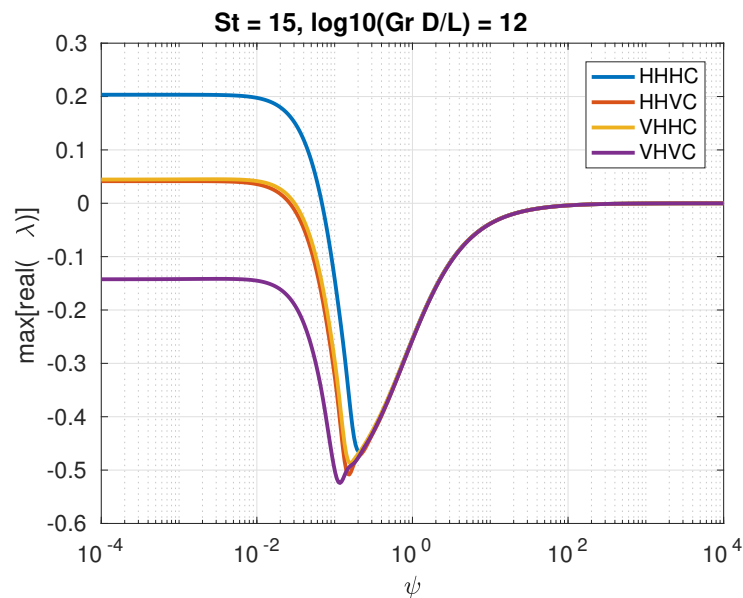


Figure 4.13: Effect of amount of water on the stability of NCL for the four orientations of heater/cooler.

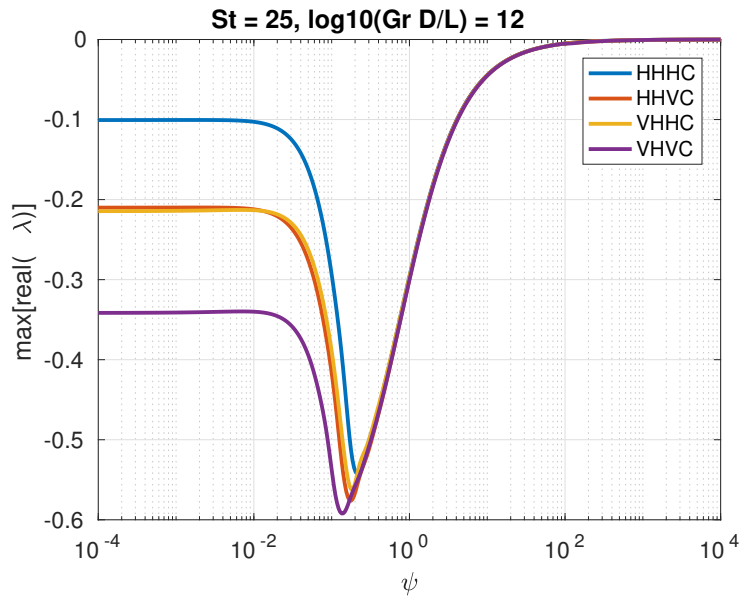


Figure 4.14: Effect of amount of water on the stability of NCL for the four orientations of heater/cooler.

What graphics of figs. 4.12-4.14 show is that there is a continuous transition between NCL without pool and with pool, with a critical value for stability, beyond which stable regimes take place over unstable ones. This result is also shown by Lima et al. [23] for a particular (dimensional) case with VHVC configuration. Another aspect to be noticed is that most of cases present a non-monotonic behavior, with an optimum value for ψ corresponding to the most stable condition. This can be visually confirmed from the graphics, except for the operating point $St = 5$ for the HHHC configuration, because it is unconditionally unstable (it does not have any stable operating point at all). The effect of heater/cooler orientation is also visual. The curves are shifted towards smaller values of ψ as the number of vertical components increases, which is expected after analyzing the stability maps for each configuration presented in the previous section, where the region of stability is increased with the addition of vertical components. Table 4.5 brings the numbers for this conclusion.

Another characteristic of the effect of amount of water is that for large values of ψ the linear analysis predicts a convergence to neutrally stable regimes, with the four configurations converging to this condition at the same time after a certain value of ψ . This point is close to that corresponding to the smallest $\max[\text{real}(\lambda)]$, between $\psi = 10^{-1}$ and $\psi = 10^0$, and is independent of the operating point ($St, Gr D/L$).

Table 4.5: Critical values of ψ for each of the four orientations of heater/cooler and for each of the three selected operating points shown by fig. 4.3. The three points are in $\text{Gr } D/L = 10^{12}$; only St varies.

St	critical ψ			
	HHHC	HHVC	VHHC	VHVC
5	uncond. unstable	2.44×10^{-1}	2.62×10^{-1}	4.74×10^{-2}
15	6.86×10^{-2}	2.65×10^{-2}	3.05×10^{-2}	uncond. stable
25	uncond. stable	uncond. stable	uncond. stable	uncond. stable

4.4 Summary of observations

The linear stability analysis of Natural Convection Loops with and without coupling to a pool provided the following relevant information:

- As expected, when connected to a pool, the NCL considerably tends to be “more stable” in comparison to its dynamic behavior without the pool.
- For $\psi = 1$ (eq. 2.19), the critical Stanton number is decreased by approximately two thirds with respect to that of $\psi = 0$ (no pool). This provides a quantitative measure of the effect of the pool on the NCL.
- The amount of pool (ψ) has a continuous non-monotonic impact on system stability.
- Large amounts of water in the pool drive the system to neutrally stable oscillating regimes.

5 NON-LINEAR STABILITY ANALYSIS

Linear stability analysis is important to show the initial response of a dynamical system to a small perturbation, i.e., in the vicinity of a reference state. It is therefore a useful tool in the identification of critical values for system parameters beyond which instability takes place. However, once it occurs, linear analysis is no longer applicable, given that, according to it, oscillating amplitudes would grow indefinitely to infinity. This means that to correctly predict the unstable behavior of a dynamical system one has to take the non-linear effects into account. So linear analysis is a powerful tool to indicate the conditions for which perturbations are damped and the system recovers its original state. Once linear analysis indicate that a small perturbation will grow exponentially, another method should be adopted in order to capture the non-linear effects when they grow enough to prevent oscillating amplitudes to increase indefinitely. If a certain dynamical system is characterized by a set of parameters γ , there can be a critical set of parameters γ_c for which the system stops developing damping oscillations and reaches neutrally stable dynamical behavior¹. This is a bifurcation point and it requires non-linear analysis tools for prediction and interpretation of the dynamical system in the linearly unstable region.

One way to consider non-linear effects on stability analysis is simply by observing its transient behavior, which, in numerical computation, corresponds to the solution of transient form of conservation equations. In the present work, the focus is on the stability of steady states. Therefore, by this method of non-linear analysis, a perturbation is imposed on the steady state, and the transient mass flow and temperature fields are calculated for a certain time domain. There is no limit for the magnitude of perturbations and the system phase space can evolve as far as calculation can be performed, so that the system state can be known in an arbitrary time distance from the perturbation (evidently limited by computing capabilities), for an arbitrary magnitude of perturbation.

The counterpart is that the solution of the conservation equation is associated to a computational cost, and is subject to dissipative and dispersive effects posed by the

¹Notice that this is exactly the same concept employed in the definition of the stability curves drawn in the stability maps of the previous chapter

numerical formulation. Should such obstacle be avoided, the alternative that arises for non-linear analysis is to limit attention to the local behavior of the system around a fixed point (a bifurcation point), restricting perturbations to small magnitudes, in order to keep the perturbed system in the vicinity of the fixed point. Of course linear stability analysis employ the same concept, but it differs from non-linear analysis because non-linear terms are deliberately neglected the former approach. The assumption of small perturbations allows the system state variables – mass flow and temperature field – to be expanded in power series, weighted by a parameter of small magnitude. This method is not employed in the present work, but the reader is advised to consult Nicolis [29] for details.

The analyses performed within this chapter have the following objectives:

- to evaluate the effect of different magnitudes of perturbations on the system
- to observe how the pool influences the transient behavior of an NCL
- to analyze the conditions for which the NCL develop periodic and aperiodic oscillations

After testing the effect of perturbation size on the system stability, in sec. 5.1, the following three sections will present data for different dynamic regimes, always taking coupling to the pool and orientation into account. Section A.1 shows the transients for stable stationary points, sec. A.2 present unstable systems without pool which are "stabilized" when pool is considered, and sec. ?? shows unstable transients, irrespective of connection to a pool. The operating points for simulation were selected based on the stability maps of chapter 4, and the same loop used to generate the maps, described by table 4.2, defines the geometry for simulations.

5.1 Effect of perturbation

The method of analysis consists on obtaining the transient response of the system after a perturbation on the steady state mass flow rate. This was the same method of perturbation employed by Nayak et al. [28].

To study the influence of the magnitude of perturbations, the steady states for one stable configuration and for an unstable configuration were each disturbed by three different magnitudes of perturbation on the mass flow rate. For each one, the time evolution of mass flow were analyzed. The loop selected for these tests was that described by table 3.3, in chapter 3, in HHHC configuration, for having small dimensions in comparison to the circuit of table 4.2, which produces faster evolution of system properties. The two operating points selected for the test are

	heat input	cooler heat transfer coefficient
stable operating point	200 W	1800 W/m ² /K
unstable operating point	200 W	900 W/m ² /K

with perturbations of -16%, -40% and -100% on mass flow rate. Figure 5.1 shows the mass flow over time for the three perturbation magnitudes. For each one, oscillating amplitudes in frequency domain are presented in figs. 5.2 to 5.4.

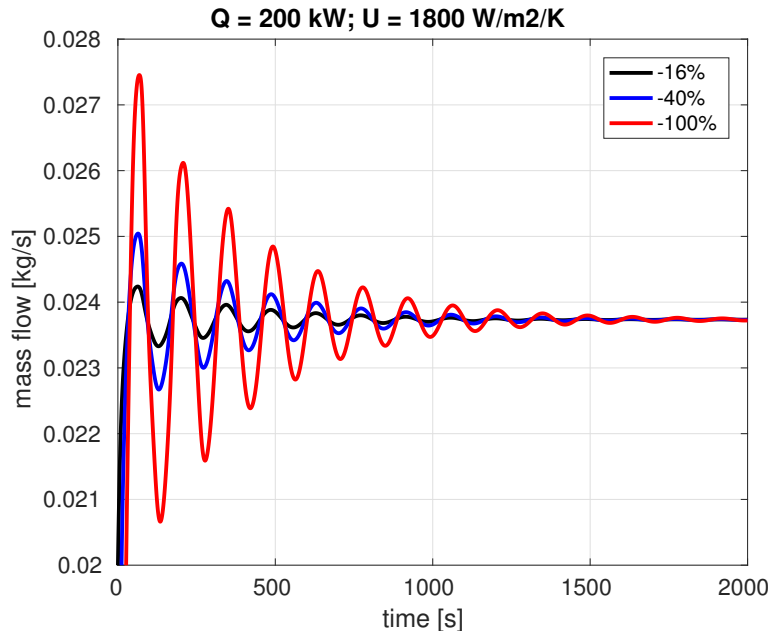


Figure 5.1: Effect of magnitude of perturbation on transient mass flow rate for a stable system.

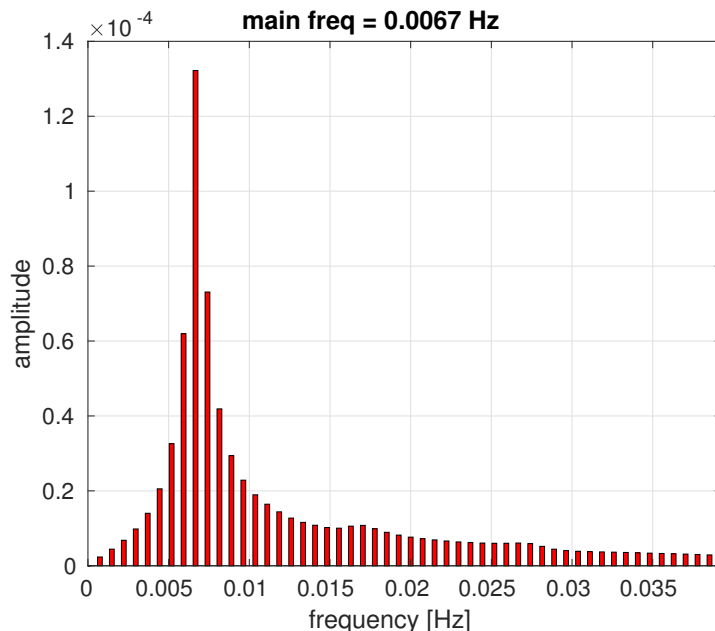


Figure 5.2: Effect of magnitude of perturbation on transient mass flow rate for a stable system: frequency domain for -16% perturbation.

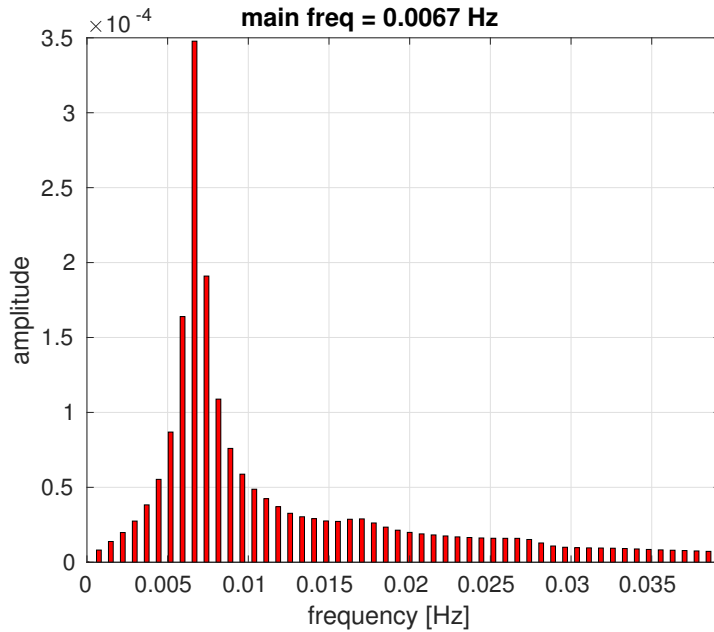


Figure 5.3: Effect of magnitude of perturbation on transient mass flow rate for a stable system: frequency domain for -40% perturbation.

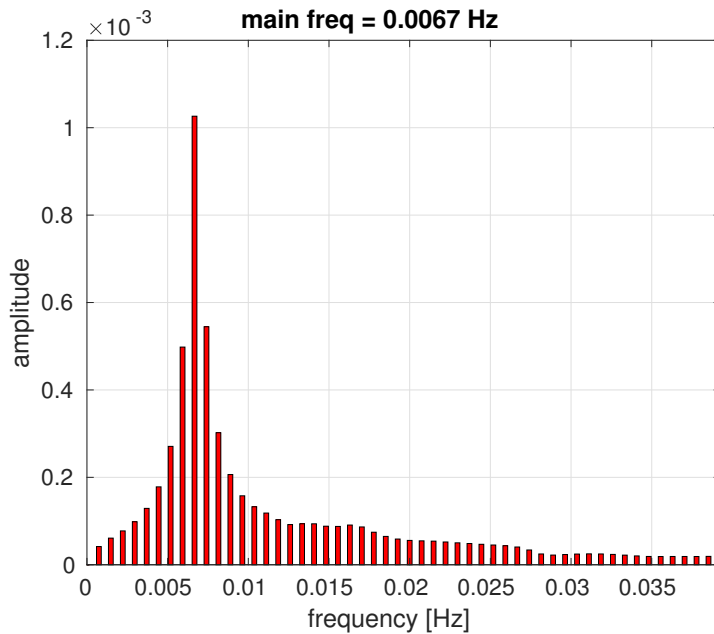


Figure 5.4: Effect of magnitude of perturbation on transient mass flow rate for a stable system: frequency domain for -100% perturbation.

It can be realized from fig. 5.1 that the period of oscillation is not altered by the initial perturbation. The decay rate is, however, different to compensate the initial amplitude so that the stable system converges approximately at the same time to the initial state. Fourier transforms confirm the independence of oscillating frequency on initial perturbation, showing a main frequency of 0.0067 Hz. The same test is now applied to unstable regime. Results are shown in fig. 5.5 (time series of mass flow rate) and figs. 5.6 to 5.8.

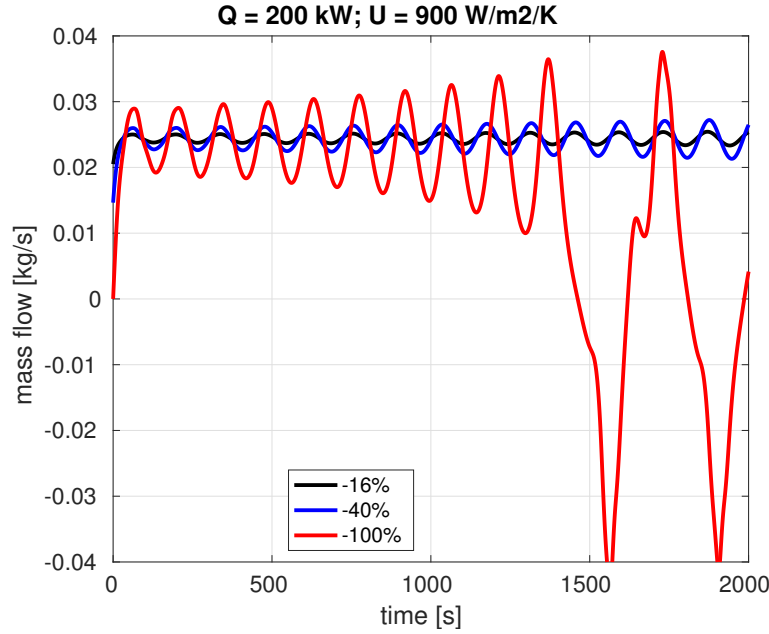


Figure 5.5: Effect of magnitude of perturbation on transient mass flow rate for an unstable system.

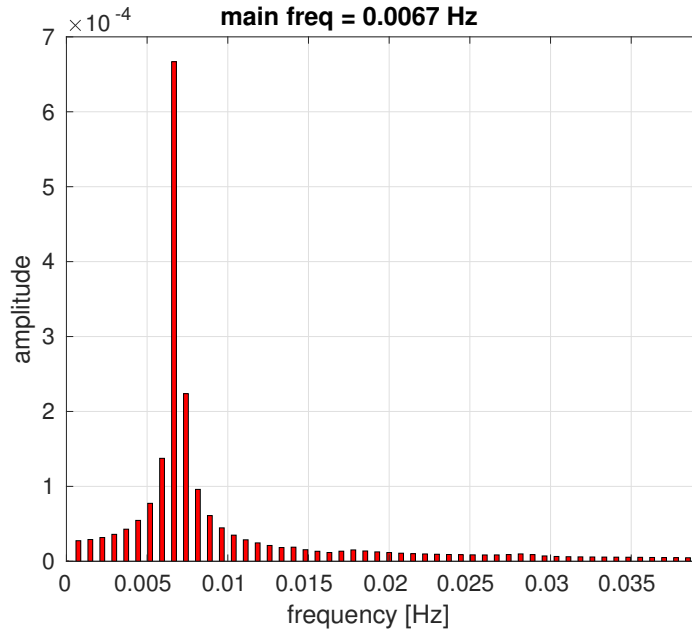


Figure 5.6: Effect of magnitude of perturbation on transient mass flow rate for an unstable system: frequency domain for -16% perturbation.

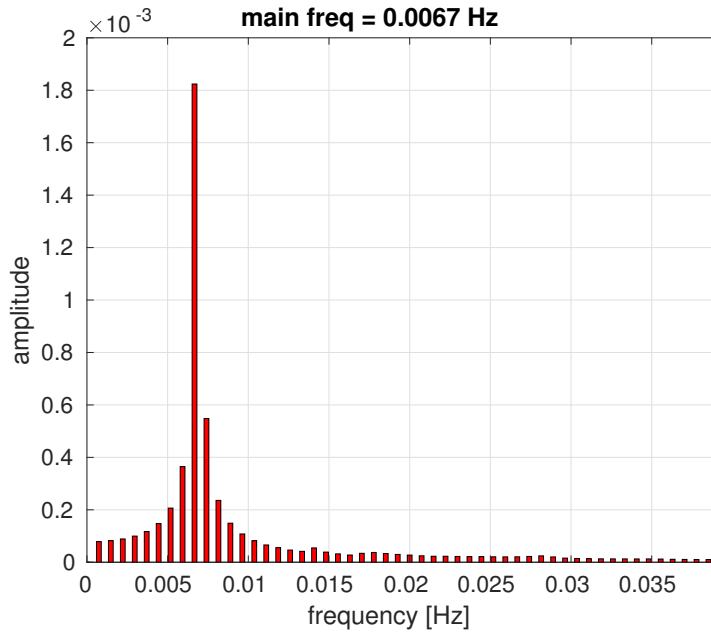


Figure 5.7: Effect of magnitude of perturbation on transient mass flow rate for an unstable system: frequency domain for -40% perturbation.

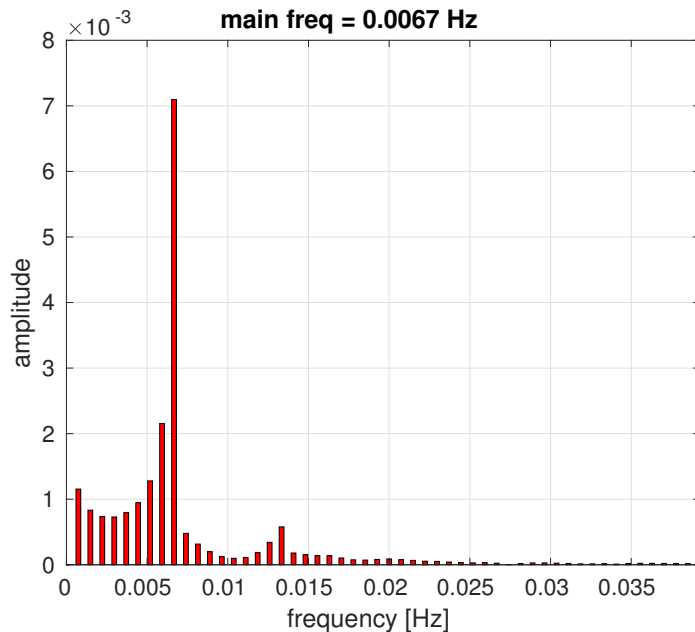


Figure 5.8: Effect of magnitude of perturbation on transient mass flow rate for an unstable system: frequency domain for -100% perturbation.

As results show, irrespective of the initial perturbation, frequency of oscillation is the same for the three magnitudes. More than this, the frequency is the same as that for the stable regime: 0.0067 Hz. The difference in the unstable regime is that flow reversal is anticipated as the magnitude of perturbation increases, as shown by table, where

It can be concluded that the magnitude of perturbation does not alter the system stability. It does however shifts the time when flow reversal occurs for unstable systems. Based on this conclusion, the transients presented in the following sections will depart

Table 5.1: Points of flow reversal for the same loop and operating parameters, but with different magnitudes of perturbation.

perturbation	time of first reversal
-16%	1460 s
-40%	4568 s
-100%	7880 s

from -100% perturbations.

5.2 Transient results

The objective of this chapter is to provide information about the dynamic behavior of NCLs taking into account three variants:

1. Operating regime; based on the stability maps generated by the linear analysis, three operating points were selected, which are applied to the four possible configurations (HHHC, HHVC etc.). This sections is subdivided according to these operating points,, each one corresponding to a stability condition for the system (stable, stable with pool and unstable without it, and unstable regimes).
2. The second variant is the orientation of heater and cooler. For each operating point, the for possible configurations – HHHC, HHVC, VHHC and VHVC – are simulated.
3. The third variant is coupling to a pool, focus of this thesis, where two cases are considered: NCL with pool and NCL without pool. both situations are characterized by the parameter ψ , with $\psi = 0$ for no pool and $\psi = 1$ for system with pool, under the definitions of ψ given by eq. 2.19.

Hence, the cases analyzed in this chapter are a combination of operating regime, orientation and coupling to the pool. The chapter is structured according to the nature of the NCL dynamics, with a section dedicated to stable cases (sec. 5.2.1), one for periodic oscillatory regimes (sec. 5.2.2), and one for chaotic regimes (sec. 5.2.3).

As previously mentioned, the concept of stability employed here is associated to the stability of the stationary state. The system is considered stable if, after a perturbation, it returns to its original (steady) state. Therefore, periodic oscillations are considered instabilities herein. Transient data then results from a perturbation of 100% on mass flow.

Three operating points were selected in the basis of the pair (St,Gr D/L), following stability maps of chapter 4. They were selected in a way that the areas of interest in terms of stability would be covered, i.e., one point in the stable region, irrespective of the

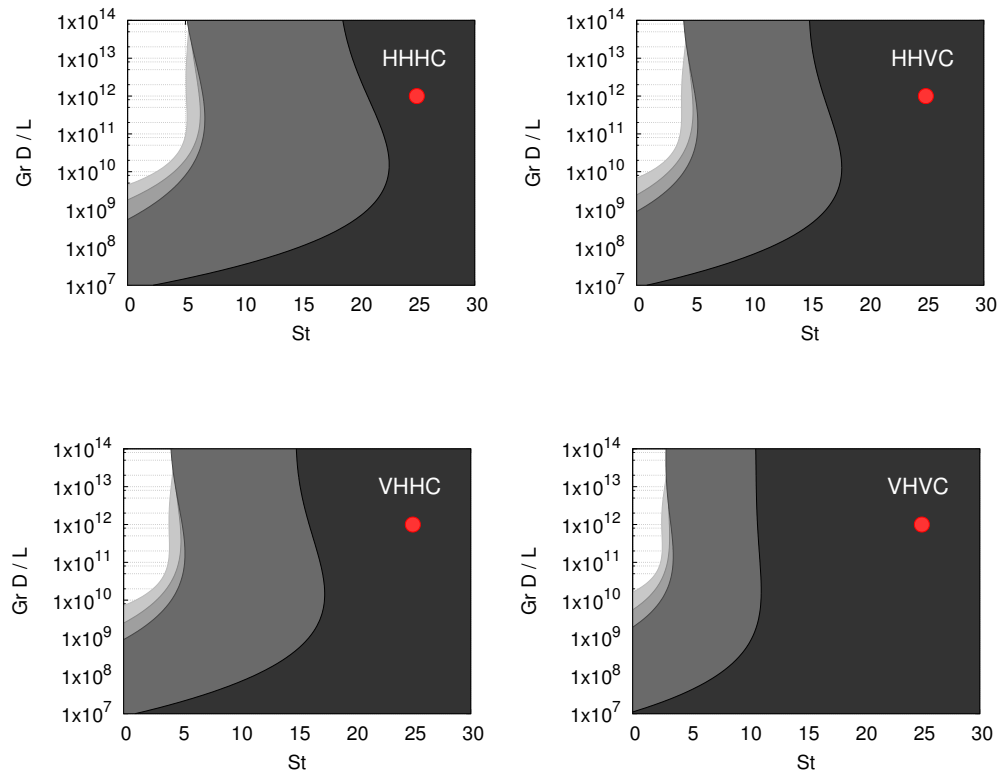
Table 5.2: Operating points for the transient simulations.

stable regime	$St = 25; Gr D/L = 10^{12}$
stable with pool/unstable without pool	$St = 10; Gr D/L = 10^{11}$
unstable regime	$St = 2; Gr D/L = 10^{11}$

connection to a pool, one in the region of unstable regimes only without pool, and a third operating point in the region of unstable regimes irrespective of the connection to a pool. The three operating points are listed in table 5.2. So the database for the analyses that are presented in this chapter is composed by results for these three operating points, each one for the four configurations, in the variants with and without pool. This amounts to 24 cases, 8 for each operating point. The results are all presented in Appendix A.

5.2.1 Stable steady states

Figure 5.2.1 shows the location of the operating point on the stability maps for which steady states are stable, resulting in decaying oscillating transients.

**Figure 5.9:** Points selected in stability maps for simulation loop transients.

Even for stable regimes independent of the connection to pool, a huge difference in the dynamic behavior can be observed between NCL with pool and without it. For the coupled case, oscillations are rapidly damped, while in the uncoupled, the system properties asymptotically converge to the original state. This conclusion can be visually confirmed for the four configurations, both by the time-series and the space-time charts.

In the HHHC configuration, the transient of mass flow actually stops oscillating after four oscillations (fig. A.6). It then evolves exponentially (with zero imaginary component) to the original state. The initial oscillations are also clear from the space-time charts (figs. A.5, A.11, A.17 and A.23), where a fringe appears in the beginning and then no more oscillation is observed.

With respect to configuration, as expected, “more stable” transients are observed when components switch to vertical position. In other words, HHHC configuration is the “less stable” one as VHVC is the “most stable”. This can be inferred from the amplitude of oscillations, which are smaller for the latter case. Figure 5.2.1 illustrates this conclusion with a comparison between the four time series for mass flow. The period of oscillation is also slightly decreased from HHHC to VHVC, as confirmed by the numbers in table 5.3, which also lists the decay rates for each case. The coefficient of determination R^2 is the quality of the fitting process to determine the decay rate, where $R^2 = 1$ corresponds to perfect fitting.

This conclusion is in accordance to results found in literature [30, 50], and is associated to the action of buoyancy forces in the vertical heat transfer sections. The presence of buoyancy forces the water to flow upwards, in the case of heater, and downwards, in case of cooler. The effect on stability is that when a perturbation comes in, resulting oscillations experience stronger damping after passing through vertical heater or vertical cooler. In the case simulated here, the heater length is larger than that of the cooler, which makes VHHC configuration more stable than HHVC.

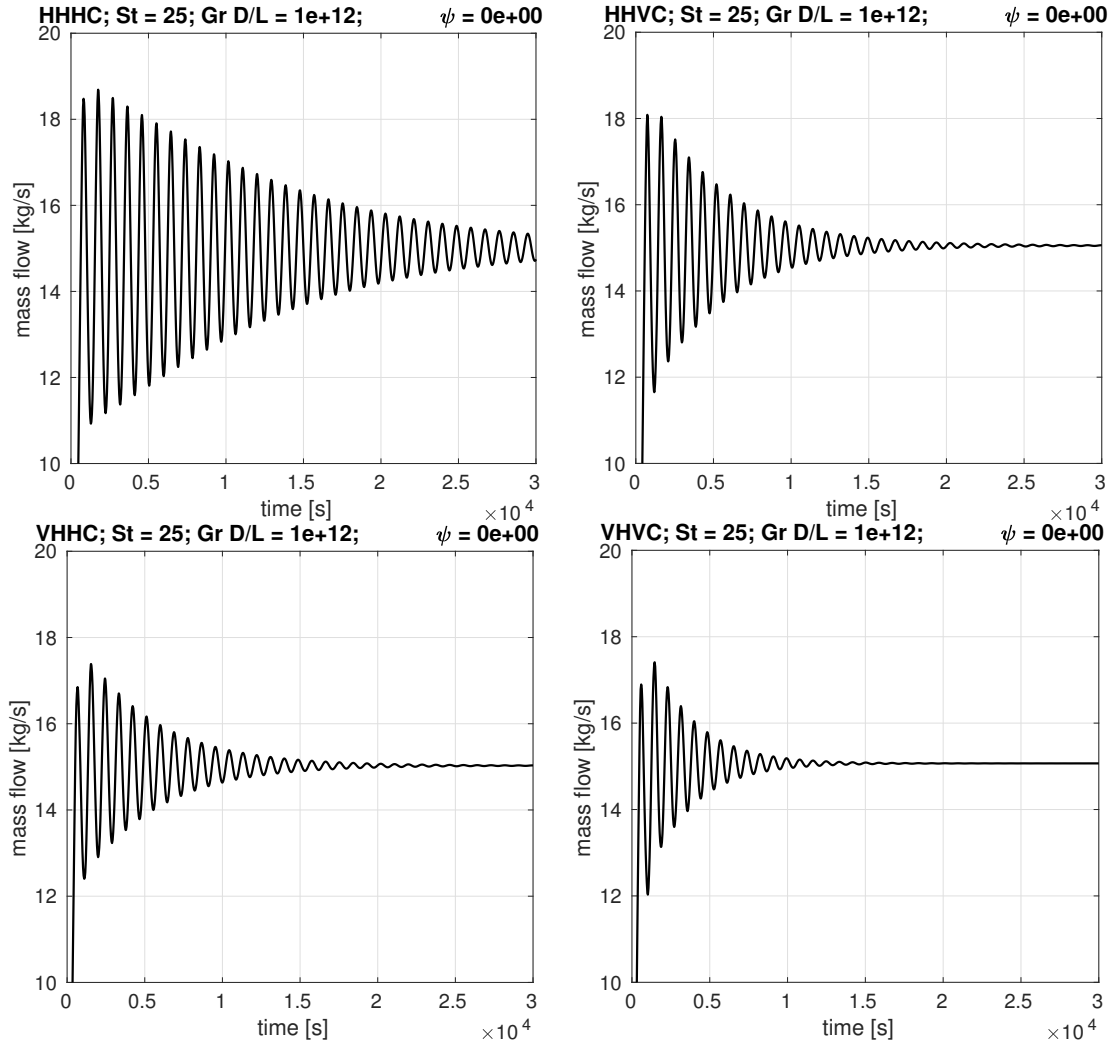


Figure 5.10: Comparison of mass flow time series for the four orientations for system without pool, showing a reduction in oscillating amplitude as vertical components are added to the circuit. Operating point ($St = 25, Gr D/L = 10^{12}$).

However, the effect of orientation is considerably smaller for the cases with pool. For the four configurations, oscillations stop after four cycles. This observation is in agreement with the results shown by fig. 4.14, in chapter 4. The Fourier Transform indicates a high amplitude oscillating mode in the lowest frequency part and a second mode

Table 5.3: Period and decaying rate of stable steady states for all orientations for system without pool.

	period [s]	decay rate	coeff.	determination
HHHC	937.47	-7.15^{-06}	0.9620	
HHVC	882.32	-5.17^{-06}	0.7065	
VHHC	882.32	-4.01^{-06}	0.7122	
VHVC	857.11	-3.20^{-06}	0.5443	

with smaller amplitude and larger frequency, similar to that of the cases without pool. Apparently, when pool is considered in the problem, a very low frequency mode dominates the flow, with rapid conversion to the original state. Similarly to the cases without pool, VHHC and VHVC orientations produces much stronger damping of flow oscillations, acting on the mode with higher frequency.

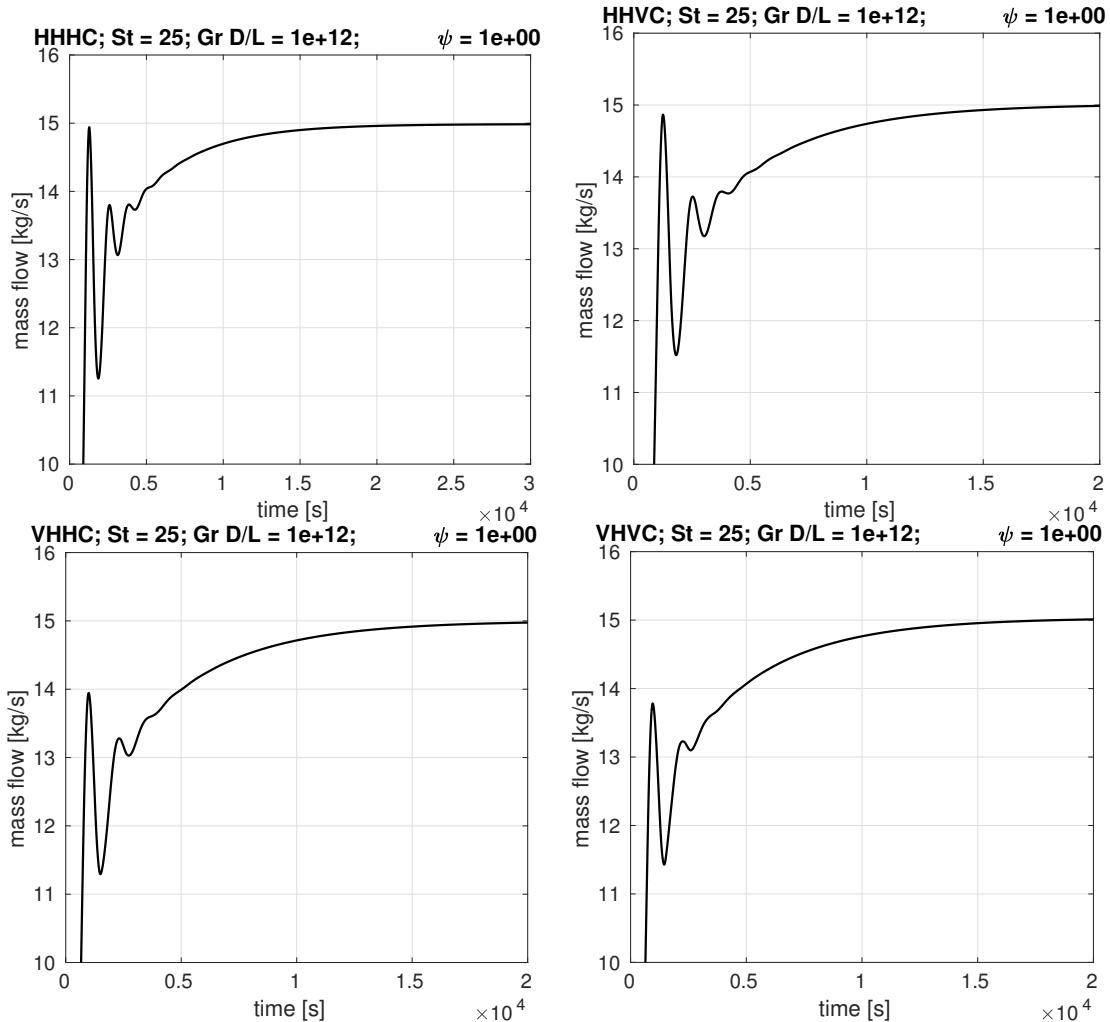


Figure 5.11: Comparison of mass flow time series for the four orientations for NCLs with the pool. Operating point ($St = 25, Gr D/L = 10^{12}$).

When Stanton number is reduced, the decay rate is decreased. For the same loop, a variation of the Stanton number consists essentially of variation of the heat transfer coefficient. So when Stanton is reduced from $St = 25$ to $St = 10$, heat transfer coefficient also decreases: from $U = 20.07 \text{ kW/m}^2/\text{K}$ to $U = 6.27 \text{ kW/m}^2/\text{K}$, keeping the same value of 10^{12} for $Gr D/L$. If U decreases, the system loses part of its capacity to dissipate energy and therefore becomes “less stable” or “more unstable”, with increase in oscillating amplitudes.

Figure 5.2.1 shows the time series for mass flow for the second operating point ($St = 10, Gr D/L = 10^{11}$), showing a clear difference in comparison to the transients of fig. 5.2.1. Plots are shown in the same time interval of those in fig. 5.2.1.

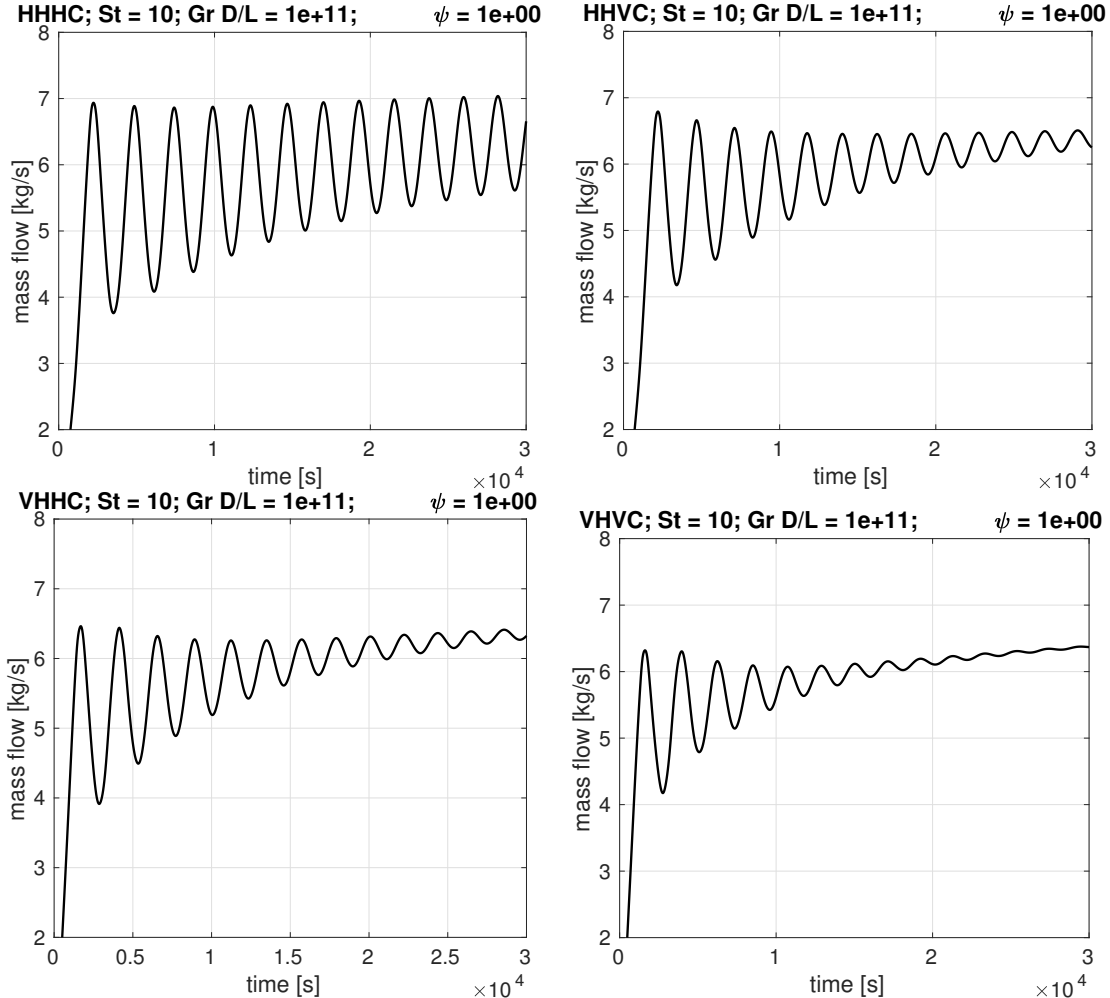


Figure 5.12: Comparison of mass flow time series for the four orientations for NCLs with the pool. Operating point ($St = 10, Gr D/L = 10^{11}$)

One last observation is that, from the space-time charts, that the loop flowed in the same direction in all cases, because the inclination of temperature fringes are always to the same side.

5.2.2 Periodic regimes

In this section, the cases identified as periodic among those for $St = 10$ and $St = 2$, both for $Gr D/L = 10^{11}$, sections A.2 and A.3 of appendix A, are analyzed.

For the operating point ($St = 10, Gr D/L = 10^{11}$), only one result presented periodic behavior: the VHHC configuration without pool. For the more instable operating point ($St = 2, Gr D/L = 10^{11}$), HHHC configuration presented periodic motion with pool, the VHHC without pool showed a mixed dynamic behavior, with a starting chaotic transient followed by a periodic motion, same pattern of the VHVC with pool.

Transients were identified as periodic when some repeating cycle could be devised. However, no distinction is made between periodic and quasi-periodic signals², although the cases here analyzed are multi-periodic and possibly quasi-periodic. In either cases, the oscillating regime, which is reached after a perturbation on the steady state, is called limit cycle. Just when the perturbation is applied, linear instabilities occur. If they are not damped (stable steady states, situations of the previous section) amplitude grows linearly until non-linear effects start to become important. So in the beginning, just after the perturbation, non-linear effects are negligible. This is the region where linear stability theory apply. The limit cycle occurs when non-linear effects saturate, and the system oscillates within a maximum amplitude.

Figure 5.2.2 shows the transient result for mass flow rate and the projection of the phase space on the plane mass flow *vs* temperature difference across heater. The system takes a couple of cycles to reach the periodic regime, after approximately 10^5 seconds. The phase plot contains this initial transients before the periodic motion, which contributes to the enlargement of the thickness. Figure 5.13 shows a detailed image of the periodic cycles and the decomposition on frequency domain. Three main oscillating modes can be identified from the frequency spectrum, with three other of smaller amplitudes and higher frequency. The dynamic behavior essentially shows a oscillation inside the same flow direction (without reversal), followed by another one with flow reversal.

²A quasi-periodic signal is a multi-periodic one with irrational ratio between the frequencies of oscillation [29, 8]

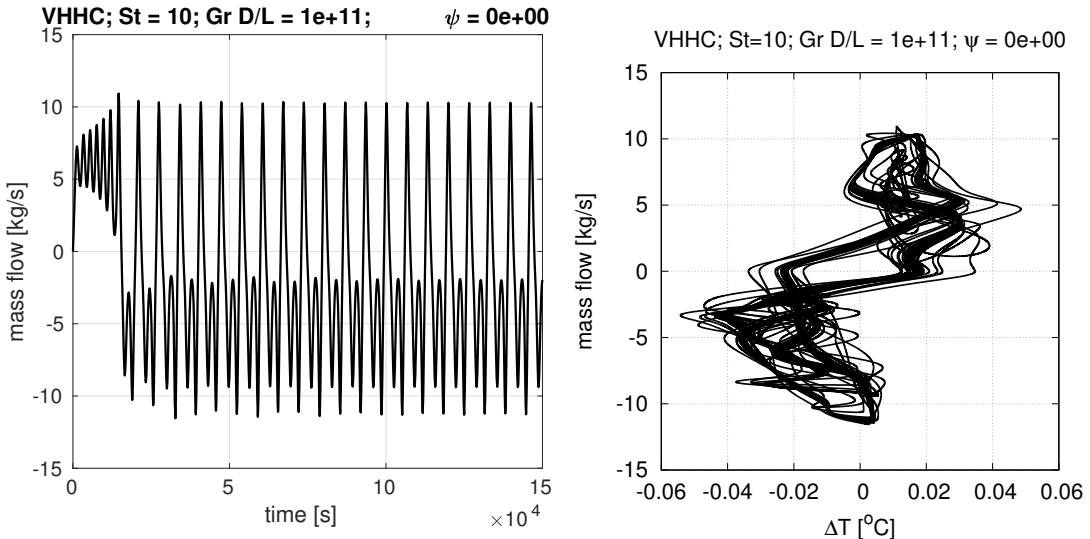


Figure 5.13: Mass flow over time (left) and projection of phase space on the plane mass flow *vs* temperature difference across heater (right). Operating point ($\text{St} = 10, \text{Gr } D/L = 10^{11}$).

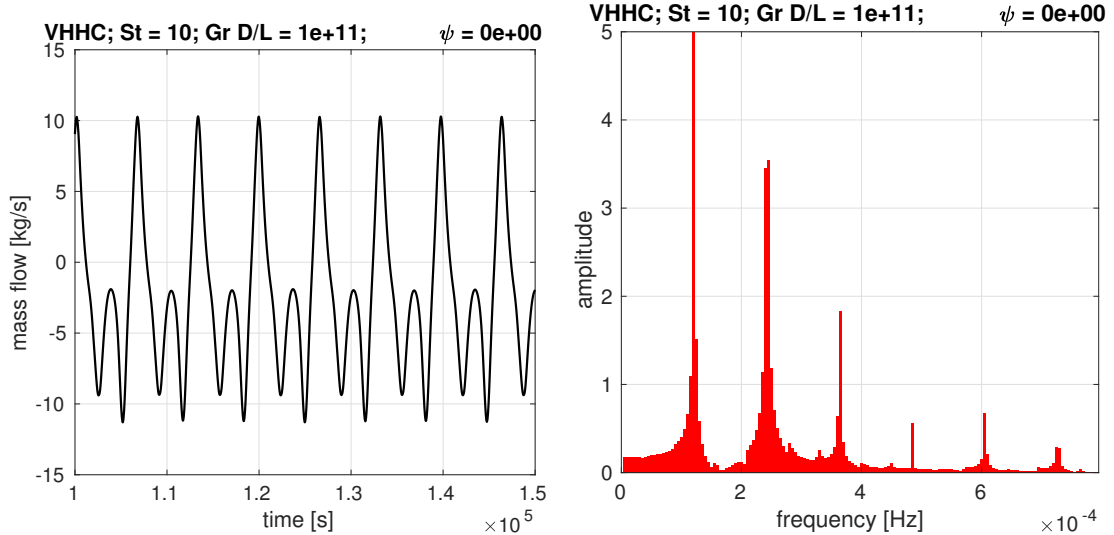


Figure 5.14: Detail of mass flow cycle (left) and the frequency spectrum of mass flow (right). Operating point ($\text{St} = 10, \text{Gr } D/L = 10^{11}$)

The conditions necessary for a NCL to develop stable steady states are clear from the stability maps, which are coherent with the transient results just described in sec. 5.2.1. Consequently, the conditions for unstable steady states, generating increasing amplitudes and limit cycles, are also clear. The question that arises is whether such unstable regimes

are periodic or aperiodic. Figures 5.2.2 and 5.13 just showed that the response of the VHHC configuration in the operating point ($St = 10, Gr D/L = 10^{11}$) without pool for a -100% perturbation on mass flow produces periodic oscillations. An interesting result comes when Stanton is slightly increased by 1%, i.e., $St = 10.1$. Figure 5.13 shows the result. Periodicity is apparently lost (at least for the time interval simulated), as shown by left image in fig. 5.13. The phase plot in the right side of fig. 5.13 is also a symptom of aperiodic signal, with trajectories are spread over the attractor.

For a symmetric comparison to the periodic result, a zoomed image (left side) and the frequency spectrum (right side) are shown in fig. 5.17. The Fourier transform is typical of aperiodic regimes.

So a slight change in the Stanton number produces a complete different nature of dynamics. The same occurs for a change in the magnitude of perturbation from -100% to -99%, as well as the numerical formulation (e.g., a different number of mesh nodes and time CFL). Extending the time interval, it can be observed that periodic regime is reached after a certain number of chaotic cycles for $St = 10.1$ (fig. 5.13).

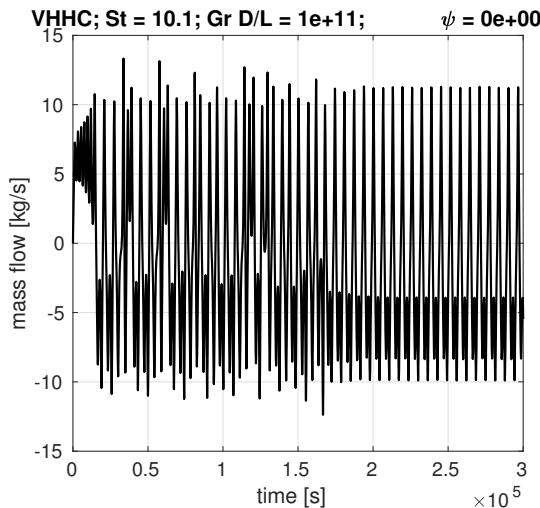


Figure 5.15: Extended time interval for simulation VHHC configuration ar $St = 10.1$, $Gr D/L = 10^{11}$ without pool.

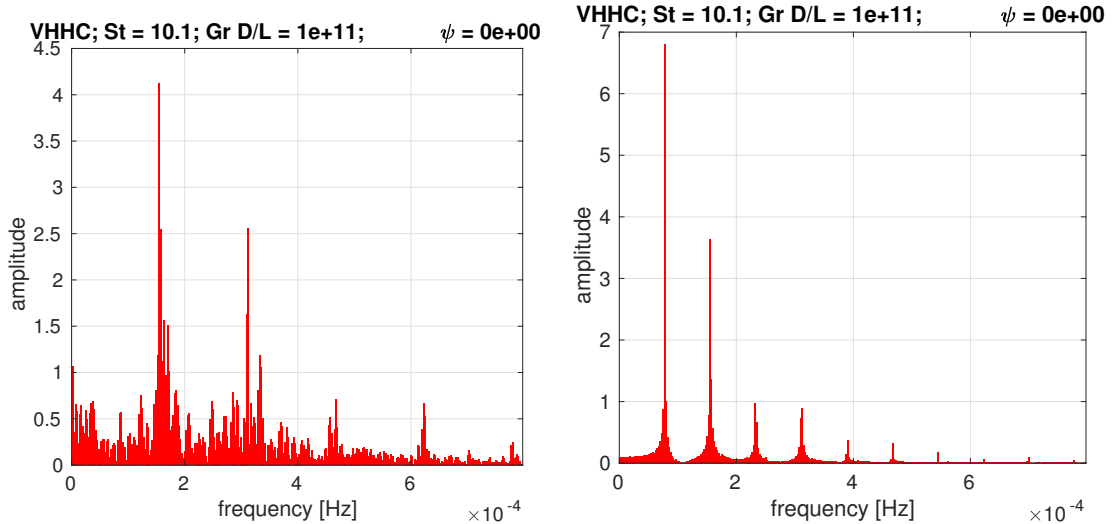


Figure 5.16: Frequency spectra for the full time range (left) and for the time range after 200 thousand seconds (right). Operating point ($St = 10.1, Gr D/L = 10^{11}$).

Figure 5.13 shows the result from the Fourier transform of the transient mass flow output for the full time range and for the interval where periodic regime exists, clearly illustrating the different nature of flow oscillations in the two phases captured by the simulation.

It is worth to mention that these conclusions are drawn based on results for just one circuit, which is particularly susceptible to instabilities due its large diameter. In fact, many experimental works reported periodic oscillations [25, 30, 50, 51], for loops with diameter smaller than 40 mm (the one considered for the transient results has 800 mm of diameter). Some these experimental data were compared to numerical results of Lima and Mangiavacchi [22], which showed periodic oscillations of the loop described in table 3.3.

Chaotic regimes are a subject of the next section, where transients with the same nature of that of figs. 5.13 and 5.17 are analyzed a little deeper.

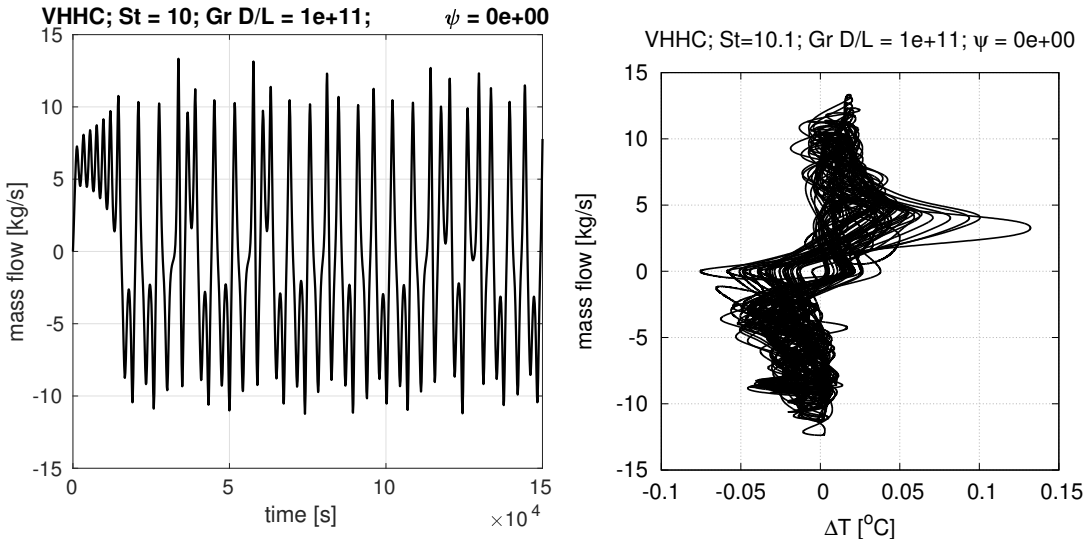


Figure 5.17: Mass flow over time (left) and projection of phase space on the plane mass flow *vs* temperature difference across heater (right). Operating point ($\text{St} = 10.1, \text{Gr } D/L = 10^{11}$).

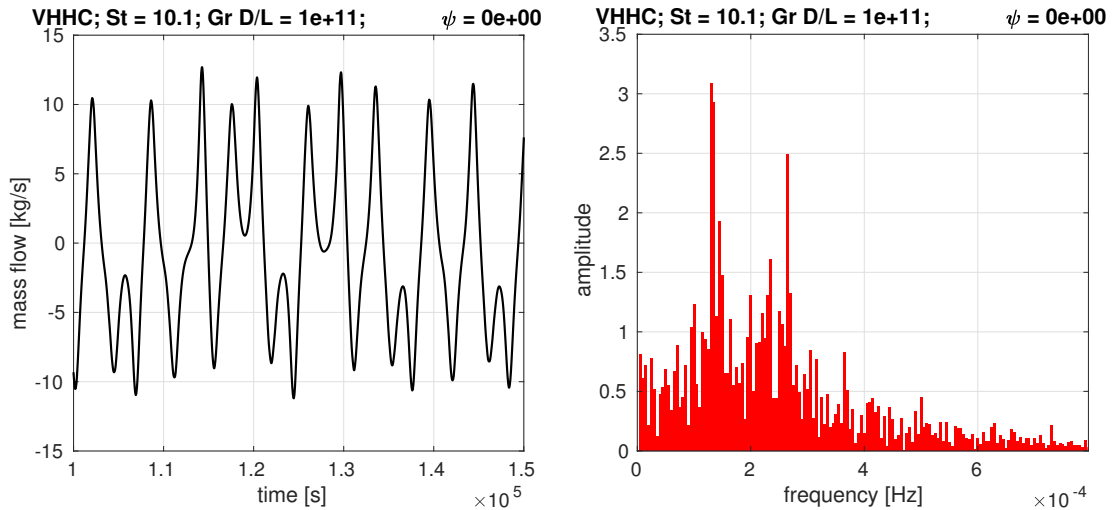


Figure 5.18: Detail of mass flow cycle (left) and the frequency spectrum of mass flow (right). Operating point ($\text{St} = 10.1, \text{Gr } D/L = 10^{11}$)

5.2.3 Chaotic regimes

It is not intention of this thesis to make a deep analysis of elements of chaos in the transient outputs obtained from the numerical results. The objective is to employ basic

tools to characterize the aperiodic responses that NCLs may present depending on the geometrical and operating parameters. Two methods of analysis are employed:

- Fourier transform of time-series
- a calculation of the attractor dimension
- a measure of the deviation growth for two close initial states, an application of the concept behind Lyapunov exponents

Dynamic behaviors were apparently chaotic in eight of the 12 unstable cases simulated. They are just “apparently” because it is hard to categorize a signal as chaotic without analysis, otherwise it is possible that the system has a period of oscillation larger than the interval of visualization [41].

The frequency spectra of mass flow serve as an indicator of aperiodic signal. Scattered spectra, such as that of fig. A.29 can be signs of a chaotic signal. As Bergé et al. [8] explains, when a time dependent signal is at hand, it is of interest to know the dynamic nature of the system: if it has a dominating mode of oscillation, if it has multiple modes or if it is something other than these two cases. Previous section showed two completely different frequency spectra, one for a periodic state (or quasi-periodic) and another for an aperiodic response.

The attractor dimension also indicates the presence of a chaotic system. The time evolution of a dynamical system generates trajectories in the phase space. Nicolis [29] explains the concept of trajectory as a sequence of phase space points, in a way that, given a certain point \mathcal{P} , any other point in the same trajectory is uniquely determined by \mathcal{P} . This conclusion comes from the property of non-intersection between trajectories [29, 8]. The set of all trajectories constitutes what is called flow in the theory of dynamic systems. Given an initial point, the system (its phases) flows to an invariant manifold, called attractor. The subset of the phase space where the attractor exerts its influence is called basin of attraction. For the mathematical formulation of the NCL described in chapter 2, with a scalar field of temperature, a discrete problem arises after the numerical formulation, transforming a infinite dimension problem into a finite dimension one (finite number of degrees of freedom). So, for the NCL coupled to the pool, the dimension of the phase space is equal to the number nodal values of temperature plus two: one dimension for mass flow and another for the global temperature in the pool. For dissipative systems, such as our NCL-pool system, the attractor dimension is smaller than that of the phase space. For periodic and quasi-periodic signals, the attractor has integer dimension. For aperiodic signals, the attractor has a fractional dimension (the so called strange attractors). Attractors can be fixed points or limit cycles. Hence, the calculation of the attraction dimension is a way of characterizing the dynamic behavior of a system.

Strange attractors therefore exist in chaotic systems, and have fractal dimension. By the discrete formulation used in this work, simulations generate finite sets of phase states (or phase points), with a dimension \lceil equal to the number of mesh nodes plus two. The determination of the fractal dimension consists essentially on the counting of the phase points. One way to perform such counting is by the Hausdorff method, which produces the Hausdorff dimension, \mathcal{D}_H . The counting process is made by covering the phase space with \lceil -dimensional hypercubes in several steps. At each step, the cubes are subdivided into smaller ones of size ϵ . The Hausdorff dimension is obtained in the limit

$$\mathcal{D}_H = \lim_{\epsilon \rightarrow 0} \frac{\ln N(\epsilon)}{\ln(1/\epsilon)} \quad (5.1)$$

where $N(\epsilon)$ is the number phase points contained in the hypercubes of size ϵ . When the attractor is a single point (a stationary solution), the dimension is zero (because $N(\epsilon) = 1$ always); when it is a n -dimensional line, it has dimension one. It is worth to mention is that attractors always have zero volume.

The Hausdorff dimension however has the drawback of requiring large computational effort when the phase space has dimension larger than two. An alternative is the so called correlation dimension, \mathcal{D}_C . It is similar to the Hausdorff method, also consisting of a counting of points. But instead of hypercubes with decreasing size, it uses hyperspheres with increasing radius, and is determined from the rate of points “captured” by the sphere as it grows. Writing the number of points contained in the sphere of radius r as $N(r)$, we have that

$$N(r) \propto r^{\mathcal{D}_C} \quad (5.2)$$

Details on the formulation of both methods can be found in [8]. In this work, attractor dimensions are computed by the correlation method.

Table 5.4 presents the correlation dimensions for both regimes of the VHHC loop analyzed in the previous section. The dimension is calculated by means of the fitting of a power function in the curve of $N(r)$ as function r , so the coefficient of determination is also provided in table 5.4.

Tables 5.5 and 5.6 list the attractor dimensions of the other chaotic identified regimes

Table 5.4: Correlation dimensions for the VHHC loop with $\text{Gr } D/L = 10^{11}$ and $\psi = 0$ and two values of St.

St	oscillating regime	dimension \mathcal{D}_C	coeff. determination
10	periodic	0.9839	0.9811
10.1	aperiodic	1.6911	0.9509

Table 5.5: Correlation dimensions for the unstable regimes reported in sec. A.2 for $\text{St} = 10$, $\text{Gr } D/L = 10^{11}$ and $\psi = 0$.

orientation	dimension \mathcal{D}_C	coeff. determination
HHHC	1.3131	0.8694
HHVC	1.3008	0.8737
VHHC	0.9839	0.9811
VHVC	1.3930	0.8656

of the simulations reported in appendix A.

Notice that there are some incompatible dimensions in table 5.6: case with aperiodic response had attractor dimension close to one. It should be mentioned that the number produced by the algorithm for calculation of the correlation dimension is sensible to many parameters, like the size of time interval. So conclusions upon those numbers must be very careful, possibly taking another method of analysis into account.

A known measure for characterizing chaotic regimes are the Lyapunov exponents (or Lyapunov numbers). The concept behind this parameter is simple, but implementation of the calculation procedure is not. Therefore, a qualitative evaluation of the Lyapunov exponents was performed in this work. References [8, 29, 41] are suggestions for more details on computation of Lyapunov numbers.

The Lyapunov exponents are associated to the concept of Lyapunov stability. According to it, the phase state \mathcal{P} is stable if, for any neighborhood U_ϵ of \mathcal{P} , there is a neighborhood $U_{\delta(\epsilon)} \subset U_\epsilon$ such that any trajectory departing from $U_{\delta(\epsilon)}$ remains within U_ϵ . The Lyapunov exponents are a measure of the rate of deviation of a phase state $\mathcal{P}_\epsilon \in U_{\delta(\epsilon)}$ from \mathcal{P} . If the point \mathcal{P} is Lyapunov stable, then the trajectory departing from \mathcal{P}_ϵ remains within U_ϵ , and the deviation may, at most, experience a linear increase. For such cases, all Lyapunov exponents \mathcal{L} are such that $\mathcal{L} \leq 0$. If \mathcal{P} is unstable in the Lyapunov sense, then the deviation will grow exponentially until an upperbound defined by the amplitude

Table 5.6: Correlation dimensions for the unstable regimes reported in sec. A.2 for $\text{St} = 10$, $\text{Gr } D/L = 10^{11}$, $\psi = 0$ and $\psi = 1$.

orientation	ψ	dimension \mathcal{D}_C	coeff. determination
HHHC	0	1.0581	0.9615
HHVC	0	1.0671	0.9645
VHHC	0	1.0541	0.9479
VHVC	0	1.1116	0.9659
HHHC	1	0.9703	0.9539
HHVC	1	1.1322	0.9814
VHHC	1	1.1312	0.9802
VHVC	1	1.1238	0.9797

of the limit cycle is reached. Deviation is prevented to grow indefinitely because of the action of the attractor, which holds trajectories towards itself. In such cases, the Lyapunov exponents are positive, indicating the exponential increase of deviation between trajectories. Figure 5.2.3 shows a typical shape of the trajectories deviation (error) for a Lyapunov unstable phase state.

For a discretized problem, with finite number of degrees of freedom, one Lyapunov exponent is defined for each phase of the system. As explained by Seydel [41], the sum of all Lyapunov exponents represents the average of volume contraction rate. For a dissipative system, it results that this value is negative.

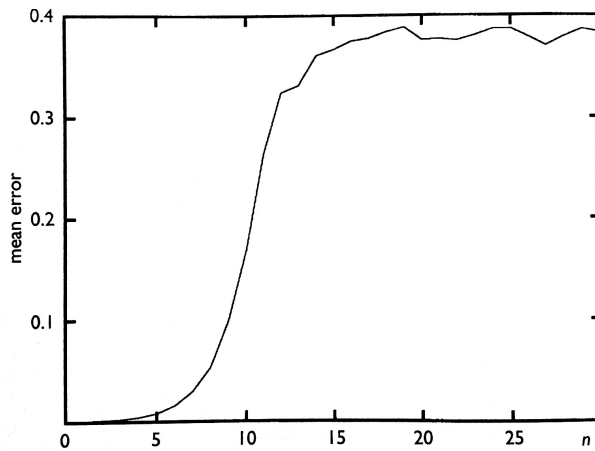


Figure 5.19: Typical curve of mean deviation between trajectories for unstable Lyapunov unstable point. Extracted from [29].

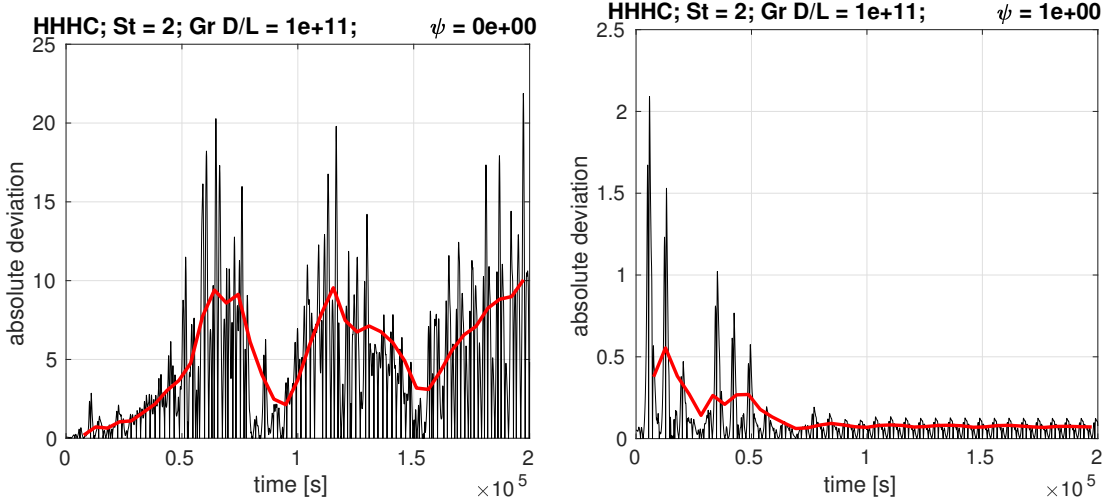
This concept of stability is different from that employed along this work, which is much more strict. From the Lyapunov stability point of view, a limit cycle can be stable, which is interpreted as instability for a NCL.

We take one periodic regime and an aperiodic one for comparison. The HHHC transients for $St = 2$ and $Gr D/L = 10^{11}$ are aperiodic without pool and become periodic when the pool is connected (figs. A.60 and A.61). Figure 5.2.3 shows the deviation for both variants, calculated only for the mass flow, i.e., only one phase was considered. The Lyapunov exponent was calculated for each case (cf. table 5.7). The result was obtained by shifting the initial value for mass flow by 1% from the first simulation.

Coherently with expectation, the Lyapunov numbers are positive for the aperiodic case negative for the periodic case. The coefficient of determination is also presented in table 5.7, showing a bad fitting quality for the case for $\psi = 1$ with periodic regime, which does not affect the evaluation of the system dynamic behavior.

Table 5.7: Lyapunov exponents for HHHC at $\text{St} = 2$, $\text{Gr } D/L = 10^{11}$ with $\psi = 0$ and $\psi = 1$.

$\psi = 0$	$\mathcal{L} = 6.0363 \times 10^{-5}$	$R^2 = 0.9480$
$\psi = 1$	$\mathcal{L} = -1.8524 \times 10^{-5}$	$R^2 = 0.5318$

**Figure 5.20:** Deviation of mass flow rate for an unstable case (left) and a stable one (right).

Nature contains periodic and aperiodic dynamical systems. Sometimes an apparent chaotic motion is periodic (or quasi-periodic), but the superposition of oscillating modes is large enough to build up an illusion of chaos, as do water surfaces in some situations. The opposite is harder to happen, but, as said before, an apparent chaotic signal can be just part of a single period which is larger than the interval of observation. Hence, methods of analysis are of fundamental importance in the evaluation of a dynamical system. Nevertheless, the expectations from the results reported in appendix A were correct with respect to whether the transients were chaotic or not as confirmed by the analyses presented in this section.

6 SUMMARY AND CONCLUSION

The thesis is devoted to evaluate how the dynamical behavior of Natural Convection Loops is impacted when a pool is connected to the system. Most of safety passive cooling systems in nuclear power plants, specially in the recent designs, consists of natural convection circuits which transfer heat from or to a heat absorbing pool¹. The main result of the work is in the stability maps presented in chapter 4, with eight maps showing how the pool changes the area of stable operation for different configurations of heater and cooler. A quantitative evaluation was made by defining a critical Stanton number St_c so that for $St > St_c$ the system is stable for any value of $Gr D/L$. Results showed that when the pool is considered, the value of St_c is reduced by approximately two thirds in all configurations (cf. table 4.4), demonstrating a significant impact of the pool on the stability of Natural Convection Loops.

To arrive at this result, a classical mathematical model for single-phase natural convection loops was modified to take the coupling to the pool into account. Chapter 2 described the model, and employed a scaling criterion to build up the non-dimensional for of the model. The modification on the mathematical model consisted essentially of the addition of a global energy balance in the pool, coupled to the energy balance in the loop by the source term in the heater. Some numerical aspects were also addressed in this chapter, explaining how the procedure for calculation of the steady states are stabilized by a relaxation parameter.

Throughout this thesis, beside the influence of the pool on the system stability, another variant observed was the orientation of heater and cooler. It follows the pioneering work of Vijayan et al. [50], who addressed this topic highlighting the great difference it makes to consider the heater and/or cooler horizontally or vertically oriented. The text adopted the nomenclature used by Vijayan et al. [50] – HHHC, HHVC, VHHC and VHVC – using H and V to designate respectively horizontal and vertical orientation and H and C for heater and cooler, respectively.

¹A curiosity about the coupling loop-pool: one can write “pool” by writing “loop” from right to left.

In the following sections, the main outcomes from each chapter are summarized.

6.1 Steady state

As confirmed by several published works, the choice of the friction factor correlation is a critical point in the modeling of NCLs. Section 3.1 in chapter 3 analyzed six correlations, comprised of three classical models and three proposed by authors working in the context of natural convection loops, in order to study the influence each one has in the prediction of NCL thermo-hydraulics. The six evaluated correlations were

- a combination of Poiseuille-Blasius' correlation, eq. 3.9
- a combination of Poiseuille-Colebrook's correlation, eq. 3.12
- Churchill's correlation, eq. 3.11
- the model proposed by Ruiz et al. [36], eq. 3.16
- the model proposed by Naveen et al. [27], eq. 3.15
- the model proposed by Vijayan et al. [51], eq. 3.12

Comparisons against two experimental campaigns were presented. One resulted in best agreement for the correlation of Vijayan et al. [51] (cf. table 3.2), but considered only HHHC orientation. In the other comparison, this correlation has the worst performance, while forced flow correlations performed better, together with the model proposed by Ruiz et al. [36], which is actually a combination of forced flow correlations with a continuous transition between laminar and turbulent flow regimes. All stability analyses performed in this work employed the friction correlation proposed by Ruiz et al. [36].

6.2 Linear stability analysis

Stability in this work is associated to the stability of steady states, i.e., given a perturbation on the steady state, if the system returns to its original (steady) state, then it is interpreted as stable.

The importance of linear stability analysis relies on the determination of the critical parameters for stable fixed points, which are exactly the stationary solutions of the set of equations. In this sense, chapter 4 provided eight stability maps, as function of three non-dimensional parameters – Stanton number St , Grashof number times a geometrical relation $Gr D/L$ and the parameter ψ , which essentially measures the amount of water in the pool. In the first four maps, stable regions are projected over the $(St, Gr D/L)$ plane

for each configuration, and in the other four, stability regions are drawn over the (ψ, St) plane.

Beyond evaluating the effect of having a pool coupled to the circuit, this chapter also analyzed the influence of different amounts of water in the pool. The somewhat surprising result is that the amount of water exerts a non-monotonic influence on the system stability, as shown in section 4.3. Results also show that there are critical values of ψ for linear stability, compiled in table 4.5.

6.3 Non-linear stability analysis

In this chapter, focus was on the dynamic behavior of the systems. Three sets of transient results were generated, oriented by stability regions in the maps of chapter 4 – stable regimes, unstable only without pool and unstable regimes. All results are compiled in appendix A. But before simulation the system transients, an evaluation of the effect of the magnitude of perturbations was made, concluding that it has no influence on the stability behavior of the system (sec. 5.1).

Non-linear stability analysis was then performed on the transient data, grouping results into three sets of distinct dynamical nature.

The first was composed by stable points. The rate of decay for the system with pool and without it was emphasized, with much stronger damping when pool is considered. It is interesting that apparently an additional oscillating mode appears in the system with pool (figs. A.2 and A.3, among others).

The second group was composed by the periodic (and quasi-periodic) regimes. A periodic transient was selected for analysis by means of Fourier transform and compared to the same loop and operating parameters, but applying a change of 1% in the Stanton number, which produced chaotic oscillations in the initial transients.

The third group consisted of chaotic regimes. Some classical methods of non-linear stability analysis – Fourier transform, determination of the attractor dimension and calculation Lyapunov exponents – were employed in the results. Intention was to characterize the dynamic behavior of the system.

6.4 Conclusion

The research on single-phase natural convection loops has reached a mature state of knowledge in the end of the 2001-2010 decade in terms of the main effects of geometrical and operating parameters on the heat removal capacity and stability properties, which are the main concerns in the design process of such a system. During the past five to six years, the level of detail has increased, with contributions on the mathematical model

and considering different operating conditions. Modeling of the expansion tank and heat capacity of pipe walls are examples of current stage of mathematical modeling of NCLs, and the operation dynamic tilting angle, simulating a passive cooling system for ship applications, exemplifies new operating conditions taken into account in recent studies.

This thesis is inserted in this stage of scientific works on the topic. The cooling system integrating convection circuit and pool however is not simply a new operating condition. It is, as already explained, a common configuration to many heat removal systems. The model developed in this thesis consisted of a global energy balance for the pool, not taking the convection currents in it into account.

The results generated by the present work indicate a significant influence of the pool on stability of passive heat removal systems. It is just an indication, requiring further investigations with more sophisticated mathematical models and experimental research. Nevertheless, based on this indication, the design margins of passive cooling systems would be significantly enlarged, allowing for higher heat removal capacities without loss of stability. Recalling that mass flow and thermo-hydraulic stability compete one with another – if the system allows for larger mass flows, it loses stability. In other words, the results indicate the existence of design margins for much more compact passive cooling systems. It is clear that nuclear industry employ diverse simulation tools and make use of prototypes and is, therefore, capable of offering optimized designs. Notwithstanding, the process of establishing parametric limits for stability is of great relevance for any area of engineering because it optimizes the design process itself, which is the case of a nuclear supplier, but also serve as a subsidy for evaluation of technical solutions for a nuclear utility, for example.

From the present work, by writing the geometrical and operating parameters in terms of the following three dimensionless groups:

- Stanton number defined by eq. 2.10
- Grashof number defined by eq. 2.11 times the ratio between diameter and loop length – Gr D/L
- ratio between water mass in the pool and the product of reference density per volume of the loop

it is possible to know the stability behavior of a NCL integrated to pool.

6.5 Comment on electricity matrix

This work deals with passive cooling system having as main motivation its applicability to nuclear power industry. More specifically, this thesis was originated in the context

of the spent fuel assemblies storage unit, a project developed by Eletronuclear which incorporated the concept of passive cooling, employing a heat removal system designed by French company AREVA NP.

Here in Brazil or in other countries, nuclear power sector is constantly working to improve safety, and the incorporation of passive systems is part of this effort. The main reason is simple: any industrial installation must pursue the highest level of safety, both for its workers and the surrounding people². A second reason is the public rejection against atomic power. As a result, the number of fatalities per produced energy in nuclear power is among the lowest.

Whenever possible, electricity production should rely on renewable, clean and safe energy sources. Brazil has one of the cleanest electricity matrices in the world thanks to its hydroelectric fleet. However, every study on the hydro power potential left for electricity production in Brazil addresses the current shortage of possibilities for construction of large reservoirs. At this point, it is important that decisions related to the expansion of electricity matrix are based on sustainable and scientific concepts. Great part of the rejection to nuclear power comes from the fact that the general public does not know about the technology. Once they do not know, imagination converges to the worst scenarios. This is confirmed by movies about monsters in the area of Chernobyl plant. It is also not wise to defend a fully nuclear electricity matrix, when wind and solar power are developing and constitute the best solution for remote areas, for example.

For these cases, lack of information produces incoherent conclusions as well. Regarding wind power, for example, it is very common to hear about the impact it has on bird deaths due to collision. But when numbers are objectively compared, wind turbines appear as the less relevant cause of bird deaths. According to a study published by for Sustainable Energy [14], in ten thousand occurrences, less than 1 bird dies because of wind power. Cats respond for 1,060 cases, and collision to building respond to 5,820 cases. Hence, energy production should be planned on a basis of objective, realistic information.

²This thesis was written approximately one year after the accident at the Fundão mining waste dam, occurred on November 5th, 2015, at the city of Mariana, Brazil. It caused 18 fatalities and was classified by many representations as the Brazilian worst ambient disaster cause by human activities.

Bibliography

- [1] W. Ambrosini and J. C. Ferreri. Prediction of stability of one-dimensional natural circulation with a low diffusion numerical scheme. *Annals of Nuclear Energy*, 30: 1505–1537, 2003.
- [2] W. Ambrosini, N. Forgione, J. C. Ferreri, and M. Bucci. The effect of wall friction in single-phase natural circulation stability at the transition between laminar and turbulent flow. *Annals of Nuclear Energy*, 31:1833–1865, 2004.
- [3] G. Angelo, D. A. Andrade, E. Angelo, W. M. Torres, G. Sabundjian, L. A. Macedo, and A. F. Silva. A numerical and three-dimensional analysis of steady state rectangular natural circulation loop. *Nuclear Engineering and Design*, 244:61–72, 2012.
- [4] M. Angelucci, W. Ambrosini, and N. Forgione. Numerical estimation of wall friction ratio near the pseudo-critical point with CFD-models. *Nuclear Engineering and Design*, 264:71–79, 2013.
- [5] D. N. Basu, S. Bhattacharyya, and P. K. Das. Development of a unified model for the steady-state operation of single-phase natural circulation loops. *International Journal of Heat and Mass Transfer*, 62:452–462, 2013.
- [6] Dipankar N. Basu, S. Bhattacharyya, and P.K. Das. Dynamic response of a single-phase rectangular natural circulation loop to different excitations of input power. *International Journal of Heat and Mass Transfer*, 65:131–142, 2013.
- [7] Dipankar N. Basu, S. Bhattacharyya, and P.K. Das. Influence of geometry and operating parameters on the stability response of single-phase natural circulation loop. *International Journal of Heat and Mass Transfer*, 58:322–334, 2013.
- [8] Pierre Bergé, Yves Pomeau, and Christian Vidal. *Order within chaos: towards a deterministic approach to turbulence*. John Wiley & Sons, 1986.
- [9] J. A. Boure, A. E. Bergles, and L. S. Tong. Review of two-phase flow instability. *Nuclear Engineering and Design*, 25:165–192, 1973.

- [10] Weiwei Chen and Xiande Fang. A new heat transfer correlation for supercritical water flowing in vertical tubes. *International Journal of Heat and Mass Transfer*, 78:156–160, 2014.
- [11] X. Cheng and T. Schulenberg. Heat transfer at supercritical pressures-literature review and application to an HPLWR. Technical report, Karlsruhe Institute of Technology, 2001.
- [12] H.F. Creveling, J.F. De Paz, J.Y. Baladi, and R.J. Schoenhals. Stability characteristics of a single-phase free convection loop. *Journal of Fluid Mechanics*, 67:65–84, 1975.
- [13] Xiande Fang, Yu Xu, and Zhanru Zhou. New corelations of single-phase friction factor for turbulent pipe flow and evaluation of existing single-phase friction factor correlations. *Nuclear Engineering and Design*, 241:897–902, 2011.
- [14] Centre for Sustainable Energy. Common concerns about wind power. Technical report.
- [15] GenIV. Annual report - 2013. Technical report, Generation IV International Forum, 2013.
- [16] M. Ishii and I. Kataoka. Scaling laws for thermal-hydraulic system under single phase and two-phase natural circulation. *Nuclear Engineering and Design*, 81:411–425, 1984.
- [17] Joseph B. Keller. Periodic oscillations in a model of thermal convection. *Journal of Fluid Mechanics*, 26:599–606, 1966.
- [18] Mayur Krishnani and Dipankar N. Basu. On the validity of boussinesq approximation in transient simulation of single-phase natural circulation loops. *International Journal of Thermal Sciences*, 105:224–232, 2016.
- [19] Jayaraj Yallappa Kudariyawar, Abhishek Kumar Srivastava, Abhijeet Mohan Vaidya, Naresh Kumar Maheshwari, and Polepalle Satyamurthy. Computational and experimental investigation of steady state and transient characteristics of molten salt natural circulation loop. *Applied Thermal Engineering*, 99:560–571, 2016.
- [20] K. Kiran Kumar and M. Ram Gopal. Steady-state analysis of CO₂ based natural circulation loops with end heat exchangers. *Applied Thermal Engineering*, 29:1893–1903, 2009.

-
- [21] Adrienne S. Lavine, Ralph Greif, and Joseph A. C. Humphrey. A three-dimensional analysis of natural convection in a toroidal loop - the effect of Grashof number. *International Journal of Heat and Mass Transfer*, 30:251–262, 1987.
 - [22] Leon Lima and Norberto Mangiavacchi. 1D stability analysis of single-phase Natural Circulation Loops. In *Inproceedings of COBEM 2015, Rio de Janeiro*, 2015.
 - [23] Leon Lima, Norberto Mangiavacchi, and Lucio Ferrari. Stability analysis of passive cooling systems for nuclear spent fuel pool. *Journal of the Brazilian Society of Mechanical Sciences and Engineering*, page Online first article, 2016.
 - [24] José March-Leuba and José M. Rey. Coupled thermohydraulic-neutronic instabilities in boiling water nuclear reactors: a review of the state of the art. *Nuclear Engineering and Design*, 145:97–111, 1993.
 - [25] Kumar Naveen, J.B. Doshi, and P.K. Vijayan. Investigations on the role of mixed convection and wall friction factor in single-phase natural circulation loop dynamics. *Annals of Nuclear Energy*, 38:2247–2270, 2011.
 - [26] Kumar Naveen, Kannan N. Iyer, J. B. Doshi, and P. K. Vijayan. Investigations on single-phase natural circulation loop dynamics. part 1: Model for simulating start-up from rest. *Progress in Nuclear Energy*, 76:148–159, 2014.
 - [27] Kumar Naveen, Kannan N. Iyer, J. B. Doshi, and P. K. Vijayan. Investigations on single-phase natural circulation loop dynamics. part 2: Role of wall constitutive laws. *Progress in Nuclear Energy*, 75:105–116, 2014.
 - [28] A. K. Nayak, P. K. Vijayan, D. Saha, and V. Venkat Raj. Mathematical modeling of the stability characteristics of a natural circulation loop. *Mathl. Comput. Modelling*, 22:77–87, 1995.
 - [29] G. Nicolis. *Introduction to nonlinear science*. Cambridge University Press, 1995.
 - [30] D. S. Pilkhwal, W. Ambrosini, N. Forgione, P. K. Vijayan, D. Saha, and J. C. Ferri. Analysis of the unstable behaviour of a single-phase natural circulation loop with one-dimensional and computational fluid-dynamic models. *Annals of Nuclear Energy*, 34:339–355, 2007.
 - [31] Gonella V. Durga Prasad, Manmohan Pandey, and Manjeet S. Kalra. Review of research on flow instabilities in natural circulation boiling systems. *Progress in Nuclear Energy*, 49:429–451, 2007.

- [32] Y. F. Rao, K. Fukuda, and R. Kaneshima. Analytical study of coupled neutronic and thermodynamic instabilities in a boiling channel. *Nuclear Engineering and Design*, 154:133–144, 1995.
- [33] E. H. Ridouane, C. M. Danforth, and D. L. Hitt. A 2d numerical study of chaotic flow in a natural convection loop. *International Journal of Heat and Mass Transfer*, 53:76–84, 2009.
- [34] E. H. Ridouane, D. L. Hitt, and C. M. Danforth. A numerical investigation of 3d flow regimes in a toroidal natural convection loop. *International Journal of Heat and Mass Transfer*, 54:5253–5261, 2011.
- [35] M. Rohde, C. P. Marcel, C. T’Joen, A. G. Class, and T.H.J.J. van der Hagen. Downscaling a supercritical water loop for experimental studies on system stability. *International Journal of Heat and Mass Transfer*, 54:65–74, 2011.
- [36] D. E. Ruiz, A. Cammi, and L. Luzzi. Dynamic stability of natural circulation loops for single-phase fluids with internal heat generation. *Chemical Engineering Science*, 126:573–583, 2015.
- [37] G. Sabundjian, D. A. Andrade, P. E. Umbehaun, W. M. Torres, L. A. Macedo, T. N. Conti, R. N. Mesquita, and G. Angelo. Comparison between experimental data and numerical modeling for the natural circulation phenomenon. *J. of the Braz. Soc. of Mech. Sci. and Eng.*, 33:227–232, 2011.
- [38] T. Schulenberg, J. Starflinger, P. Marsault, D. Bittermann, C. Maráczky, E. Laurien, J.A. Lycklama à Nijeholt, H. Anglart, M. Andreani, M. Ruzickova, and A. Toivonen. European supercritical water cooled reactor. *Nuclear Engineering and Design*, 241: 3505–3513, 2011.
- [39] T. Schulenberg, L. K. H. Leung, and Yoshiaki Oka. Review of R&D for supercritical water cooled reactor. *Progress in Nuclear Energy (article in press)*, 2014.
- [40] M. Sen, E. Ramos, and C. Trevi no. On the steady-state velocity of the inclined toroidal thermosyphon. *J. Heat Transfer*, 107:974–977, 1985.
- [41] Ruediger Seydel. *Practical Bifurcation Stability Analysis*. Springer, 2010.
- [42] Manish Sharma, P.K. Vijayan, D.S. Pilkhwal, and Yutaka Asako. Natural convective flow and heat transfer studies for supercritical water in a rectangular circulation loop. *Nuclear Engineering and Design*, 273:304–320, 2014.

- [43] A.K. Srivastava, Jayaraj Y. Kudariyawar, A. Borgohain, S.S. Jana, N.K. Maheshwari, and P.K. Vijayan. Experimental and theoretical studies on the natural circulation behavior of molten salt loop. *Applied Thermal Engineering*, 98:513–521, 2016.
- [44] J. Starflinger, T. Schulenberg, Ph. Marsault, and D. Bitterman. Public final report - assessment of the HPLWR concept. Technical report, Karlsruhe Institute of Technology, December 2010.
- [45] B. T. Swapnalee and P. K. Vijayan. A generalized flow equation for single-phase natural circulation loops obeying multiple friction laws. *International Journal of Heat and Mass Transfer*, year = 2011, volume = 54, pages = 2618–2629, owner = single-phase NCL.
- [46] P. K. Vijayan and H. Austregesilo. Scaling laws for single-phase natural circulation loops. *Nuclear Engineering and Design*, 152:331–347, 1994.
- [47] P.K. Vijayan. Experimental observations on the general trends of the steady state and reliability behavior of single-phase natural circulation loops. *Nuclear Engineering and Design*, 215:139–152, 2002.
- [48] P.K. Vijayan and A. K. Nayak. Natural circulation systems: advantages and challenges. *IAEA-TECDOC-1474*, pages 89–100 (Annex 3), 2005.
- [49] P.K. Vijayan and A. K. Nayak. Introduction to instabilities in natural circulation systems. *IAEA-TECDOC-1474*, pages 173–201 (Annex 7), 2005.
- [50] P.K. Vijayan, M. Sharma, and D. Saha. Steady state and stability characteristics of single-phase natural circulation in a rectangular loop with different heater and cooler orientations. *Experimental Thermal and Fluid Sciences*, 31:925–945, 2007.
- [51] P.K. Vijayan, A. K. Nayak, D. Saha, and M. R. Gartia. Effect of loop diameter on the steady state and stability behaviour of single-phase and two-phase natural circulation loops. *Science and Technology of Nuclear Installations*, from Hindawui Publishing Corporation, page Article 672704, 2008.
- [52] E. Wacholder, S. Kaizerman, and E. Elias. Numerical analysis of the stability and transient behavior of natural convection loops. *Int. J. Engng. Sci.*, 20:1235–1254, 1982.
- [53] Pierre Welander. On the oscillatory instability of a differentially heated fluid loop. *Journal of Fluid Mechanics*, 29:17–30, 1967.
- [54] Y. Zvirin. The effect of dissipation on free convection loops. *International Journal of Heat and Mass Transfer*, 22:1579, 1979.

- [55] Y. Zvirin. The instability associated with the onset of motion in a thermosyphon. *International Journal of Heat and Mass Transfer*, 28:2105–2111, 1985.
- [56] Y. Zvirin and R. Greif. Transient behavior of natural circulation loops: Two vertical branches with point heat source and sink. *Internatinal Journal of Heat and Mass Transfer*, 22:499, 1979.
- [57] Y. Zvirin, C. W. Sullivan, Romney B. Duffey, and P. R. III Jeuck. Experimental and analytical investigation of a pwr natural circulation loop. *EPRI*, NP-1364-SR, 1980.

A TRANSIENT RESULTS

This appendix contains all transient outputs for considering the three variants described in chapter 5, viz. operating regime, orientation and coupling to the pool. For each one, results are presented in the form of

1. time series of mass flow rate
2. time series of mass flow rate together with power input, in cases with pool
3. frequency spectrum of mass flow oscillating amplitudes for
4. space-time plots of temperature field
5. comparison of mass flow rate and temperature difference across heater for $\psi = 0$ and $\psi = 1$

There is an exception regarding the mass flow on frequency domain, which are not presented for the stable cases, since they essentially highlight the main oscillating mode, without adding information on the system dynamics.

The three operating points are listed in table A.1.

All simulations then consist of perturbations on the steady state. Table A.2 present the Reynolds numbers for all simulated case.

Table A.1: Operating points for the transient simulations.

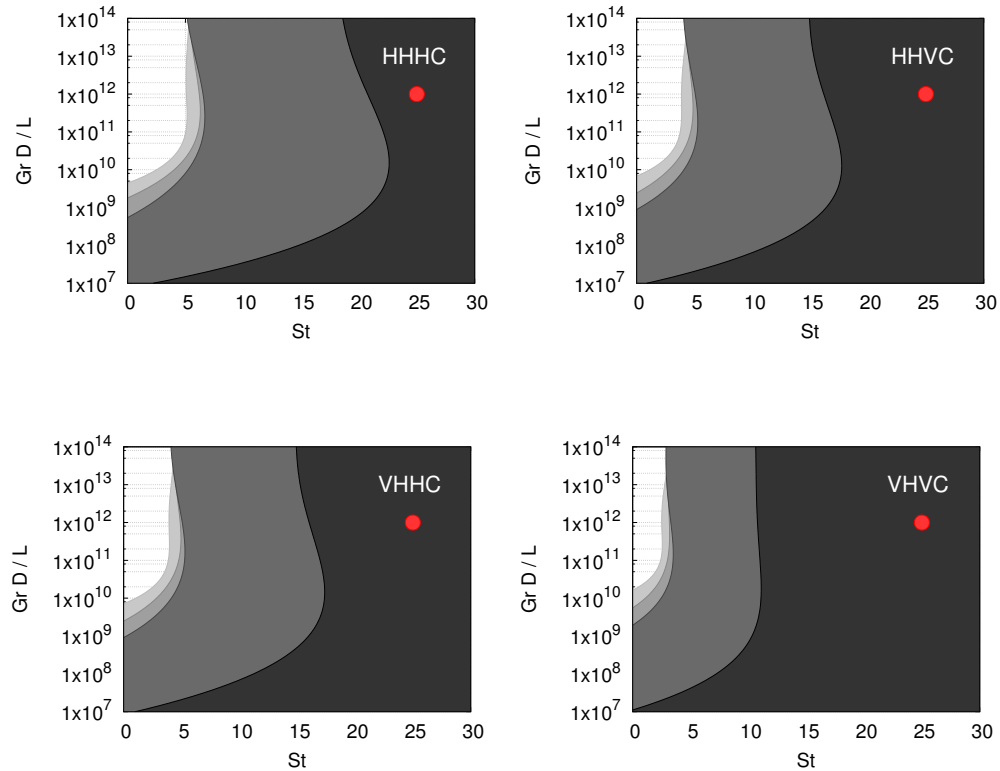
stable regime	$St = 25; Gr D/L = 10^{12}$
stable with pool/unstable without pool	$St = 10; Gr D/L = 10^{11}$
unstable regime	$St = 2; Gr D/L = 10^{11}$

Table A.2: Steady state Reynolds numbers for the simulated cases.

	HHHC		HHVC	
	$\psi = 0$	$\psi = 1$	$\psi = 0$	$\psi = 1$
$St = 25; Gr D/L = 10^{12}$	3.02×10^4	2.06×10^4	3.04×10^4	2.07×10^4
$St = 10; Gr D/L = 10^{11}$	1.12×10^4	8.18×10^3	1.13×10^4	8.21×10^3
$St = 2; Gr D/L = 10^{11}$	1.08×10^4	7.82×10^3	1.08×10^4	7.85×10^3

	VHHC		VHVC	
	$\psi = 0$	$\psi = 1$	$\psi = 0$	$\psi = 1$
$St = 25; Gr D/L = 10^{12}$	3.02×10^4	2.12×10^4	3.04×10^4	2.14×10^4
$St = 10; Gr D/L = 10^{11}$	1.12×10^4	8.27×10^3	1.13×10^4	8.31×10^3
$St = 2; Gr D/L = 10^{11}$	1.07×10^4	7.79×10^3	1.08×10^4	7.83×10^3

A.1 Stable regimes

**Figure A.1:** Points selected in stability maps for simulation loop transients.

A.1.1 HHHC

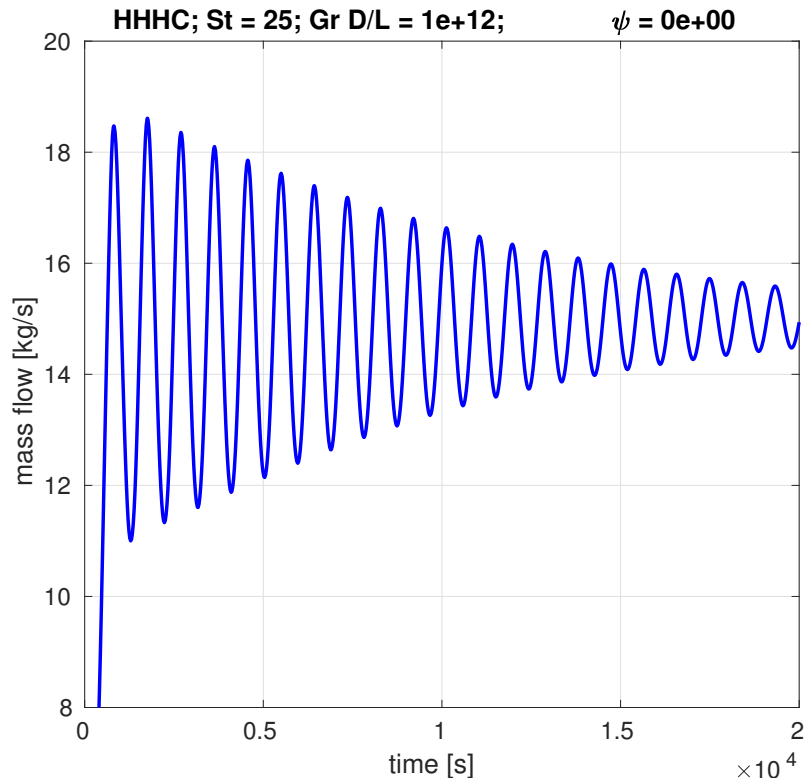


Figure A.2: Transient mass flow rate for HHHC loop, $St = 25$, $Gr D/L = 10^{12}$, $\psi = 0$.

Table A.3: Operating, numerical and geometrical data of HHHC 800 mm diameter loop considered for simulation of stable operating points – $St = 25$ and $Gr D/L = 10^{12}$.

L_h [m]	2.000
L_c [m]	0.800
local losses	1.8
mesh nodes	750
CFL	1
loop internal pressure	1 bar
$Gr D/L$	10^{12}
St	25
T_s [°C]	30
perturbation	-100%
friction correlations:	Ruiz et al. [36]

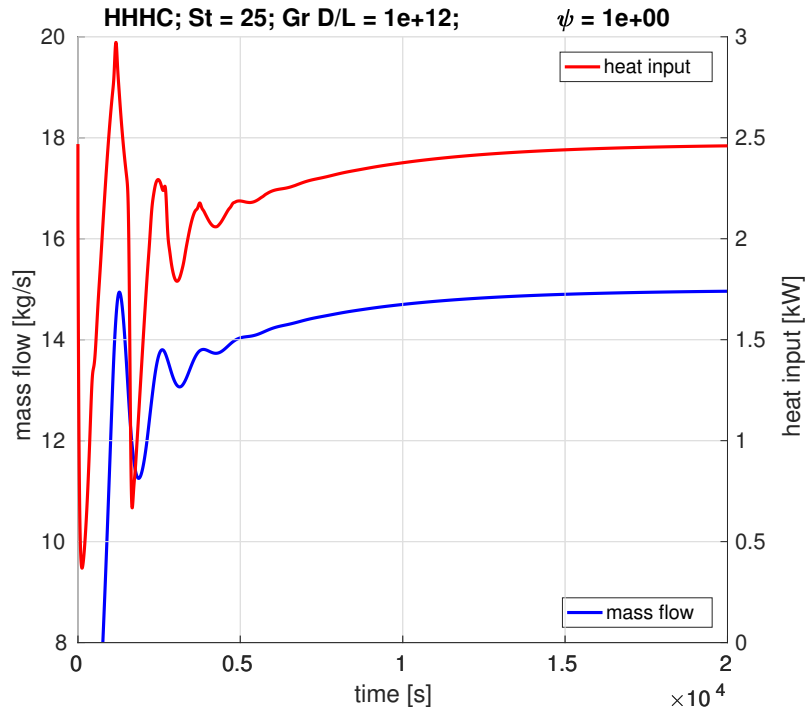


Figure A.3: Transient mass flow rate for HHHC loop, $St = 25$, $Gr D/L = 10^{12}$, $\psi = 1$.

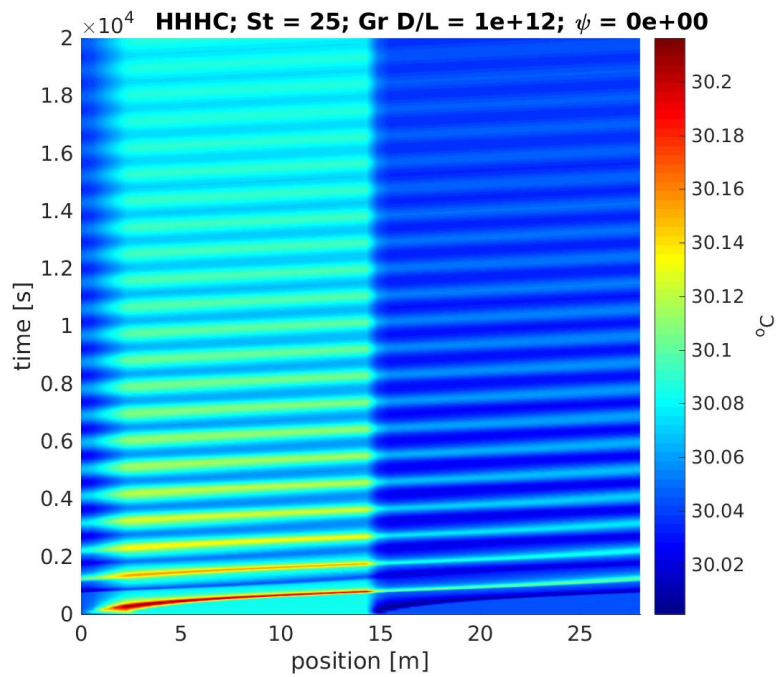


Figure A.4: Space-time chart for temperature in HHHC loop, $St = 25$, $Gr D/L = 10^{12}$, $\psi = 0$.

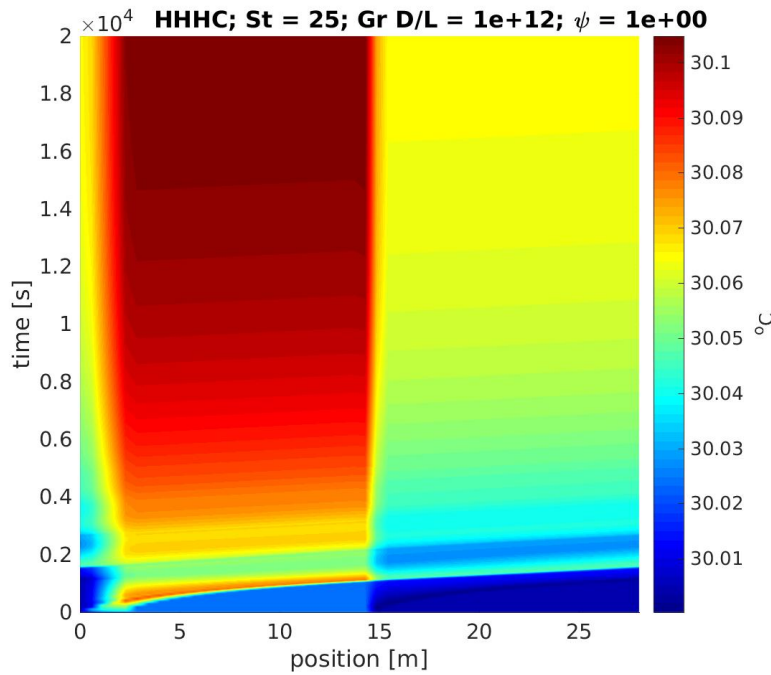


Figure A.5: Space-time chart for temperature in HHHC loop, $\text{St} = 25$, $\text{Gr } D/L = 10^{12}$, $\psi = 1$.

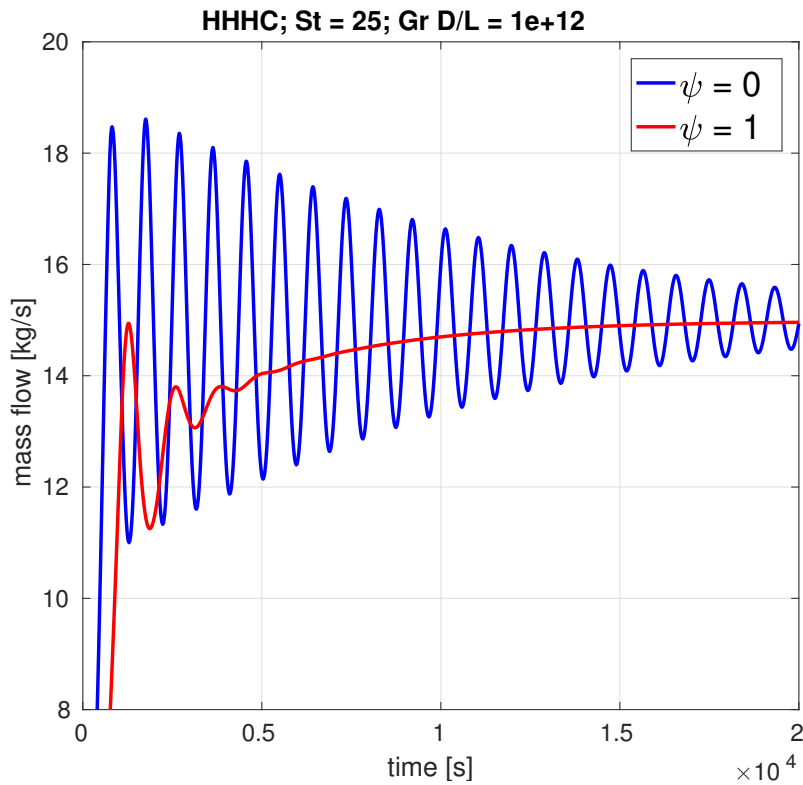


Figure A.6: Comparison of time series for mass flow rate using $\psi = 0$ and $\psi = 1$, in HHHC loop, $\text{St} = 25$, $\text{Gr } D/L = 10^{12}$.

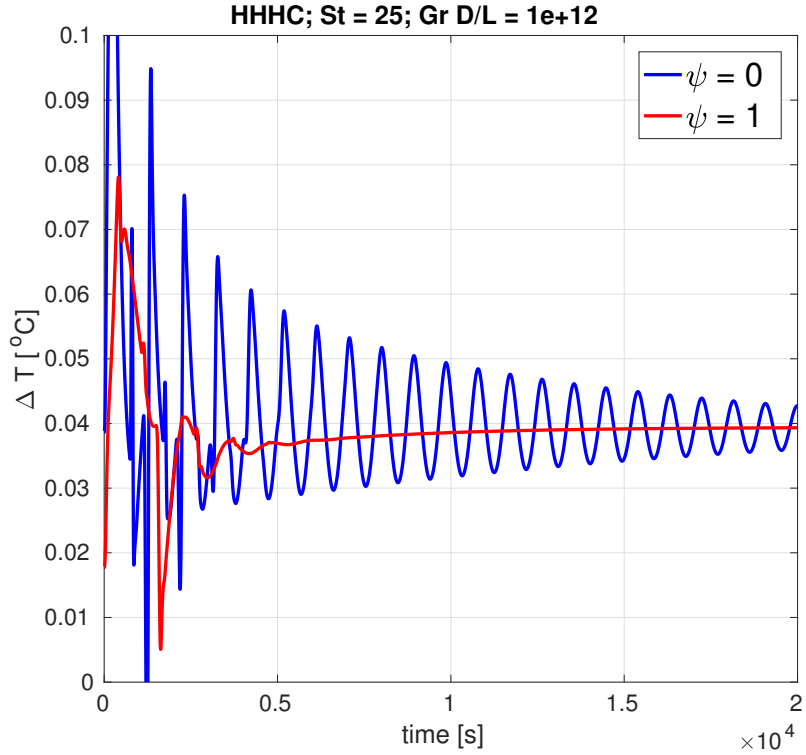


Figure A.7: Comparison of time series for temperature difference across heater using $\psi = 0$ and $\psi = 1$, in HHHC loop, $\text{St} = 25$, $\text{Gr } D/L = 10^{12}$.

A.1.2 HHVC

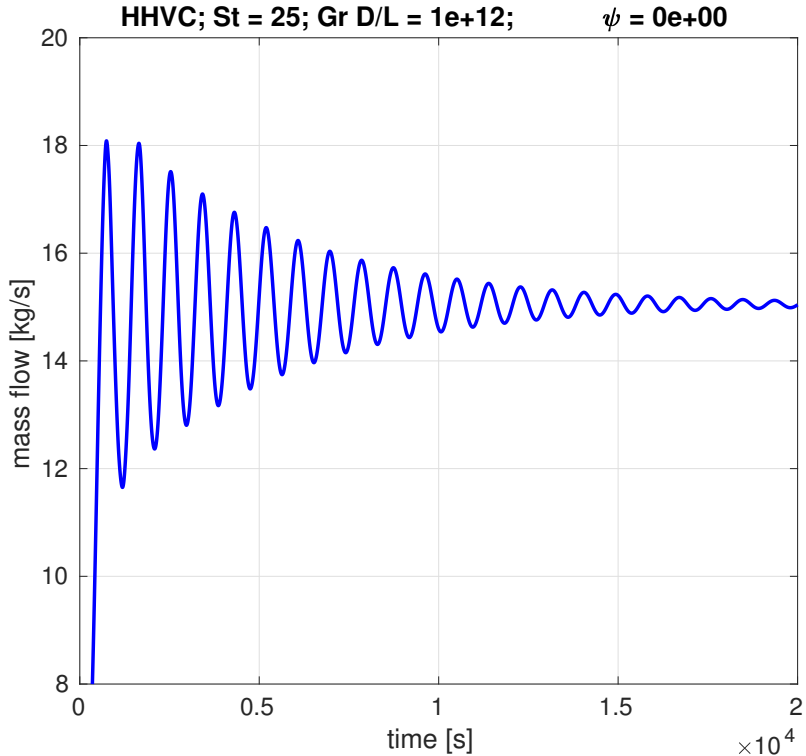


Figure A.8: Transient mass flow rate for HHVC loop, $\text{St} = 25$, $\text{Gr } D/L = 10^{12}$, $\psi = 0$.

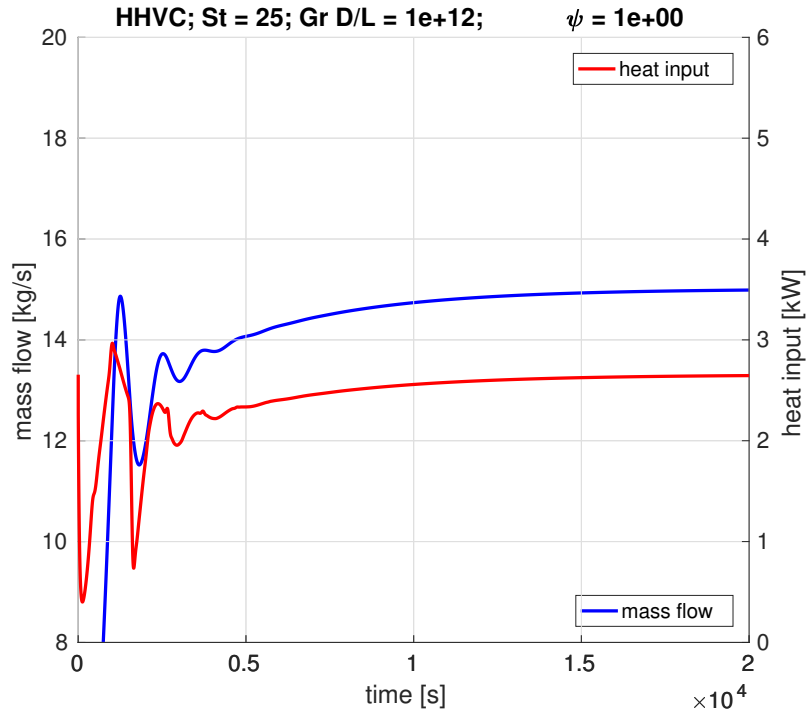


Figure A.9: Transient mass flow rate for HHVC loop, $St = 25$, $Gr D/L = 10^{12}$, $\psi = 1$.

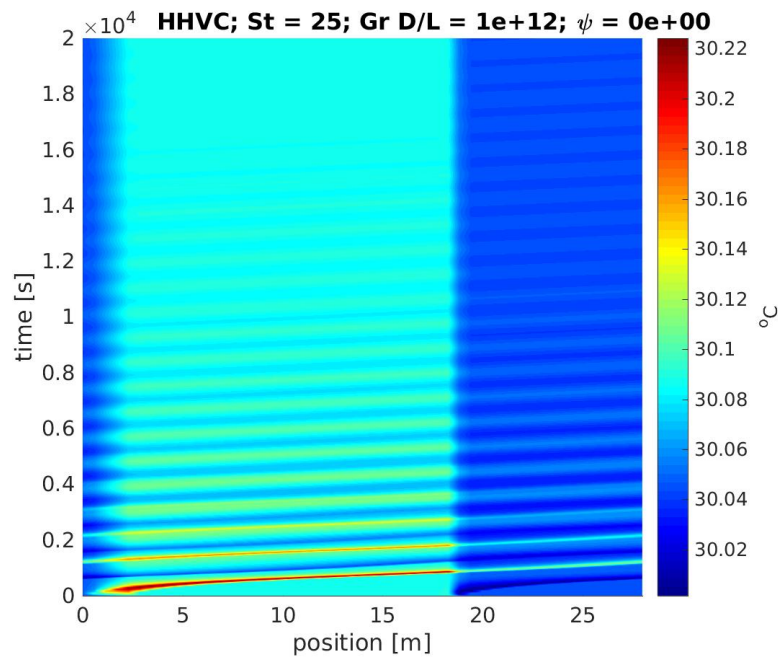


Figure A.10: Space-time chart for temperature in HHVC loop, $St = 25$, $Gr D/L = 10^{12}$, $\psi = 0$.

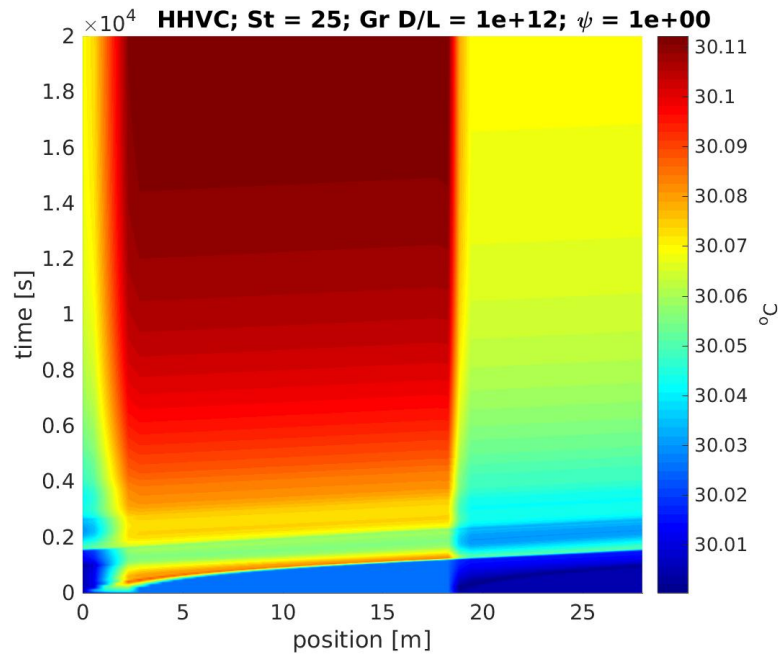


Figure A.11: Space-time chart for temperature in HHVC loop, $\text{St} = 25$, $\text{Gr } D/L = 10^{12}$, $\psi = 1$.

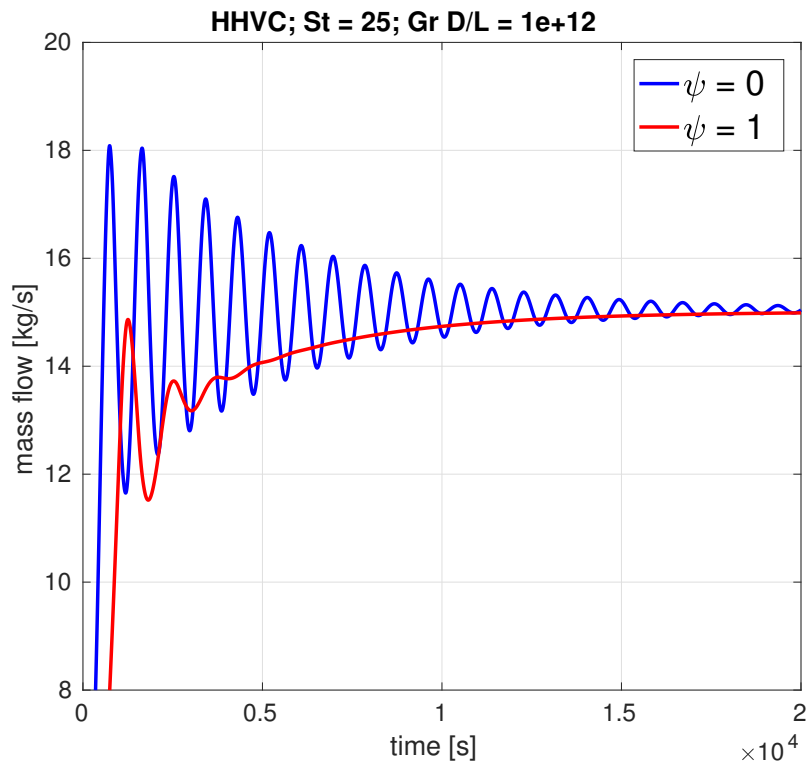


Figure A.12: Comparison of time series for mass flow rate using $\psi = 0$ and $\psi = 1$, in HHVC loop, $\text{St} = 25$, $\text{Gr } D/L = 10^{12}$.

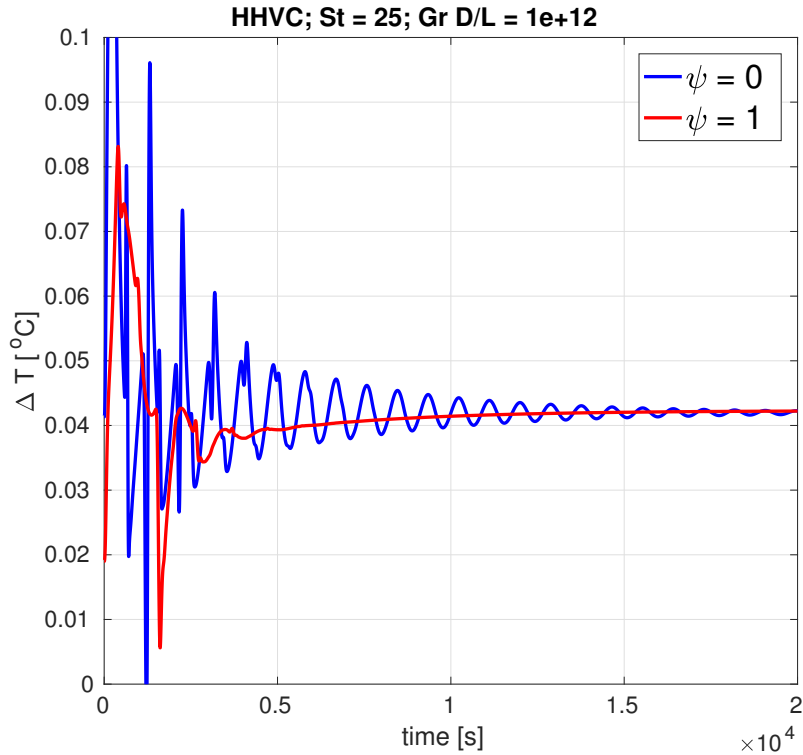


Figure A.13: Comparison of time series for temperature difference across heater using $\psi = 0$ and $\psi = 1$, in HHVC loop, $\text{St} = 25$, $\text{Gr } D/L = 10^{12}$.

A.1.3 VHHC

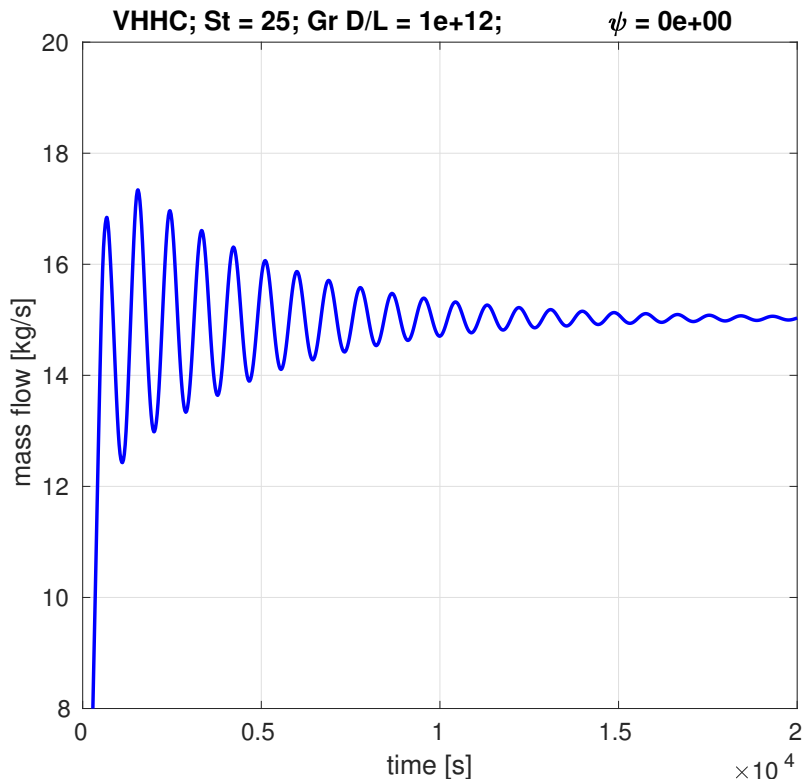


Figure A.14: Transient mass flow rate for VHHC loop, $\text{St} = 25$, $\text{Gr } D/L = 10^{12}$, $\psi = 0$.

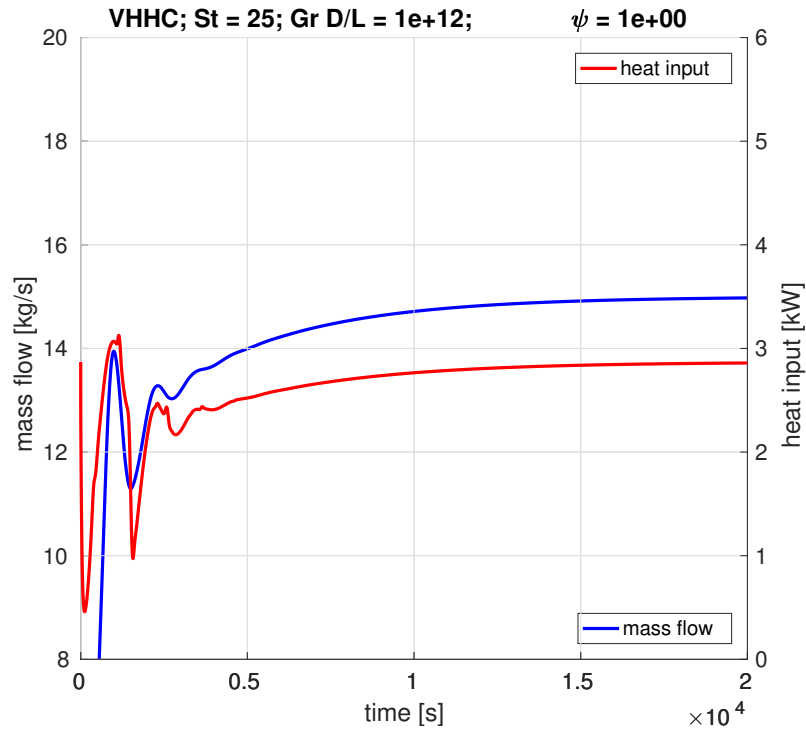


Figure A.15: Transient mass flow rate for VHHC loop, $St = 25$, $Gr D/L = 10^{12}$, $\psi = 1$.

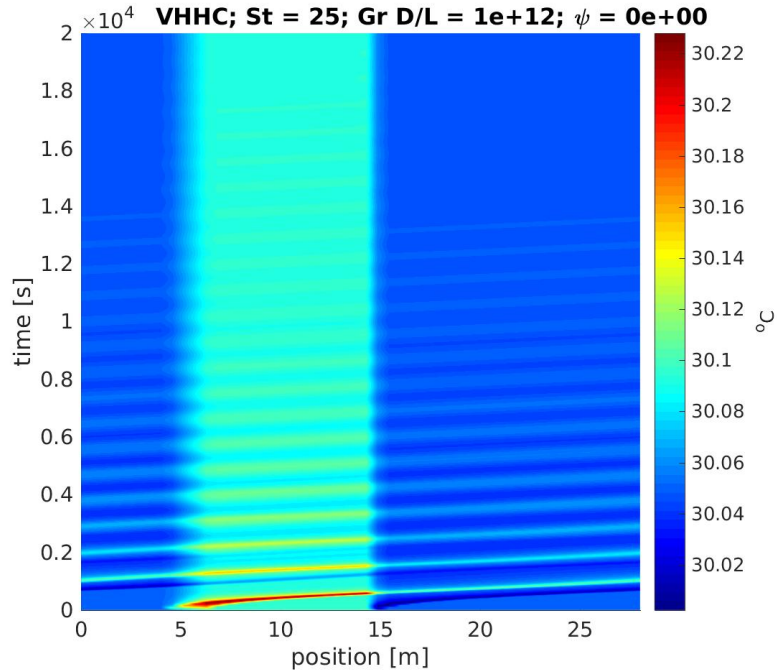


Figure A.16: Space-time chart for temperature in VHHC loop, $St = 25$, $Gr D/L = 10^{12}$, $\psi = 0$.

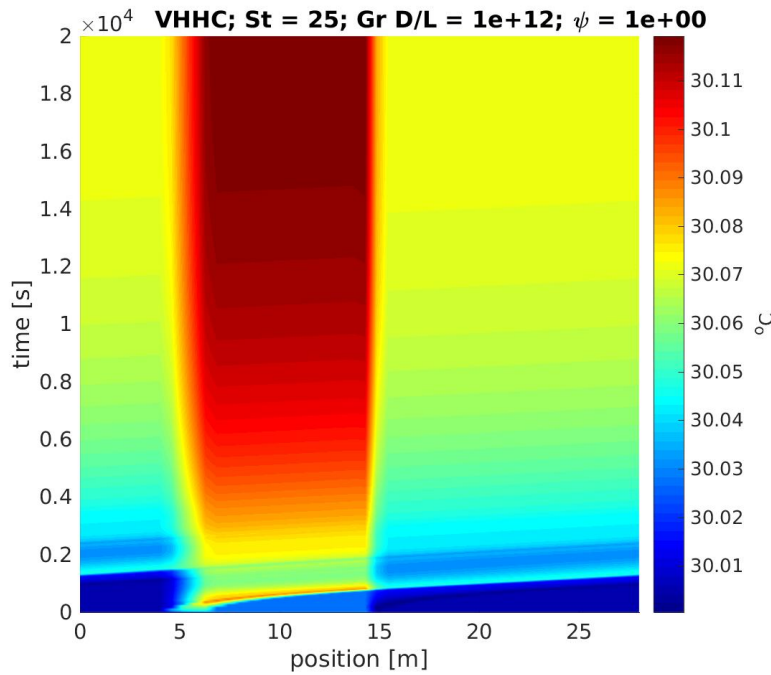


Figure A.17: Space-time chart for temperature in VHHC loop, $St = 25$, $Gr D/L = 10^{12}$, $\psi = 1$.

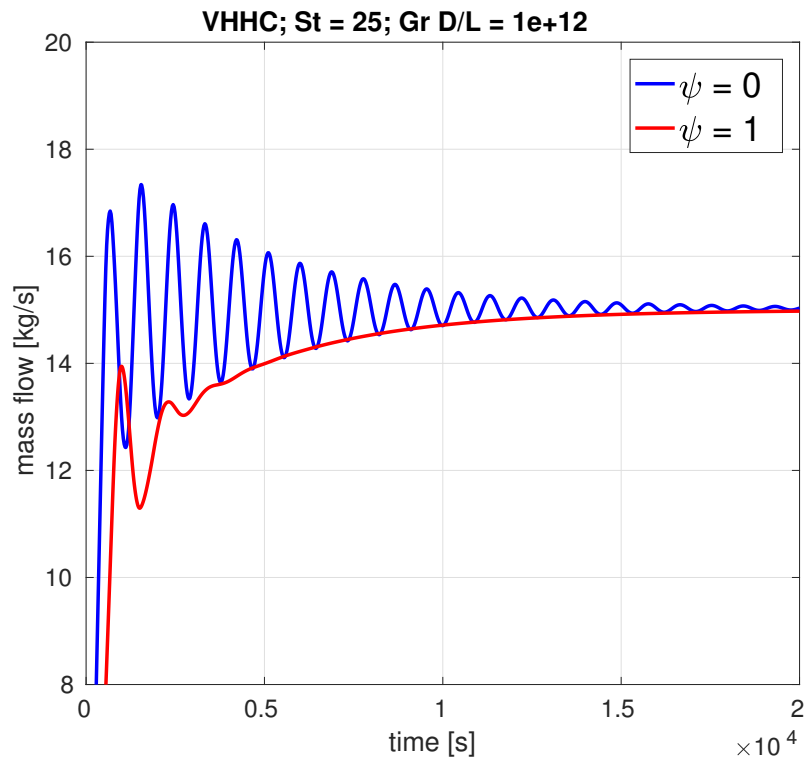


Figure A.18: Comparison of time series for mass flow rate using $\psi = 0$ and $\psi = 1$, in VHHC loop, $St = 25$, $Gr D/L = 10^{12}$.

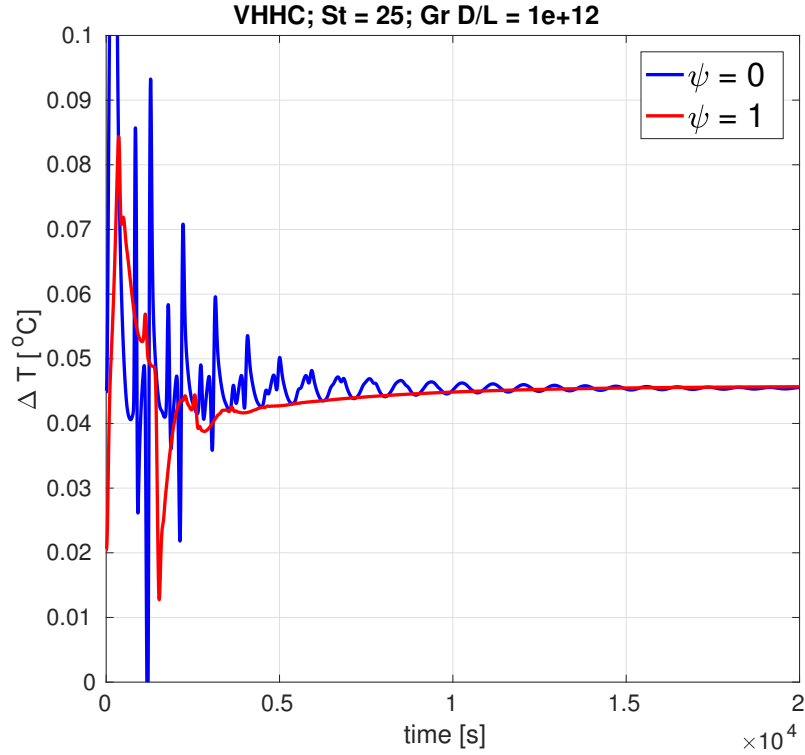


Figure A.19: Comparison of time series for temperature difference across heater using $\psi = 0$ and $\psi = 1$, in VHHC loop, $\text{St} = 25$, $\text{Gr } D/L = 10^{12}$.

A.1.4 VHVC

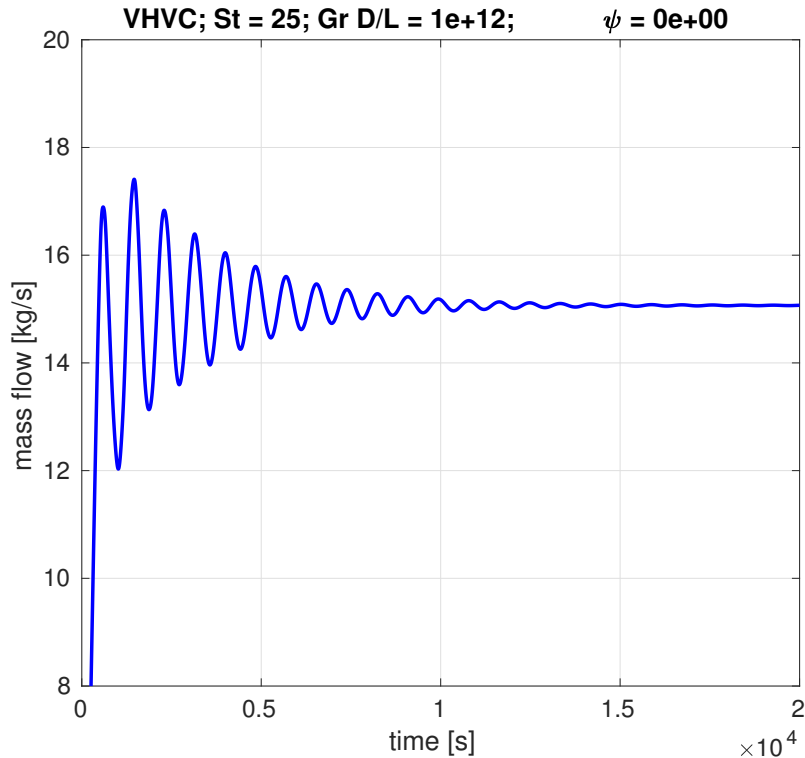


Figure A.20: Transient mass flow rate for VHVC loop, $\text{St} = 25$, $\text{Gr } D/L = 10^{12}$, $\psi = 0$.

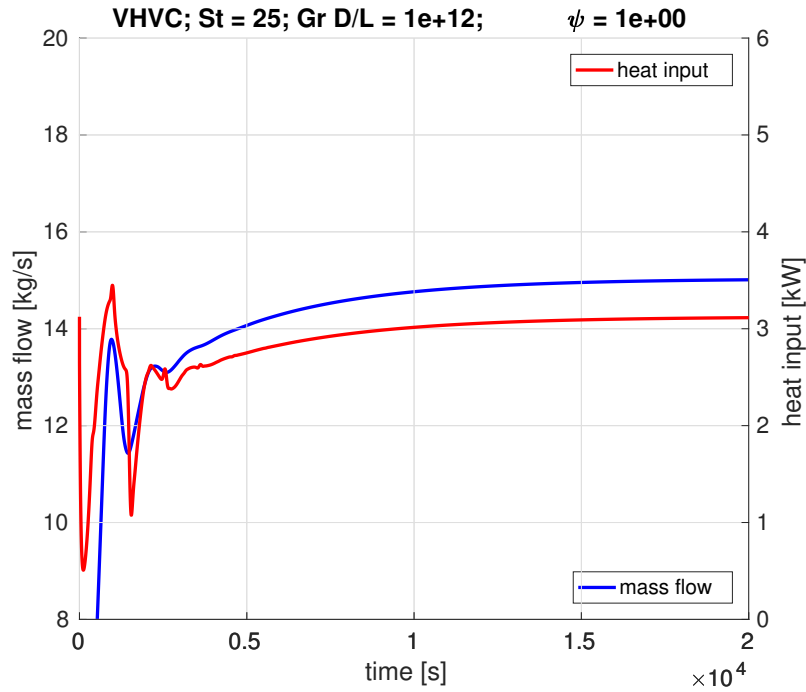


Figure A.21: Transient mass flow rate for VHVC loop, $St = 25$, $Gr D/L = 10^{12}$, $\psi = 1$.

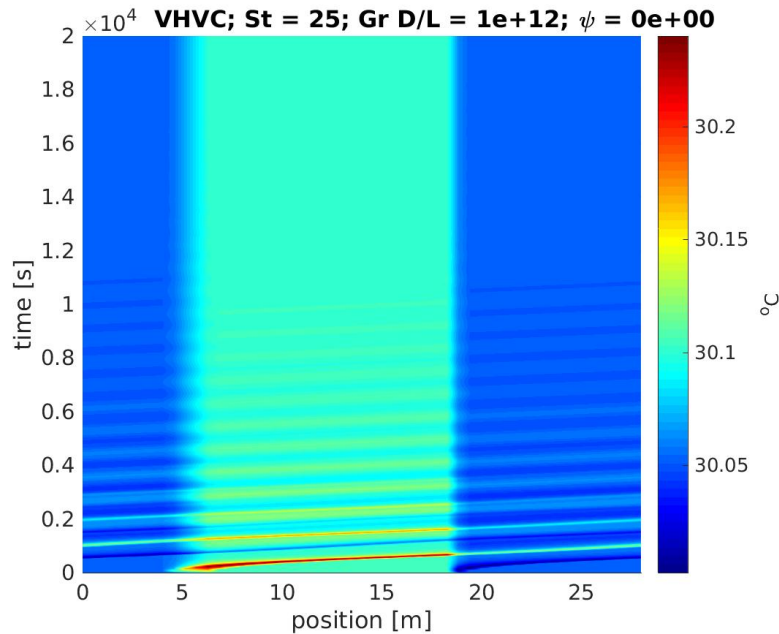


Figure A.22: Space-time chart for temperature in VHVC loop, $St = 25$, $Gr D/L = 10^{12}$, $\psi = 0$.

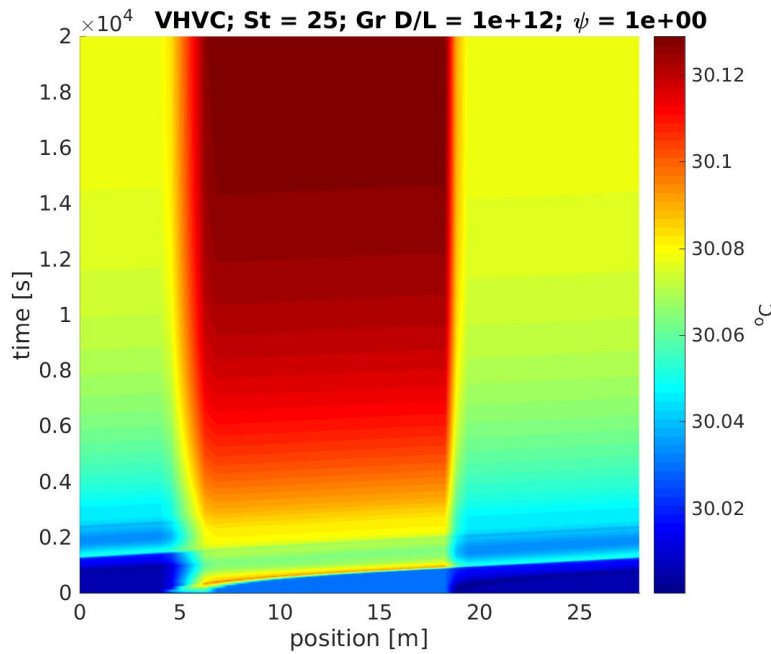


Figure A.23: Space-time chart for temperature in VHVC loop, $St = 25$, $Gr D/L = 10^{12}$, $\psi = 1$.

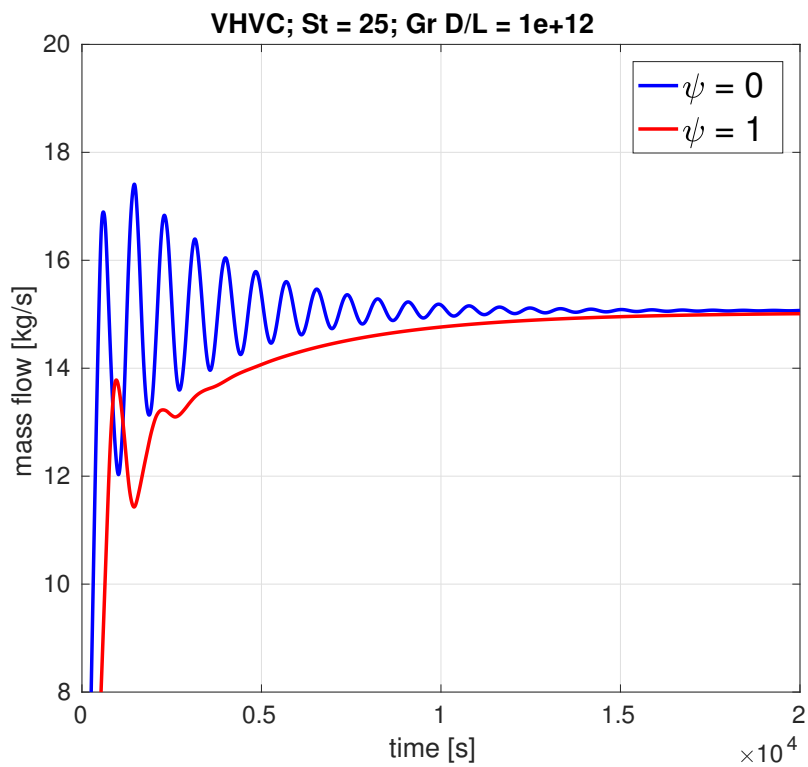


Figure A.24: Comparison of time series for mass flow rate using $\psi = 0$ and $\psi = 1$, in VHVC loop, $St = 25$, $Gr D/L = 10^{12}$.

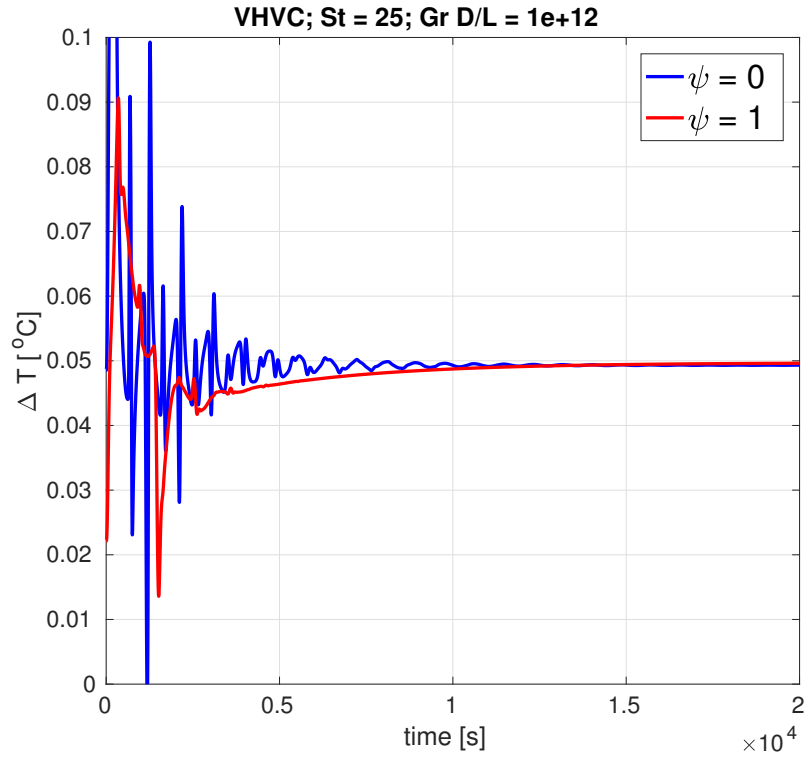


Figure A.25: Comparison of time series for temperature difference across heater using $\psi = 0$ and $\psi = 1$, in VHVC loop, $\text{St} = 25$, $\text{Gr } D/L = 10^{12}$.

A.2 Unstable regimes without pool, stable with pool

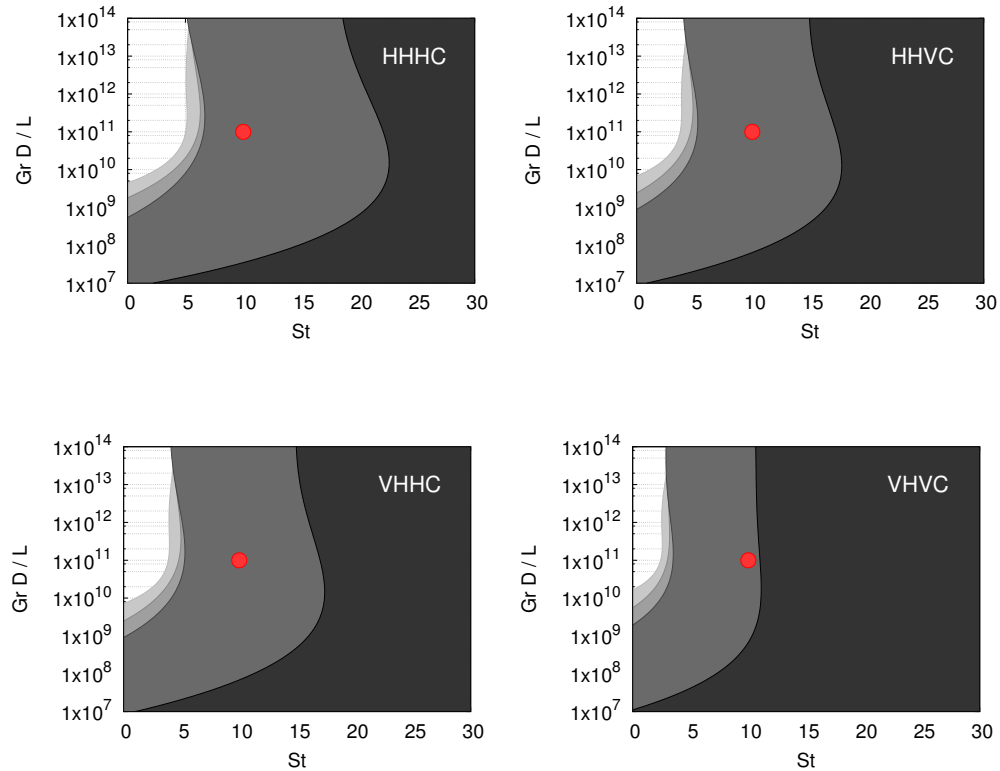


Figure A.26: Points selected in stability maps for simulation loop transients.

Table A.4: Operating, numerical and geometrical data of HHHC 800 mm diameter loop considered for simulation of the operating points $\text{St} = 10$ and $\text{Gr } D/L = 10^{11}$, which, according to the results of previous chapter (cf. figs. 4.2 to 4.5), is unstable for $\psi = 0$ (without pool) but is stable $\psi = 1$ (with pool).

L_h [m]	2.000
L_c [m]	0.800
local losses	1.8
mesh nodes	750
CFL	1
loop internal pressure	200 bar
$\text{Gr } D/L$	10^{12}
St	25
T_s [$^\circ\text{C}$]	30
perturbation	-100%
friction correlations:	Ruiz et al. [36]

A.2.1 HHHC

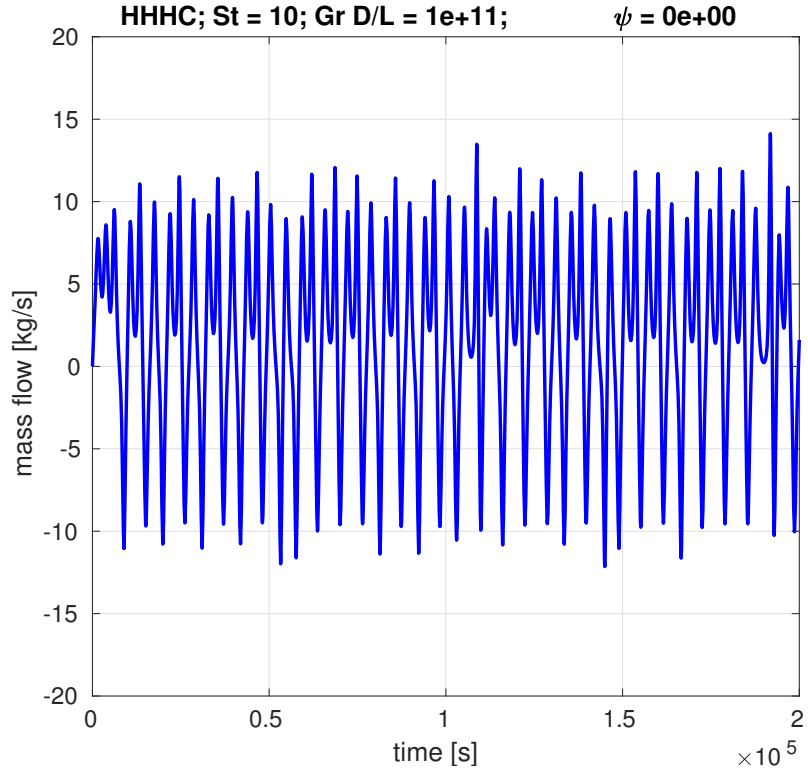


Figure A.27: Transient mass flow rate for HHHC loop, $\text{St} = 10$, $\text{Gr } D/L = 10^{11}$, $\psi = 0$.

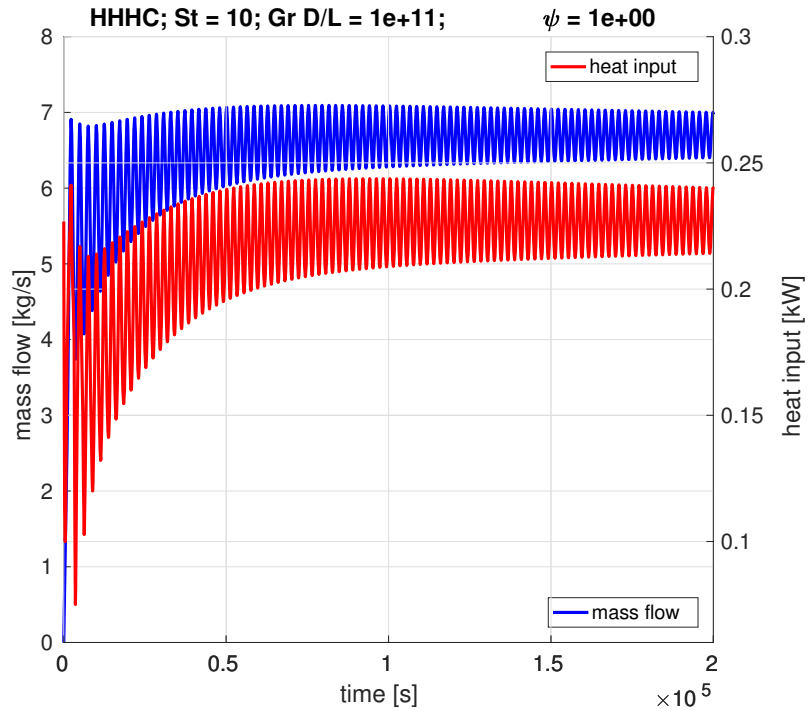


Figure A.28: Transient mass flow rate for HHHC loop, $\text{St} = 10$, $\text{Gr } D/L = 10^{11}$, $\psi = 1$.

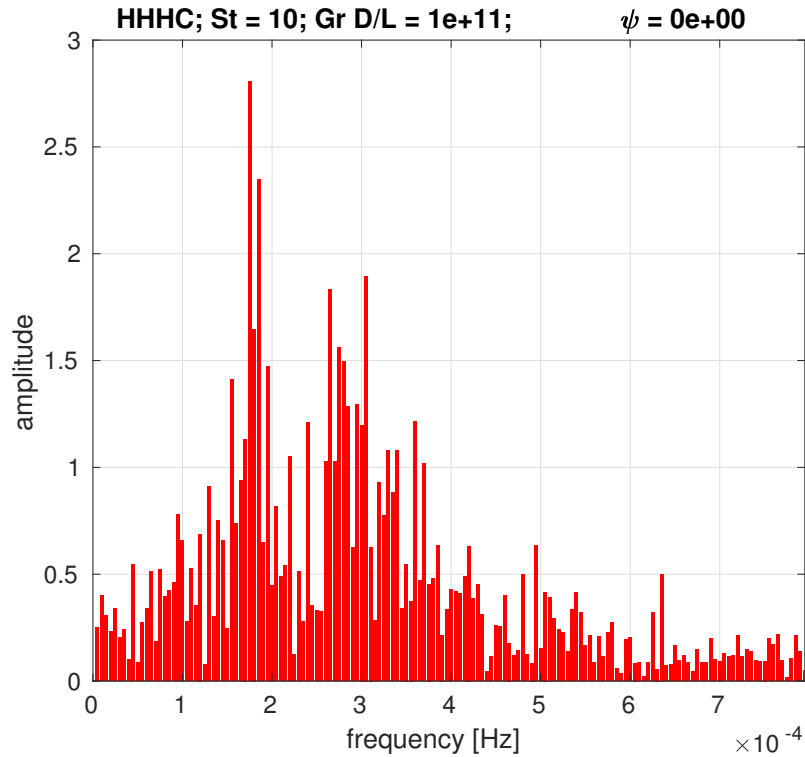


Figure A.29: Frequency domain of mass flow for HHHC loop, $St = 10$, $Gr D/L = 10^{11}$, $\psi = 0$.

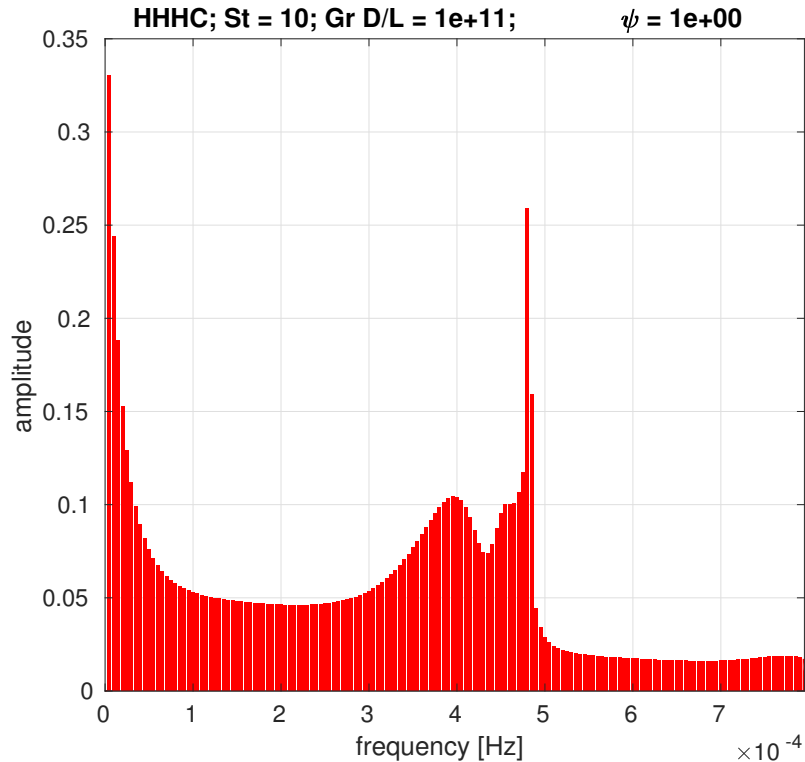


Figure A.30: Frequency domain of mass flow for HHHC loop, $St = 10$, $Gr D/L = 10^{11}$, $\psi = 1$.

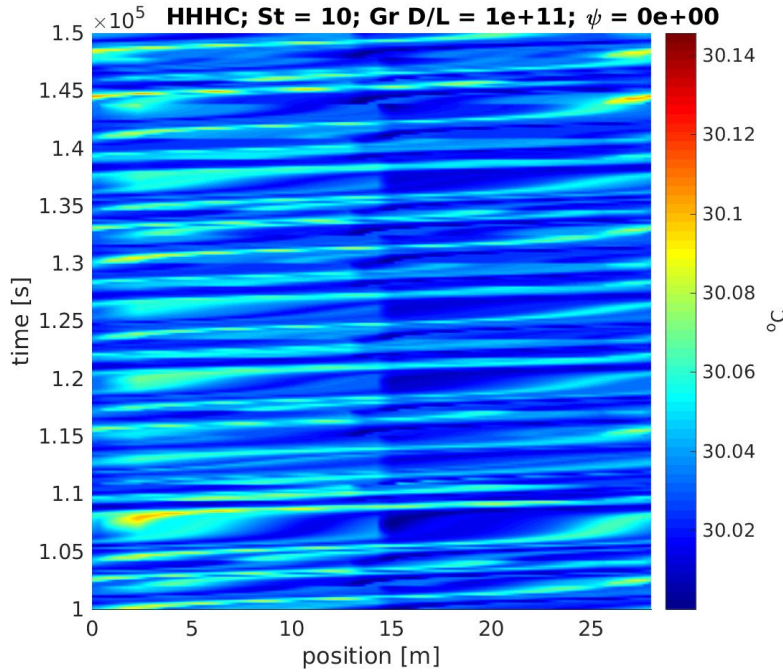


Figure A.31: Space-time chart for temperature in HHHC loop, $\text{St} = 10$, $\text{Gr } D/L = 10^{11}$, $\psi = 0$.

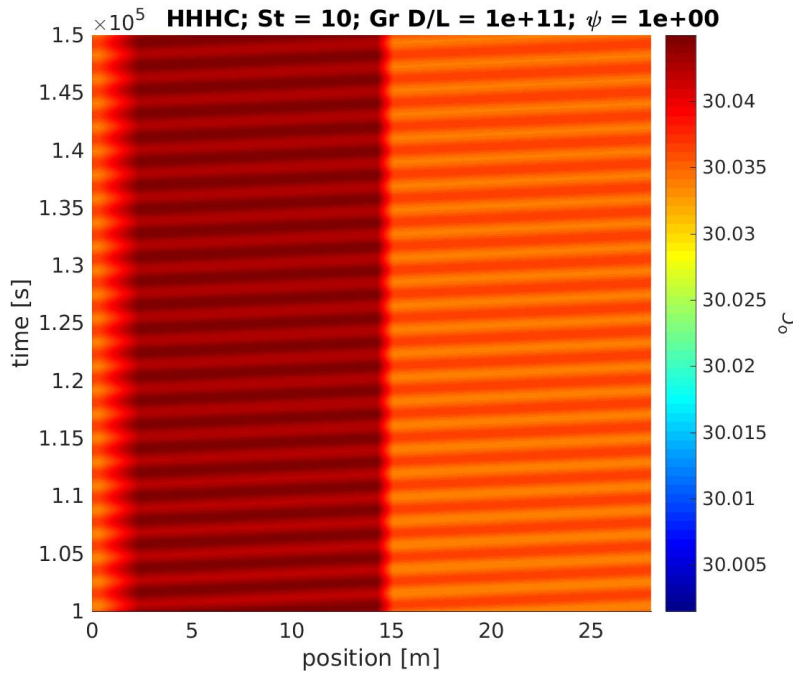


Figure A.32: Space-time chart for temperature in HHHC loop, $\text{St} = 10$, $\text{Gr } D/L = 10^{11}$, $\psi = 1$.

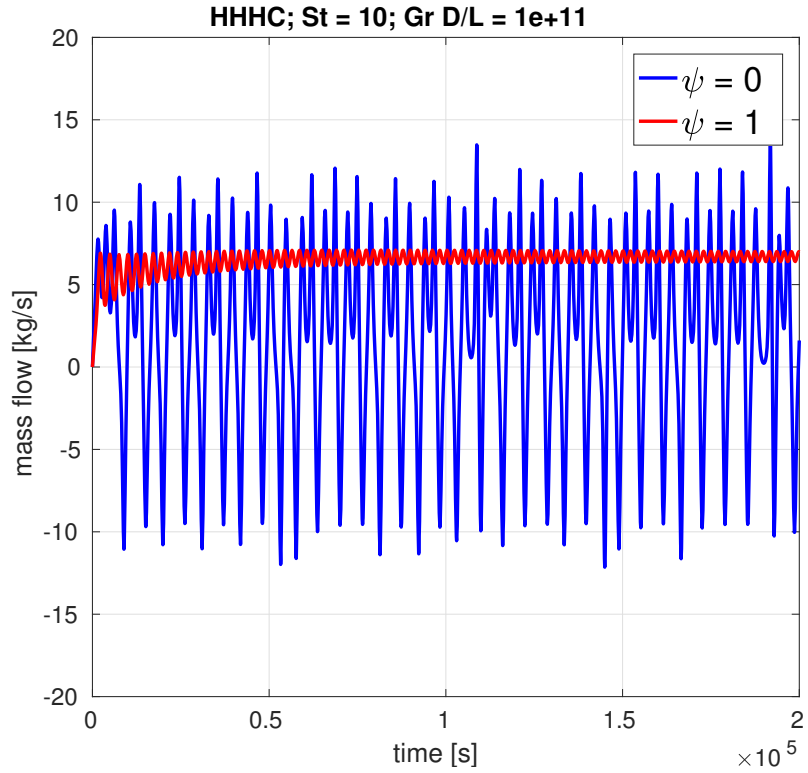


Figure A.33: Comparison of time series for mass flow rate using $\psi = 0$ and $\psi = 1$, in HHHC loop, $St = 10$, $Gr D/L = 10^{11}$.

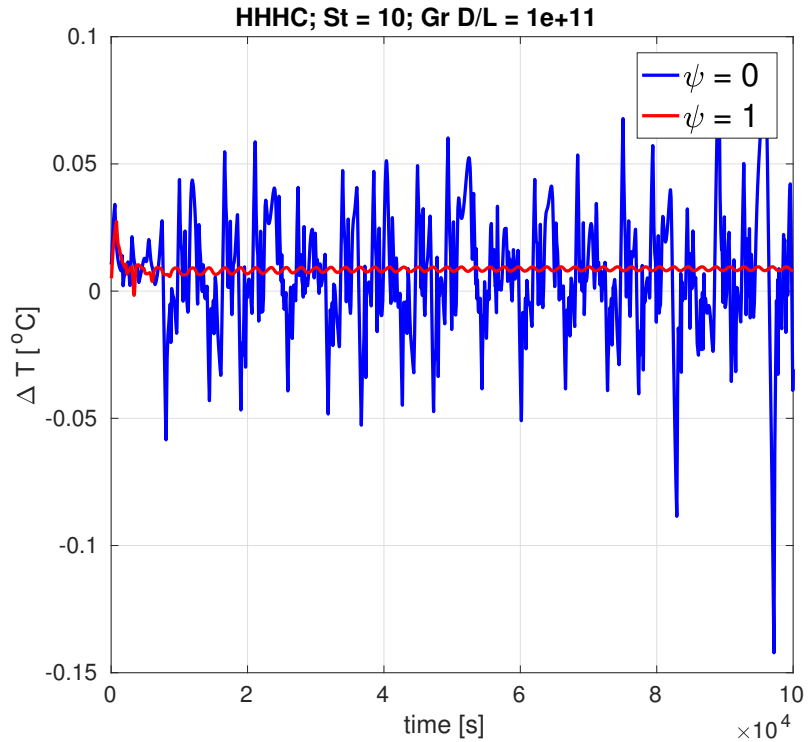


Figure A.34: Comparison of time series for temperature difference across heater using $\psi = 0$ and $\psi = 1$, in HHHC loop, $St = 10$, $Gr D/L = 10^{11}$.

A.2.2 HHVC

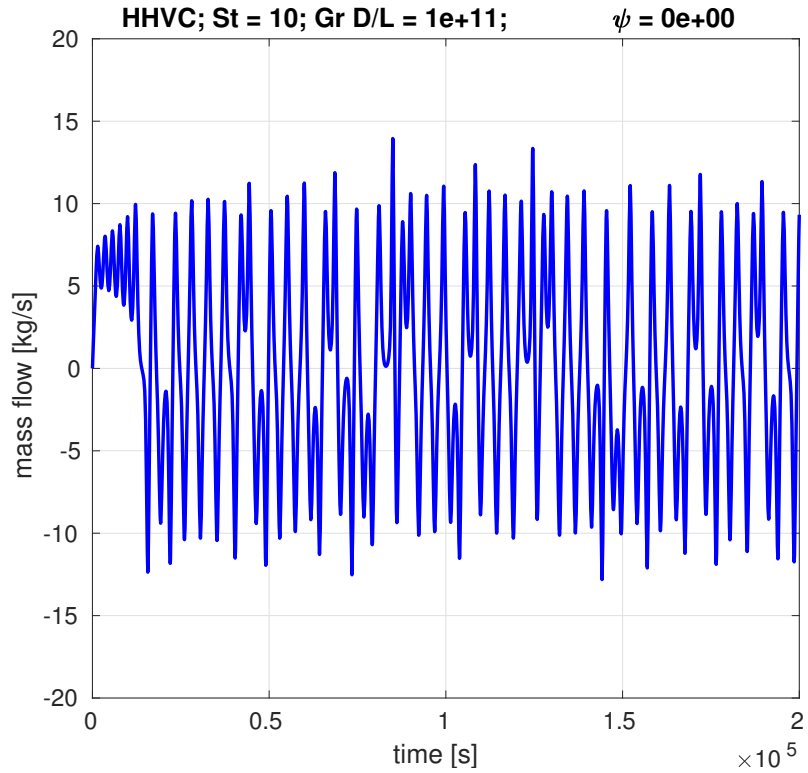


Figure A.35: Transient mass flow rate for HHVC loop, $St = 10$, $Gr D/L = 10^{11}$, $\psi = 0$.

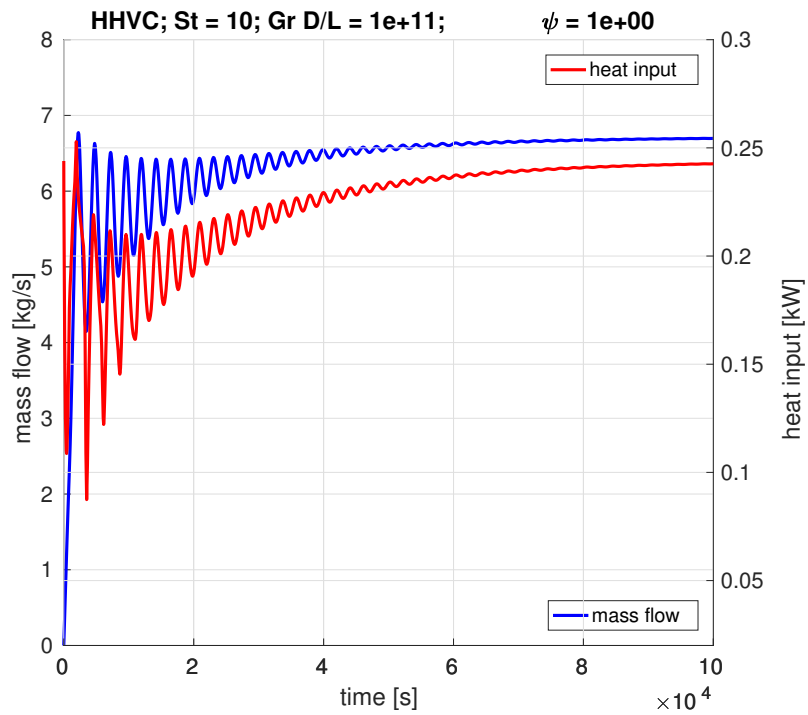


Figure A.36: Transient mass flow rate for HHVC loop, $St = 10$, $Gr D/L = 10^{11}$, $\psi = 1$.

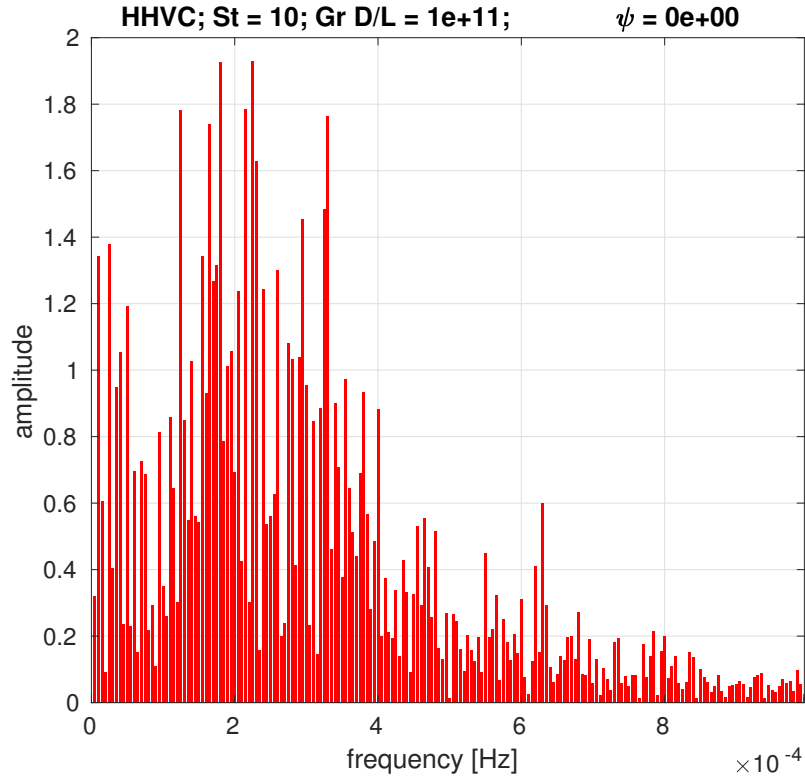


Figure A.37: Frequency domain of mass flow for HHVC loop, $St = 10$, $Gr D/L = 10^{11}$, $\psi = 0$.

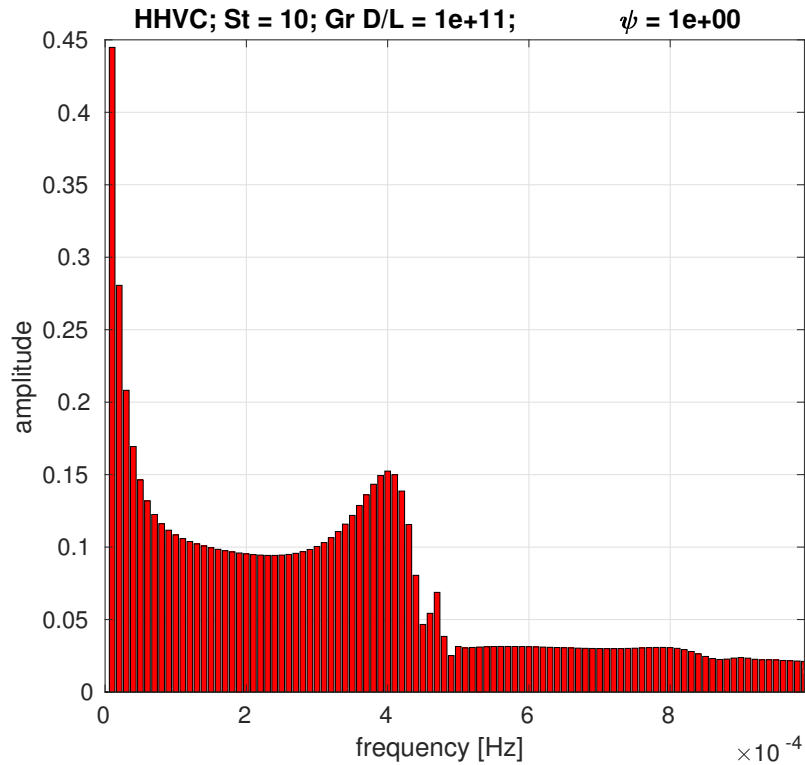


Figure A.38: Frequency domain of mass flow for HHVC loop, $St = 10$, $Gr D/L = 10^{11}$, $\psi = 1$.

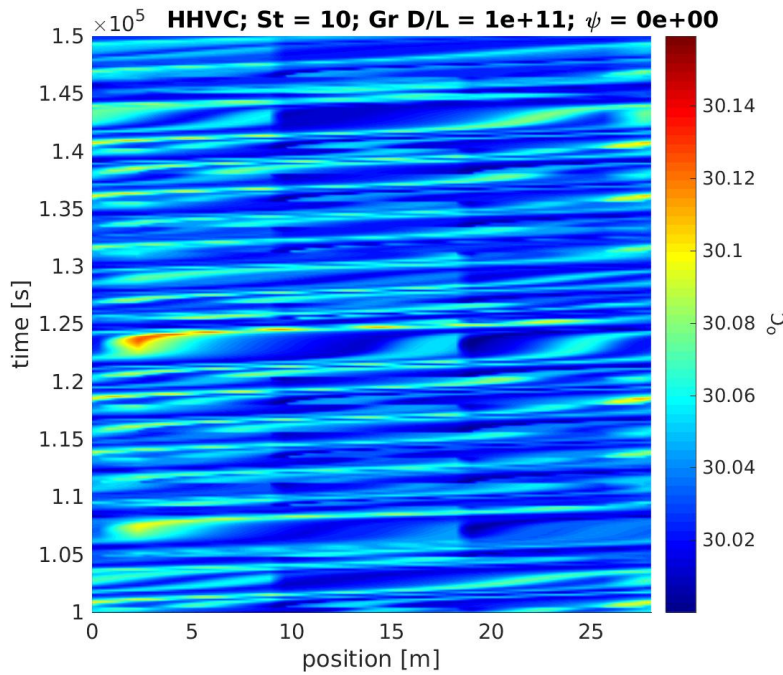


Figure A.39: Space-time chart for temperature in HHVC loop, $St = 10$, $Gr D/L = 10^{11}$, $\psi = 0$.

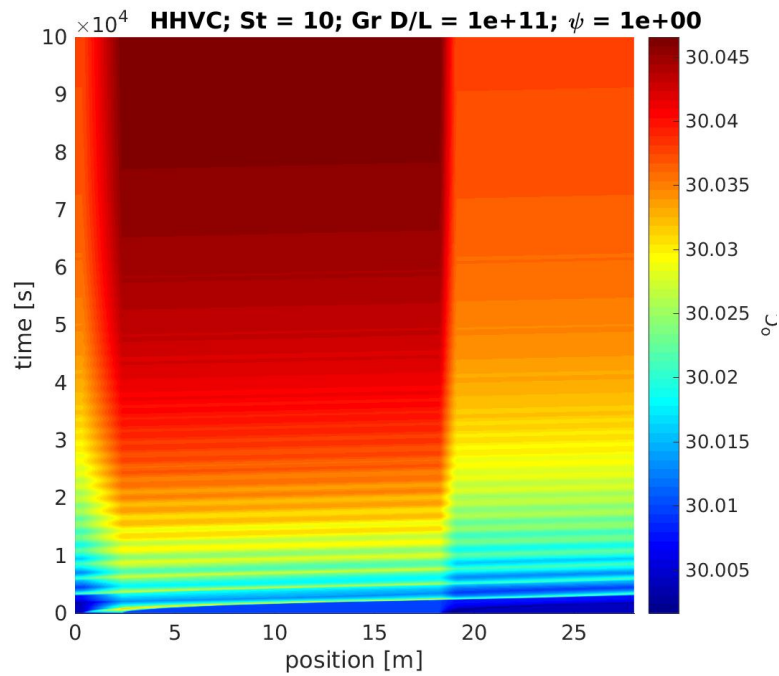


Figure A.40: Space-time chart for temperature in HHVC loop, $St = 10$, $Gr D/L = 10^{11}$, $\psi = 1$.

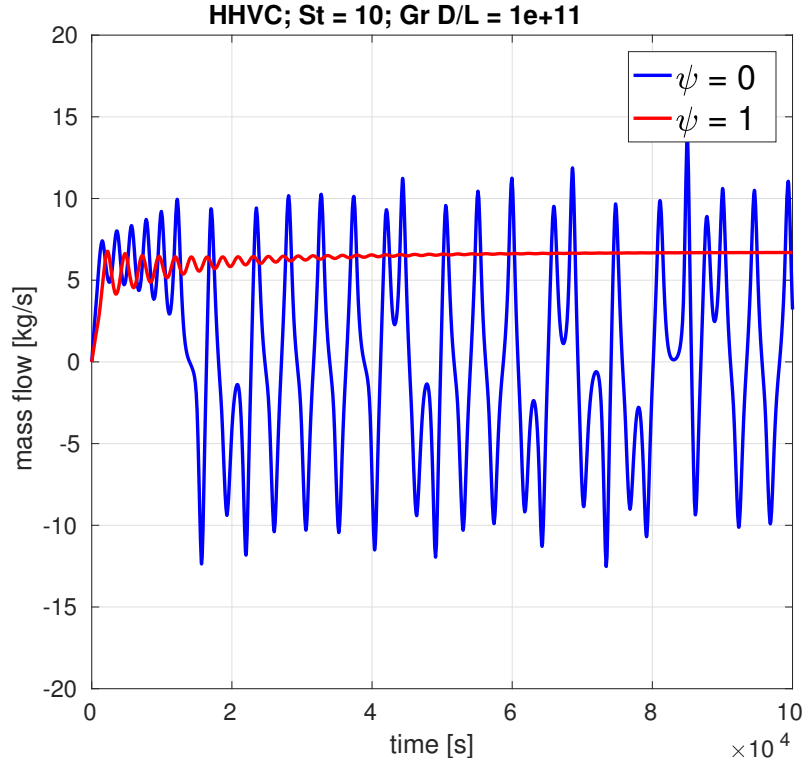


Figure A.41: Comparison of time series for mass flow rate using $\psi = 0$ and $\psi = 1$, in HHVC loop, $St = 10$, $Gr D/L = 10^{11}$.

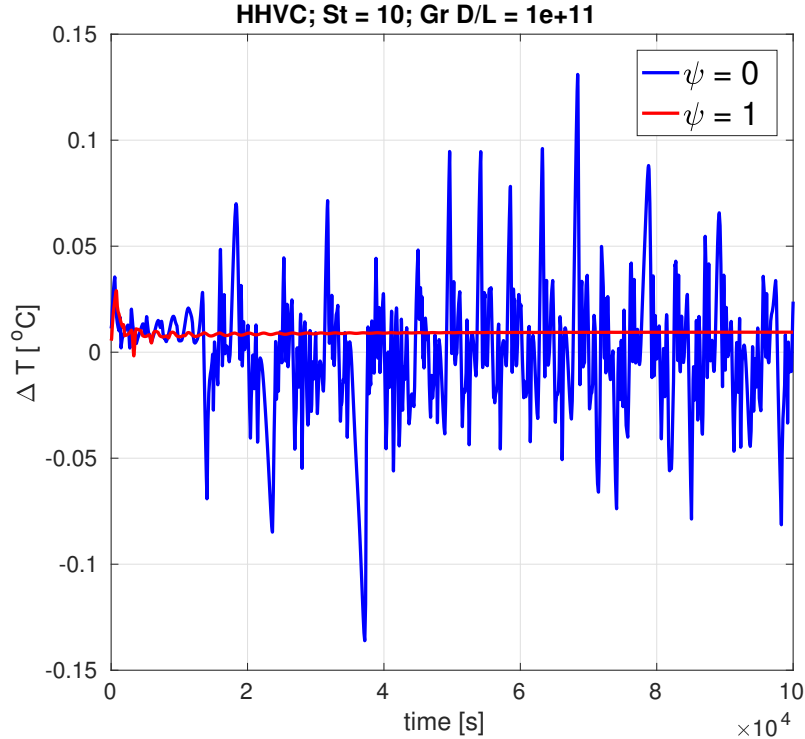


Figure A.42: Comparison of time series for temperature difference across heater using $\psi = 0$ and $\psi = 1$, in HHVC loop, $St = 10$, $Gr D/L = 10^{11}$.

A.2.3 VHHC

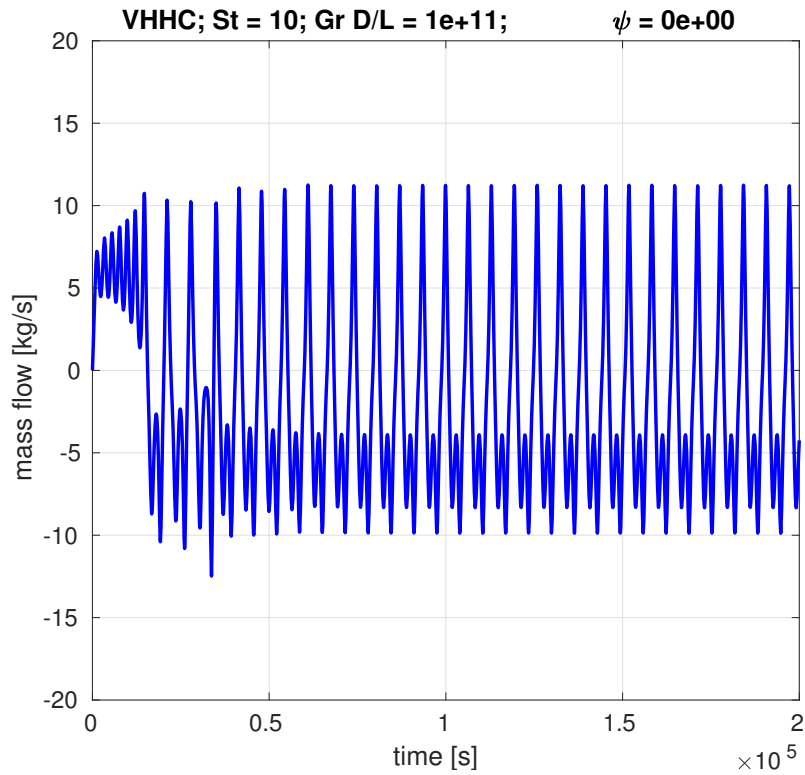


Figure A.43: Transient mass flow rate for VHHC loop, $St = 10$, $Gr D/L = 10^{11}$, $\psi = 0$.

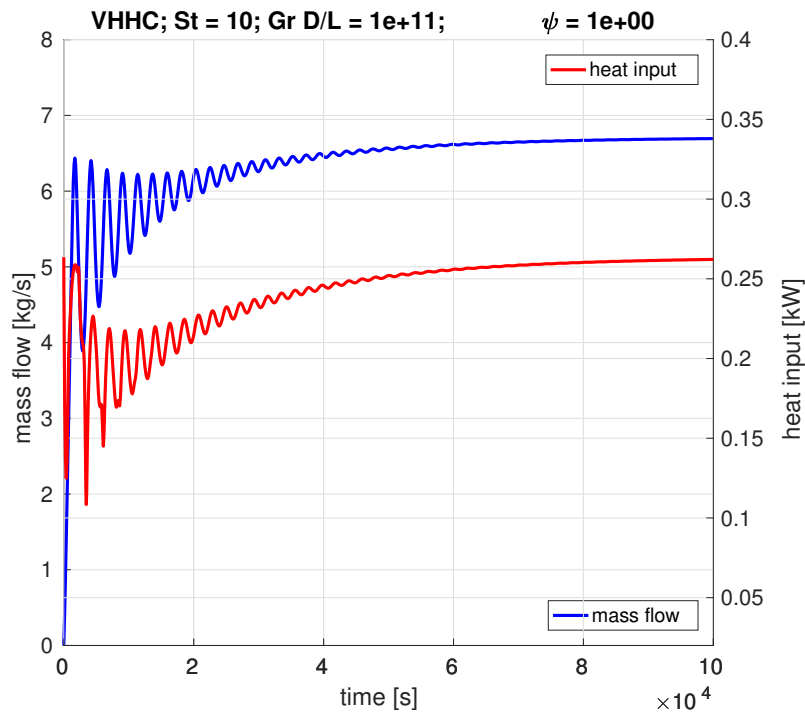


Figure A.44: Transient mass flow rate for VHHC loop, $St = 10$, $Gr D/L = 10^{11}$, $\psi = 1$.

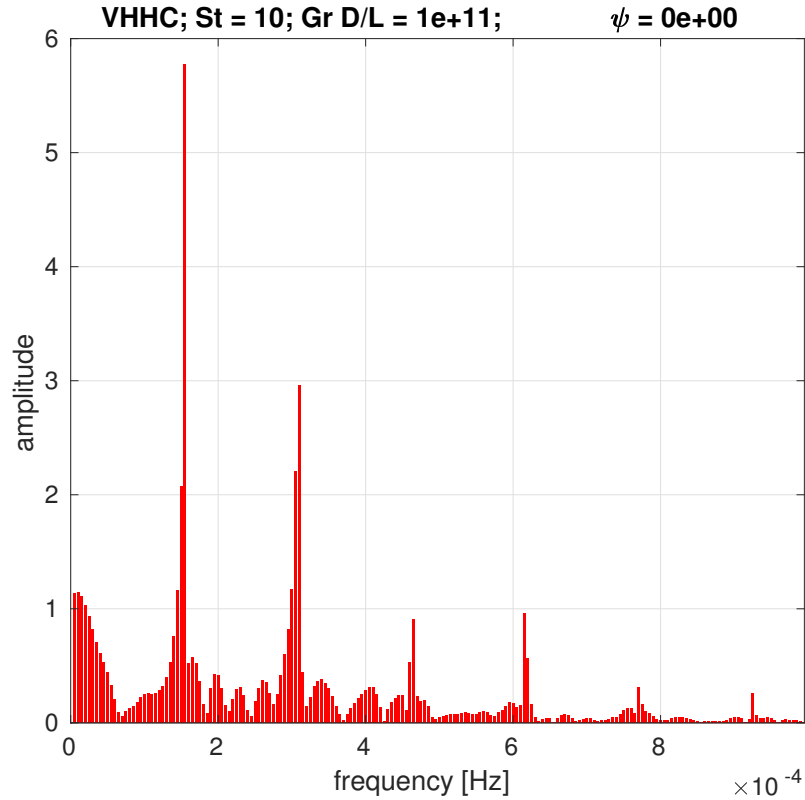


Figure A.45: Frequency domain of mass flow for VHHC loop, $St = 10$, $Gr D/L = 10^{11}$, $\psi = 0$.

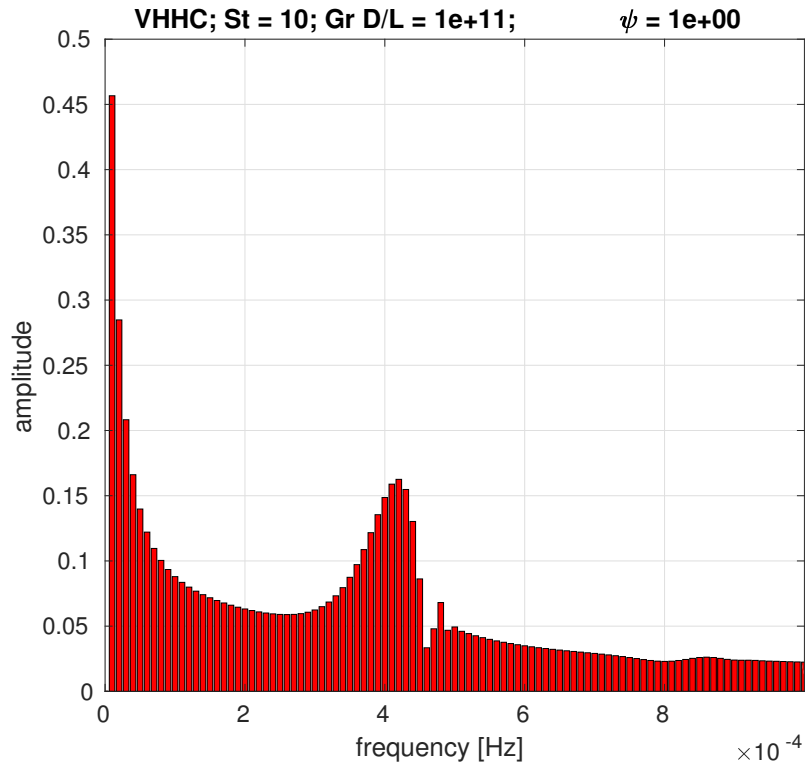


Figure A.46: Frequency domain of mass flow for VHHC loop, $St = 10$, $Gr D/L = 10^{11}$, $\psi = 1$.

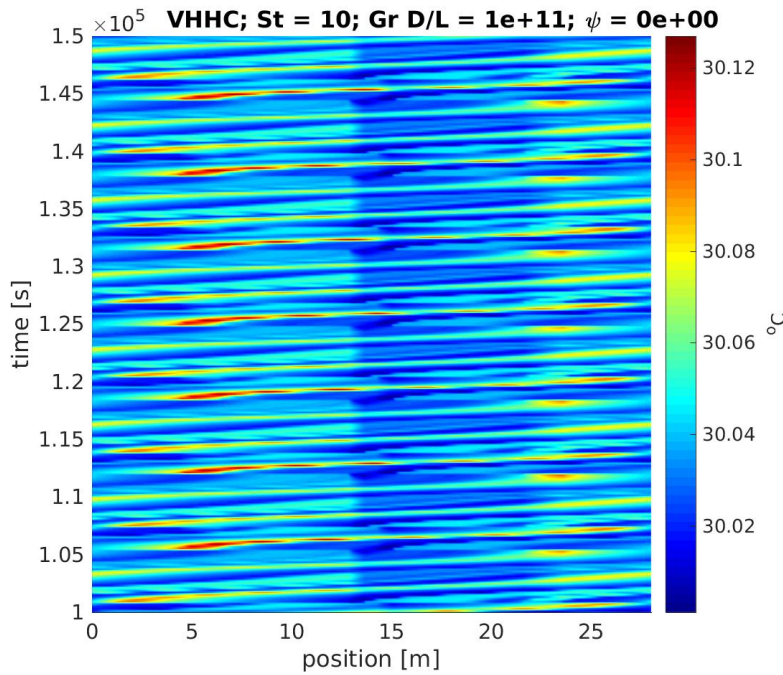


Figure A.47: Space-time chart for temperature in VHHC loop, $St = 10$, $Gr D/L = 10^{11}$, $\psi = 0$.

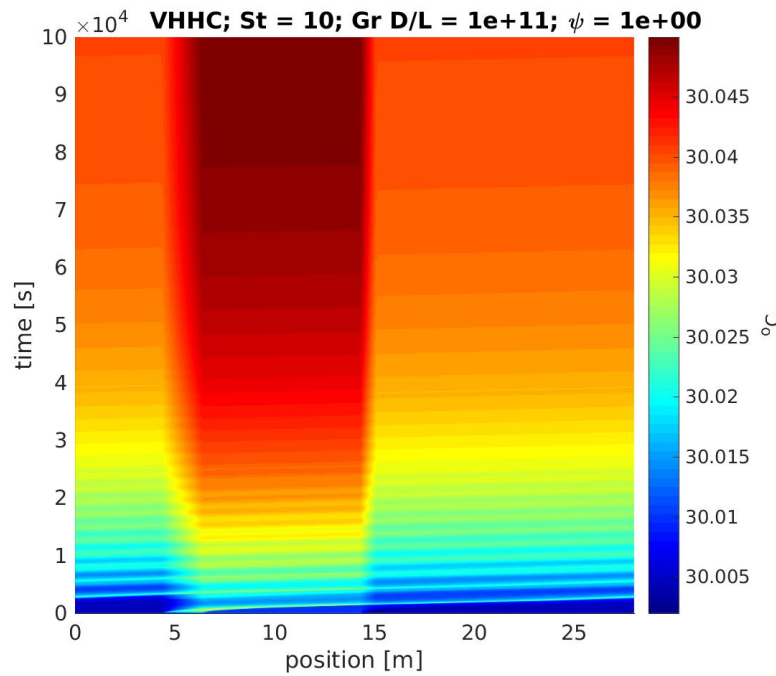


Figure A.48: Space-time chart for temperature in VHHC loop, $St = 10$, $Gr D/L = 10^{11}$, $\psi = 1$.

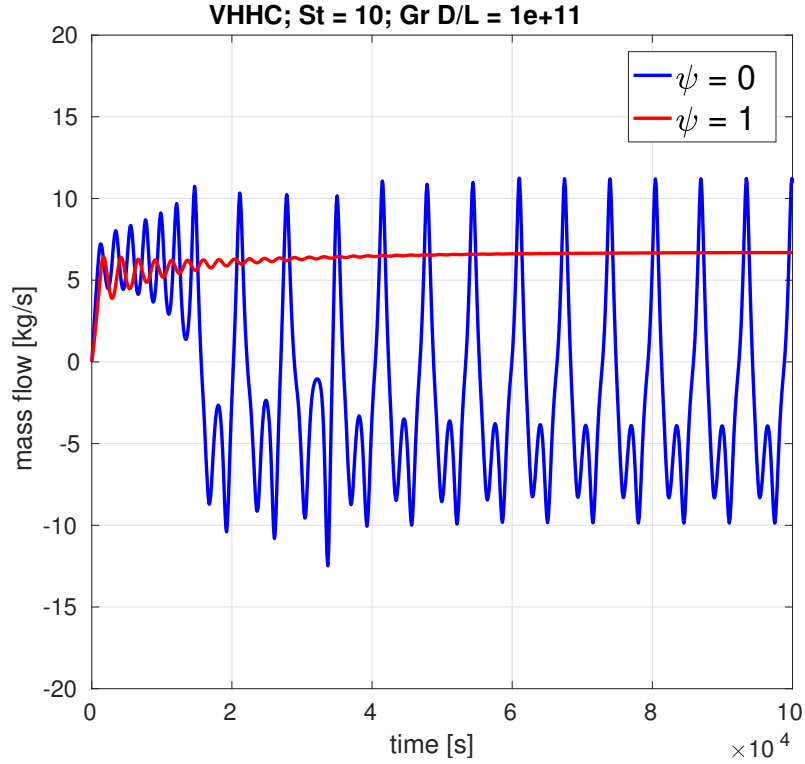


Figure A.49: Comparison of time series for mass flow rate using $\psi = 0$ and $\psi = 1$, in VHHC loop, $St = 10$, $Gr D/L = 10^{11}$.

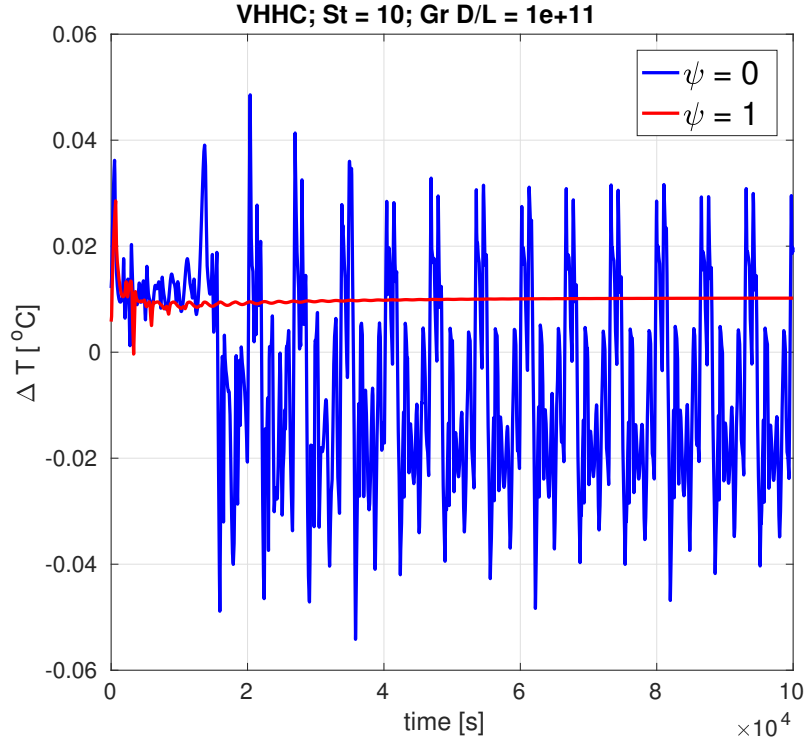


Figure A.50: Comparison of time series for temperature difference across heater using $\psi = 0$ and $\psi = 1$, in VHHC loop, $St = 10$, $Gr D/L = 10^{11}$.

A.2.4 VHVC

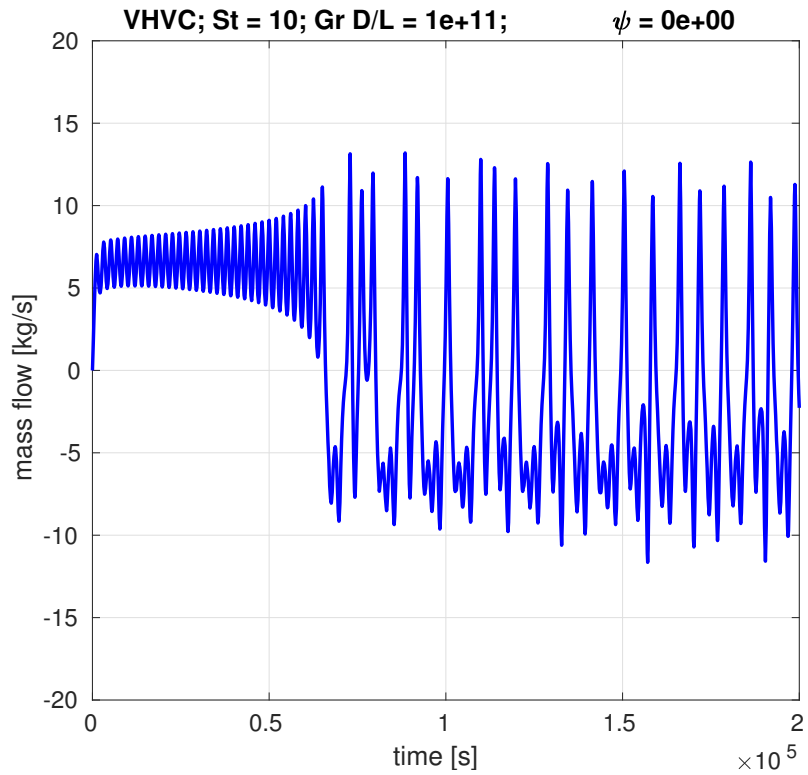


Figure A.51: Transient mass flow rate for VHVC loop, $St = 10$, $Gr D/L = 10^{11}$, $\psi = 0$.

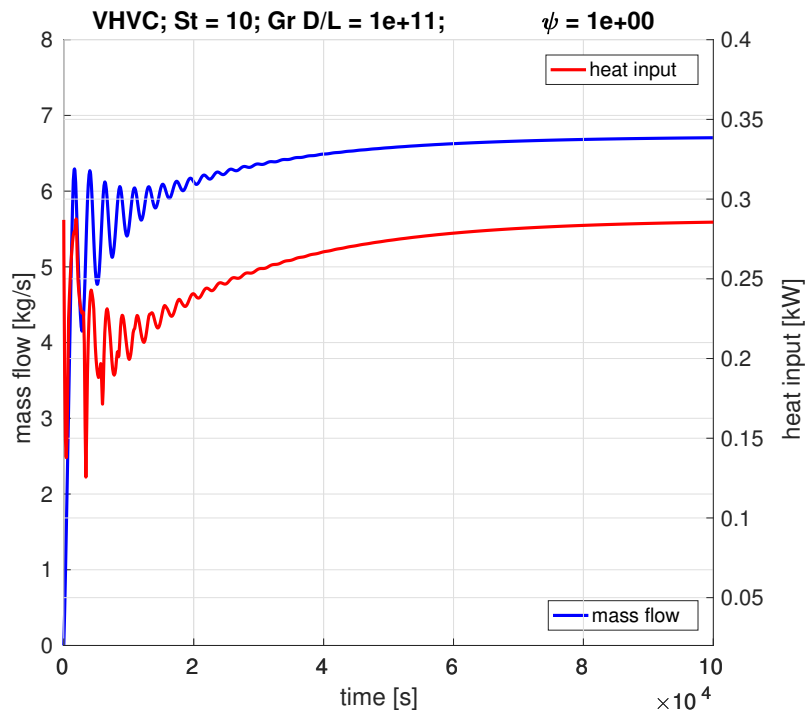


Figure A.52: Transient mass flow rate for VHVC loop, $St = 10$, $Gr D/L = 10^{11}$, $\psi = 1$.

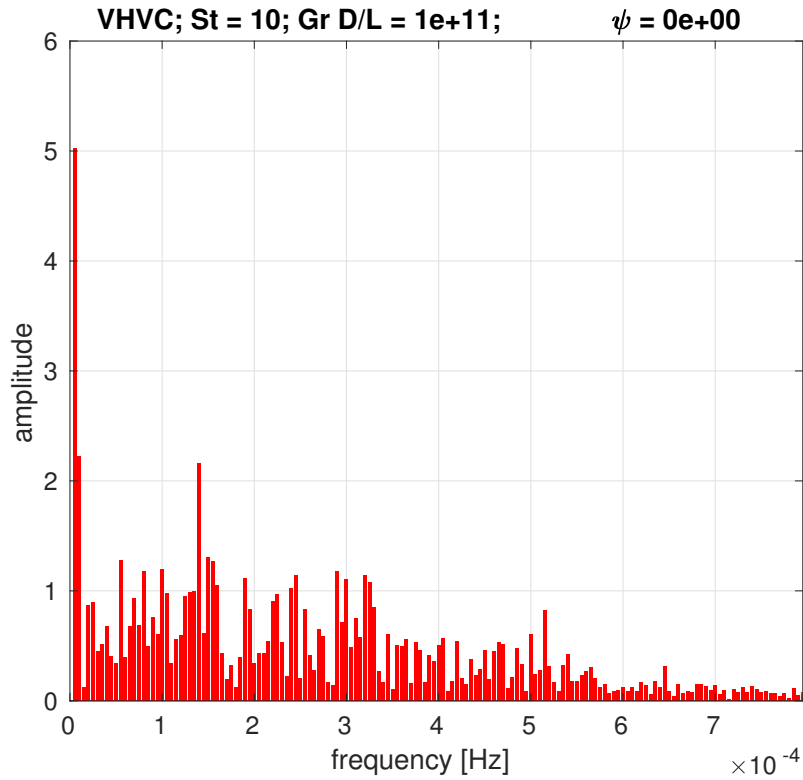


Figure A.53: Frequency domain of mass flow for VHVC loop, $St = 10$, $Gr D/L = 10^{11}$, $\psi = 0$.

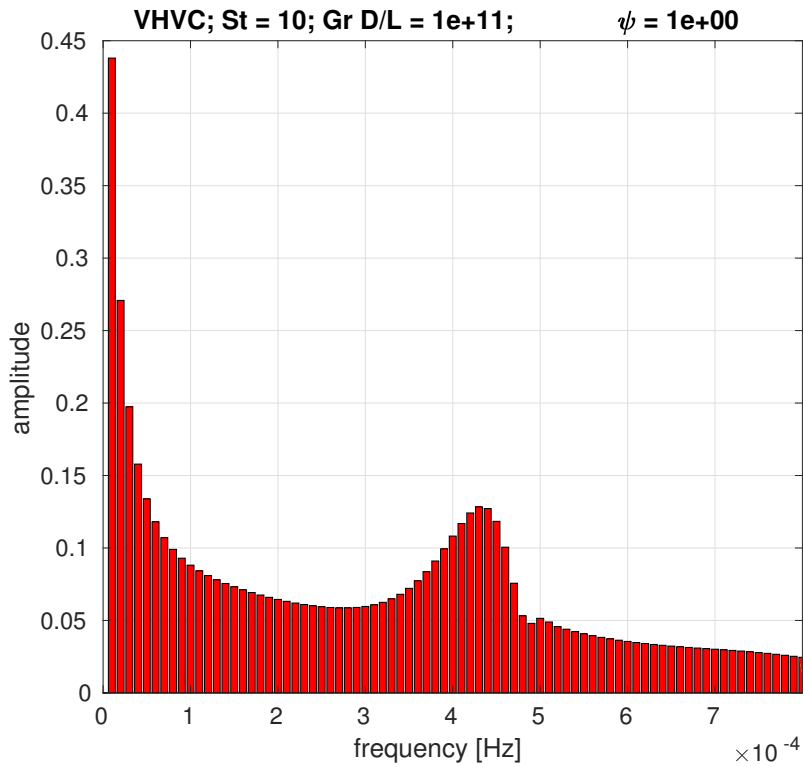


Figure A.54: Frequency domain of mass flow for VHVC loop, $St = 10$, $Gr D/L = 10^{11}$, $\psi = 1$.

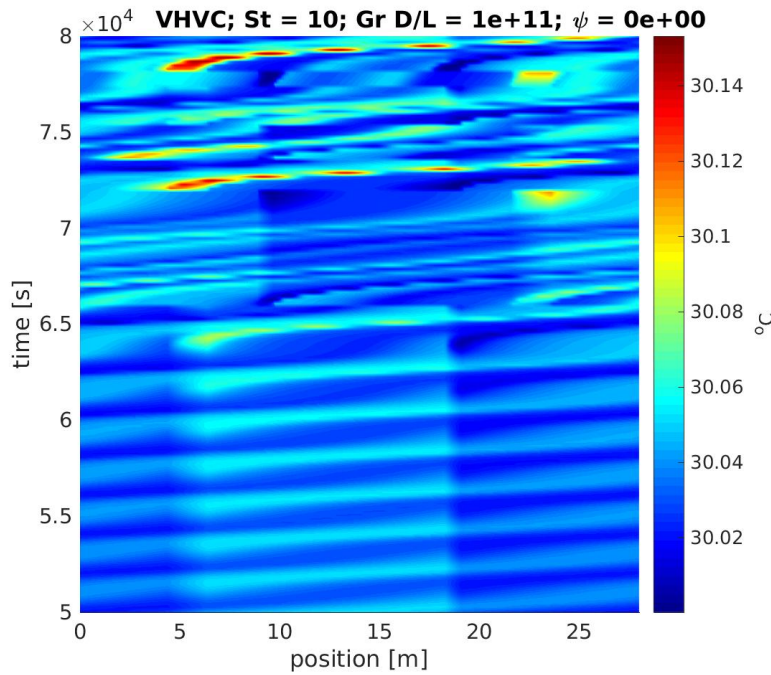


Figure A.55: Space-time chart for temperature in VHVC loop, $\text{St} = 10$, $\text{Gr } D/L = 10^{11}$, $\psi = 0$.

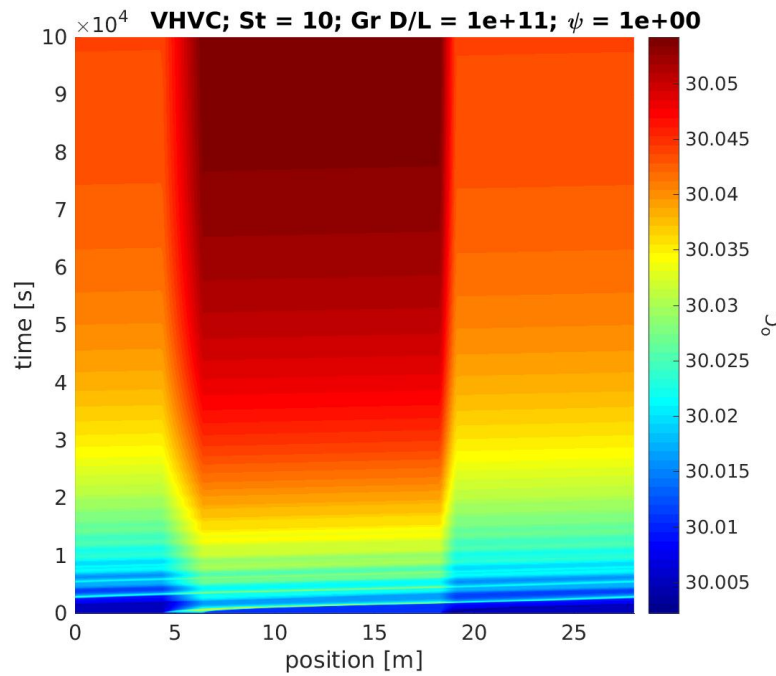


Figure A.56: Space-time chart for temperature in VHVC loop, $\text{St} = 10$, $\text{Gr } D/L = 10^{11}$, $\psi = 1$.

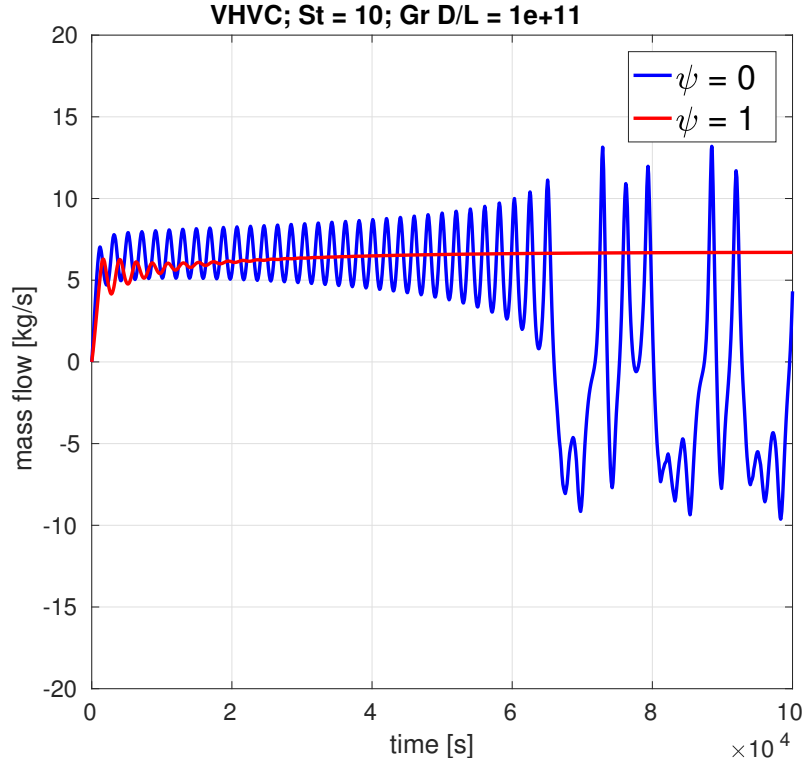


Figure A.57: Comparison of time series for mass flow rate using $\psi = 0$ and $\psi = 1$, in VHVC loop, $St = 10$, $Gr D/L = 10^{11}$.

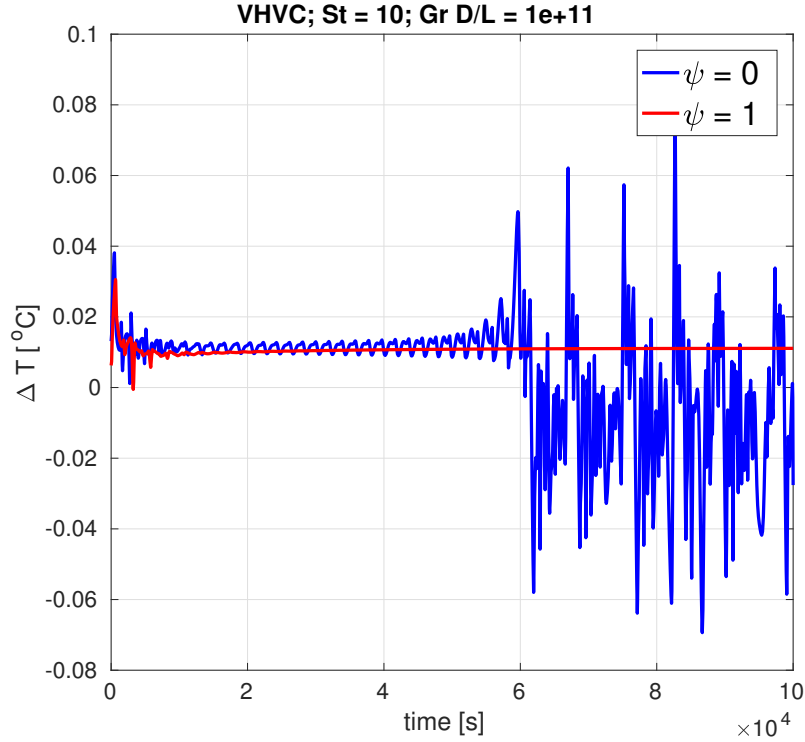


Figure A.58: Comparison of time series for temperature difference across heater using $\psi = 0$ and $\psi = 1$, in VHVC loop, $St = 10$, $Gr D/L = 10^{11}$.

A.3 Unstable regimes

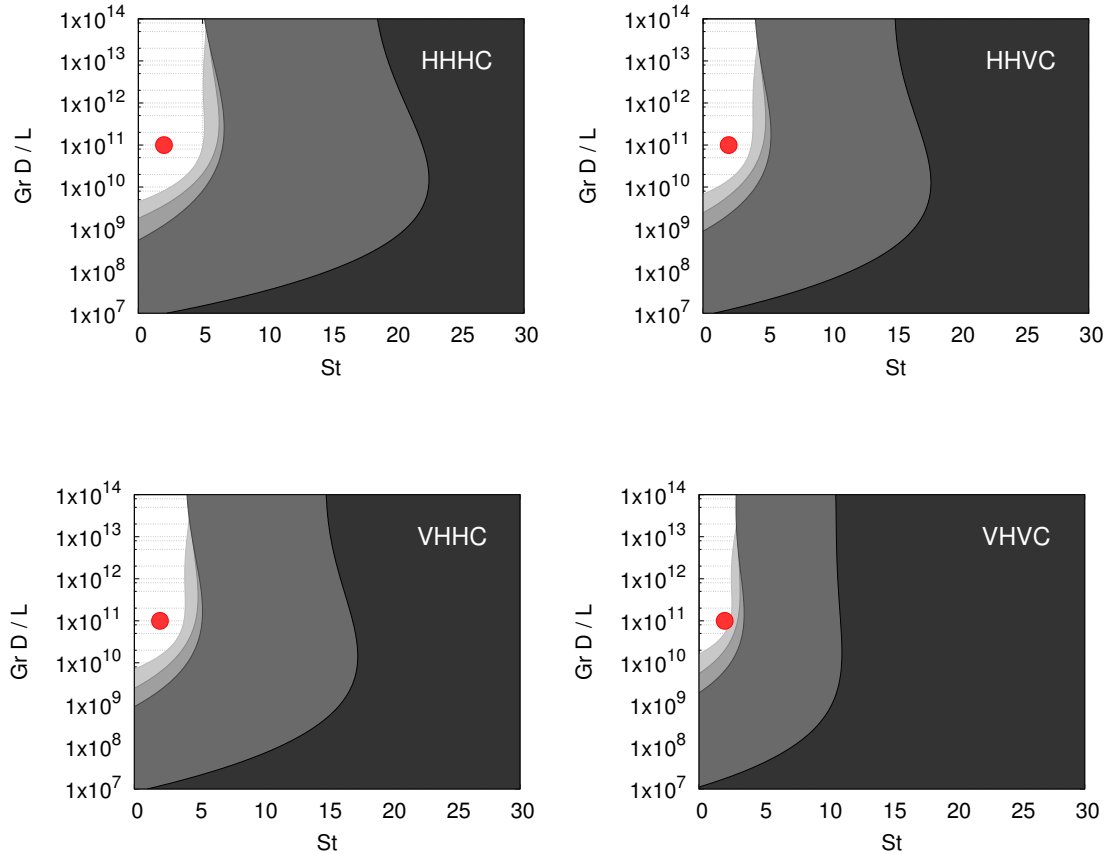


Figure A.59: Points selected in stability maps for simulation loop transients.

F

Table A.5: Operating, numerical and geometrical data of HHHC 800 mm diameter loop considered for simulation of the operating points $\text{St} = 2$ and $\text{Gr } D/L = 10^{11}$, unstable with and without pool according to results of previous chapter (cf. figs. 4.2 to 4.5).

L_h [m]	2.000
L_c [m]	0.800
local losses	1.8
mesh nodes	750
CFL	1
loop internal pressure	200 bar
$\text{Gr } D/L$	10^{12}
St	25
T_s [$^\circ\text{C}$]	30
perturbation	-100%
friction correlations:	Ruiz et al. [36]

A.3.1 HHHC

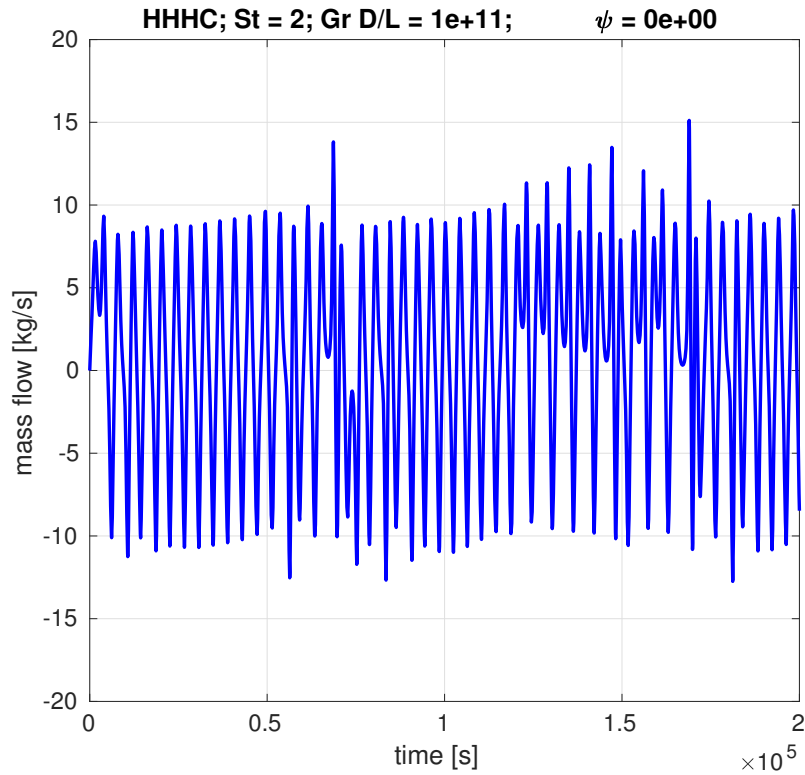


Figure A.60: Transient mass flow rate for HHHC loop, $St = 2$, $Gr D/L = 10^{11}$, $\psi = 0$.

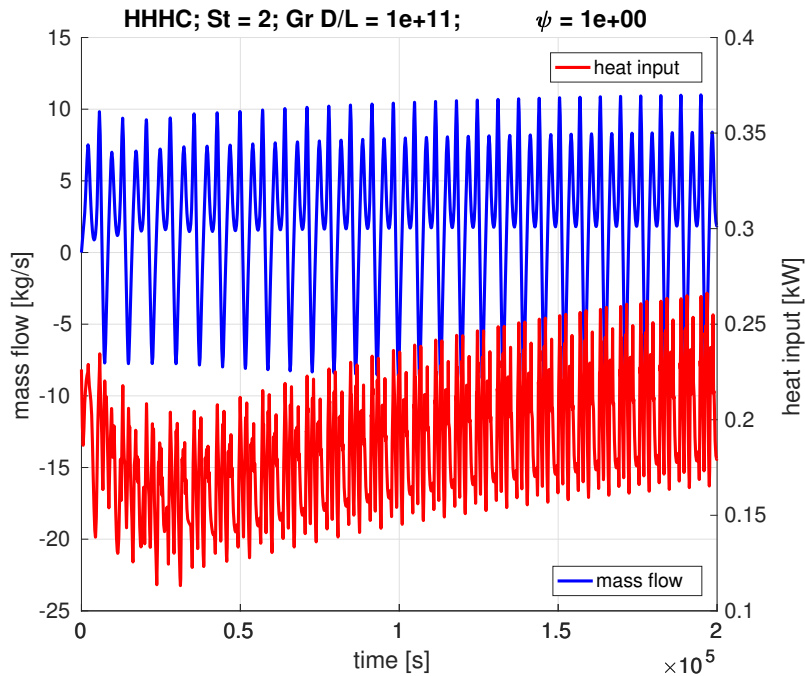


Figure A.61: Transient mass flow rate for HHHC loop, $St = 2$, $Gr D/L = 10^{11}$, $\psi = 1$.

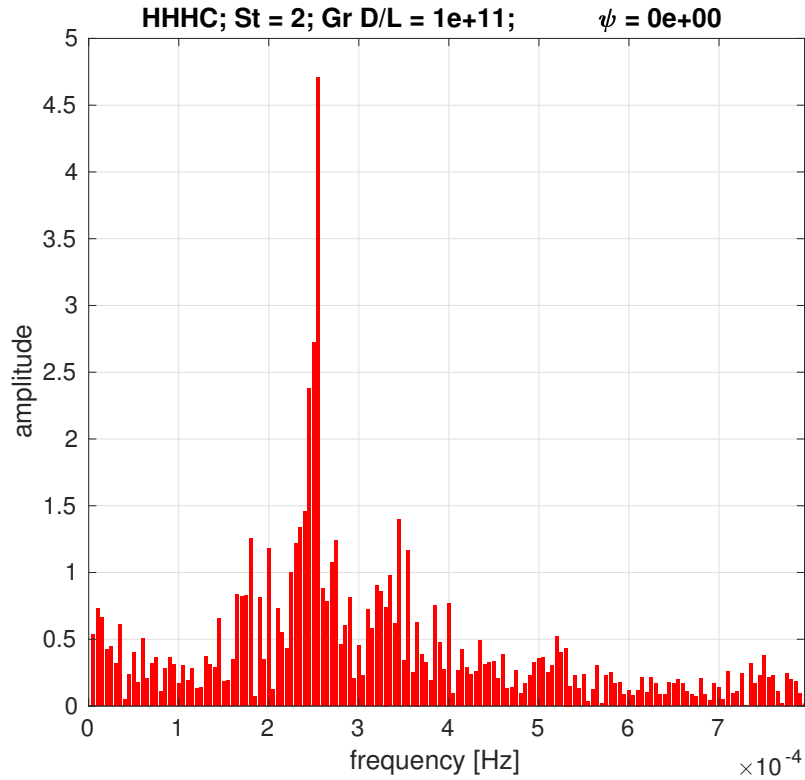


Figure A.62: Frequency domain of mass flow for HHHC loop, St = 2, Gr $D/L = 10^{11}$, $\psi = 0$.

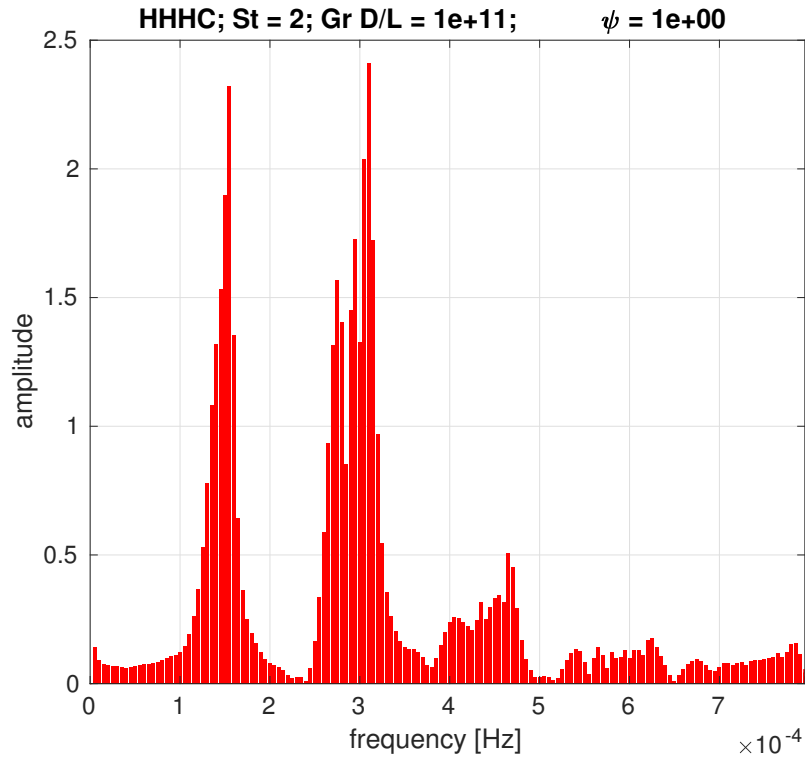


Figure A.63: Frequency domain of mass flow for HHHC loop, St = 2, Gr $D/L = 10^{11}$, $\psi = 1$.

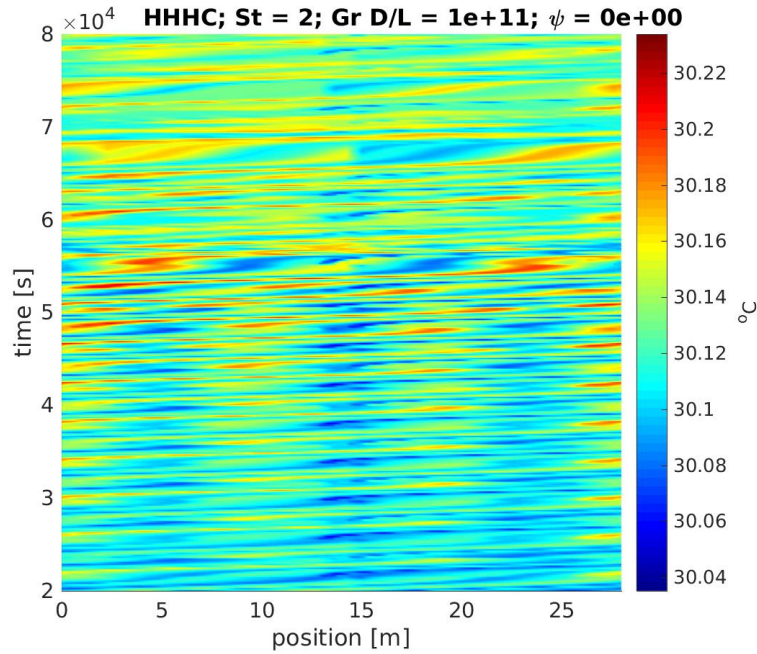


Figure A.64: Space-time chart for temperature in HHHC loop, $\text{St} = 2$, $\text{Gr } D/L = 10^{11}$, $\psi = 0$.

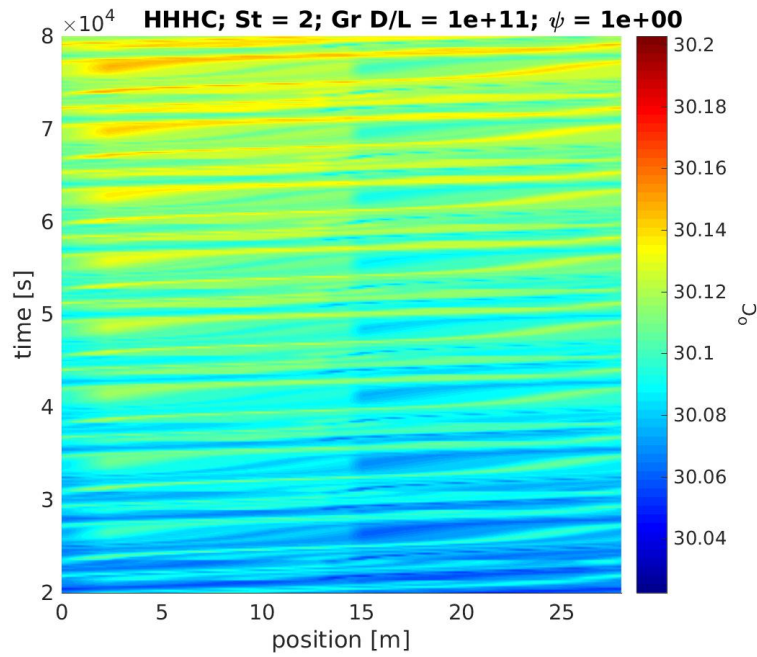


Figure A.65: Space-time chart for temperature in HHHC loop, $\text{St} = 2$, $\text{Gr } D/L = 10^{11}$, $\psi = 1$.

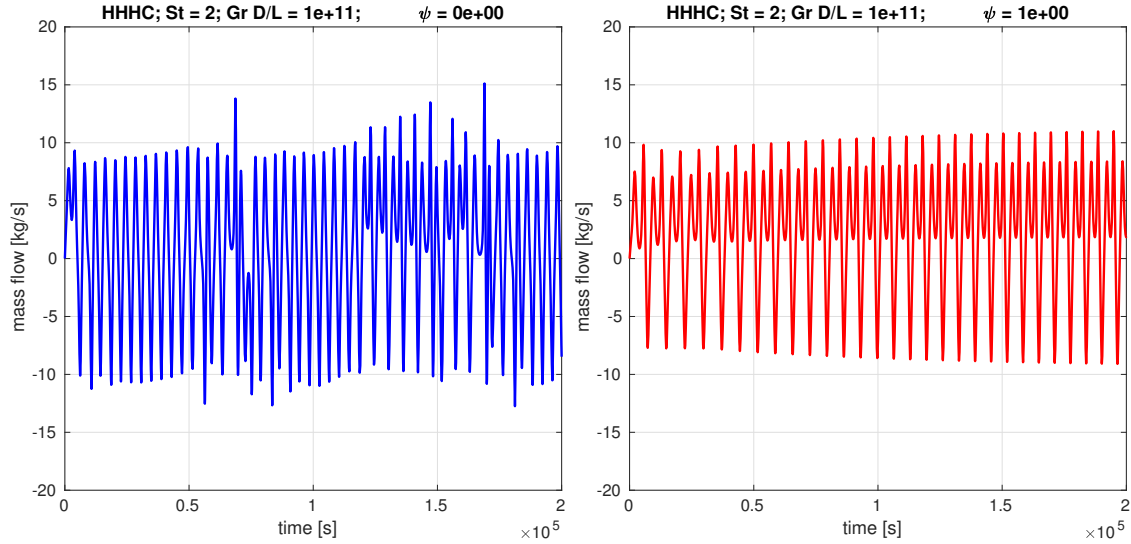


Figure A.66: Comparison of time series for mass flow rate using $\psi = 0$ and $\psi = 1$, in HHHC loop, $St = 2$, $Gr D/L = 10^{11}$.

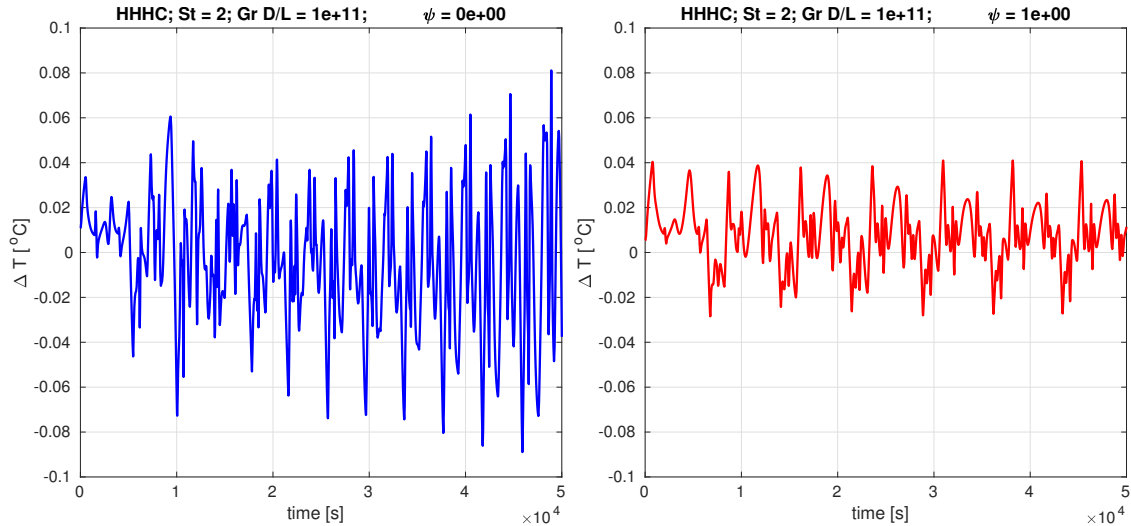


Figure A.67: Comparison of time series for temperature difference across heater using $\psi = 0$ and $\psi = 1$, in HHHC loop, $St = 2$, $Gr D/L = 10^{11}$.

A.3.2 HHVC

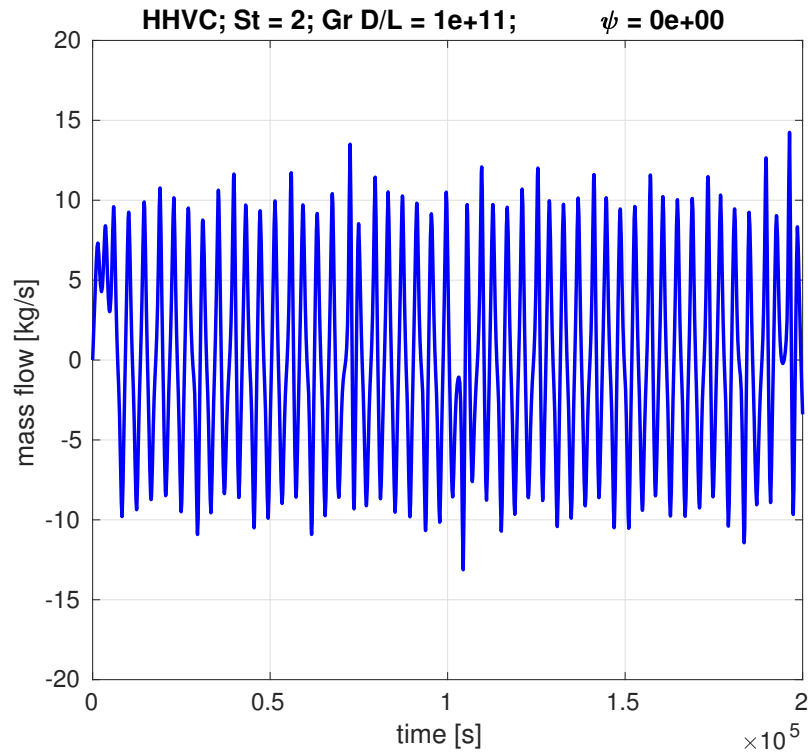


Figure A.68: Transient mass flow rate for HHVC loop, $St = 2$, $Gr D/L = 10^{11}$, $\psi = 0$.

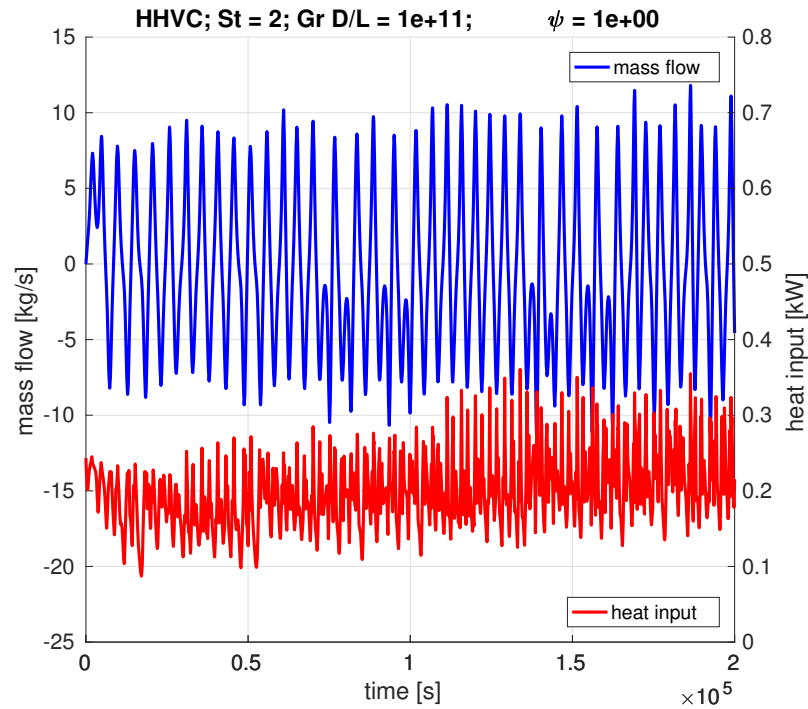


Figure A.69: Transient mass flow rate for HHVC loop, $St = 2$, $Gr D/L = 10^{11}$, $\psi = 1$.

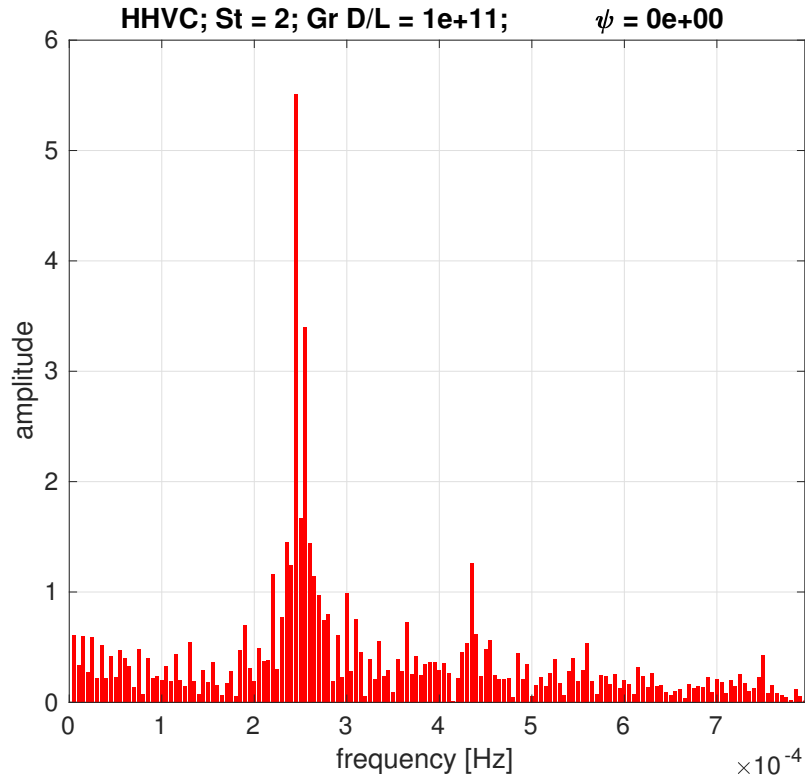


Figure A.70: Frequency domain of mass flow for HHVC loop, $St = 2$, $Gr D/L = 10^{11}$, $\psi = 0$.

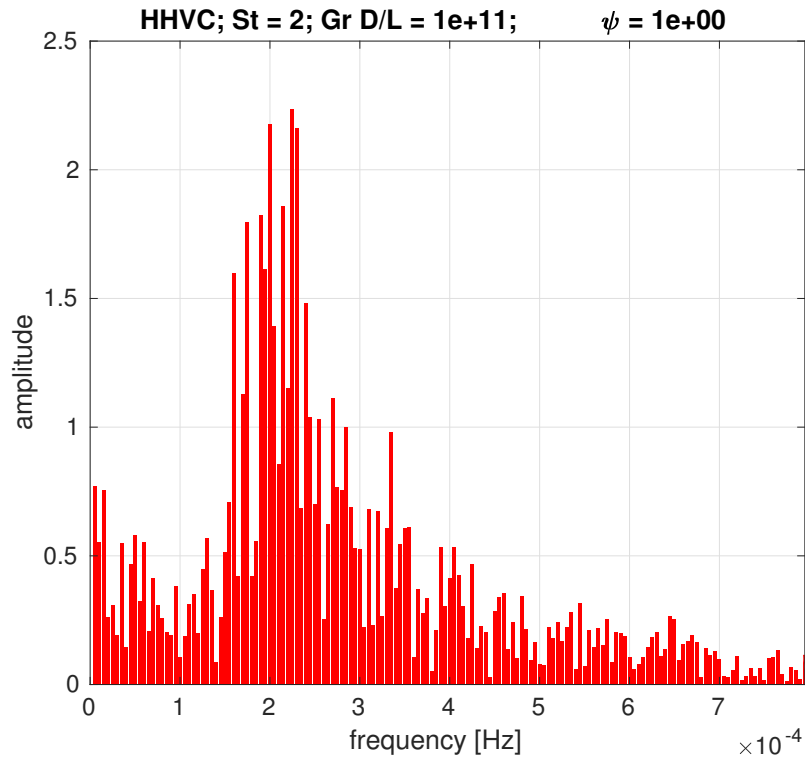


Figure A.71: Frequency domain of mass flow for HHVC loop, $St = 2$, $Gr D/L = 10^{11}$, $\psi = 1$.

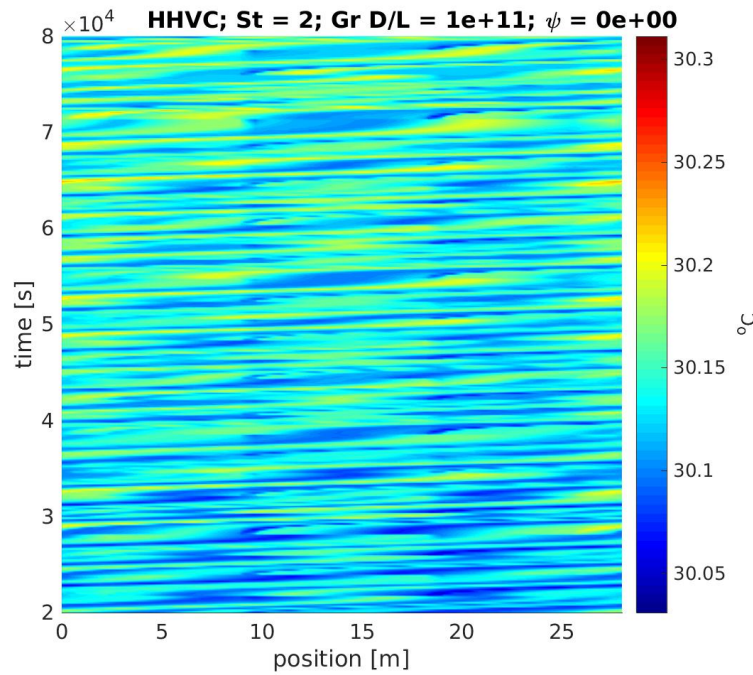


Figure A.72: Space-time chart for temperature in HHVC loop, $St = 2$, $Gr D/L = 10^{11}$, $\psi = 0$.

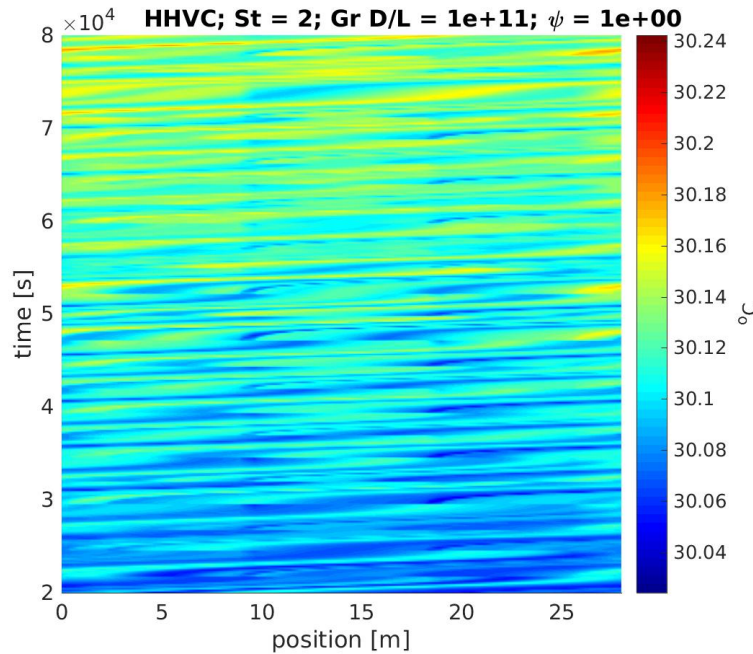


Figure A.73: Space-time chart for temperature in HHVC loop, $St = 2$, $Gr D/L = 10^{11}$, $\psi = 1$.

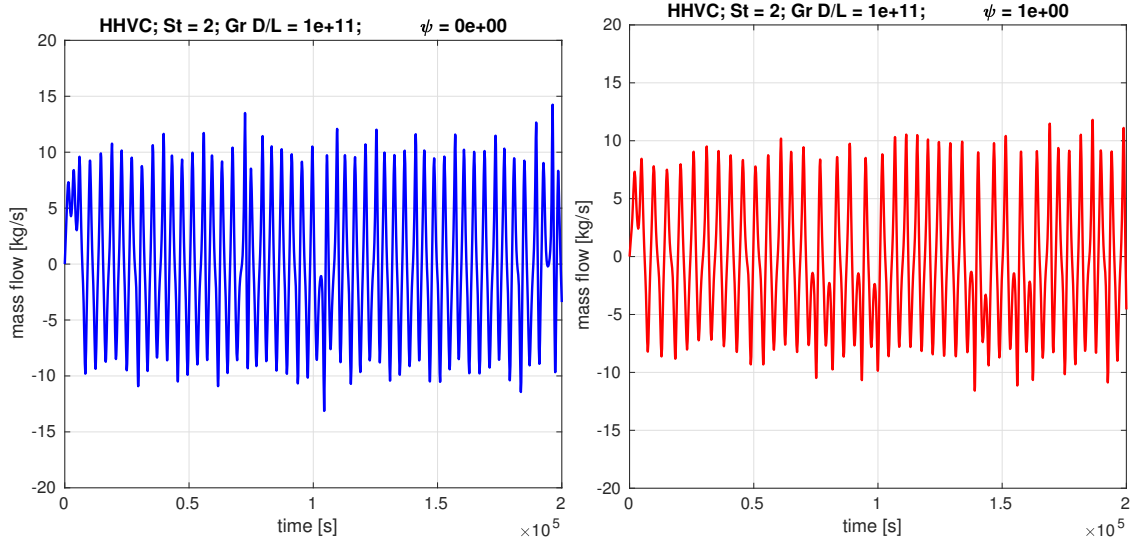


Figure A.74: Comparison of time series for mass flow rate using $\psi = 0$ and $\psi = 1$, in HHVC loop, $St = 2$, $Gr D/L = 10^{11}$.

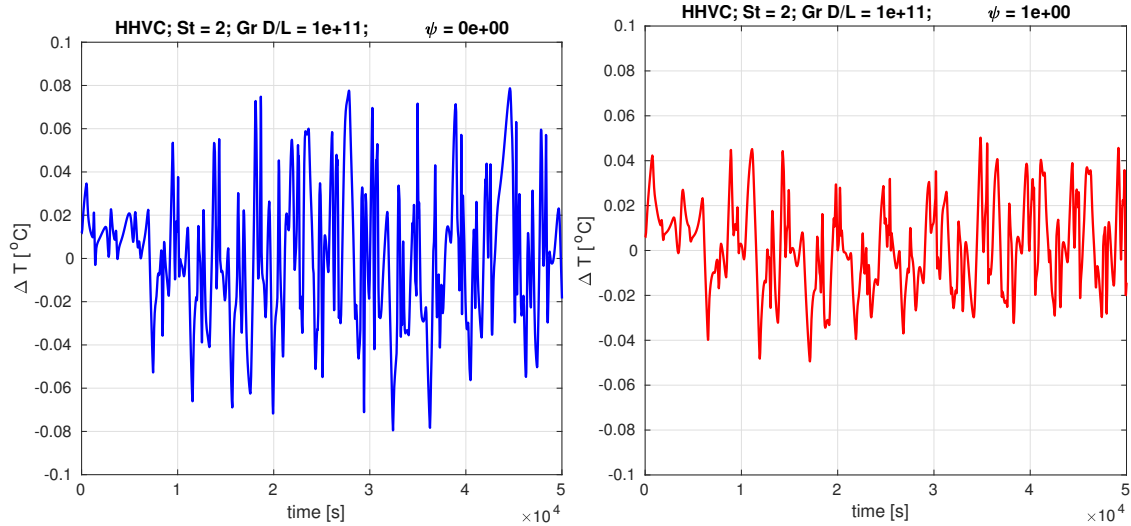


Figure A.75: Comparison of time series for temperature difference across heater using $\psi = 0$ and $\psi = 1$, in HHVC loop, $St = 2$, $Gr D/L = 10^{11}$.

A.3.3 VHHC

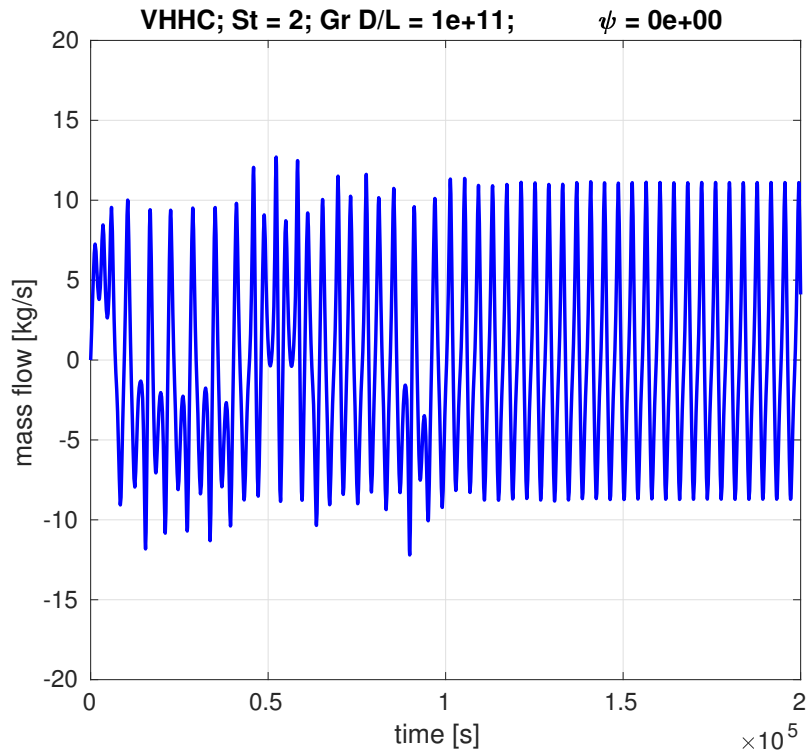


Figure A.76: Transient mass flow rate for VHHC loop, $St = 2$, $Gr D/L = 10^{11}$, $\psi = 0$.

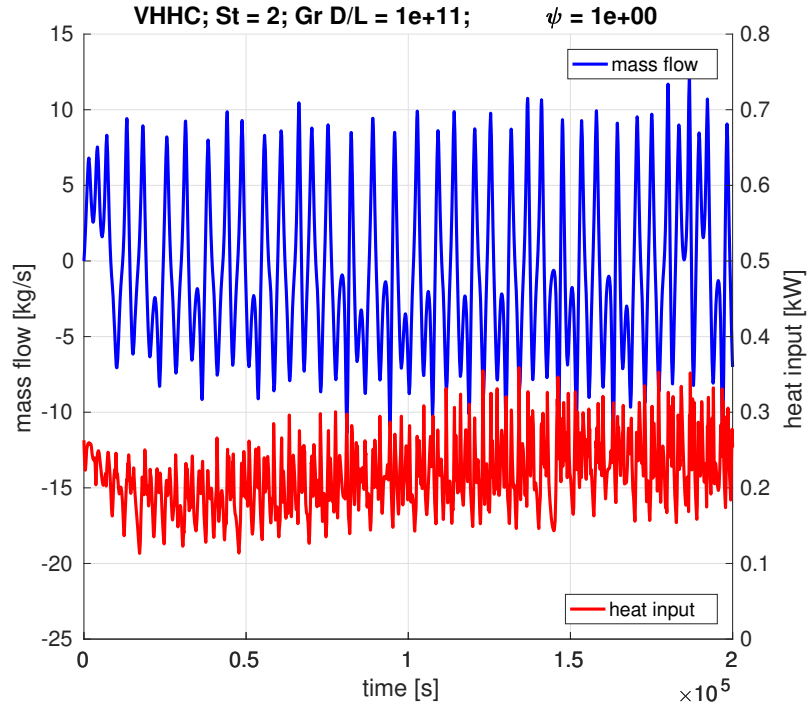


Figure A.77: Transient mass flow rate for VHHC loop, $St = 2$, $Gr D/L = 10^{11}$, $\psi = 1$.

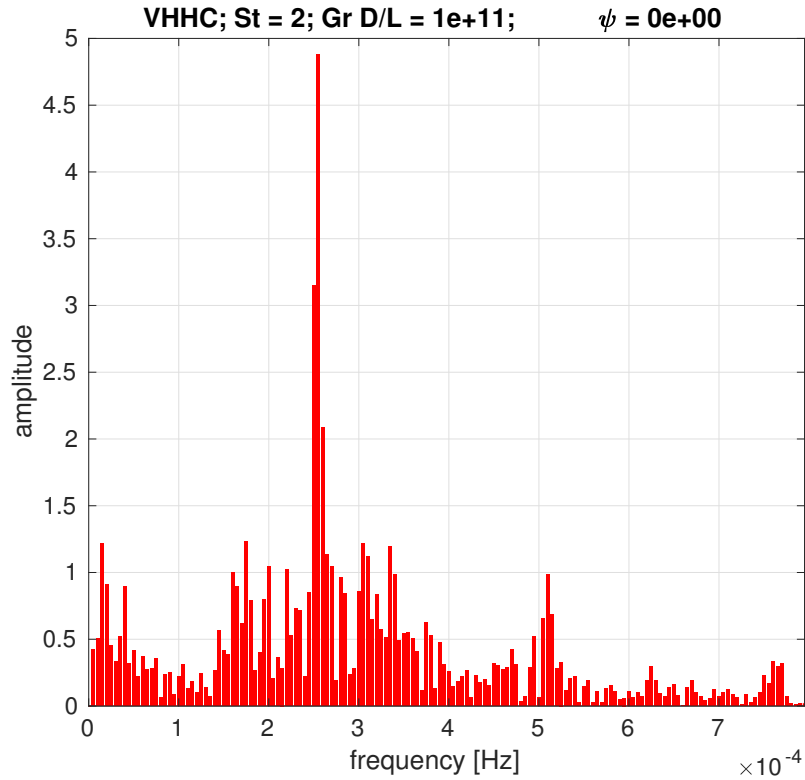


Figure A.78: Frequency domain of mass flow for VHHC loop, $St = 2$, $Gr D/L = 10^{11}$, $\psi = 0$.

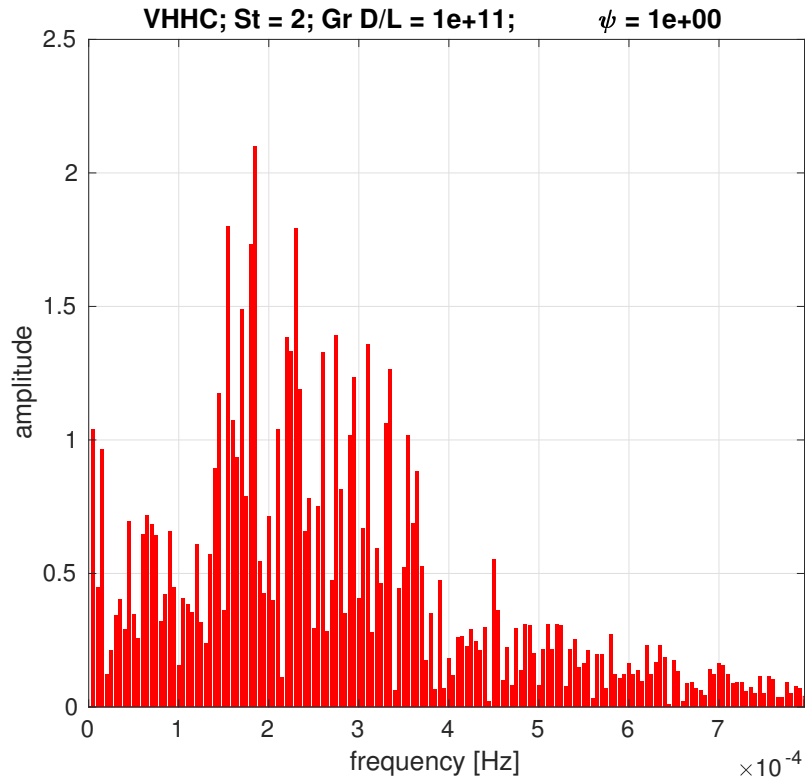


Figure A.79: Frequency domain of mass flow for VHHC loop, $St = 2$, $Gr D/L = 10^{11}$, $\psi = 1$.

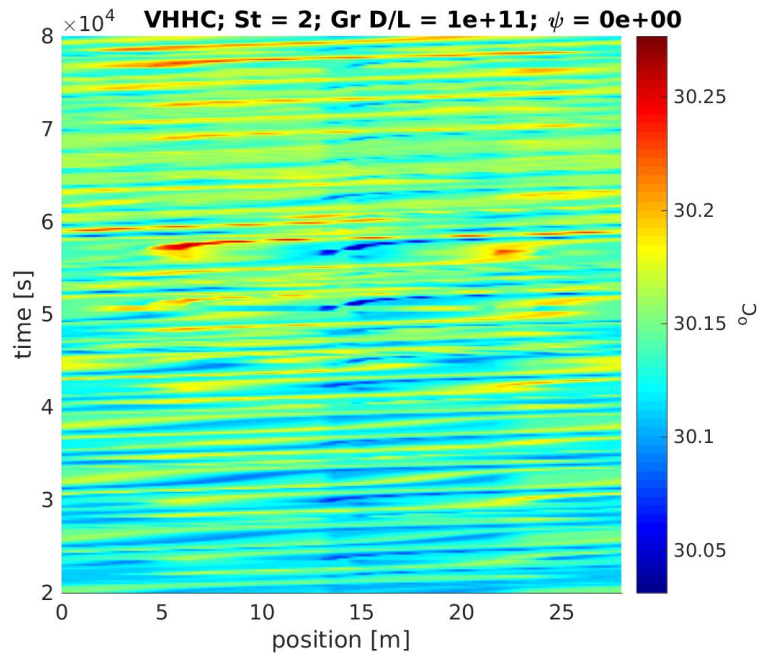


Figure A.80: Space-time chart for temperature in VHHC loop, $\text{St} = 2$, $\text{Gr } D/L = 10^{11}$, $\psi = 0$.

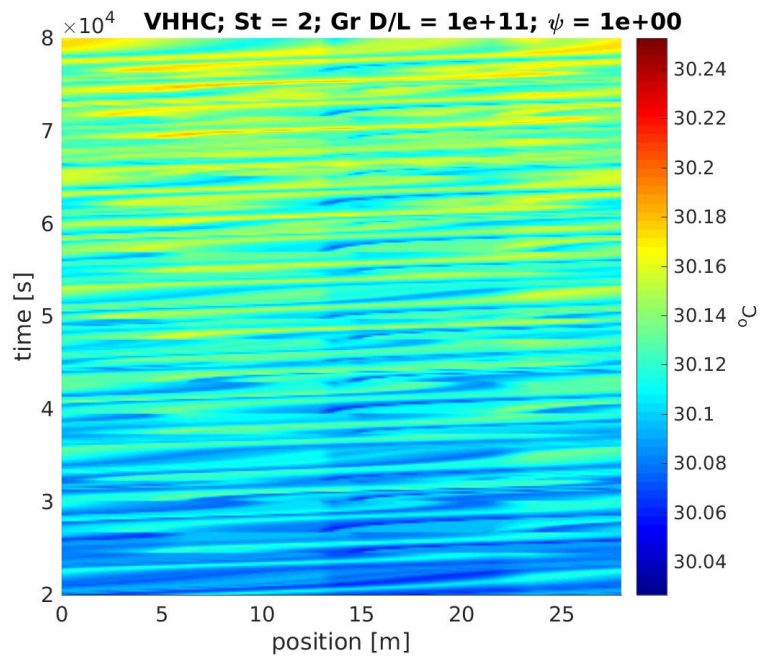


Figure A.81: Space-time chart for temperature in VHHC loop, $\text{St} = 2$, $\text{Gr } D/L = 10^{11}$, $\psi = 1$.

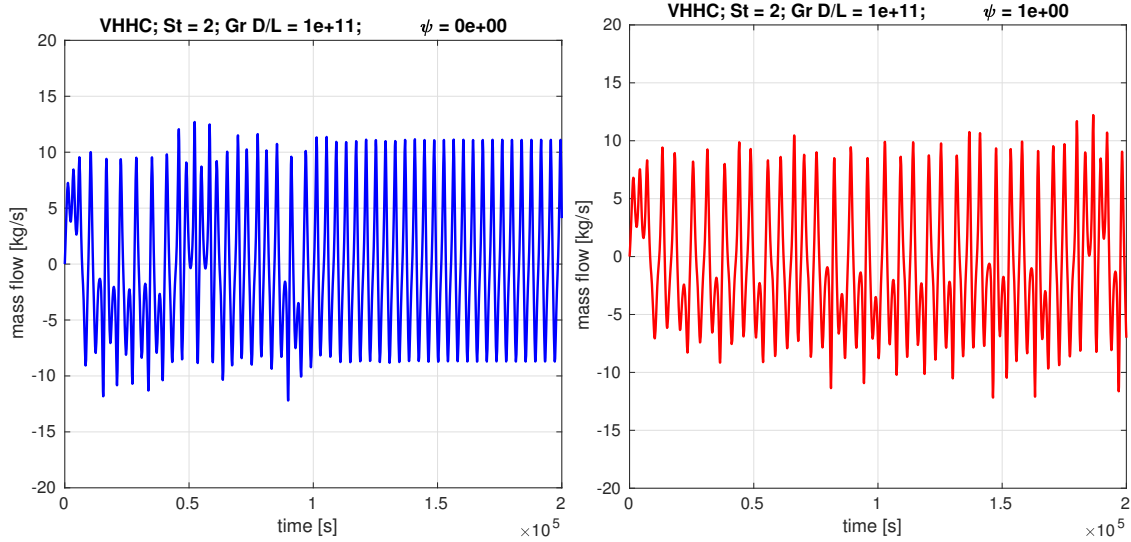


Figure A.82: Comparison of time series for mass flow rate using $\psi = 0$ and $\psi = 1$, in VHHC loop, $St = 2$, $Gr D/L = 10^{11}$.

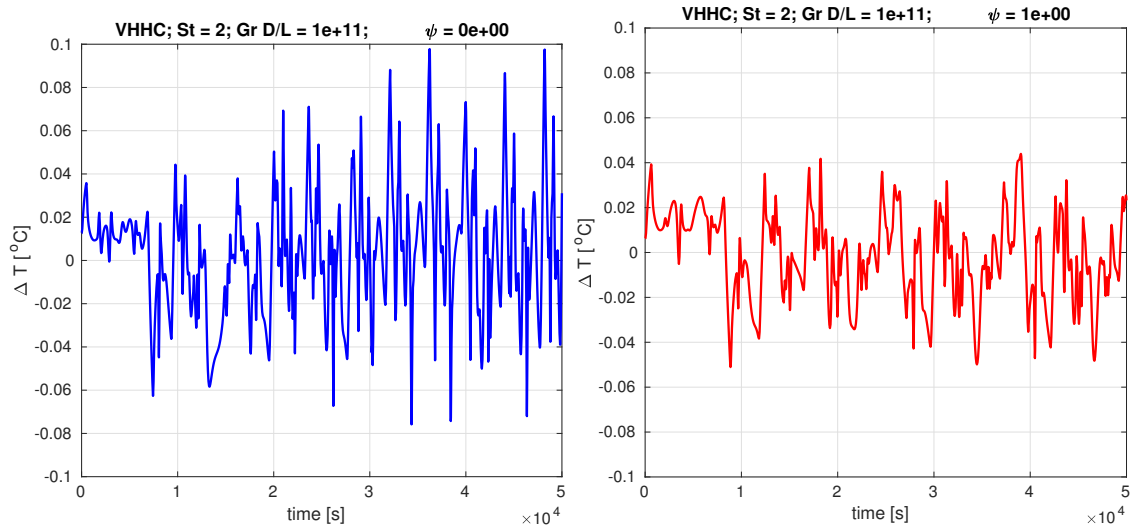


Figure A.83: Comparison of time series for temperature difference across heater using $\psi = 0$ and $\psi = 1$, in VHHC loop, $St = 2$, $Gr D/L = 10^{11}$.

A.3.4 VHVC

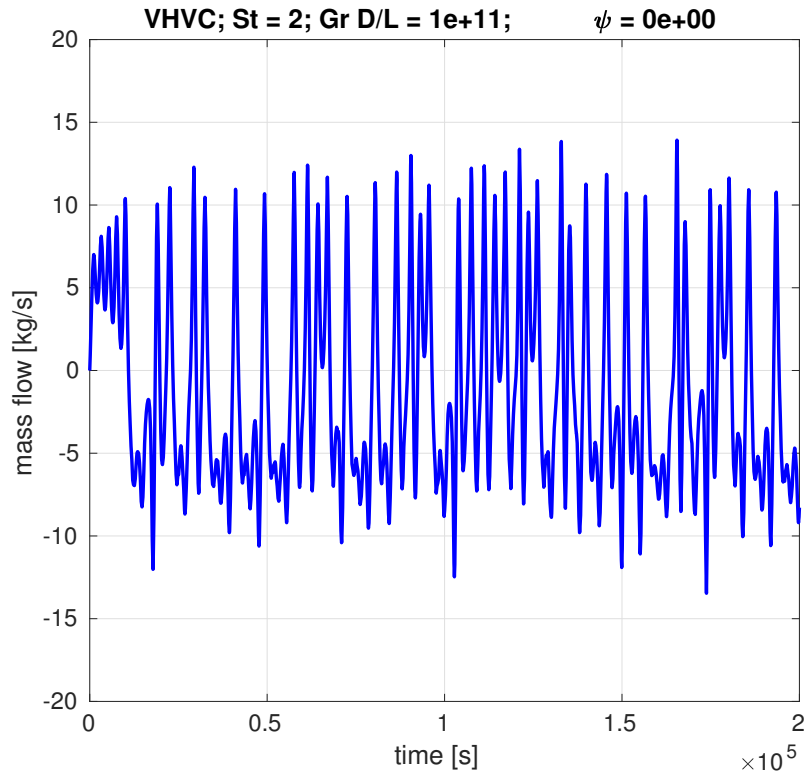


Figure A.84: Transient mass flow rate for VHVC loop, $St = 2$, $Gr D/L = 10^{11}$, $\psi = 0$.

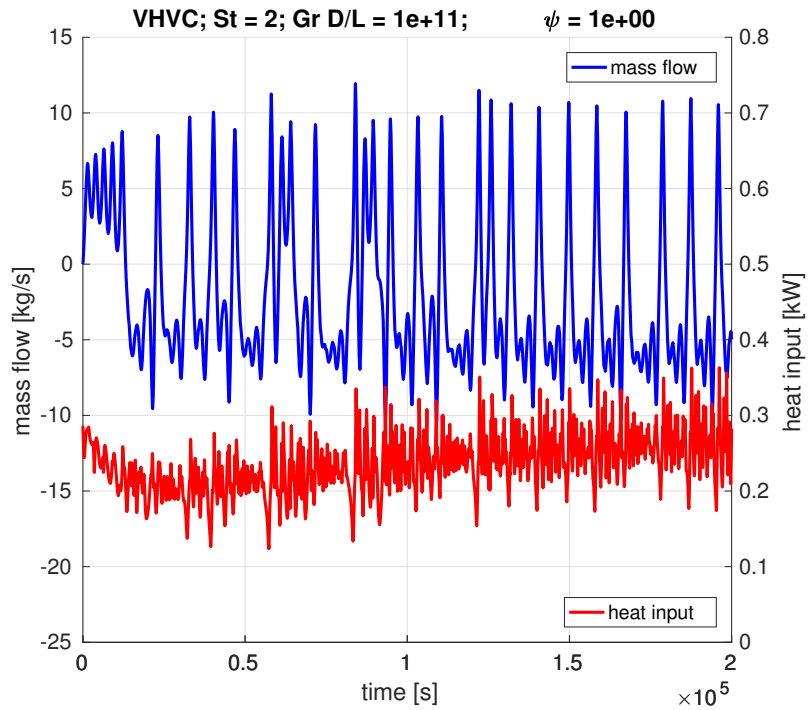


Figure A.85: Transient mass flow rate for VHVC loop, $St = 2$, $Gr D/L = 10^{11}$, $\psi = 1$.

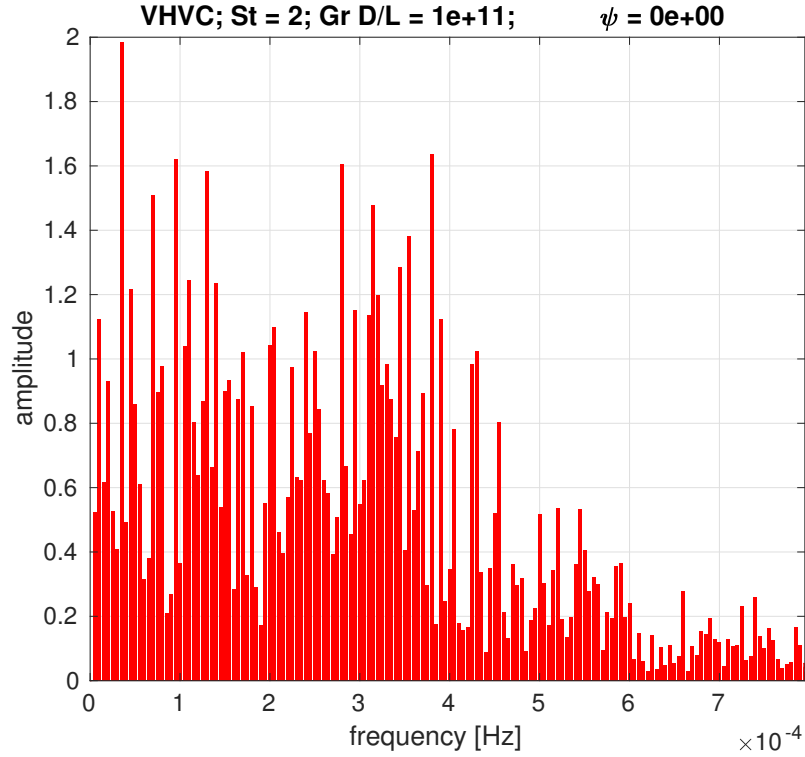


Figure A.86: Frequency domain of mass flow for VHVC loop, $St = 2$, $Gr D/L = 10^{11}$, $\psi = 0$.

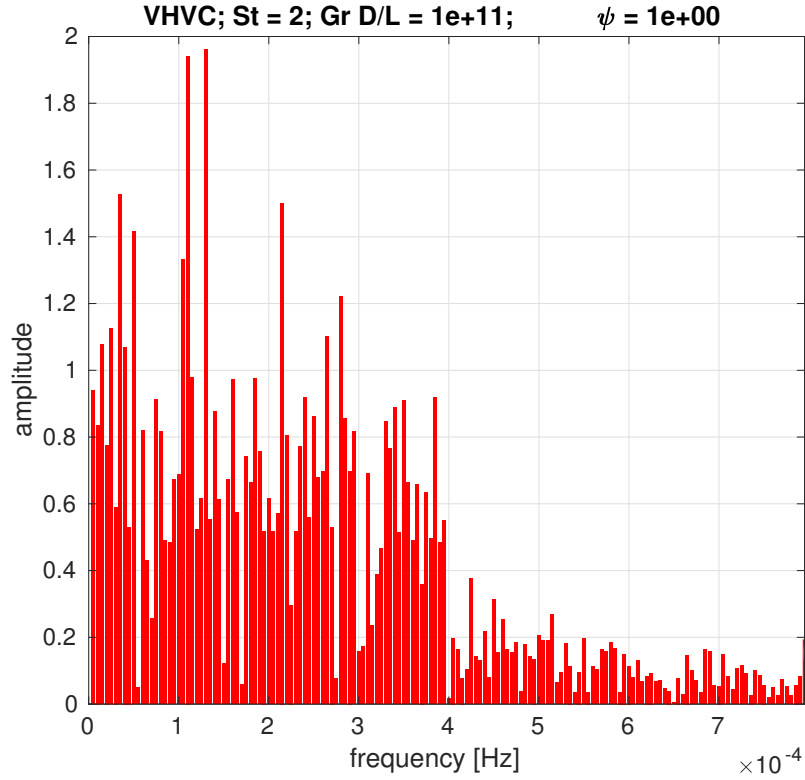


Figure A.87: Frequency domain of mass flow for VHVC loop, $St = 2$, $Gr D/L = 10^{11}$, $\psi = 1$.

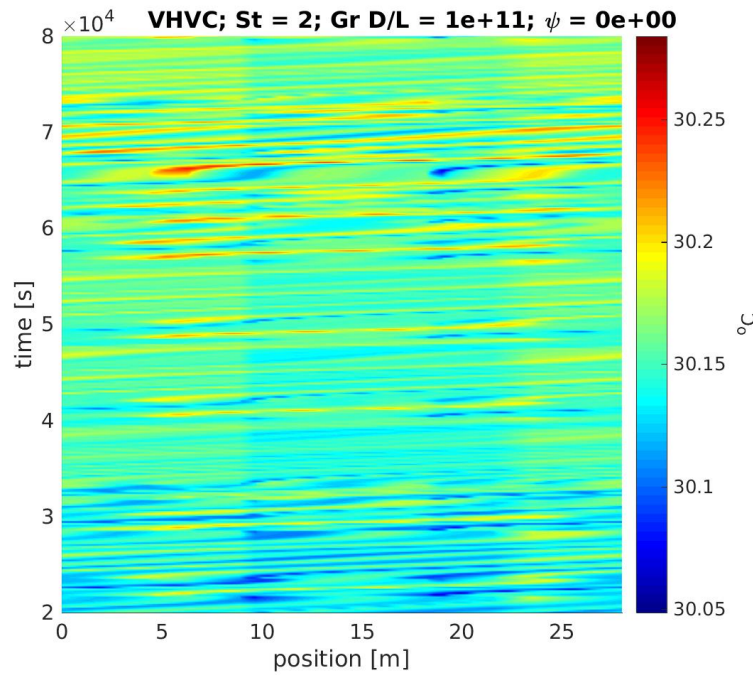


Figure A.88: Space-time chart for temperature in VHVC loop, $St = 2$, $Gr D/L = 10^{11}$, $\psi = 0$.

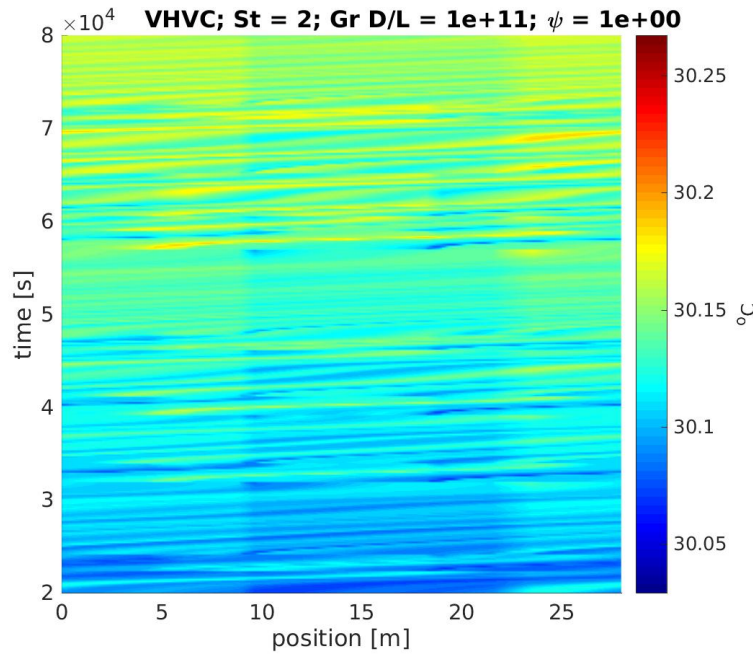


Figure A.89: Space-time chart for temperature in VHVC loop, $St = 2$, $Gr D/L = 10^{11}$, $\psi = 1$.

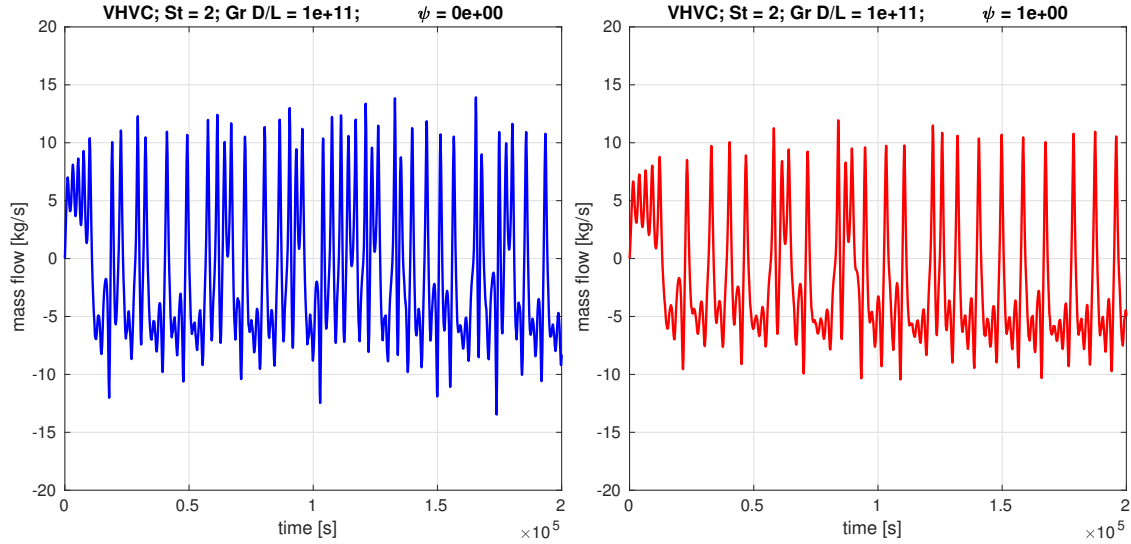


Figure A.90: Comparison of time series for mass flow rate using $\psi = 0$ and $\psi = 1$, in VHVC loop, $St = 2$, $Gr D/L = 10^{11}$.

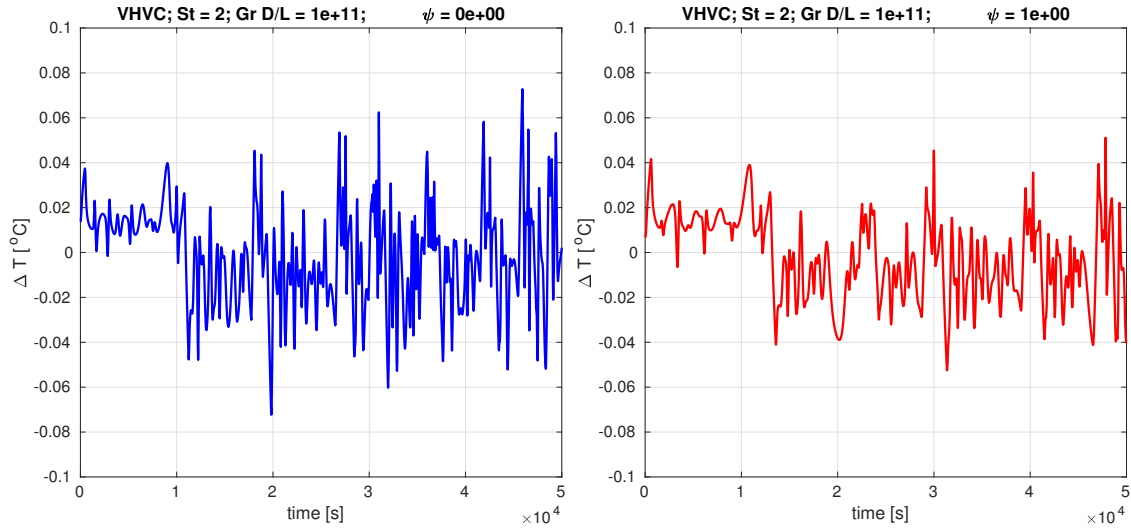


Figure A.91: Comparison of time series for temperature difference across heater using $\psi = 0$ and $\psi = 1$, in VHVC loop, $St = 2$, $Gr D/L = 10^{11}$.